SAIMM
JOURNAL OF THE SOUTHERN AFRICAN INSTITUTE OF MINING AND METALLURGY
FOUNDED 1894
VOLUME 117 NO. 7 JULY 2017

We add real value to your mining projects.

THE MSA GROUP

The leading, black-owned mining consultancy

Tel: +27 (0)11 880 4209

Email: info@msagroupservices.com

www.msagroupservices.com

/company/the-msa-group

themsagroup

@TheMSAGroup

BBBEE level 2

rbh royal bafokeng holdings

mms mogs mining services a member of **rbh**

Educating and leading mining engineers to become Imagineers

The broad-based curriculum of the **Department of Mining Engineering** at the University of Pretoria, emphasises the international engineering education model of conceptualising, designing, implementing and operating mines.

We offer a range of programmes:

- Undergraduate Programmes [Accredited by the Engineering Council of South Africa (ECSA)]
- Postgraduate Programmes
- Research Programmes
- Continued Professional Development (CPD) Courses

A degree from this Department covers all aspects of mining engineering — from pre-feasibility assessments to closure of mines, whether it be hard rock or coal deposits, surface or underground operations. The development of management and people skills are incorporated in some of the final year modules in the undergraduate programme.

The Department hosts the first-in-Africa **Kumba Virtual Reality Centre for Mine Design** as well as the **Mining Resilience Research Institute** at its state-of-the-art facilities.

The portfolio of undergraduate, postgraduate and research degree programmes provide an excellent basis for a rewarding career in mining.

For more information contact the Head of Department:

Prof Ronny Webber-Youngman
Tel +27 (0) 12 420 3763
Email daleen.gudmanz@up.ac.za

UNIVERSITEIT VAN PRETORIA
UNIVERSITY OF PRETORIA
YUNIBESITHI YA PRETORIA

Faculty of Engineering, Built Environment and Information Technology

Fakulteit Ingenieurswese, Bou-omgewing en Inligtingtegnologie / Lefapha la Boetšenere, Tikologo ya Kago le Theknolotši ya Tshedimošo

www.up.ac.za/ebit

The Southern African Institute of Mining and Metallurgy

OFFICE BEARERS AND COUNCIL FOR THE 2016/2017 SESSION

Honorary President
Mike Teke
President, Chamber of Mines of South Africa

Honorary Vice-Presidents
Mosebenzi Zwane
Minister of Mineral Resources, South Africa

Rob Davies
Minister of Trade and Industry, South Africa

Naledi Pandor
Minister of Science and Technology, South Africa

President
C. Musingwini

President Elect
S. Ndlovu

Senior Vice-President
A.S. Macfarlane

Junior Vice-President
M. Mthenjane

Immediate Past President
R.T. Jones

Honorary Treasurer
J. Porter

Co-opted Member
Z. Botha

Ordinary Members on Council

V.G. Duke
I.J. Geldenhuys
M.F. Handley
W.C. Joughin
M. Motuku
D.D. Munro
G. Njowa
A.G. Smith
M.H. Solomon
M.R. Tlala
D. Tudor
D.J. van Niekerk
A.T. van Zyl

Past Presidents Serving on Council

N.A. Barcza
R.D. Beck
J.R. Dixon
M. Dworzanowski
H.E. James
G.V.R. Landman
J.C. Ngoma
S.J. Ramokgopa
M.H. Rogers
D.A.J. Ross-Watt
G.L. Smith
W.H. van Niekerk
R.P.H. Willis

Branch Chairpersons

Botswana	L.E. Dimbungu
DRC	S. Maleba
Johannesburg	J.A. Luckmann
Namibia	N.M. Namate
Northern Cape	C.A. van Wyk
Pretoria	P. Bredell
Western Cape	C.G. Sweet
Zambia	D. Muma
Zimbabwe	S. Matutu
Zululand	C.W. Mienie

Corresponding Members of Council

Australia:	I.J. Corrans, R.J. Dippenaar, A. Croll, C. Workman-Davies
Austria:	H. Wagner
Botswana:	S.D. Williams
United Kingdom:	J.J.L. Cilliers, N.A. Barcza
USA:	J-M.M. Rendu, P.C. Pistorius

PAST PRESIDENTS

*Deceased

* W. Bettel (1894–1895)
* A.F. Crosse (1895–1896)
* W.R. Feldtmann (1896–1897)
* C. Butters (1897–1898)
* J. Loevy (1898–1899)
* J.R. Williams (1899–1903)
* S.H. Pearce (1903–1904)
* W.A. Caldecott (1904–1905)
* W. Cullen (1905–1906)
* E.H. Johnson (1906–1907)
* J. Yates (1907–1908)
* R.G. Bevington (1908–1909)
* A. McA. Johnston (1909–1910)
* J. Moir (1910–1911)
* C.B. Saner (1911–1912)
* W.R. Dowling (1912–1913)
* A. Richardson (1913–1914)
* G.H. Stanley (1914–1915)
* J.E. Thomas (1915–1916)
* J.A. Wilkinson (1916–1917)
* G. Hildick-Smith (1917–1918)
* H.S. Meyer (1918–1919)
* J. Gray (1919–1920)
* J. Chilton (1920–1921)
* F. Wartenweiler (1921–1922)
* G.A. Watermeyer (1922–1923)
* F.W. Watson (1923–1924)
* C.J. Gray (1924–1925)
* H.A. White (1925–1926)
* H.R. Adam (1926–1927)
* Sir Robert Kotze (1927–1928)
* J.A. Woodburn (1928–1929)
* H. Pirow (1929–1930)
* J. Henderson (1930–1931)
* A. King (1931–1932)
* V. Nimmo-Dewar (1932–1933)
* P.N. Lategan (1933–1934)
* E.C. Ranson (1934–1935)
* R.A. Flugge-De-Smidt (1935–1936)
* T.K. Prentice (1936–1937)
* R.S.G. Stokes (1937–1938)
* P.E. Hall (1938–1939)
* E.H.A. Joseph (1939–1940)
* J.H. Dobson (1940–1941)
* Theo Meyer (1941–1942)
* John V. Muller (1942–1943)
* C. Biccard Jeppe (1943–1944)
* P.J. Louis Bok (1944–1945)
* J.T. McIntyre (1945–1946)
* M. Falcon (1946–1947)
* A. Clemens (1947–1948)
* F.G. Hill (1948–1949)
* O.A.E. Jackson (1949–1950)
* W.E. Gooday (1950–1951)
* C.J. Irving (1951–1952)
* D.D. Stitt (1952–1953)
* M.C.G. Meyer (1953–1954)
* L.A. Bushell (1954–1955)
* H. Britten (1955–1956)
* Wm. Bleloch (1956–1957)
* H. Simon (1957–1958)
* M. Barcza (1958–1959)
* R.J. Adamson (1959–1960)
* W.S. Findlay (1960–1961)
* D.G. Maxwell (1961–1962)
* J. de V. Lambrechts (1962–1963)
* J.F. Reid (1963–1964)
* D.M. Jamieson (1964–1965)
* H.E. Cross (1965–1966)
* D. Gordon Jones (1966–1967)
* P. Lambooy (1967–1968)
* R.C.J. Goode (1968–1969)
* J.K.E. Douglas (1969–1970)
* V.C. Robinson (1970–1971)
* D.D. Howat (1971–1972)

J.P. Hugo (1972–1973)

* P.W.J. van Rensburg (1973–1974)
* R.P. Plewman (1974–1975)
* R.E. Robinson (1975–1976)
* M.D.G. Salamon (1976–1977)
* P.A. Von Wielligh (1977–1978)
* M.G. Atmore (1978–1979)
* D.A. Viljoen (1979–1980)
* P.R. Jochens (1980–1981)

G.Y. Nisbet (1981–1982)
A.N. Brown (1982–1983)

* R.P. King (1983–1984)

J.D. Austin (1984–1985)
H.E. James (1985–1986)
H. Wagner (1986–1987)

* B.C. Alberts (1987–1988)

C.E. Fivaz (1988–1989)
O.K.H. Steffen (1989–1990)

* H.G. Mosenthal (1990–1991)

R.D. Beck (1991–1992)

* J.P. Hoffman (1992–1993)
* H. Scott-Russell (1993–1994)

J.A. Cruise (1994–1995)
D.A.J. Ross-Watt (1995–1996)
N.A. Barcza (1996–1997)

* R.P. Mohring (1997–1998)

J.R. Dixon (1998–1999)
M.H. Rogers (1999–2000)
L.A. Cramer (2000–2001)

* A.A.B. Douglas (2001–2002)

S.J. Ramokgopa (2002-2003)
T.R. Stacey (2003–2004)
F.M.G. Egerton (2004–2005)
W.H. van Niekerk (2005–2006)
R.P.H. Willis (2006–2007)
R.G.B. Pickering (2007–2008)
A.M. Garbers-Craig (2008–2009)
J.C. Ngoma (2009–2010)
G.V.R. Landman (2010–2011)
J.N. van der Merwe (2011–2012)
G.L. Smith (2012–2013)
M. Dworzanowski (2013–2014)
J.L. Porter (2014–2015)
R.T. Jones (2015–2016)

Honorary Legal Advisers
Scop Incorporated

Auditors
Messrs R.H. Kitching

Secretaries
The Southern African Institute of Mining and Metallurgy
Fifth Floor, Chamber of Mines Building
5 Hollard Street, Johannesburg 2001 • P.O. Box 61127, Marshalltown 2107
Telephone (011) 834-1273/7 • Fax (011) 838-5923 or (011) 833-8156
E-mail: journal@saimm.co.za

Typeset and Published by
The Southern African Institute of Mining and Metallurgy
P.O. Box 61127
Marshalltown 2107
Telephone (011) 834-1273/7
Fax (011) 838-5923
E-mail: journal@saimm.co.za

Printed by
Camera Press, Johannesburg

Advertising Representative
Barbara Spence
Avenue Advertising
Telephone (011) 463-7940
E-mail: barbara@avenue.co.za

The Secretariat
The Southern African Institute of Mining and Metallurgy

ISSN 2225-6253 (print)
ISSN 2411-9717 (online)

SAIMM
JOURNAL OF THE SOUTHERN AFRICAN INSTITUTE OF MINING AND METALLURGY
FOUNDED 1894

VOLUME 117 NO. 7 JULY 2017

Contents

SAIMM
JOURNAL OF THE SOUTHERN AFRICAN INSTITUTE OF MINING AND METALLURGY
VOLUME 117 NO. 7 JULY 2017

Contents *(continued)*

PAPERS OF GENERAL INTEREST

Seeing beyond the cloud, repositioning the African minerals industry

The future of any country lies with its youth. This statement is especially true for the African minerals industry. The minerals industry continues to play a pivotal role in the establishment of a strong economic base in various countries on the continent. However, the minerals industry is faced with complex challenges and stiff competition for foreign direct investment. The collapse of this industry will have dire consequences for the citizens of countries whose economies are reliant on mining. However, these challenges present industry leaders and young professionals with an opportunity to create a vision for the mining industry that will inspire confidence for the future of Africa. Young professionals must create and own a roadmap that describes the steps necessary to realize this future. To create this roadmap, it is necessary to take cognisance of the mining policies, human capital, and techno-economic conditions needed to change the status quo and position Africa as a destination of choice for capital investment.

One of the ways to map out the future of the minerals industry was to host a conference at which young professionals could engage in dialogue on what this future will look like. This dialogue was supplemented with networking sessions with industry leaders.

This edition of the *Journal* contains some of the papers that were presented during the conference. The first paper discusses unlocking the potential of deep-level mining through multi-stakeholder collaborations. The next two papers focus on the necessary design considerations towards integrated mine planning and creating a technology map to facilitate modernization in the minerals industry. The last three papers cover topics in mineral processing, *vis-à-vis* investigating cost-effective ways of recovering rare earth elements from alternative sources; development of a technique for nickel electrodeposition from sulphate electrolytes; and investigation and optimization of the industrial process for extraction of iron, vanadium, and titanium from titanomagnetite. The remainder of the papers addresses various issues affecting the minerals industry.

The minerals industry is in need of young professionals to develop solutions for the numerous complex challenges alluded to earlier. Solving these challenges will require a collaborative effort involving the different stakeholders such as academic and research institutions, the minerals industry, governments, and communities. I wish to take this opportunity to thank all individuals and organizations that made this Young Professionals Conference a success.

S. Nhleko
Chairperson of the Organizing Committee

Skills for Mining Labour Productivity Improvement

It is amazing how quickly time passes by – just nine articles ago, I invited you to join me in reading my thoughts as you enjoyed your cup of coffee and to keep company with me for some more coffee chats. In this article, which is my penultimate one as President of the SAIMM, I would like to share with you my recent engagement with the Chamber of Mines of South Africa.

On 23 May 2017 I delivered a Keynote Address at the Chamber of Mines pre-AGM dinner. The focus of the address was the role of the mining industry in Higher Education Institutions (HEIs) during these challenging times in the HEI landscape, and how HEIs should be addressing the mining industry's skills needs. As a point of departure, my address touched on productivity as a theme on which both the mining industry and HEIs should be having robust discussion. I therefore would like to share with you my thoughts on this subject.

Productivity is a very relevant and important discussion point for the mining industry. It is so, given that our industry has been experiencing declining productivity in the past decade, although equipment efficiencies have been increasing. For example, according to a McKinsey study released in 2015, US mining labour productivity had declined nearly 30% since 2007, while other production sectors such as motor vehicle manufacturing had improved their productivity by nearly 180% over the same period. The same report also indicated that mining labour productivity in two other major mining countries, Australia and South Africa, had declined since 2007 by about 50% and 35%, respectively. In contrast, original equipment manufacturers (OEMs) have been reporting increased equipment efficiencies. For example, Atlas Copco reported an approximate 50% increase in the efficiency of their drilling equipment between 2000 and 2005. Why is it that the mining industry's labour productivity is regressing, yet equipment efficiencies are improving? As professionals in the mining industry, should we not be thinking seriously about the urgency and different ways of improving productivity?

It is not 'rocket science' that by increasing productivity it becomes possible to improve profitability. If profitability increases, companies are able to do the things they would like to do and those that government, labour unions, and communities expect or require them to do. Given the importance of increasing productivity, how can we get productivity on the right path given that, as an industry, we seem not to be adequately exploiting improved equipment efficiencies? Two of the papers in this edition of the Journal touch on this important aspect by relating production, productivity, and technology (including technology maps, as described in one of the papers). These ideas extend to mechanization and modernization as alluded to in the two papers.

The mismatch between productivity and equipment efficiency stems from a lack of the unique skills that are required to convert the improved equipment efficiencies into increased productivity. It is people with the right skills set that can correct the mismatch, because mining production systems cannot drive themselves. Even autonomous mining production systems require people – mines cannot operate themselves, processes cannot operate themselves, and the production system is not self-maintaining without human intervention. The designing, planning, and operation of a mining production system as a *system* requires the incorporation of systems engineering approaches. It also requires a mind-set change away from traditional approaches of designing, planning, and operating mining production systems in 'silos'. Whether or not one is of the view that 'mechanization' or 'modernization' is the panacea for the productivity challenges that our mining industry faces, it is imperative to incorporate systems engineering throughout the mining process. In order to incorporate systems engineering or systems thinking, four high-end skills are required. These are a high intelligence quotient (IQ) required for problem-solving, emotional quotient (EQ) required for managing relationships, creative quotient (CQ) required for innovation using multidisciplinary knowledge, and adaptive quotient (AQ) required for embracing change. A high IQ is required because the mining operating environment is becoming increasingly complex. A high EQ is needed because the ever-increasing stakeholder demands on the mining industry require good relationship skills, negotiating capability, and management and leadership skills, to mention but a few. A high CQ is required for a systems engineering mind-set in order to accomplish work in multi-disciplinary teams. A high AQ is required because the only constant in our industry is change, which requires us to adapt to address existing and new challenges. I am convinced that as the SAIMM, we will remain relevant into the future by ensuring that our programmes and conferences address the key skills that are required to improve mining labour productivity.

C. Musingwini
President, SAIMM

http://dx.doi.org/10.17159/2411-9717/2017/v117n7a1

Multi-stakeholder collaboration to unlock the potential of deep-level mining in South Africa

by K.M. Letsoalo*

Synopsis

South Africa's narrow-reef mining operations are facing challenges such as volatile commodity prices, operational cost increases in excess of inflation, health and safety issues, and depletion of less geologically complex reserves. These challenges have resulted in declining production profiles for many mining companies. Data collected and modelled from South Africa's three principal gold mining companies, AngloGold Ashanti, Harmony Gold, and Sibanye Gold, indicates that 592 Mt of mineable gold resources remain, with up to 496 Mt of potential reserves available if miners adopt mechanized systems. These resources have the potential to extend the life of gold mining operations beyond the year 2045. A similar situation exists in the platinum sector, where 360 Mt of production can be exploited with the application of non-conventional mining methods.

During investigations as part of the Phakisa initiative, it was noted that current industry challenges require solutions that are specific to the South African tabular mining environment. These solutions include increasing local mining research and development capacity, encouragement of local equipment manufacturing and associated procurement, and technology and skills transfer. Owing to the magnitude of the changes required to establish a sustainable mining industry, stakeholders agreed to a collaborative approach through a public-private partnership.

This paper seeks to provide a background to the Mining Phakisa initiative and the drivers behind collaboration of various stakeholders to ensure sustainability of the South African deep-level mining industry. The collaboration drivers are discussed by highlighting challenges in South Africa in relation to mining.

Keywords
narrow-reef mining, sustainability, mining R&D, public-private partnership, technology readiness.

Introduction

Modern commercial mining in South Africa dates back to 1846 with the exploitation of copper in Namaqualand. The economic viability of the venture was hampered by the remote location of the deposit, adverse geological conditions, poor excavation stability, and the extraction method used. South Africa's deep-level mining operations find themselves in a similar situation today. Increased geotechnical and rock engineering challenges, increased mining depth, low productivity, and dwindling available mineral reserves are some of the factors contributing to the economic impediment of the platinum and gold mining sectors. Figure 1 indicates South Africa's contribution to the global production of gold. Historically, South Africa was the largest gold-producing country, but it has now dropped to seventh place.

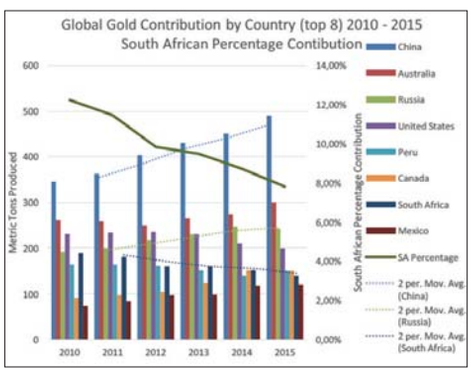

Figure 1—The top eight global gold producers, and South Africa's production and percentage contribution (Fenn, 2016)

Fenn (2016) concluded that the trends presented in Figure 1 do not coincide with those seen in other emerging economies. Emerging economies like China and Russia have a positive production growth, while that for South Africa is negative. South Africa's contribution to global production of gold declined by 7.89% between 2014 and 2016. Despite the decline in production, South Africa's reserves of the following commodities are ranked number one the in world, (Hermanus, 2016) :

- PGMs (87.7%)
- Chromium (72.4%)
- Manganese (80%)
- Titanium (65%)
- Gold (12.7%).

The available mineral resources in South Africa, particularly platinum and gold, justify a change in mindset and approach towards metalliferous mining. The value of existing resources depends on the extraction methods and the efficiency of mining operations. Without a change in these, South Africa's mining outputs will continue to decline.

* *Chamber of Mines of South Africa.*
 ISSN 2225-6253. This paper was first presented at the 3rd Young Professionals Conference, *9–10 March 2017, Innovation Hub, Pretoria, South Africa.*

Multi-stakeholder collaboration to unlock the potential of deep-level mining

The state of the South African mining industry

Declining employment

The mining industry in South Africa is considered as one of the key employers, with approximately 450 000 people directly employed in the sector, each employee having at least nine dependants (Chamber of Mines, 2014). The industry shed 47 000 jobs between 2012 and the first quarter of 2015, which had an indirect impact on 423 000 people. Statistics South Africa (Stats SA) (2016) indicated that employment in the mining industry continues to decline, with eight consecutive quarterly decreases since the fourth quarter of 2014.

Despite the decline in employment, gross earnings paid to employees across the mining sectors increased by R30 million in the quarter ending June 2016. The total gross remuneration increased by 6.3% (R31 billion) compared to the previous year (Statistics South Africa, 2016). The total earnings by employees in the mining industry amounted to R523 billion between June 2015 and June 2016 (Statistics South Africa, 2016).

The platinum wage strike in 2012 was one of the major reasons behind the decline in employment statistics. During the Mining Phakisa Lab it was noted that the mining sector is still recovering from the 515 971 man-days that were lost due to industrial action between 2012 and 2013.

Contribution to the gross domestic product

Mining's contribution to the GDP is linked with, and measured on, production output, which has declined in recent years. Mining contributed close to 21% to the GDP in 1970, but this figure had fallen to 7.7% by 2015. Gold and uranium were the main commodities in 1970, accounting for 17% of the 21% contribution. Structural factors in the sector, rather than falling commodity prices, have been the main cause of the decline in GDP contribution over recent years (Pirouz, 1999). The infrastructure on most of the gold operations is over 20 years old, and this, coupled with mine design and layout, has constituted the biggest challenge to production output.

Resources and reserves

South Africa's mineral resources are still considered to be among the foremost in the world, but deep-level operations are facing challenges with the depletion of easily accessible resources. Geological surveys indicate that South Africa has approximately 1.9 billion ounces of remaining gold resources (Chamber of Mines South Africa, 2015), only 0.2 billion ounces of which have been converted into reserves. This leaves the country with close to 1.7 billion ounces of gold resources that have the potential to be converted into reserves. However, significant changes in the extraction methods will be needed in order to economically exploit these resources.

Approximately 1.4 billion ounces of platinum resources are available in South Africa, and only 0.2 billion ounces have been mined to date (Chamber of Mines South Africa, 2015). Half (0.7 billion ounces) of the remaining platinum resources are at a depth between 2 and 4 km, and are potentially economically viable. Like gold operations, significant changes are required in the extraction methods to render these resources economically viable. The deepest platinum operation is currently just below 2.2 km, and ventilation and geothermal heat are among the major challenges.

Productivity

Productivity in the South African mining industry peaked in the year 2000, with gold and platinum production at 2 kg and 2.3 kg per person, respectively. However, the industry has experienced a decline in productivity levels since then, and productivity is currently at its lowest point. According to Singh (2016), platinum output per worker declined by 49% between 1999 and 2014, while the real labour cost per kilogram increased by 309%.

Research

South Africa's Chamber of Mines Research Organisation (COMRO) was considered to be one of the best mining research organizations in the world. COMRO was established in 1964 to carry out research on a collaborative basis on behalf of member companies of the Chamber of Mines South Africa. COMRO experienced a funding reduction in the late 1980s, which led to its closure in 1992, resulting in the loss of South African researchers to countries like Australia and Canada.

DeepMine, PlatMine, and FutureMine are some of the collaborative research programmes that were established between 1998 and 2005, after COMRO (Rupprecht, 2017). These programmes, which were set up to operate over fixed periods, were introduced to address specific mining challenges, including the mining of gold at depths greater than 3000 m. The funding and scale of these programmes were not equivalent to that of COMRO.

Following the closure of COMRO, mining companies such as Anglo American took it upon themselves to conduct in-house research. This has proven to be a challenge during commodity price slumps. It was noted during engagements with mining companies that research projects are the first to suffer budget cuts during price slumps. From a national perspective, in-house research initiatives do not assist with capacity-building because this type of research is focused on competitive advantage and business sustainability, as opposed to the sustainability of the sector as a whole.

Technology in narrow-reef mining

Narrow-reef mining methods, technology, and mechanized equipment have not changed much over the last century, despite the productivity fluctuations. There have been three significant innovations (Pickering, 2004):

- The introduction of hand-held pneumatic rock-drills around 1970, which were designed to replace rig-mounted units. Industry is currently exploring the potential of electrohydraulic drills
- Scraper winches were introduced in the 1920s to replace shovels for moving rock. Most mining operations today rely on scraper winches for rock moving in stopes
- Hydraulic props were introduce in the 1960s as a form of yielding support, and are still used in the industry today.

The minimal changes in the technology used in

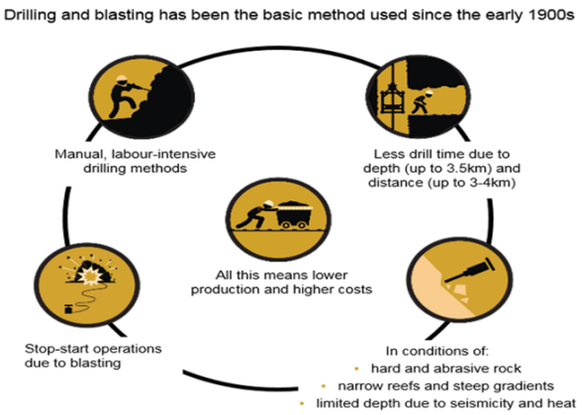

Figure 2—Current state of deep-level mining (Chamber of Mines South Africa, 2015)

conventional mining reflect the lack of overall change in deep-level operations over the years. Narrow-reef metalliferous operations in South Africa are still cyclical and labour-intensive; production activities are interdependent and a significant amount of labour is required to complete a production cycle. The cyclical nature of the operations, as shown in Figure 2, is inherent in the drilling and blasting process that has been used since the early 1900s. Mining a panel in a mechanized mine (*e.g.* a manganese mine) requires only six or so crew members, while in a conventional mining operation an average crew of 14 members is required to complete the production cycle. The underground coal mining industry has introduced new technologies like continuous miners, resulting in improved safety and productivity.

New developments: the Phakisa initiative

The Phakisa initiative is a multi-stakeholder collaborative process that was convened by the government of South Africa. Operation Phakisa was designed to address and fast-track implementation of solutions that are critical to national development (Department of Planning, Monitoring and Evaluation, 2016). The programme involves a range of key stakeholders, including government, private companies, and research organizations in the sectors that plan and oversee the implementation of initiatives. The intention is for the initiatives to have a positive impact on economic growth and society. The areas of focus include mining, the oceans, and education.

The idea adopted by the South African government based was on a Malaysian development programme called the Industrial Collaboration Programme (ICP). The aim of this programme is to reaffirm government's commitment to the development of national technology, industry, and the economy (Malaysia Government, 2013). ICP is designed to improve Malaysia's competitiveness in the global market, supported by a systematic development strategy and a holistic view of the economy (Malaysia Government, 2013).

Like the ICP, the objective of the Phakisa initiative is to 'develop collaborative interventions that will ultimately have tangible impacts on the short- and medium-term challenges faced by the mining cluster. These interventions need to take into [account] economic and socio-economic historical,

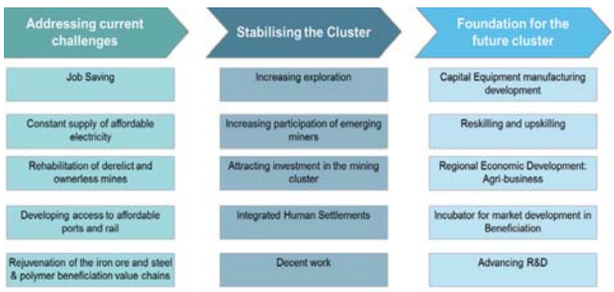

Figure 3—Mining Phakisa – Advancing the Cluster building blocks (Operation Phakisa, 2015)

structure, and immediate challenges that exist in the cluster. Collaboration should be entrenched in the institutional mechanisms that will be applied to address the challenges' (Operation Phakisa, 2015).

The goal of the Mining Phakisa is to intervene as far as possible to keep the industry afloat during commodity price slumps. Additional goals include putting in place initiatives that will position the mining cluster on a firm foundation to grow, transform, and optimize the contribution of the industry to the economic and social development of mining-related communities and the country as a whole.

The execution of the Mining Phakisa outcomes is built on a three-phase horizon, as seen in Figure 3. The first phase includes addressing the challenges that are currently experienced by the cluster (these challenges are not limited to those presented in the diagram). Once the current challenges are addressed, the next phase would involve stabilizing the cluster in order to yield results over the medium to long term. The last phase is focused on setting up initiatives that are geared towards developing the future South African mining industry. The lack of upfront timeframes on the building blocks of the Phakisa initiative constitutes a shortfall of the initiative. The author is of the opinion that the foundation for the future cluster should be the primary building block, supported by the stabilizing and addressing of current challenges.

Five work streams were established during the Mining Phakisa Lab workshops to design initiatives that will address the challenges faced by the mining industry. These five work streams are (Operation Phakisa, 2015):

- *Cluster Employment work stream*—the core responsibility of this group is to address issues around reskilling and upskilling of mineworkers, job saving initiatives, and decent work categorization
- *Win-win Beneficiation work stream*—this group is responsible for developing initiatives that will rejuvenate the iron ore, steel, and polymer beneficiation value chains. The group is also required to act as an incubator for market development in beneficiation
- *Sustainable Communities work stream*—focuses on the challenges around integrated human settlements, regional economic development (agri-business), and rehabilitation of derelict and ownerless mines
- *Reviving Investment and Access to Affordable and Reliable Infrastructure*—the initiatives that were mandated to this work stream include attracting

investment in the mining cluster, increasing exploration, increasing participation of emerging miners, constant supply of affordable electricity, and development of access to affordable ports and rail transport
- *Advancing the Cluster work stream*—the key challenges that were mandated to this stream are the development of mining capital equipment manufacturing capability and mining-related research and development.

Current status

After the Phakisa Lab workshops, the Chamber of Mines South Africa (CoM) adopted an internal strategic framework for modernization. This modernization does not involve only mechanization or the gradual introduction of new technology, which are often associated with the replacement of people with machinery, resulting in direct job losses. The CoM considered modernization as a process of transition and transformation of the mining industry, involving (Chamber of Mines, 2016):

- Turning South Africa's mineral resources to account in the safest, most efficient, cost-effective, and sustainable manner possible
- Recognizing that people are at the heart of the industry, and focusing on improving skills, health, quality of life, and personal fulfilment of employees
- Conservation of natural resources, preservation and restoration of the environment
- Contributing to the development of local and labour-sending communities
- Transformation and growth as key imperatives for the mining industry and the nation.

A case study on the three principal gold mining companies (AngloGold Ashanti, Harmony Gold, and Sibanye Gold) indicated that, for a single mine, every 1 g/t reduction in the cut-off grade would result in 10 Mt of additional ore containing 200 t of gold being mined over the operation's extended life (Chamber of Mines, 2016). Margins are gradually closing in on narrow-reef operations due to challenges around operational costs and productivity, which sees the industry potentially closing around 2030. The study indicates that modernization of existing operation has the potential to extend the operational life of the sector beyond 2045 (Chamber of Mines, 2016) .

There were two strategic outcomes from the Mining Phakisa process within the Advancing the Cluster work stream:

- Mining R&D Programmes: a collaborative research and development model that focuses on a systematic approach to mining's R&D needs and enables the establishment of centres of excellence in collaboration with South African research institutions. The key focus of the research would be on addressing underground deep-level mining challenges
- Mining Equipment Manufacturing Cluster: a cluster that is embedded within other existing clusters and initiatives. The cluster will ensure that development requirements are translated into coherent R&D programmes, enabling local partnerships to develop and manufacture equipment for mining systems (Singh, 2016).

These strategic outcomes have gained substantial traction to date. A mining precinct has been established at the old COMRO facilities in Johannesburg. The precinct is intended to house local researchers, manufacturers, and mining companies on a project basis. This process will be coordinated by the Mining Hub, which is based on a 'hub-and-spoke' approach with all stakeholders playing collaborative roles. The concept of collaboration is embedded in the composition of the Mining Hub management structure. Key stakeholders include government, the mining industry, and manufacturers, who will jointly form a public-private partnership.

The primary objective of the Mining Hub is to act as a partner that advances the cluster by:

- Coordinating the research and development activities, with an initial focus on narrow-reef mining systems
- Facilitating skills development for future metalliferous mining systems
- Developing South Africa's mining equipment manufacturing capacity to address industry's equipment needs.

The hub-and-spoke model provides opportunities for broader research programmes to build capacity and capability in areas that constitute challenges to the mining industry, allowing the leveraging of existing strengths in various organizations.

Five research thematic areas have been identified within the Mining Hub as the key quick-win programmes (Mining Hub, 2017):

- *Advanced orebody knowledge:* this entails the development and evaluation of techniques that will provide more detail in relation to reef position, structure, grade, and rock characteristics
- *Modernization of current mining operations:* the focus is on increasing the efficiency of extraction and improving occupational health and safety while reducing operational costs
- *Platinum and gold mechanized mining:* the development of a fully mechanized mining system that will allow for drilling and extraction of narrow reefs with minimum dilution. Mechanized mining in the platinum sector has progressed extensively over the last decade
- *Non-explosive rock-breaking:* this requires the development of complete mining systems for extraction that are completely independent of the use of explosives
- *Real-time information management systems:* the focus is on improving the quality of communication in the underground environment and developing data management systems that will enable informed decision-making.

The process of identifying research areas involved compiling a list of user requirement specifications (URS) post the Mining Phakisa Lab workshops. A detailed description of the operational challenges experienced by narrow-reef operations was compiled and grouped into the thematic areas listed above. In the process of gathering user needs, companies indicated R&D projects that they are currently undertaking. The intended outcome is to allow the sharing of information among companies and enable the involvement of research institutions on a collaborative basis. In the past,

mining companies believed that research work was conducted purely for academic purposes. The process of identifying URS seeks to encourage more applied research that will directly address industry needs and build local capacity in research and manufacturing.

The outcomes of the manufacturing strategy have seen the establishment of Mining Equipment Manufacturing of South Africa (MEMSA), a Section 21 company comprising local manufacturers of mining equipment ranging from rail-bound to trackless. MEMSA is supported by the Department of Trade and Industry with aim of executing the recommendations of the Mining Phakisa. It is realized that linkages to the mining value chain such as local equipment manufacturing have the potential to increase overall economic growth, as opposed to total reliance on mining itself. The involvement of manufacturers in the collaborative forum will allow research outcomes to be developed into prototypes, and possibly new products.

Table I

Technology Readiness Levels

Basic research and technology creation: TRL 1 to 3

Technology Readiness Level	Purpose	Example
TRL 1 Basic principles observed: Scientific research begins to be translated into fundamental and/or applied research and development (R&D). Much of this work comprises desktop and literature studies wherein essential characteristics and behaviours of potential systems and architectures are formulated.	This is to establish certain basic principles, where there are unknowns that require basic desktop or laboratory-scale test work.	Tungsten carbide is observed to be hard and abrasive enough to be used as the key material for the rock-cutting tool. The basic concept of the continuous rock cutting machine is developed.
TRL 2 Concept formulated (invention): Once basic principles are known, practical applications can be invented. Applications are speculative, and there may be no proof or detailed analysis to support the assumptions, but work on the critical component design begins. Characteristics of the application are described and analytical tools are developed for simulation or analysis of the application.	The basic principles are tested and the concept is characterized.	Tungsten carbide would be a suitable material for the rock-cutting tool, and the cutting tool can be designed. Cutting rates based on rock hardness are identified.
TRL 3 Proof of concept: active R&D is initiated. This includes analytical studies and laboratory studies to physically validate the analytical predictions of separate elements of the technology. Technical feasibility is demonstrated.	Concept designed and the components of the critical parts of the rock cutter are characterized.	Tungsten carbide pick tested on a linear tester in a lab – confirmed that it cuts rock and that it can do so at rock hardnesses typical of the target applications. This work would be done in a specialist research facility such as a university.

Application Development: TRL 4 to 6

Technology Readiness Level	Purpose	Example
TRL 4 Component integration and validation in a lab: basic technological components are integrated to establish that they will work together. This is relatively low-tech compared with the eventual system, and works with the most critical part/s of the system, as a standalone prototype.	Key components of the system are integrated into a working tool.	Tungsten carbide pick integrated into cutting drum and tested in a lab or industry test site, such as the Mining Precinct, cutting typical rock blocks, as a prototype rock cutting head.
TRL 5 System optimized: The basic technological components are integrated with reasonably realistic supporting elements so they can be tested in a simulated environment. The working system design needs to be finalized for prototype development.	Ensure that the technology is optimized, and that it can be mounted on a machine/carrier that has been proven to work in a mining environment. At this stage, power systems need to be identified.	Pick configurations are modified and optimized, and the design of the working machine is completed through to prototype development.
TRL 6 System demonstration: Representative model or prototype system, which is well beyond that of TRL 5, is tested in a relevant environment. Engineering feasibility fully demonstrated in actual system application. Represents a major step up in a technology's demonstrated readiness.	Full system demonstration in relevant environment.	Cutting drum mounted on machine and tested on-mine but not in a production section. Thus it is probably tested on surface.

Product development and commercialization: TRL 7 to 9

Technology Readiness Level	Purpose	Example
TRL 7 System prototype trial: Prototype near or at planned operational system. Represents a major step up from TRL 6 by requiring demonstration of an actual system prototype in an operational environment. The system is now at or near the full scale of the operational system, with most functions available for demonstration and testing.	Demonstrated in an operational . environment This stage is critical in terms of demonstrating 'mine-worthiness' and identifying critical controls that need to be developed.	Machine demonstrated underground in a test stope but with limited interference with production.
TRL 8 Actual system qualified: Technology has been proven to work in its final form and under expected conditions. In almost all cases, this TRL represents the end of true system development. Fully integrated with operational hardware and software systems. Most user documentation, training documentation, and maintenance documentation is completed. All functionality has been tested in simulated and operational scenarios. Verification and validation (V&V) of URS are completed and signed off.	Qualified through test. It is critical that sufficient time is dedicated to this phase to ensure maturity of the system. It is during this phase that critical support systems must be identified and developed (for example, maintenance cycles, critical component monitoring, communication systems, performance monitoring systems etc.).	Machine in operational trial meeting market requirement (as specified in the URS) in a full production environment. The system is ready for commercialization through tendering.
TRL 9 System proven: Actual application of the technology in its final form and under mission conditions, such as those encountered in operational test and evaluation (OT&E). Commercialization is based on proven performance, market demand, and economy of scale.	Proven through operation.	Machine in routine use.

Technology Readiness Level (TRL) for South African mining

Projects like mechanization of underground mines and introduction of new technology have been tried and tested in the past with minimal success. One of the factors that contributed to the failure of the projects includes the low maturity level of the technology and the resulting problems in adapting it to a production environment. Companies agreed to modify and adopt the National Aeronautics and Space Administration (NASA) version of Technology Readiness Level (TRL) for the South African mining industry. This will allow companies and other stakeholders to use a common language when describing mining projects and the maturity level of new technologies.

TRL is a tool used to measure and monitor technology maturity, from the conceptual stage to proving of the technology's capabilities and demonstration of the product. Technology is rated on a scale of 1 to 9, as seen in Table I. Initiatives that are TRL 6 and below are considered to be in the R&D phase, while those at TRL 7 and above are considered as manufacturing. This guides and informs the involvement of various government departments; the Department of Science and Technology would be more involved in initiatives that are below TRL 6 as they involve fundamental research, while the Department of Trade and Industry would be more involved in TRL7 and above as these levels relate to commercialization.

Table I illustrates the links between scientific concepts and the development of products that meet user needs. Learnings from the past indicated the gaps between researchers and mining operations. The flaws lay in the aim and outcomes of research. Mining companies believe that focus should be placed on applied research, and the adoption of TRLs will allow research work to satisfy both the user and the researcher. The process of developing stage-gates and a purpose across each TRL provides the end-user with tangible outcomes that can be measure during a project.

Conclusion

The paper has attempted to paint a comparative picture of South Africa's mining industry today in relation to the past. South Africa has ceased to maximize its mineral endowment benefits due to various challenges that have been discussed in the paper. These challenges presented themselves as key enablers to multi-stakeholder collaboration. For South Africa's mining industry to remain competitive and sustainable, there is a need to embrace a collaborative approach to addressing the immediate and future challenges.

Mining research organizations should strive to build centres of excellence in specific mining areas. The competitive culture in research cripples the capacity of research organizations and the country as the amount of available funding is reduced. Centres of excellence will allow stronger long-term partnerships with local universities and mining companies. Allowing end-users to define R&D needs will ensure a continuous network that will drive fundamental and applied research coherently.

The Mining Phakisa initiative presented an opportunity for stakeholders to develop programmes that will address issues such as productivity, safety, mine design, operational costs, and people issues. Collaboration will allow South Africa to build local capacity and design solutions that are suitable for local mining conditions. The concept of internal capacity-building will allow the industry to sustain itself.

It is recommended that time-frames are attached to the various Phakisa initiatives and communicated with a broader audience. The inclusion of various organizations affected by mining in South Africa in the Phakisa initiative will yield more positive results. As learnt from past technology and mechanization initiatives, people should form the centre of programmes. The success of any mining R&D and technology will rely entirely on the support of the workforce and surrounding communities.

In conclusion, South Africa must realize that the responsibility for a sustainable mining industry lies with everyone. The notion of relying on mining as a sole economic contributor has passed—mining should be used as a platform for developing secondary industries and industrialization initiatives for South Africa. Continuous understanding of the broader mining value chain by various stakeholders and South Africa's contribution to the value chain will ensure the sustainability of the industry.

References

Chamber of Mines South Africa. 2014. Mining in SA. http://www.chamberofmines.org.za/sa-mining [Accessed 31 October 2016].

Chamber of Mines South Africa. 2015. Next generation mining: research for Mining Phakisa 8 September. Johannesburg.

Chamber of Mines South Africa. 2016. Modernisation: towards the mine of tomorrow. Johannesburg.

Department of Planning, Monitoring and Evaluation. 2016. Operation Phakisa. http://www.operationphakisa.gov.za/pages/home.aspx [Accessed 7 November 2016].

Fenn, A. 2016. Unlocking value by reorganizing the operational. *Proceedings of the Colloquium: New Technology and Innovation in the Minerals Industry*, 9 June 2016. Southern African Institute of Mining and Metallurgy, Johannesburg.

Hermanus, M. 2016. Mine health and safety twenty years on, http://www.mine2030.co.za/downloads/send/3-fact-sheet/4-mine-health-and-safety-twenty-years-on [Accessed 7 November 2016].

Malaysia Government., 2013. Policy and guidelines on industry collaboration program in government procurement. http://tda.my/wp-content/uploads/2016/03/ICPpolicyBI.pdf [Accessed 13 October 2016].

Mining Hub. 2017. Charter documents. Johannesburg.

Operation Phakis. 2015. Mining Phakisa Lab Summary. Department of Planning, Monitoring and Evaluation, Pretoria.

Pickering, R. 2004. The optimization of mining method and equipment. *Proceedings of the First International Platinum Conference 'Platinum Adding Value', Sun City, South Africa*, 3–7 October 2004. South African Institute of Mining and Metallurgy, Johannesburg.

Pirouz, J.F.A.F. 1999. The role of mining in the South African economy. Economic Research Southern Africa, Johannesburg.

Rupprecht, S.M. 2017. The need for material change in the South African mining industry. University of Johannesburg. http://hdl.handle.net/10210/93356 [Accessed 19 April 2017].

Singh, N. 2016. Riding the perfect storm facing the mining sector. *Proceedings of the Colloquium: New Technology and Innovation in the Minerals Industry Colloquium,* 9 June 2016. Southern African Institute of Mining and Metallurgy, Johannesburg.

Statistic South Africa. 2016. SA jobs shrink in Q2. http://www.statssa.gov.za/?p=8574 [Accessed 31 October 2016]. ◆

http://dx.doi.org/10.17159/2411-9717/2017/v117n7a2

The application of process mineralogy on a tailings sample from a beach placer deposit containing rare earth elements

by A. Moila*†, D. Chetty*, and S. Ndlovu†‡

Synopsis

The rare earth elements (REE) are significant in the context of world economic growth and modern technology. This research is aimed at investigating an alternative source of REE by exploring cost-effective ways of processing REE minerals from an existing beach placer deposit operation, currently mined for titanium. In order to recover REE through economically optimum means, upfront mineralogical investigations are a necessity to reduce the ore processing costs. An approach involving mineralogical characterization and hydrometallurgical test work was therefore chosen. The sample for the study – a tailings fraction from a heavy mineral concentration plant in the titanium industry – was screened into four size classes, and each size class was mineralogically characterized. The minerals present in the sample were monazite, zircon, epidote, pyroxene, amphibole, rutile, quartz, leucoxene, titanite, and almandine. The main REE-bearing minerals, monazite and zircon, were preferentially concentrated in the finer (-150 μm) fractions, which constituted about 50 mass % of the sample and which would be amenable to direct leaching without prior upgrading to a concentrate. Leaching test work was carried out on the combined fractions passing 150 μm. Mineralogical examination of the residues from different leach stages showed that monazite was cracked and the REE released to solution in the final leach stage. Zircon was not as reactive under the conditions used, and REE release was not expected from this mineral. The mineralogical findings were correlated against bulk chemical analyses of the leach products to establish whether a good reconciliation was achieved.

Keywords
rare earth elements, beach placer deposit, process mineralogy, leaching.

Introduction

The rare earth elements (REE), which constitute the lanthanide group in the Periodic Table, are a major constituent of many advanced materials, especially in the high technology and green energy sectors. This group of elements is very important in the world economy and modern technology. Resources of REE are globally distributed, but production is largely monopolised by China, which controls approximately 95% of the world's REE Market (Wübbeke, 2013; Massari and Ruberti, 2013).

Early in 2005, China as the leading REE producer decided to limit its REE exports by establishing quotas and banning the sale of some REE outside the country, so as to meet its own domestic requirements (Morrison and Tang, 2012). This resulted in a high global demand and strained supply (Figure 1). As a result, other countries were faced with the challenge of exploring means of closing the REE demand-and-supply deficit gap created by the change in China's export regulations.

The reduction in supply quotas of REE by China led to a drastic increase in global demand for REE, thus creating an opportunity for other countries to look into alternative sources of REE.

Japan made plans to extend the search for highly concentrated REE in deep-sea mud of the Pacific Ocean (Gordon, 2011), as well as to recycle old batteries and electronic equipment for their REE contents and to secure alternative supplies of REE from Mongolia (Tabuki, 2010).

India planned to resuscitate its REE production from Indian Rare Earths Limited (IREL), which ceased production in 2004. Other plans to enhance the development of REE supply in India and Vietnam were made by Toyota Motor Corporation in 2011 and 2013 (Montgomery, 2011).

This paper outlines the approaches used to investigate an alternative REE resource; a by-product from an existing titanium recovery operation in South Africa. The process involved the characterization of the REE from the beach placer deposit before processing. The investigation was carried out subsequent to China's decision to implement new export regulations limiting REE exports. Research studies have been conducted globally on REE from carbonatite and placer deposits; in particular in China and the USA, which have the world's largest carbonatite-hosted rare earth reserves. Extensive work has been conducted on the South African carbonatite

* *Mintek, Randburg, South Africa.*
† *School of Chemical and Metallurgical Engineering, University of the Witwatersrand, South Africa.*
‡ *DST/NRF SARChI, Hydrometallurgy and Sustainable Development, University of the Witwatersrand, South Africa.*

 ISSN 2225-6253. This paper was first presented at the 3rd Young Professionals Conference, *9–10 March 2017, Innovation Hub, Pretoria, South Africa.*

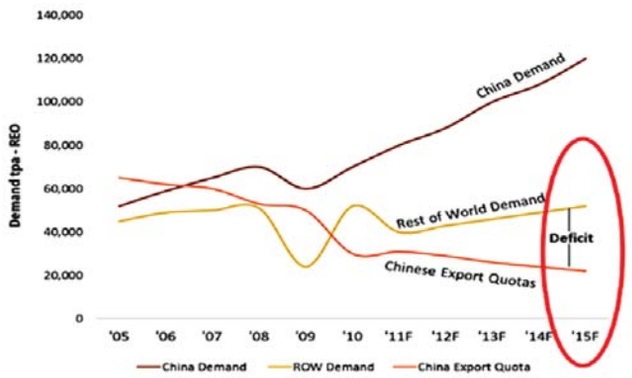

Figure 1—Demand and supply curves, showing an increase in the deficit created by the decline in export of REE from China (Liu, 2011)

deposits, namely, Steenkampskraal and Zandkopsdrift, but very little work has been done on beach placer deposits for REE.

The South African REE deposits are mainly of primary origin, consisting of carbonatite and hydrothermal deposits, accompanied by secondary (beach placer) deposits. The primary carbonatite deposits are associated with igneous and hydrothermal processes, whereas the secondary (placer) deposits are formed by sedimentary processes and weathering (Sappin and Beaudoin, 2015). Beach placer deposits, which constitute the world's second-largest REE reserves (Haxel, Hedrick, and Orris, 2002), occur in Australia, Brazil, China, India, Malaysia, South Africa, Sri Lanka, Thailand, and the USA.

The beach placer deposits in South Africa are mainly mined for titanium and little work has been done on their REE potential, particularly as regards tailings from existing titanium production. Most heavy mineral deposits or beach placer deposits are mined for titanium minerals and zircon, with monazite and leucoxene considered as tailings. The heavy mineral tailings from existing titanium production therefore constitute a potential source of REE as byproducts.

The Eneabba placer deposit in Australia produces titanium as a primary product and monazite as a byproduct. In Australia, monazite is a significant REE resource, with 6.1 Mt processed annually and an estimated 2.1 Mt of rare earth oxides (REO) production reported in 2014 (Roskill, 2015).

Beach placer deposits are naturally deposited sediments along rivers and coastlines, in which common minerals such as monazite, zircon, quartz, ilmenite, garnet, and magnetite are found. Beach placer deposits are mined for titanium hosted in minerals such as ilmenite, rutile, and other titanium and iron alteration products such as leucoxene (Roskill, 2015). Monazite is the chief REE-bearing mineral, although some of the other heavy minerals may contain various REE substitutiing in their crystal structures (Deysel, 2007).

The current study is part of an ongoing research project on the process mineralogy and extraction of REE from beach placers, the ultimate aim being to assess the cost-effective utilization of beach placer tailings from the titanium industry as an additional source of REE. An important aim is to show that mineralogical studies are a vital factor in REE extraction (Pawlik, 2013).

Diverse techniques have been applied by different companies to recover REEs. There are various well-known processes for decomposing the REE-bearing minerals, and in order to select an appropriate beneficiation and leaching method the mineralogy of the ore is an important consideration. In spite of this, very few published flow sheets are accompanied by the process mineralogical aspects, in particular those relating to the products.

Figure 2 shows an idealized flow sheet of REE extraction from primary (bastnaesite) and secondary (monazite) deposits used in the USA and China.

The leaching of REE involves two processing routes, namely the acidic route and the alkaline route, (Figure 2). Leaching is carried out on upgraded material in the form of a concentrate. The concentrates or products are either treated directly by acidic or alkaline reagents, or first undergo thermal treatment prior to leaching (Fatherly *et al.*, 2008). The choice of leaching route is highly dependent on the mineralogy of the ore.

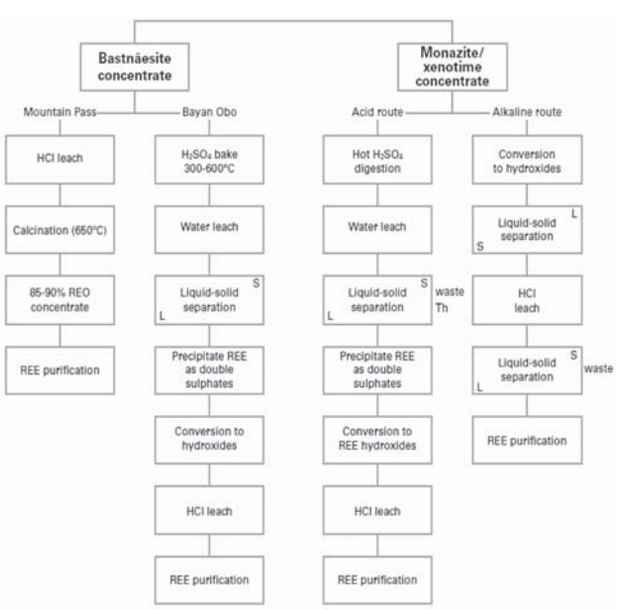

Figure 2—An idealized flow sheet for extracting REE from bastnaesite (carbonatite-hosted REE) and monazite (placer-hosted REE) (Chegwidden and Kingsnorth, 2010)

Methods

Tailings sample characterization

A tailings sample from a South African beach sand titanium operation was split into four size fractions: +212 μm, –212+150 μm, –150+106 μm, and –106 μm.

Each size fraction was weighed and recorded (Table I).

Each fraction was individually characterized using X-ray diffraction (XRD), optical microscopy, scanning electron microscopy (SEM), electron microprobe analysis (EMPA), and automated SEM.

X-ray diffraction analysis

X-ray powder diffraction was used for phase identification of the crystalline minerals, to provide information on the bulk mineralogy of the sample. Pulverized samples were subjected to analysis using a Bruker D8 Advance diffractometer with Co Kα radiation, a 2θ scan range of 5–80°, a step size of 0.02° 2θ, and a counting time of 3 seconds per step. Note that only crystalline minerals present in mass percentages greater than approximately 3% are detected by this method.

Optical microscopy/SEM analysis

Polished sections were prepared for examination using the reflected light microscope and a Zeiss EVO MA1 SEM. The reflected light microscope was used to identify REE-bearing and gangue minerals, as well as to determine their mode of occurrence in each of the size fractions. The Zeiss EVO MA1 SEM, equipped with quantitative energy dispersive spectrometry (EDS), was used to verify the presence of REE-bearing minerals and to determine their elemental compositions.

Elemental maps were captured to illustrate and verify the mode of occurrence of REE-bearing minerals and other elements associated with REE minerals. Element mapping is a procedure available on the SEM where specific selected chemical elements can be 'searched' within a microscopic field of view, and the relative concentrations of the element are illustrated with different selected colours. If one particular element is present in a particle, the specific particle is highlighted with the colour for that element.

When particles contain more than one mineral phase, the individual element colour concentration is highlighted according to its occurrence in the minerals. If the element is absent an overall background colour appears.

Table I

Particle size distribution

Size fraction	Mass (g)	Mass in (%)
+212 μm	198.5	8.5
–212 + 150 μm	946.9	40.4
–150 = 106 μm	797.2	34.0
–106 μm	401.4	17.1
Total	2343.9	100

Electron microprobe analysis

A Cameca SX50 electron microprobe equipped with four wavelength dispersive spectrometers (WDS) was used to determine the mineral chemistry on various grains. A maximum of 365 grains were analysed in all size fractions. REE calibration was performed using the REE orthophosphate reference samples from the Smithsonian Microbeam Standards collection. Other elements analysed were calibrated using appropriate reference standards. The standard excitation conditions used were 20 kV and 30 nA, with a spot size of 5 μm.

AutoSEM analysis

A Mineral Liberation Analyser (MLA) was used to quantitatively distinguish the mineral abundance in the sample. The measurement mode employed in this study was extended backscattered electron liberation analysis (XBSE). The XBSE mode implements area X-ray analysis to efficiently and effectively analyse ore samples containing phases with sufficient BSE contrast to ensure effective segmentation. The BSE image is then captured and segmented to delineate mineral grain boundaries in each particle. Each mineral grain is then subjected to X-ray analysis (Gu, 2003).

Hydrometallurgical test work and mineralogical evaluation of products

The detailed mineralogical analysis showed that monazite and zircon were preferentially concentrated in the finer fractions (-150 μm), which constituted approximately 50 mass % of the sample (Figure 4). The +212 μm and –212+150 μm fractions contained only trace amounts of monazite and zircon. The –150+106 μm and –106 μm size fractions were composited to form a –150 μm sample (referred to as the composite sample), and a mass of 400 g was ground using a ball mill to 100% passing 45 μm for subsequent hydrometallurgical test work.

The composite sample was subjected to a series of hydrometallurgical tests that involved caustic cracking, water leaching, and selective leaching (Figure 3). Sub-samples were taken from each leaching stage and washed for mineralogical characterization using the Zeiss EVO MA1 SEM.

Caustic cracking involves the decomposition of monazite using 50% (m/m) NaOH solution (Gupta and Krishnamurthy, 2005), with the aim being to break down the monazite ($(Ce,La,Nd,Th)PO_4$) into trisodium phosphate and REE hydroxides. The caustic cracking was conducted for 4 hours using 50% (m/m) NaOH solution at a temperature of 140°C, in a 5 L stainless steel reactor.

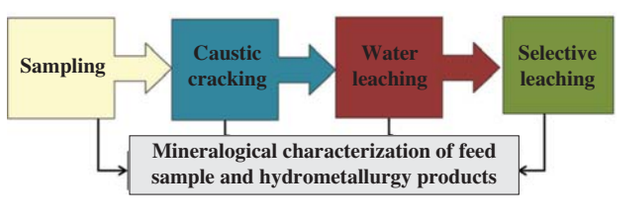

Figure 3—Experimental approach

The cracked residue was washed three times using deionized water to remove the majority of the entrained NaOH (Mokoena, 2016).

The washed residue was leached with water to convert the REE into hydroxides, followed by selective leaching of the REE using 32.0 % HCl in a 3 L thermoplastic coated reactor. The lixiviant temperature was ambient, with the recorded redox potential averaged at 441.8 mV. After each leaching stage, the residues were washed prior to the next leaching stage. Samples of the residues from each leaching and washing stage were taken for mineralogical characterization.

A total of ten leach and washed residues were prepared and were mounted on a carbon-coated stub for examination by SEM, using a Zeiss EVO MA1 instrument equipped with EDS, in order to identify REE-containing phases and determine their compositions.

Results and discussion

Mineralogy of the tailings samples

The mineralogical results derived from the autoSEM analysis showed that the sample consisted of monazite, zircon, amphibole, diopside, augite, epidote, rutile, quartz, leucoxene, titanite, and almandine. Monazite and zircon were the chief REE-containing minerals. The mineralogy of the sample varied per size fraction. The coarser fractions (+212 μm and –212+150 μm) were dominated by epidote, followed by minor amounts of diopside, augite, and amphibole. Mineralogical variations were more evident in the two smallest size fractions (–150+106 μm and –106 μm), which contained the majority of the zircon, rutile, and monazite and which together constituted approximately 50 mass % of the tailings sample (Figure 4). Based on these findings, a composite of these size fractions was further subjected to REE extraction test work.

Mineralogy of the hydrometallurgical test products

Mineralogical characterization of the ten leach and washed residues showed distinctive changes in each hydrometallurgical stage.

Caustic crack residues

The NaOH crack residues were studied and the findings showed that the phosphate ion was successfully cracked from the monazite ($(Ce,La,Nd,Th)PO_4$). However, the zircon grains did not appear to have reacted with the NaOH (see Figure 5, NaOH crack sample on grains number 3 and 5).

Subsequent to NaOH cracking, the residues were washed three times in order to remove the entrained NaOH solution prior to water leaching and HCl leaching. The two repulp washing results on the residue showed a general decrease in Na content relative to the unwashed cracked residue (Table II). The zircon grains showed very little reaction with NaOH; this is indicated by high Zr and Si values, very similar to the original zircon composition (Table II).

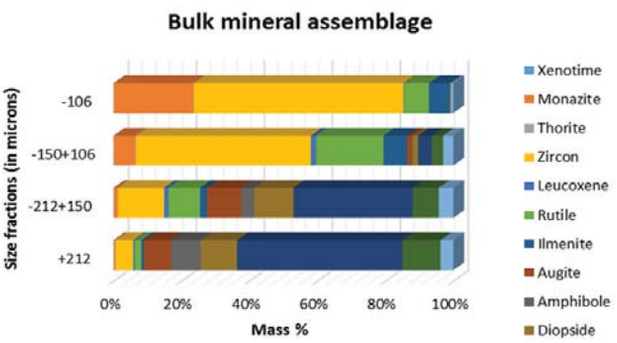

Figure 4—Bulk mineral assemblage of the tailings sample

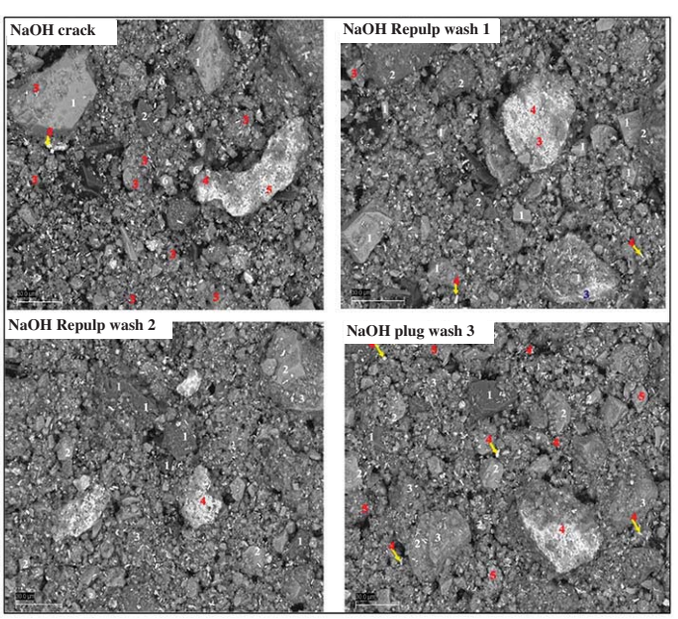

Figure 5—Backscattered electron (BSE) images of residues from caustic cracking and washing tests; analyses of the numbered points are given in Table II. The BSE images also show the cracked monazite grains and unreacted zircon. (Point 2 of NaOH crack was identified as an oxide phase; points 2 and 3 of NaOH repulp wash 1 and point 2 of NaOH repulp wash 2, as well as points 1, 3 and 5 of NaOH plug wash 3, refer to oxide and silicate phases)

Table II

Averaged analyses of residues from caustic cracking and washing tests (wt.%)

Sample	Analysed points	O	Na	Mg	Al	Si	Ca	Ti	Fe	Sr	Zr	La	Ce	Nd	Eu	Th	Comments
NaOH crack	1	28	5			10		1			40				0		Unreacted zircon
NaOH crack	3	27	4			10		2			38						Unreacted zircon
NaOH crack	4	25	5		5	8	4	3	12		3	2	4	2		0	Cracked monazite
NaOH crack	5	13	5			1					2	13	28	11		5	Cracked monazite
NaOH crack	6	16	10			1	0	5	3		3	8	17	7		3	Cracked monazite
NaOH repulp wash 1	1	32				13					50						Unreacted zircon
NaOH repulp wash 1	4	18	8	1		3	1	7	4	0	6		9	4		3	Cracked monazite
NaOH repulp wash 1	5	14	6			4	0				2	8	17	9		8	Cracked monazite
NaOH repulp wash 1	6	31				12		2			46						Unreacted zircon
NaOH repulp wash 2	1	30	1			11		3			43				1		Unreacted zircon
NaOH repulp wash 2	3	20	7	1		2	1	10	5		5	9	13	5		3	Cracked monazite
NaOH repulp wash 2	4	13	5			2	0		2		2	15	22	6		4	Cracked monazite
NaOH plug wash 3	2	28	1			10		1	1		41						Unreacted zircon
NaOH plug wash 3	4	14	3			2		2			4	12	23	9		4	Cracked monazite

*Note that as powdered material was examined, EDS data is not quantitative, but will give an indication of the types of phases present

The third wash, which was the plug wash, was aimed at further removal of NaOH solution entrained in the residue. The removal of NaOH across three washes yielded similar results in terms of Na content (Table II).

Water leach residues

The mineralogical results showed that the REE-containing phases are compounds containing a mixture of Ce, La, and Th with Al, Mg, Si, Ca, and Fe. (Figure 6 and Table III). The zircon grains remained unreacted from this procedure; this is expected, since zircon failed to react with NaOH at a temperature of 140°C. The decomposition of zircon occurs at temperatures higher than 500°C (Farias da Silva, Dutra, and Afonso, (2012).

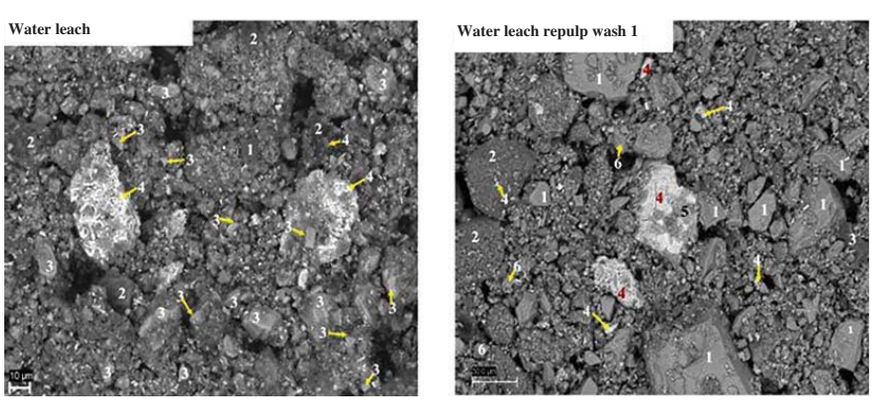

Figure 6—Backscattered electron (BSE) images of residues from water leaching and washing tests; analyses of the numbered points are given in Table III. The BSE images also show the cracked monazite grains and unreacted zircon. (The numbered points 1 and 3 of water leach product and points 2,3 and 4 of the water leach repulp wash 1 refer to oxide and silicate phases)

Table III

Averaged analyses of water leaching and washing tests residues (wt.%)

Sample	Analysed points	O	Na	Mg	Al	Si	Ca	Ti	Fe	Sr	Zr	La	Ce	Nd	Eu	Th	Comments
Water leach	2	27				11		1			42						Unreacted zircon
Water leach	4	13	2		0	1		2				14	29	9		6	Cracked monazite
Water leach repulp wash 1	1	23				9					36						Unreacted zircon
Water leach repulp wash 1	5	25				10		1			38				0		Unreacted zircon

*Note that as powdered material was examined, EDS data is not quantitative, but will give an indication of the types of phases present

The SEM analysis confirmed the presence of Eu in some of the zircon grains and also showed the consistent Zr:Si ratio of unreacted zircon grains. There were no notable differences between the residues from the water leach and repulp wash. The REE-containing phases are likely to be converted into hydroxides during the water leach process (Table III), which was the aim of this step.

Selective (HCl) leaching residues

The water leach repulp washed residues were subjected to HCl leaching for 4 hours at a pH of 3 under ambient temperature at varying redox potentials of pH levels 4.1 to 3.054. The HCl leach and subsequent washes successfully removed the remaining Na from the water-washed residue (Table III). A decrease is observed in La, Nd, and Ce contents relative to the first two stages (Tables II and III), indicating the successful solubilization of these elements by HCl leaching. Th concentrations were found to increase markedly compared with the first two stages (Tables II, III, and IV). Some of the REE-containing phases showed associations with Al, Si, Ca, Mg, and Fe compounds (Figure 7 and Table IV).

Table IV

Averaged analyses of HCl leaching and washing test residues (wt.%)

Sample	Analysed points	O	Na	Mg	Al	Si	C1	Ca	Ti	Fe	Zr	La	Ce	Nd	Th	Comments
HCl leach unwashed	1	23				9					36					Unreacted zircon
HCl leach unwashed	7	18				3		0		2		8	14	6	3	Cracked monazite
HCl leach wash 1	2	25				9			2	1	36					Unreacted zircon
HCl leach wash 1	3	24				8			4	2	33					Unreacted zircon
HCl leach wash 1	6	20				1		0		1		9	17	6	3	Cracked monazite
HCl leach wash 1	7	18				3		0		2		8	14	6	3	Cracked monazite
HCl leach wash 2	3	25				10					39					Unreacted zircon
HCl leach wash 2	5	13				2			5	3	4		17		11	Cracked monazite
HCl leach wash 2	6	12				2			5	2	5		13		11	Cracked monazite
HCl leach wash 2	7	16				3			6	3	8		4		31	Cracked monazite
HCl leach wash 3	1	25				10					39					Unreacted zircon
HCl leach wash 3	2	18			0	4		0	3	2	9	4	8	3	24	Cracked monazite
HCl leach wash 3	3	18				3			9	5	7		7		18	Cracked monazite
HCl leach wash 3	6	29				11			4	2	39					Unreacted zircon

*Note that as powdered material was examined, EDS data is not quantitative, but will give an indication of the types of phases present

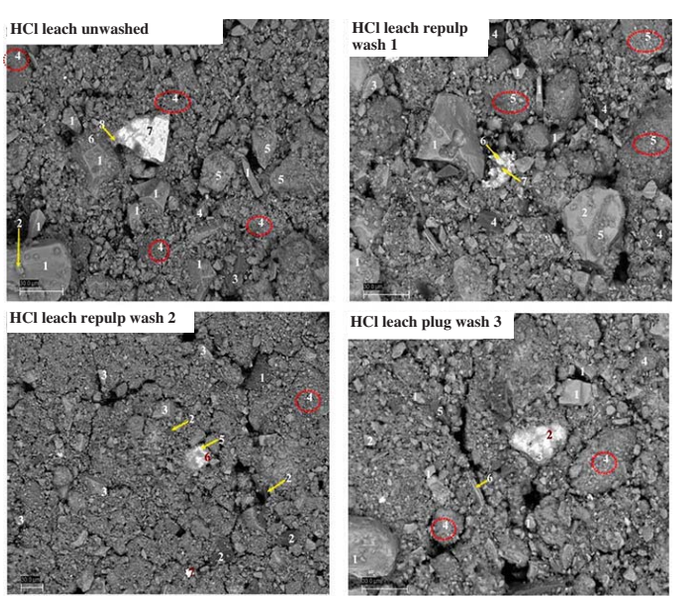

Figure 7—BSE images of residues from HCl leaching and washing tests; analyses of the numbered points are given in Table IV. The BSE images also show the cracked monazite grains and unreacted zircon. Circles indicate fine-grained phases. (Points 2 to 6 and 8 of HCl leach unwashed; points 1, 4, and 5 of HCl repulp wash 1; points 1, 2, and 4 of HCl leach wash 2, and points 4 and 5 of HCl leach wash 3 refer to oxide and silicate phases)

Conclusion

This investigation has demonstrated that mineralogical characterization plays a vital role in processing method selection for REE. Detailed mineralogical characterization of the as-received tailings sample showed that the key REE-bearing minerals, monazite and zircon, were naturally concentrated in the two finer size fractions (–150 and –106 μm), hence these composited fractions were subjected to direct leaching. This shows the value of introducing mineralogical characterization of the ore before embarking on any REE extraction processes.

The phosphate ion of monazite was successfully removed by NaOH cracking. NaOH is highly reactive towards monazite, but the NaOH did not react with zircon. The NaOH leaching temperature is therefore sufficient for phosphate ion cracking but not sufficient to crack the silica within the zircon structure ($ZrSiO_4$), as shown by the consistent ratio of Zr to Si in the EDS analyses. During the NaOH cracking process, it was anticipated that the NaOH would decrease with each wash; however, both the plug and the two repulp wash residues returned similar phase chemistries, based on the mineralogical observations of the Na content.

Water leaching of the residue from cracking enhanced the removal of NaOH solution, and likely converted the cracked monazite into REE hydroxides. The REE-containing phases were also associated with Al, Si, Ca, and Fe. Examination of the residues from selective HCl leaching and washing showed that remnant Na from NaOH was entirely removed during the leaching.

The decrease in REE content of phases from the second to the third stage (*i.e.* water leach to HCl leach) indicates that REE dissolution by HCl took place. This will be quantified by bulk chemical analysis of the products. Subsequently, the Th content tends to increase drastically, indicating that Th is not solubilized through HCl leaching.

Finally, the mineralogical analysis shows that monazite cracking and subsequent leaching of REE appear to have been successful. Further test work will be required, as guided by the recovery data, to obtain the optimum REE extraction from the composite sample.

Thus far, this study shows that by conducting mineralogical investigations beforehand, it is possible to minimize other stages of mineral processing such as ore upgrading or production of a concentrate prior to hydrometallurgical treatment. Based on the mineralogical investigation, it was observed that monazite and zircon were naturally concentrated in the finer fractions (–150 +106 and –106 μm), which constituted approximately 50 mass % of the sample. These two size fractions were therefore composited prior to direct leaching. Mineralogical studies on the leach products also provide insights into REE extraction. Together, these investigations are indispensable when developing suitable process and extraction flow sheets.

References

Chegwidden, J. and Kingsnorth, D.J. 2010. Rare earths: facing the uncertainties of supply. *Proceedings of the 6th International Rare Earths Conference*, Hong Kong, November 2010. http://www.slideshare.net/Tehama/rare-earths-facing-the-uncertaintys-of-supply

Deysel, K. 2007. Leucoxene study: A mineral liberation analysis (MLA) investigation. *Proceedings of the 6th International Heavy Minerals Conference 'Back to Basics'*, Richards Bay Minerals, Natal, South Africa. Southern African Institute of Mining and Metallurgy, Johannesburg. pp. 167–172.

Farias da Silva, J.R., Dutra, A.J.B., and Afonso, J.C. 2012. Alkali fusion followed by a two-step leaching of a Brazilian zircon concentrate. *Hydrometallurgy*, vol. 117-118. pp. 93–100.

Fatherly, N., O'Neill, M., and Glemza, A. 2008. Formerly used sites remedial action program (FUSRAP) W.R. Grace feasibility study (FS) alternative development process challenges and successes. *Proceedings of WM'08: Waste Management Symposium*, Phoenix, AZ, 24-28 February 2008. http:// http://www.wmsym.org/archives/2008/pdfs/8255.pdf

Gordon, J. 2011. Analysis: underwater rare earths likely a pipe dream. http://www.reuters.com/article/2011/07/06/us-rareearths-underwater-idUSTRE7655M320110706

Gupta, C.K. and Krishnamurthy, N. 2005. Extractive Metallurgy of Rare Earths. CRC Press, Boca Raton, FL. 502 pp.

Haxel, G.B., Hedrick, J.B., and Orris, G.J. 2002. Rare earth elements—critical resources for high technology. Fact sheet 087-02. US Geological Survey, Reston, VA.

Liu, Y. 2011. A rare earths crisis. *Queen's Business Review*. http://www.qbreview.org/a-rare-earths-crisis/ [accessed July 2014].

Massari, S. and Ruberti, M. 2013. Rare earth elements as critical raw materials: Focus on international markets and future strategies. *Resources Policy*, vol. 23, pp. 36–48.

Mokoena, S. 2016. Personal communication. Hydrometallurgy Division, Mintek, Randburg, South Africa.

Montgomery, M. 2011. Rare earths recycling enter the new reality. *IB Times*, 23 February. http://www.ibtimes.com/articles/115379/20110223/rare-earth-recycling-enter-the-new-reality.htm

Morrison, W.M. and Tang, R. 2012. China's rare earth industry and export regime. Economic and trade implications for the United States. Congressional Research Service Report. pp. 1–36

Pawlik, C. 2013. Recovery of rare earth elements from complex and low grade deposits. *Proceedings of the ALTA Uranium-REE Conference*, Perth, 25 May–1 June. Alta Metallurgical Services.

Roskill. 2015. Rare Earths: Market Outlook to 2020. 15th edn.

Sappin, A.A. and Beaudoin, G. 2015. Rare earth elements in Québec, Canada: Main deposit types and their economic potential. *Proceedings of the Symposium on Strategic and Critical Materials*, Victoria, British Columbia, 13–14 November 2015. Simandl, G.J. and Neetz, M. (eds.). British Columbia Ministry of Energy and Mines. British Columbia Geological Survey Paper 2015-3. pp. 265–273.

Tabuki, H. 2010. Japan recycles minerals from used electronics. *New York Times*, 4 October. http://www.nytimes.com/2010/10/05/business/global/05recycle.html

Wübbeke, J. 2013. Rare earth elements in China: Policies and narratives of reinventing an industry. *Resources Policy*, vol. 38. pp. 384–394. ◆

The Southern African Institute of Mining and Metallurgy (SAIMM) in cooperation with the International Atomic Energy Agency (IAEA), the Canadian Institute for Mining, Metallurgy and Petroleum (CIM), the Namibian Uranium Institute, and the Namibia University of Science and Technology (NUST) is proud to host the

URANIUM 2017 INTERNATIONAL CONFERENCE

Extraction and Applications of Uranium — Present and Future

11 September 2017—Short Courses and Technical Visit
12–13 September 2017—Conference
14 & 15 September 2017—Technical Visits
Swakopmund Hotel, Swakopmund, Namibia

Namibia is currently ranked the fifth-largest producer of uranium in the world and is set to become the world's second-largest producer once

Swakop Uranium's Husab Mine is fully operational. This will undoubtedly position Namibia as a major uranium mining hub and will see the industry playing a more significant role in the national and regional economies.

Uranium as a material, and its applications, are often controversial. Yet, nuclear reactors are still being built despite the growth in energy generation through renewable sources and despite highly publicised nuclear accidents. Several countries are pursuing uranium enrichment

programmes. Although prices are currently subdued, it is highly likely that there will be continued and sustained demand for uranium for the foreseeable future.

This conference aims to bring together professionals in the uranium industry. A broad range of topics will be discussed, ranging from mining to some of the applications of uranium, and including safety, and post-operations closure and remediation issues. Innovations in the extraction and applications of uranium are constantly being made, and this conference provides a platform for the discussion of advances and for generating new ideas.

It is fitting that the conference takes place in Swakopmund, Namibia. Not only do Namibia and this town have much to offer in scenic beauty, but Swakopmund (apart from being a favourite seaside resort) is also the centre of uranium extraction in the country. Most mines are located in the Namib Desert, within easy driving distance of the conference venue. The oldest uranium mine, Rössing Uranium, celebrated its 40th anniversary last year, having commenced operations in 1976. Pre- and post-conference visits are available.

The Uranium 2017 Conference will bring together internationally and locally recognized experts, operating personnel, engineering providers,

policy makers, R&D establishments, academia, as well as students, to explore how future uranium extraction technologies can:

- Assist in sustainable uranium extraction
- Lower energy costs
- Minimize the impact on the environment
- Play an enhanced role in the medical field

EXHIBITION/SPONSORSHIP

Sponsorship opportunities are available. Companies wishing to sponsor or exhibit should contact the Conference Co-ordinator.

CONTACT: **Head of Conferencing**
Camielah Jardine
E-mail: camielah@saimm.co.za
Tel: +27 11 834 1273/7

SAIMM
THE SOUTHERN AFRICAN INSTITUTE OF MINING AND METALLURGY

http://dx.doi.org/10.17159/2411-9717/2017/v117n7a3

Accurate measurement of polarization potentials during electrodeposition of nickel metal from sulphate electrolytes

by L. Schoeman* and K.C. Sole

Synopsis

Extraction of nickel from either laterite or sulphide ores involves various complex hydrometallurgical processes, the final step of which is often electrowinning to produce pure nickel metal. Methods to investigate, monitor, and control the electrowinning process are therefore of importance for producing nickel metal of desirable quality and purity. The significance of potential measurements during the electrowinning process is well established. Many potential measurement methods, however, are not sufficiently accurate or repeatable, and it is therefore often difficult to monitor and control the electrodeposition process accurately. The relationship between nucleation (deposition of the first nickel clusters to the cathode surface) and growth (as more and more nickel clusters deposit) during electrodeposition is paramount for controlling the formation and quality of the nickel metal electrodeposit. A need therefore still exists for accurate measurement of both nucleation and plating overpotentials during the early stages of electrodeposition. In this investigation, a polarization measurement technique was developed for nickel electrodeposition from sulphate electrolytes under typical commercial electrowinning conditions. This method is repeatable and accurate within approximately 10 mV, and enables the quick and concise monitoring of both nucleation and plating during nickel electrodeposition.

Keywords

nickel electrowinning, polarization potential measurement, sulphate electrolyte, galvanodynamic scan.

Introduction

Nickel electrodeposition reactions

In order to evaluate nickel electrodeposition, it is imperative to understand the reactions taking place in the electrolyte. Conditions should be conducive to promoting the main nickel deposition reaction while limiting unwanted or side reactions that could hinder or interfere with the main deposition reaction. The process of nickel electrodeposition from sulphate electrolyte involves the passing of a direct current between two electrodes immersed in a sufficiently conductive solution of nickel sulphate salt. Nickel cations are reduced to nickel metal at the cathode (Equation [1]) while oxidation of water at the anode (Equation [2]) releases the required electrons. The nickel ions consumed at the cathode are replenished from the nickel ions in the electrolyte. All standard potentials are given relative to the Ag/AgCl (saturated KCl) reference electrode (Holm and O'Keefe, 2000; Crundwell *et al.*, 2011):

At the cathode: $Ni^{2+} + 2e^- \rightarrow Ni$ $E^0 = -0.449$ V [1]

At the anode: $2H_2O \rightarrow O_2 + 4H^+ + 4e^-$ $E^0 = 1.030$ V [2]

Net reaction: $2NiSO_4 + 2H_2O \rightarrow 2Ni + 2H_2SO_4 + O_2$ $E^0 = 1.280$ V [3]

The reduction of species other than that of the sought metal should be avoided because this will reduce the current efficiency of the nickel metal plating process, and interfere with the nature and purity of the plated metal. In the case of nickel specifically, the nickel ions are thermodynamically more stable in aqueous solutions than hydrogen ions. Therefore, the reduction of hydrogen to hydrogen gas (Equation [4]) is thermodynamically more favourable and will occur simultaneously with the reduction of nickel cations (Holm and O'Keefe, 2000; Kittelty, 2002; Di Bari, 2010; Crundwell *et al.*, 2011):

$2H^+ + 2e^- \rightarrow H_2$ $E^0 = -0.199$ V [4]

This reaction needs to be controlled or minimized in such a way that nickel cation reduction is optimally promoted. One such precaution to minimize the interference of hydrogen bubbles is used almost exclusively, in which the anode and cathode are separated by an ion-permeable membrane. The electrolyte ions can freely move through the membrane, but gas bubbles are trapped on either side where they are produced. Membranes, or cathode bags, are commonly made from a material such as polyethylene or polyester (Crundwell *et al.*, 2011).

Another factor that needs to be kept in mind is that, although the stoichiometry and thermodynamics are accurately described by

* *University of Pretoria, South Africa.*

 ISSN 2225-6253. This paper was first presented at the 3rd Young Professionals Conference, *9–10 March 2017, Innovation Hub, Pretoria, South Africa.*

the reactions given above, the simultaneous transfer of more than one electron in an electrochemical process is unlikely to occur. There are many proposed mechanisms for the nickel reduction process, most of which assume that electrocrystallization occurs in two steps of electron transfer involving an intermediate adsorbed species (Equations [5] and [6]) (Aaboudi *et al.*, 2001; Kittelty, 2002; Di Bari, 2010, Crundwell *et al.*, 2011):

$$\text{First step: } Ni^{2+} + e^- \rightarrow Ni^+_{ads} \quad [5]$$

$$\text{Second step: } Ni^+_{ads} + e^- \rightarrow Ni \quad [6]$$

Even though there are many proposed ligands, the most common and simplest one to consider is the hydroxide ion that originates from the water present in the electrolyte solution. Hydroxides easily coordinate to the nickel ions according to the proposed reactions in Equations [7] to [10] (Munoz *et al.*, 2003; Di Bari, 2010). The charge-transfer reaction responsible for the formation of the $Ni(OH)_{ads}$ complex (Equation [8]) is typically considered as the rate-determining step (Di Bari, 2010). The $Ni(OH)_{ads}$ complex is believed to act either as a catalyst for the reduction of the metal ion or as an intermediate that is consumed to form the reduced metal species, as shown in Equations [9] and [10] (Munoz *et al.*, 2003; Di Bari, 2010):

$$Ni^{2+} + H_2O \rightarrow Ni(OH)^+ + H^+ \quad [7]$$

$$Ni(OH)^+ + e^- \rightarrow Ni(OH)_{ads} \quad [8]$$

$$Ni(OH)_{ads} + Ni^{2+} + 2e^- \rightarrow Ni + Ni(OH)_{ads} \quad [9]$$

$$Ni(OH)_{ads} + e^- \rightarrow Ni + OH^- \quad [10]$$

Effect of conditions and parameters on nickel electrodeposition

In order to obtain good quality nickel electrodeposits with a fine-grained, uniform morphology, low strain, and minimal hydrogen pitting, frequent nucleation and simultaneous growth should occur. The nucleation should be fast enough for initially formed nickel clusters to pack tightly onto the substrate surface, and each of these initial clusters should then grow sufficiently to promote three-dimensional (3D) growth. If the growth rate is fast and nucleation is slow, nickel deposits in a more columnar fashion with large, fast-growing crystals and open spaces between the crystals. Under such conditions, highly strained isolated crystals can form, or even large dendrites which can grow through the cathode bags and cause short-circuits (Winand, 1994; Budevski *et al.*, 2000; Kittelty, 2002).

Crucial parameters that need to be controlled in order to optimize the relationship between nucleation and growth during nickel electrodeposition have been established: nickel, sodium sulphate, and boric acid concentrations, temperature, and pH of the sulphate electrolyte (Holm and O'Keefe, 2000; Di Bari, 2010; Crundwell *et al.*, 2011). At sufficiently high nickel concentrations (60 g/L or higher), the conductivity of the electrolyte and mobility of the nickel cations toward the cathode increase. Rapid nucleation with simultaneous growth is promoted and desired uniform, fine-grained deposits form preferentially (Abyaneh and Hashemi-Pour, 1994; Ji and Cooper, 1995; Wu *et al.*, 2003). The sodium sulphate concentration is also kept relatively high (between 80 g/L and 100 g/L) to increase the conductivity of the electrolyte. If sodium sulphate is added in large excess, however, the viscosity of the electrolyte increases significantly, which in turn decreases nickel cation activity and mobility (Abyaneh and Hashemi-Pour, 1994; Holm and O'Keefe, 2000; Wu *et al.*, 2003). At higher temperatures (60°C or higher), mobility and conductivity increase, reactions rates are faster, and nickel deposition is promoted. Rounder, low-strained, uniform deposits are formed and current efficiency increases (Lantelme and Seghiouer, 1998; Holm and O'Keefe, 2000; Lupi *et al.*, 2006). The pH of the electrolyte is important for a number of reasons. At low pH (normally controlled between 2 and 3), the formation of nickel hydroxide species (which occurs freely at around pH 5) is limited and pure deposits are expected (Amblard *et al.*, 1983). The pH also plays an important role in controlling the hydrogen reduction reaction (Equation [4]). Boric acid is added as a buffering agent, and it is known that at boric acid concentrations of at least 4 g/L and at low pH (2–3) of the electrolyte, the nickel deposition reaction is promoted and the hydrogen evolution reaction is limited (Armyanov and Sotirova-Chakarove, 1992; Gadad and Harris, 1998). Under these conditions, good quality nickel deposits with low hydrogen pitting, low strain, and good morphology are expected. The mechanism and function of boric acid is still largely unknown and polarization techniques may be able to shed some light on this much-debated subject (Amblard *et al.*, 1983; Tripathy and Das, 2001).

Measurement techniques

Accurate measurement of nucleation and growth in order to evaluate the effect of changes in the crucial parameters is still a challenge. One of the earliest techniques that proved useful in obtaining such information during the electrodeposition process was cyclic voltammetry. This is a potentiodynamic (controlled-potential) polarization technique that measures plating potential (E_p), *i.e.*, the potential at which growth is initiated. This potential is identified by a sudden increase in the cathodic current, as illustrated in Figure 1. The overpotential is sensitive to changes in electolyte parameters, conditions, concentrations, and additives or impurities that may be present in the solution (Kerby *et al.*, 1977; Mackinnon and Brannen, 1977; Warren, 1985; Adcock *et al.*, 2002). This technique, however, requires an intricate and laborious set-up to produce repeatable results and it only provides information regarding changes in the plating potential (Adcock *et al.*, 2002).

Kerby *et al.* (1977) developed a successful technique known as the dual-channel continuous electrolyte quality monitor (CEQM), in which overpotential measurements were made at specific current densities for both nucleation and plating by using two individual wires that were monitored simultaneously throughout the electrodeposition process. This technique was laborious and complex, but indicated that nucleation and plating overpotentials could be measured simultaneously. It also established the importance of controlled-current (galvanodynamic) methods compared with classical controlled-potential (potentiodynamic) methods. It was this idea that led to the development, by Adcock *et al.*, (2002), of a new galvanodynamic (current-controlled) measurement technique specifically for zinc electrowinning from sulphate electrolytes. This technique makes use of a three-step galvanodynamic scanning procedure with a very

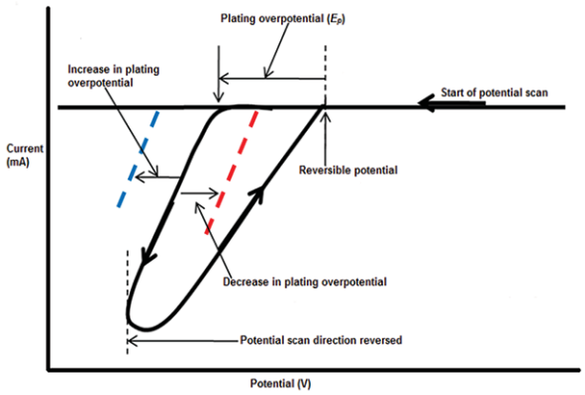

Figure 1—Schematic potentiodynamic voltammogram showing the decrease or increase in overpotential that can be observed due to changes in parameters or impurities or additives present in the electrolyte (after Kerby *et al.*, 1977)

slow initial forward scan rate to measure nucleation overpotential. An intermediate scan rate is then applied after the nucleation point is reached, and a fast scan rate is used on the reverse scan. The plating overpotential is measured at an arbitrary current density (typical of commercial processes). The advantage of using galvanodynamic instead of potentiodynamic methods is that more detail regarding the initial nucleation is observed and can therefore be measured (Adcock *et al.*, 2002). This technique is illustrated and compared with conventional potentiodynamic voltammetry in Figure 2.

The aim of the current work was to utilize the knowledge gained from the development of this galvanodynamic measurement method (Adcock *et al.*, 2002) to develop a similar method specifically for nickel electrowinning from sulphate electrolyte. The idea was to produce a simple yet reliable measurement tool with the capability of measuring both plating and nucleation potentials accurately and repeatably. This measurement method can then be used to investigate the effect of crucial operating parameters and species concentrations on the electrodeposition process, and ultimately to use the information gained to optimize, monitor, and control commercial nickel electrodeposition operations.

Experimental methods

A solution containing 75 g/L nickel, 80 g/L sodium sulphate, and 4 g/L boric acid with a pH of 3 and a temperature of 65°C was used as the standard electrolyte, representative of conditions established that produce acceptable quality nickel deposits. Thereafter, different electrolytes were prepared and tested by changing each of the parameters individually according to Table I.

Electrochemical measurements were performed in a standard three-electrode cell with a Ag/AgCl reference electrode (Metrohm). The cathode consisted of insulated titanium metal (commercial grade) with a surface area of 2.25 cm^2. The cathode was connected to conducting wire by silver epoxy glue and cold-mounted in epoxy resin, leaving only the top surface exposed. The surface was then prepared just prior to use by hand-polishing using silicon carbide (SiC) paper from P800 to P1200 while rinsing with deionized water, followed by ultrasonic cleaning in deionized water for 2 minutes. The auxiliary electrode was Pt wire. The auxiliary electrode (anode) and working electrode (cathode) were separated by a polyethylene membrane (product code D21A05, obtained from Ecotao). Fresh electrolyte solution (300 mL) was used for each experiment. The electrolyte was heated throughout each experiment by an encased water jacket with water flowing from a water bath. The temperature of the electrolyte was measured, monitored, and adjusted within ±1°C of the desired temperature using a standard thermometer. The system was connected to a potentio-/galvanostat (Solartron Schlumberger 1286 interface) and a computer with the appropriate software (*Corrware and Corrview*, obtained from Solartron Analytical).

A preferred galvanodynamic scanning method was developed in order to measure nucleation and plating overpotentials accurately and precisely. The newly prepared working electrode was introduced into the cell with prepared electrolyte for 1 minute to stabilize at zero current in galvanostatic mode. Thereafter, two sequential galvanodynamic scans were applied. The first forward cathodic scan was done at a very slow scan rate (0.1125 mA/s) in order to elucidate the precise turning point at which nucleation started. This was taken as the most cathodic potential point reached during this slow scan. This scan rate was applied from 0 mA to –0.3 mA. The second galvanodynamic scan was then applied from –0.3 mA to –90 mA in the cathodic

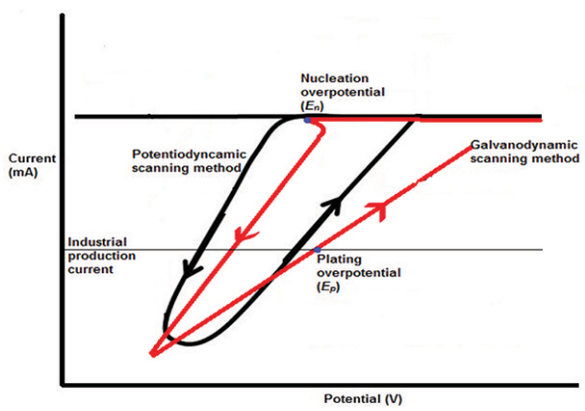

Figure 2—Schematic comparison of cyclic voltammetry (black) and a galvanodynamic scanning method (red), indicating points at which the nucleation and plating overpotentials are measured (after Adcock *et al.*, 2002)

Table I

Composition of electrolytes for development of galvanodynamic measuring technique

Electrolyte number	$[Ni^{2+}]$ (g/L)	$[Na_2SO_4]$ (g/L)	$[H_3BO_3]$ (g/L)	pH	Temperature (°C)
1	75	80	4	3	65
2	50	80	4	3	65
3	75	100	4	3	65
4	75	80	8	3	65
5	75	80	4	5	65
6	75	80	4	3	35

direction, and then from –90 mA to 0 mA in the anodic direction. This was done to obtain a value for plating overpotential (E_p). It was found that E_p was not as sensitive as nucleation overpotential (E_n), and a faster scan rate of 0.5625 mA/s could therefore be used during this second scan. Each scan consisted of a series of small steps in current with the potential measured and recorded at the end of each step. A total of 2000 points was collected and recorded for each two-step process. The nucleation potential (E_n) was measured as the most cathodic potential reached on the slow forward cathodic scan. The plating potential (E_p) was measured on the return anodic scan at an arbitrary current density of 220 A/m^2, which is commonly used as the applied current density for industrial nickel electrowinning. The scans were repeated in triplicate for each electrolyte. A typical scan indicating the nucleation and growth points is shown in Figure 3.

After each two-step galvanodynamic scan, the program was immediately set to galvanostatic deposition, during which nickel was galvanostatically deposited for 80 minutes at a current density of 220 A/m^2 under the same conditions. This was done in order to obtain a thick deposit for morphological, quality, and characteristic evaluation. Electrodeposits were stripped from the substrate surface immediately thereafter, ultrasonically cleaned in deionized water, and mounted for morphological investigation. Each mounted deposit was polished to 1 μm diamond finish and then etched for 4 seconds with 50:50 by volume nitric acid:acetic acid. The deposits were then optically inspected and classified according to quality, character, and general morphology. The current efficiency was calculated from the mass of each deposit compared with the theoretical mass determined from Faraday's Law.

Results and discussion

Table II shows the average measurement results from the triplicate scans for each electrolyte specified in Table I. An indication of the accuracy is also given, as well as the current efficiency and a description of the observed quality and morphological characteristics of the produced nickel deposit.

Typical microstructures of cross-sections of thick nickel deposits obtained from the specified electrolytes are shown in Figure 4.

The results show that both nucleation and plating overpotentials can be obtained accurately and repeatably for sulphate electrolytes with varying conditions and parameters by using the developed galvanodynamic technique. The measured overpotential values (both nucleation and plating) are clearly sensitive to and influenced by the conditions and species concentrations in the electrolyte.

If the standard electrolyte (electrolyte 1) is used as a reference point for measured overpotential values and optimum nickel electrodeposition conditions and parameters, a number of observations can be made regarding the other electrolytes. For the electrolyte with low nickel concentration (electrolyte 2), the E_n changed markedly (more negative) and the E_p only slightly (more negative). This suggests that the low concentration of nickel cations is inadequate to promote simultaneous nucleation and growth in order to form closely packed 3D structures. The deposits obtained under these conditions were strained and pitted, which could also indicate promotion of the hydrogen reaction at low nickel concentrations. The current efficiency was much lower compared with standard conditions, suggesting poor plating conditions. A strain crack can be seen in Figure 4b.

At high sodium sulphate concentration (electrolyte 3), both E_n and E_p vary; 3D growth was promoted and round, uniform, fine-grained, good quality deposits formed (Figure 4c). The relationship between nucleation and growth seemed to be optimum under these conditions. The current efficiency even increased compared with that calculated for electrolyte 1. Much the same observations can be made for deposits obtained from electrolyte 4, which had increased boric acid concentration. The relationship between nucleation and growth once again seemed optimum, even though the E_n and E_p shifted to more negative values. The exact mechanism of

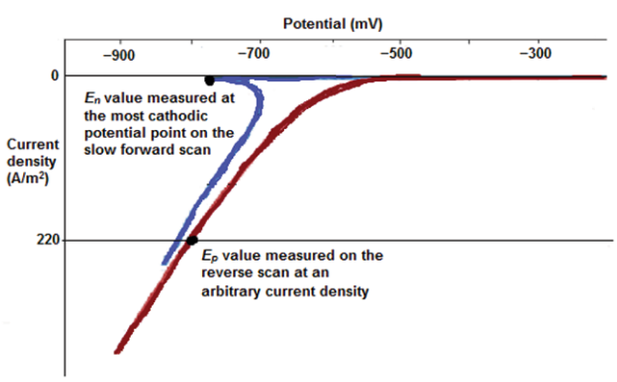

Figure 3—Typical galvanodynamic two-step scan obtained from a standard electrolyte, indicating the measurement points for nucleation (E_n) and growth (E_p)

Table II

Measured polarization parameters for various sulphate electrolytes as specified in Table I

Electrolyte number	Average E_n (mV)	Standard deviation E_n (mV)	Average E_p (mV)	Standard deviation E_p (mV)	Current efficiency (%)	Observed quality and morphology
1	–680	5	–739	3	98	Fine-grained, good quality
2	–816	3	–768	1	75	Strained, pitted
3	–624	5	–696	5	99	Fine-grained, bright
4	–746	2	–740	3	93	Fine-grained, slightly pitted
5	–629	3	–619	3	87	Strained and pitted
6	–889	4	–828	9	67	Highly strained and pitted

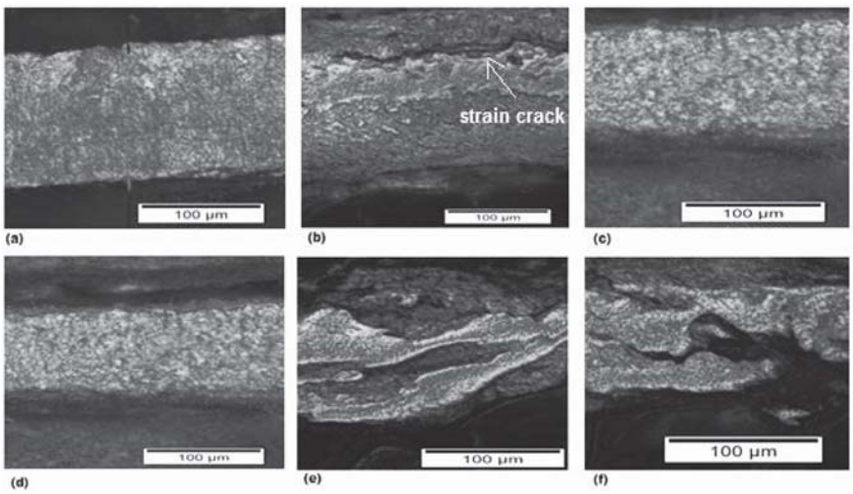

Figure 4—Micrographs showing the different quality and morphological characteristics of nickel deposits obtained from various sulphate electrolytes: (a) electrolyte 1, standard conditions; (b) electrolyte 2, lower nickel concentration; (c) electrolyte 3, higher sodium sulphate concentration; (d) electrolyte 4, higher boric acid concentration; (e) electrolyte 5, higher pH; (f) electrolyte 6, low temperature

the action of boric acid in the electrolyte is still unclear, but it is apparent that the addition thereof promotes nickel electrodeposition in a desired fashion. No hydrogen pitting was observed in the presence of higher concentrations of boric acid (Figure 4d.

An increase in pH (electrolyte 5) seemed to increase both E_n and E_p (became less negative) and the relationship between these two parameters was not ideal. Growth seemed to be promoted without frequent enough nucleation, causing strain, dendrite formation, and severe pitting (Figure 4e). The current efficiency also decreased significantly under these conditions. Similar observations were made for electrolyte 6 (low temperature): very large shifts in E_n and E_p were observed while the deposits obtained are strained, cracked, and extremely pitted. The current efficiency was very low.

It is clear that the measured E_n and E_p values as well as the relationship between E_n and E_p for each type of electrolyte play a crucial role in the type of growth, quality, and morphological characteristics of the nickel electrodeposit. Future work will further investigate and attempt to classify and correlate the relationship between polarization parameters and morphological outcomes. The developed galvanodynamic technique can also be used to investigate the effects of other variables in the electrolyte, such as additives to promote grain refinement or impurities.

Conclusions

A galvanodynamic polarization measurement technique developed specifically for nickel electrodeposition from typical sulphate electrolytes is presented. This method can be used to measure both E_n and E_p accurately, precisely, and repeatably for the various electrolytes tested. The method and experimental set-up are relatively simple and easy to operate. The measured E_n and E_p values are sensitive to changes in electrolyte concentration (nickel or sodium sulphate), the addition of boric acid, and parameters such as pH and temperature. It appears that changes in E_n and E_p, as well as the relationship between E_n and E_p, vary in a specific way, depending on conditions and parameters of the electrolyte. Therefore, the information gained from measuring the E_n and E_p can be useful to anticipate the effect that changes in an electrolyte might have. The technique can be useful in monitoring and control of the nickel electrodeposition process. Under specific conditions, the nickel deposits nucleate and grow in a specific way. It seems desirable to further investigate the relationship between E_n and E_p values measured by this galvanodynamic technique and the morphological and quality characteristics of the nickel deposits to determine any possible correlation.

References

Aaboudi, O., Amblard, J., Chopart, J.-P., and Olivier, A. 2001. A temperature and electrochemical impedance spectroscopy analysis of nickel electrocrystallization from a Watts solution. *Journal of Physical Chemistry B*, vol. 105. pp. 7205–7210.

Abyaneh, M.Y. and Hashemi-Pour, M. 1994. The effect of the concentration of boric acid on the kinetics of electrocrystallization of nickel. *Transactions of the Institute of Metal Finishing*, vol. 72, no. 1. pp. 23–26.

Adcock, P.A., Adeloju, S.B., and Newman, O.M.G. 2002. Measurement of polarization parameters impacting on electrodeposit morphology I: Theory and development of technique. *Journal of Applied Electrochemistry*, vol. 32. pp. 1101–1107.

Amblard, J., Froment, M., Maurin, G., Spurellis, N., and Trevisan-Souteyrand, E. 1983. Nickel electrocrystallization – from nucleation to textures. *Electrochimica Acta*, vol. 28, no. 7. pp. 909–915.

Armayanov, S. and Sotirova-Chakarove, G. 1992. Hydrogen desorption and internal stress in nickel coatings obtained by periodic electrodeposition. *Journal of the Electrochemical Society*, vol. 139, no. 12. pp. 3454–3457.

Budevski, E., Staikov, G., and Lorenz, W.J. 2000. Electrocrystallization nucleation and growth phenomena. *Electrochimica Acta*, vol. 45. pp. 2599–2574.

Crundwell, F., Moats, M., Ramachandran, V., Robinson, T., and Davenport, W. 2011. *Extractive Metallurgy of Nickel, Cobalt and Platinum-Group Metals*. Elsevier. pp. 327–346.

Di Bari, G.A. 2010. Electrodeposition of nickel. *Modern Electroplating*, 5th edn. Schlesinger, M. and Paunovic, M. (eds.). Wiley, Hoboken, New Jersey. pp. 79–114.

GADAD, S. and HARRIS, T.M. 1998. Oxygen incorporation during the electrodeposition of Ni, Fe and Ni-Fe alloys. *Journal of the Electrochemical Society*, vol. 145, no. 11. pp. 3699–3703.

HOLM, M. and O'KEEFE, T.J. 2000. Evaluation of nickel deposition by electrochemical impedance spectroscopy. *Journal of Applied Electrochemistry*, vol. 30. pp. 1125–1132.

JI, J. and COOPER, W.C. 1995. Surface pH measurements during nickel electrodeposition. *Journal of Applied Electrochemistry*, vol. 25. pp. 642–650.

KERBY, R., JACKSON, H., O'KEEFE, T., AND WANG, Y. 1977. Evaluation of organic additives for use in zinc electrowinning. *Metallurgical Transactions B*, vol. 8B. pp. 661–612.

KITTELTY, D. 2002. The electrocrystallization of nickel and its relationship to the physical properties of the metal. PhD thesis, Murdoch University, Australia.

LANTELME, F. and SEGHIOUER, A. 1998. Model of nickel electrodeposition from acidic medium. *Journal of Applied Electrochemsitry*, vol. 28, no. 9. pp. 907–913.

LUPI, C.M., PASQUALI, M., and DELL'ERA, A. 2006. Studies concerning nickel electrowinning from acidic and alkaline electrolytes. *Minerals Engineering*, vol. 19. pp. 1246–1250.

MACKINNON, D.J. and BRANNEN, J.M. 1977. Zinc deposit structures obtained from high purity synthetic and industrial acid sulfate electrolytes with and without antimony and glue additions. *Journal of Applied Electrochemistry*, vol. 7. pp. 451–459.

MUÑOZ, A.G., SALINAS, J.B., and BESSONE, J.B. 2003. First stages of Ni deposition onto vitreous carbon from sulfate solutions. *Thin Solid Films*, vol. 429. pp. 119–128.

TRIPATHY, B.C. and DAS, S.C. 2001. Effect of Mg^{2+}, Li^{+}, Na^{+} and K^{+} pt on the electrocrystallization of nickel from aqueous sulfate solutions containing boric acid. *Journal of Applied Electrochemistry*, vol. 31, no. 5. pp. 573–577.

WARREN, I.H. 1985. The application of polarization measurements in the control of zinc tankhouse operation. *Proceedings of Zinc '85.* Mining and Metallurgical Institute of Japan. pp. 251–264.

WINAND, R. 1994. Electrodeposition of metals and alloys - new results and perspectives. *Electrochimica Acta*, vol. 39, no. 8/9. pp. 1091–1105.

WU, R., OLIAZADEH, M., and ALFANTAZI, A.M. 2003. Electrical conductivity and density of $NiSO_4/H_2SO_4$ solutions in the range of modern nickel electrorefining and electrowinning electrolytes. *Journal of Applied Electrochemistry*, vol. 33. pp. 1043–1047. ◆

http://dx.doi.org/10.17159/2411-9717/2017/v117n7a4

Design considerations for critical coal measurement points: towards accurate reconciliation for integrated mine planning

by M. Tetteh* and F.T. Cawood*

Synopsis

Integrated coal mine planning requires integration of mine planning technical inputs like survey, geology, planning, mining, processing, and finance. A comprehensive strategy on tracking, measuring, and reconciling coal from the mine plan to the customer is needed to achieve this. The ultimate aim is to have confidence in the coal measurement, accounting, and reporting processes so that the effectiveness of the entire planning process can be measured for compliance with business standards. For such leading practice it is necessary to determine measurement protocols at carefully selected measuring points. The design of such critical measurement points to allow for integrity and accurate reconciliation in the context of integrated mine planning is the topic of this article, with reference to a typical surface (dragline) coal mine operation. A general surface coal mine flow diagram was developed. For a flow and distribution system for such a mine, five critical measurement points are expected. These are the output of mine planning and scheduling process; post-mining pit survey and highwall mapping; the quantity and quality of feed material; quantity and quality of coal product; and the coal distribution process which extends from the product to the preparation plant and point of sale to the customer. In order to prevent inherent human errors, key data must be captured and recorded electronically and automatically. A digital mining approach allowing for automation tracking, measuring, reconciling and reporting of coal along the value chain is recommended.

Keywords

integrated mine planning, processing plant, critical coal measurement points, accurate reconciliation.

Introduction

Reconciliation is basically defined as the process of comparing measurements and estimates along the mine value chain at different points in time, for the purpose of tracking and optimization of metal recovery (Marcfarlane, 2013). This implies a need for interaction between people, processes, and systems to enable an efficient and accurate accounting of the metal recovery and commodity of interest. In the broader context of mining, measuring points at which reconciliation may occur are defined for every particular operation. Marcfarlane (2011) outlined a number of reconciliation boundaries required for management control, from the model to the plant delivery. Although several mines have designed specific solutions for performing reconciliation, a systematic approach is usually required to develop and implement a successful reconciliation system. This will enable a better understanding of the flow of material from the source to the plant delivery, where the biggest variances occur, and potential metal losses.

A commodity like coal is either shipped directly to the market or processed first into saleable material according to market specifications. The process of reporting coal through continuous reconciliation between actual coal produced and planned is part of an integrated mine planning process. Measurements are critical for tracking and reconciling coal recoveries and require consistency during measurement, reconciliation, and reporting of coal production. For this to be successful, mining, technical, contractor, and plant personnel must frequently review their measurement systems for monitoring and tracking production from the pit to the customer. Planning and operating practices must aim to improve coal recovery and operational and governance requirements in order to achieve consistency and integrity.

This article discusses the issues to be considered for accurate coal measurement and reconciliation. The following are some of the critical issues that cut across the coal production chain:

- The integrated mine planning process
- Critical coal measurement principles;
- Critical measurement points and reconciliation.

A critical measurement point is defined here as any measurement that occurs in or between processes and ore systems. The objective is to describe procedures for tracking, measuring, and reconciliation at a typical surface coal mine. These need to be based on leading industry practices, but must also suit local conditions.

* *University of the Witwatersrand, South Africa.*
 ISSN 2225-6253. This paper was first presented at the 3rd Young Professionals Conference, *9–10 March 2017, Innovation Hub, Pretoria, South Africa.*

Design considerations for critical coal measurement points

The integrated mine planning process

Integrated mine planning is an initiative reflecting an optimized interaction between people, processes, and systems (Cawood and Richards, 2008) for safe, sustainable, and profitable production. Although the process varies in detail from mine to mine, it should follow a basic structure like the one depicted in Figure 1. Cawood and Richards (2007) highlighted some opportunities for coal mine surveyors to add value at the operational and corporate levels of the mining company. These opportunities include playing a role in mineral accounting and quality assurance to meet mine requirements, market specifications, and reporting. Such work must be done in a manner that is consistent with business drivers along the mine value chain.

The planning process begins with the reporting of Resources and Reserves according to the South African Code for Reporting of Exploration Results, Mineral Resources and Mineral Reserves (SAMREC Code). Reserves form the basis of the resource development plan (RDP), which provides the first benchmark for the reconciliation of coal. The RDP is used to identify economic and market criteria. Other inputs such as the mine's corporate strategy also inform the long-term plan. The medium-term plan (5-year business plan) is developed from constant revision of the life-of-mine (LoM) plan, taking into consideration medium-term economic and market criteria, corporate goals, selection of equipment, and the grade control model (GCM). The short-term plan (annual plan) is a refinement of the medium-term plan, plus other inputs such as short-term economic and market criteria, annual corporate goals, equipment updates, scheduling, and the refinement of the GCM. The last stage of the planning process is the budget mine plan (monthly or quarterly) where scheduled blocks (defined by SAMREC as the smallest modelled volume in the Reserves database and lowest scheduling entity in the planning hierarchy) are created with coal quantities and qualities calculated for each block. Adjustment factors are applied to estimate coal resource, (ROM) coal reserves, and marketable reserves. Morley and Moller (2005) categorized these observations in the planning process into four major headings:

- Resource/reserve estimation and mine planning (includes long-, medium-, and short-term planning plus annual reporting and budgeting)
- Mining, which includes resource/reserve block depletion (dispatch, survey data, and stockpiling information)
- Plant processing (feed and product)
- General observations and best practices.

The categories of a planning process outlined by Morley and Moller (2005) and the definition of an integrated mining process by Cawood and Richards (2008) emphasize the need for best practices in measurements.

All activities at every stage of the planning process are reflected in the GCM, which is the best available estimate of the coal to be mined (defined by SAMREC as the coal *in situ* within a scheduling block and within a working section targeted for mining and expressed as *in situ* tons at *in situ* moisture) and the products it will yield. The GCM is therefore fundamental for the comparison of planned and actual mining recovery. A number of opportunities become available to improve the definition of the coal to be mined as operations approach the area of interest. These areas of interest and their descriptions are outlined in Table I.

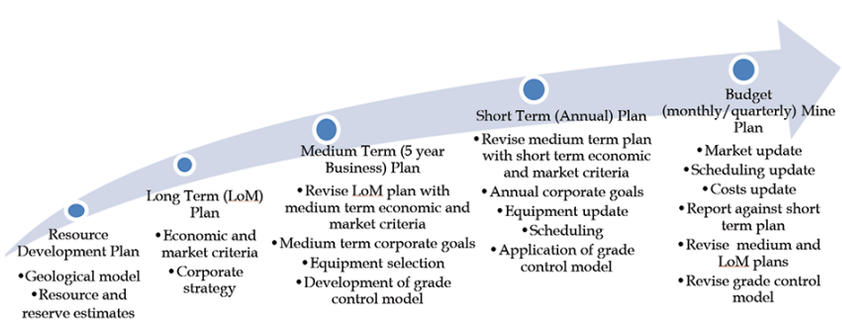

Figure 1—Typical planning process (Cawood, 2015)

Table I

Improving the definition of coal during operations

Area of interest	Description
Highwall mapping	Highwall in the previous strip to be surveyed and mapped to characterize the overburden to be blasted in the next strip. Define the roof and floor horizons for the low wall of the next strip.
Strip survey	Strip surveys for grade control include coal floor profiling, losses underneath roadways, and potential loss due to accumulations against the highwall.
Top of coal drilling and/or strip sampling	Core drilling may be required from exposed coal roof to improve the definition of coal quantity and washability.
Mining practices	Mining equipment and method influence the scale of dilution and loss.
Preparation plant simulation	Available representative washability data from pit sampling or coal drilling will enhance the short-term estimation of preparation plant yield.

Design considerations for critical coal measurement points

Coal Resources form a subset of the total tonnage of coal *in situ* (defined by SAMREC as coal in the ground, before exposure and at *in situ* moisture and density). In terms of SAMREC, the Coal Reserve is the economically mineable subset of the Coal Resource. An economic mine plan and a series of adjustment factors are required to generate Coal Reserves (ROM tonnages) and Marketable Reserves from the Coal Resource. The adjustment factors used need to describe what is expected in terms of mining and preparation plant recovery for coals from different parts of the Resource. The relationship between Coal Resources and Coal Reserves is illustrated in Figure 2.

Mineable *In Situ* Coal Reserves are subdivided, taking into consideration an increasing level of geoscientific knowledge and confidence, into Probable and Proved Mineable *In Situ* Coal Reserves. ROM Coal Reserves are further subdivided into Probable and Proved ROM Coal Reserves, also with increasing level of geoscientific knowledge and confidence.

The calculation of quantity and quality of the ROM Coal Reserves takes the following into considerations:

- Mass (tonnage) after allowing for geological losses, mine planning factors, moisture content, mining losses, mining dilution (defined in SAMREC as the waste material that is mined during mining operations and thereby forms part of the Reserve), and contamination
- The quality of the coal, expressed in parameters relevant to specific applications for *e.g.* Eskom coal, Export coal. Additional quality specifications include ash, volatile matter, sulphur, coking properties, calorific value, *etc.*

Saleable Coal is the tonnage and quality of coal available for sale, either in the raw ROM state, at a specified moisture content, or after beneficiated ROM Coal Reserves have produced materials at specified qualities, moisture contents, and size ranges. For raw ROM products, the practical product yield is typically 100%. Discard and Reject Coal (defined by SAMREC as coal or any carbonaceous material from coal processing or mining operations with quality parameters that are not within the current range of saleable coals) from the processing plant or mining operations should be measured for effective coal flow comparisons and reconciliations. Figure 3 shows the basic relationships that need to be addressed.

The outer and larger circle represents the *In Situ* Coal Resource. Some of this may be uneconomic or unmineable and is therefore excluded from the coal identified for mining. Adjustments are applied to the quantities and qualities of the coal represented by scheduling mining blocks as part of the planning process. Such mining blocks are informed mainly by the mining method that is applied. The mining process will inevitably fail to recover all of the targeted coal in a block and will include some dilution from adjacent materials. This mixture then becomes the ROM coal that is removed from the pit. ROM coal may be placed in an intermediate stockpile and later reclaimed before being fed to the plant or power station, either alone or in a blend consisting of coal from another mining area or areas.

The first beneficiation process usually involves crushing the coal in a rotary breaker, which also separates large hard fragments as reject. The remaining material is then stockpiled as crushed coal and is subsequently reclaimed as the feed to the preparation plant. The breaker reject and the yield expected from the preparation plant must be estimated for each scheduling block, based upon the relevant properties of the coal and dilution materials. Simple adjustment factors based on available borehole core samples tend to be used, in conjunction with broad efficiency factors, to generate estimates of the marketable reserves. Adjustment factors are often used in the industry to obtain a reasonable estimate of Saleable Reserves (represented by the smallest circular shape in Figure 3, called the yield). However, the general nature of these adjustment factors makes it difficult to back-analyse the performance of discrete processes or to guide specific improvements of field performance. The condition of coal is altered as it undergoes mining, handling, treatment, and transport. Other processes such as breakage, losses, contamination, and exposure to the ingress of moisture are all possible means of altering the characteristics of the coal. These effects need to be evaluated for every coal type and at all stages of the coal flow.

The next section will discuss measurement principles and requirements for ensuring that coal production is measured and reported along its critical measurement points from mining to market towards accurate reconciliation.

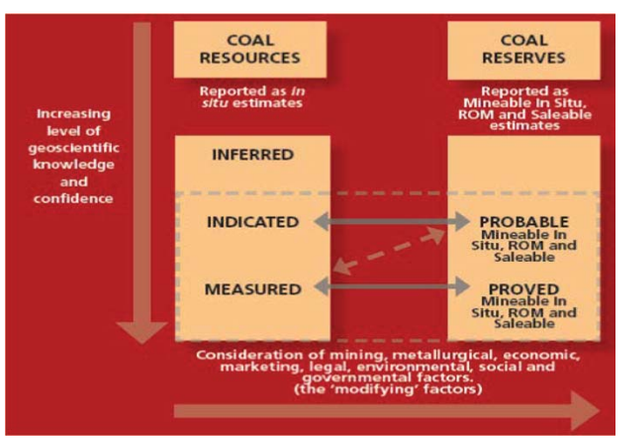

Figure 2—Relationship between Coal Resources and Coal Reserves (Source: SAMREC Code, 2016)

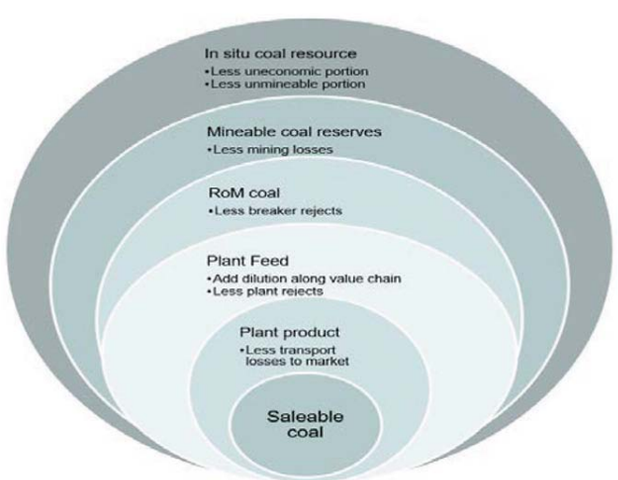

Figure 3—Transition of coal from *in situ* to saleable tonnage

Design considerations for critical coal measurement points

Critical measurement principles for accurate reconciliation

There are some basic measurement principles that need to be adhered to for ensuring reliable information is always produced throughout the coal value chain. There are many challenges in obtaining adequate measurements, which include capital cost of equipment and maintenance thereof, human resources, analysis and reporting of measured data, and assigning areas of responsibility. The measurement variables and their descriptions in Table II highlight some of the basic principles that need to be adhered to if a measurement system is to produce reliable information.

The measurement variables and descriptions in Table II are important to highlight efficiencies in the mining process. These would enable the reconciliation in the coal mining process. The accuracy of these measurements will help to bring out the 'truth' in the reconciliation results.

Measurements for meaningful reconciliation

Production monitoring and reporting outputs are needed for a successful reconciliation of coal recovery and mining performance against the actual plan. The following production measurement and reporting outputs are essential requirements for the successful reconciliation of coal recovery and mining performance against plan.

Requirement 1: Design of the critical measurement points

This is a major decision because it will require location of critical measurement points for meaningful reconciliation. Part of the design will include protocols and standard operating procedures (SOPs) at each measurement point. The design must also take the allocation of resources and budget constraints into account. Five critical points have been identified for a surface dragline coal mine operation to ensure effective control.

1. *Output of the mine planning and scheduling process*—Considers the estimate of coal resources and reserves per mining block after the GCM has been applied to it. The outcome (for reconciliation back to plan) is a short- to medium-term statement on the locality, quantity, and quality of planned coal over specific periods. The information compiled for this purpose must also meet the reporting requirements of the plant.
2. *Post-mining pit survey and highwall mapping*—This is the actual tonnage mined (defined by SAMREC as the actual volume of ROM coal washed and processed from ROM coal fed to plant over a specific period) as calculated from survey measurements done according to the mine's SOP. This does not include sampling to test the quality of the coal. However, the sampling of exposed coal will result in better certainty on the quality of coal delivered to the plant and hence enable the plant manager to plan for better product control. The reconciliation on quantity (volume and/or mass) will be in both directions, *i.e.* with planned coal and coal delivered at the plant
3. *Feed tonnage (ROM coal) and quality delivered to the plant*—These include the consideration of various measurements – on-mine stockpile surveys, coal quantities delivered to the plant but not fed immediately into the plant, truck tallies, and truck weighbridge and conveyor scale readings. The calculation includes reconciliation of mine stockpile surveys against post-mining pit survey results and ROM coal to plant against the weighbridge at the plant. This point will also consider only the mass and not include sampling – similar to the second critical measuring point
4. *Coal product tonnage and quality*—This will be determined from a combination of stockpile surveys and scales for mass, in addition to the quality parameters reported by the plant. Coal stockpile areas are typically surveyed by the plant surveyor and checked by the mine's surveyor. It is important to note that this may be the first time that the quality parameters of the coal will be compared with the planning output if samples are not taken at measurement point 2
5. *Coal sales tonnage*—This is a final measurement of mass from mechanical scales recording the tonnage that leaves the plant. These scale readings will be

Table II

Considerations for applying the principles of measurements

Measurement variables	Description
Mass and quality	These are coal parameters that need to be measured and tracked through the value chain.
Moisture	The weight of coal is meaningful only if the moisture content is known. Many of the ore loss, dilution, and recovery impacts that need to be understood and managed can be disguised by changes in moisture, which varies between 2% and 10% depending on season and location along the chain of production processes.
Accuracy and uncertainty	Measurements are subject to some level of uncertainty. These uncertainties are propagated through the production chain. A better understanding of accuracy and reliability of measurements allows a better accuracy when balancing calculations and a better interpretation of the numbers. For instance, survey results are preferred above those obtained from mechanical scales, and mechanical scales preferred above truck counts and truck factors.
Stockpile measurements	Stockpile measurement is a challenge. The traditional way of dealing with stockpile measurements is to acquire frequent reliable measurements of the stockpile volume and add or subtract measurements based on the most reliable stockpile information available. Unmanned aerial vehicle (UAV) technologies can now provide accurate, frequent updates.
Sampling	Quality estimation at any stage in the coal production process depends largely on sample representativeness. When considering the reliability of the results, it is important to note that it may not be possible to meet all the statistical requirements for sampling at some stages of the process.

compared with product stockpiles (backward) and other (forward) measurement points closer to the markets.

Figure 4 illustrates a typical flow sheet (of a surface coal mine) for the passage of coal from the ground to the point of delivery in the plant. Although this may vary from mine to mine, the same measurement principles are applicable. A number of critical measurement points are identified in the flow sheet indicating where tonnage and quality are measured in order to quantify mining performance and for reconciliation purpose.

Requirement 2: Identification, locating and tracking of coal

This starts with mining block identification as developed by the short-term planning process. Coal from each scheduling block is tracked through the mining, handling, and preparation plant processes. Unforeseen conditions and departures from the planned operations are noted and interpreted for performance. The physical factors that affect the recovery of coal, such as geological structures, geotechnical collapse, or practical mining issues, must be identified so that their impact can be separated from more routine measures of mining performance.

Requirement 3: Applying the principles of measurement correctly

The measurement principles required to ensure reliable information are applied throughout the coal value chain. Measurement errors should be reduced to a minimum. Possible sources of error include:

- Accuracy with regard to sampling
- Survey measurements, with specific reference to stockpiles
- Volume calculations of mined areas
- Errors accrued in measuring additional quality specifications such ash, vitality, density, moisture content, calorific value (CV), coking properties *etc.*

Requirement 4: Reconciling at each measuring point

Reconciliation is achieved by a structured comparison between the planned and actual values at each measuring point. Time-based production measurements will have to be adjusted to represent the performance of the same blocks of coal at different stages in the production process. It is recognized that the current planning and measurement systems at each operation may not be able to meet all of the requirements listed here. However, the progressive installation of additional measuring equipment and the reporting of basic reconciliations will quickly identify areas requiring additional resources, and will contribute to the ongoing refinement of the mine's protocols. The extent to which this comparison can be undertaken is limited only by the extent and reliability of the measurement data and the resources available to undertake the exercise. Riske *et al.* (2007) emphasized the need to capture key data through electronic and automatic means to eliminate human errors.

The next section outlines specific critical measurement points that exist along a typical coal production value chain. These critical measurement points are necessary to enable a successful reconciliation to be undertaken for effectivene planning and efficiency of mining operations.

Critical measurement points and reconciliation

For a typical surface mining, processing, and coal distribution system, taking into consideration the market requirements and mining areas serving a processing plant, the following critical measurement points are expected:

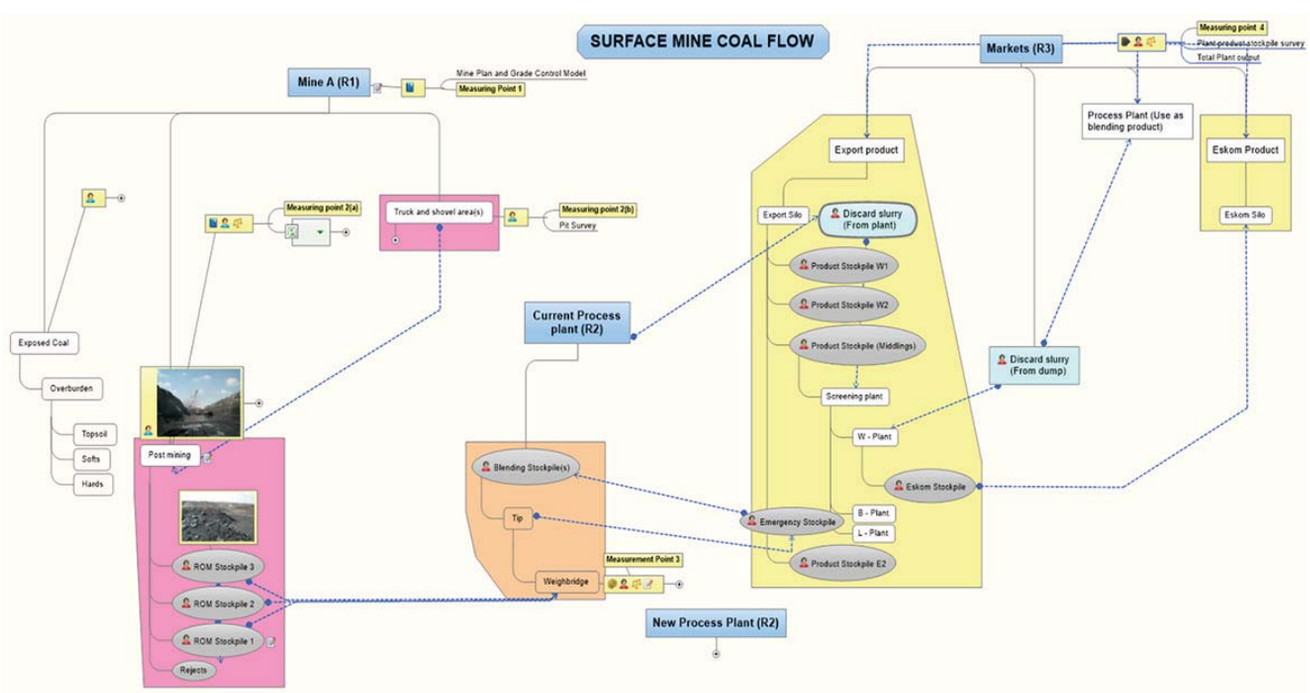

Figure 4—Typical surface coal mine flow sheet

- *Critical measuring point 1*—Output of the mine planning and scheduling process
- *Critical measurement point 2*—Post-mining pit survey and highwall mapping
- *Critical measurement point 3*—Feed ROM tons delivered to the plant
- *Critical measurement point 4*—Coal product
- *Critical measurement point 5*—Coal sales tonnage.

Table III summarizes these critical measurement points with specific reference to the measurement variables at each critical measurement point, data processing technique, and the reconciliation and reporting procedures carried out for the purpose of developing a protocol at each critical measurement point.

Critical measurement point 1 entails the definition of the *In situ* Coal and Reserves. This is the fundamental source of quantity and quality of the *In Situ* Coal and Reserves and Marketable Reserves estimated for a particular mining area. Once the coal has been exposed, surveyors can measure its actual volume and make a detailed quality measurement. At critical measurement point 2, the actual coal mined is obtained by surveying the final floor, highwall, and lowwall edges after mining is completed. Extreme care should be taken to account for any coal losses for the purpose of reconciliation. The third critical measurement point takes into consideration the quantity and quality of feed material. Sources of this data include truck counts, fleet management system, stockpile surveys, and rehandled coal. At critical measurement point 4, the tonnage and quality of the coal product is accurately determined. Very high-quality weightmeters and moisture and ash gauges are used in addition to sampling stations to determine the quality of the coal product, which is monitored constantly to meet market requirements.

Coal sales tonnage (critical measurement point 5) takes into consideration the coal distribution process. This distribution extends from the product at the preparation plant to the point of sale to the customer. This may be delivery on board a ship or to a stockpile at a power station. At every critical measurement point, accurate tonnage and quality measurements are required, taking into consideration the various processes the coal would have undergone.

Conclusion and recommendations

This article described the protocols for tracking, measuring, and reconciling in coal for an integrated mine planning process. A typical planning process begins with the reporting of Resources and Reserves based on the SAMREC Code. The measurement principles and requirement discussed enable accurate key data, such as quantity and quality, to be captured for accurate reconciliation of coal from the In-situ Coal Reserve to saleable coal. It is, however, necessary to develop detailed protocols at each of the five critical measurement points discussed in this article, namely:

1. The output of the mine planning and scheduling process
2. Post-mining pit survey and highwall mapping
3. Feed tons delivered to the plant
4. Coal product
5. Coal sales tonnage.

The authors recommend that measuring protocols at each critical measurement point should be regularly reviewed and updated. In order to reduce errors accumulated in the collection of key data, automatic and electronic means for capturing data are recommended. To carry out a routine reconciliation process at a typical surface coal mine, it is necessary to arrange site meetings with management and senior technical personnel to ensure that management is supportive of the process and willing to initiate the process. Creation of awareness of the reconciliation programme, requirements, and procedures is necessary at all levels of the operation. A digital mining approach that enables the automated tracking of quality and quantity data through sensor technologies is recommended. Further reconciliation and reporting of coal along its flow would be possible through a web-based digital mining data system.

Acknowledgement

The authors gratefully acknowledge the support received from the Wits Digital Mining Research Group, Julian Baring Fund, and the Wits School of Mining Engineering.

References

Cawood, F.C. 2015. Reporting of coal reconciling planned with actual. Sandvik International Mining School, University of the Witwatersrand.

Cawood, F.C and Richards, W.J. 2007. A review of the role of the coal mine surveyor in South Africa. *Journal of the Southern African Institute of Mining and Metallurgy*, vol. 107. pp. 109–113.

Cawood, F.C and Richards, W.J. 2008. Standardisation and formalising technical inputs into the mine planning process: A coal mine example. *Journal of the Institute of Mine Surveyors of South Africa*, vol, XXXII, no 9. pp. 659–673.

Marcfarlane, A.S. 2013. Reconciliation along the mining value chain. *Journal of the Southern African Institute of Mining and Metallurgy*, vol. 113. pp. 679–685.

Marcfarlane, A.S. 2011. Reconciliation along the base metal value chain. *Proceedings of the 6th Southern African Base Metals Conference*, Phalaborwa, South Africa, 18–21 July 2011. Southern African Institute of Mining and Metallurgy, Johannesburg. pp. 429–442.

Morley, C. and Moller, R. 2005. Iron ore reconciliation – a case study from Sishen Iron Ore Company. *Proceedings of the Iron Ore Conference*, Fremantle, Western Australia, 19–21 September 2005. Australasian Institute of Mining and Metallurgy, Melbourne. pp. 311–318.

Riske, R., Froud, J., Morley, C., and Gotte, J. 2007. The implementation of Snowden Software - a case study from Telfer. *Proceedings of the World Gold Conference*, Cairns, Queensland, 22-24 October 2007. Deschenes, G., Tuckerm D., Pocock, K., and Avraamides, J. (Eds.) Australasian Institute of Mining and Metallurgy, Melbourne. pp. 75–82.

SAMREC. 2016. South African Mineral Resource Committee The South African Code for the Reporting of Exploration Results, Mineral Resources and Mineral Reserves (the SAMREC Code). 2016 Edition. Prepared by the SAMREC Committee under the Joint Auspices of SAIMM and GSSA). ◆

Design considerations for critical coal measurement points

Table III

Critical measurement points in a coal mine

Critical measurement point	Measurement variables	Processing	Reconciliation	Reporting
CMP1- Output of mine planning and scheduling process	Tonnage, quality and locality of planned coal. Mine plan and grade control model – Area, volume/mass, relative density, losses and dilution, quality parameters such as CV, ash content, and moisture content	Volume of coal *in situ* obtained by multiplying modelled block plan area by the vertical thickness. Volume of coal in ground is same as volume of coal at *in situ* moisture. Esitmation of loss and dilution measurments of coal mass accompanied by moisture content and then mass of coal minus moisture to be determined. Coal density is obtained from the exploration borehole core samples. *In situ* mass of coal is calculated from *in situ* volume of coal and RD of coal at *in situ* moisture. Appropriate adjustment of ROM coal is first to estimate the mass of *in situ* coal and then consider any moisture adjustments gained or lost from the *in situ* to ROM.	Comparison of grade control model to coal reserves.	Production planning information generated by the mine planning department. Report generated at start of each month and contains information per seam and mining block
CMP2- Post- Mining Pit survey and highwall mapping	Volume/Mass of coal and waste material. Surveying and mapping of final floor, highwall and lowwall edges after minng. Swell factors to ensure true low wall edges and seam floor are measured. Quality parameters from sampling of exposed coal (moisture, loss and dilution).	Processing of ROM moisture content usually greater than *in situ* moisture content. The values of loss and dilution thickness are determined based on a back-calculation of previous mining supported by detailed surveys of mining operations. Issues to consider in estimating loss and dilution thickness are overcleaning possibilites, coal left behind, mining equipment used and blasting leading to loss and dilution, wet working areas will tend to increase both loss and dilution.	Comparison of ROM production to grade control model. This measurres the efficiency of the mining process. Comparison of ROM ash to *in situ* ash. Determination of apparent minng recovery (Compares ROM tonnes to *in situ* tonnes.	Tracking and reconciliation packages such as QMASTOR and Mine Track have been identified. These are used to capture production data. Existing systems are capable of acquiring, validating and reporting production data needed to perfom reconciliations required for reserve to customer
CMP3 - Feed tons delivered to the plant	Feed tonnage and quality. These include mine stockpile surveys, coal concentrations, delivered to plant and not immediately fed into the plant, truck tallies, weighbridge and conveyer scale readings. Truck tallies are compared with weighbridge readings. High-quality weightometer, moisture guage, ash guage and automatic mechanical samplers are required to monitor plant feed. The following parameters must be considered for all ROM sources. Volume/mass of ROM coal, level of foreign material in the ROM coal, moisture, ash, calorific value and size.	Volumes are calculated based on mine's standard and software programme. Variance in volumes should not exceed 5%. Analyses perforemed should include ash, moisture, size, washability by size, coking properties and contaminants. Consider monthly processsing plan and weekly processing schedules. All protocols to be observed. Ensure there is no mixing up of coal from different sources.	Comparison of plant feed to grade control model. Properties of plant feed in the grade control model are compared with the properties of the plant feed to assess the suitability of assumptions and adjustment factors used to generate GCM estimates. Dilution included during mining coal and actual mining recovery are also compared with GCM estimates.	Development of coal tracking and stockpile management systems
CMP4 - Coal product	Coal product tonnage and quality. Accurate measurements of coarse plant reject, moisture and ash content are required to interprete plant performance. Parameters required for accouting purposes are mass, yield, ash, calorific value and size.	The moisture content of washed coal is greater than the ROM coal. Processing of washabilities, ash, CV and inherent moisture should be in accordance with existing sampling and analysis protocols. Consider rotary breaker losses, processing of feed coal quality should be described in terms washabilities of the source coals and dilution materials in appropriate size fractions. Other considerations are processing preparation plant yield and blended feed and product quality.	Reconciliation between plant product and plant feed. This provides a measure of the efficiencyof the coal washing process. All existing protocols should be adhered to.	All protocols to be observed. For *e.g.* the weighing protocols of the two major companies requiring the product coal and discards to be weighed according to minimum specifications on daily basis
CMP5 - Coal sales tonnage	Coal sales tonnage at the market points. Accurate tonnage is required to guide the reconciliation of coal production and creation of coal parcels for sale. Transportation protocol of coal must be adhered to. Measurements are required for calculating clean coal volumes at silos and stockpiles. Coal from different sources are not to be mixed and same applies to coal for different purposes such as domestic and export.	Sampling and analysis protocols to be follwed. For *e.g.* analyses to be performed on coal product on trains. These include export coal trains: CV, total moisture and sulphur. Domestic coal trains: CV, total miosture, sulphur, abrasive index, hardgrolve index and sizing.	Comparison of coal sold to marketable reserves. Includes coal produced and sold from a giving mining area. This also validates the assupmtions used to estimate the marketable reserves.	Apply existing protocls for *e.g.* Plant must prepare a reconciliaton report at end of every month with the following: comparison of ROM coal versus throughput, reconciliaition of metallurgical balance, reconciling ROM coal with clean coal, reconciling predicted with actual yields, reconciling losses with discard materials and explaining deviations and investigating losses.

We strive to offer you the lowest cost of ownership

Weir Minerals is a leading designer and manufacturer of mine dewatering solutions, slurry pumps, hydrocyclones, valves, screens, centrifuges, crushers, feeders, washers, conveyers, rubber lining, hoses and wear-resistant linings for the global mining and minerals processing, sand and aggregate, and power and general industrial sectors.

For more information contact us on +27 11 9292600

WEIR

Minerals
www.minerals.weir
www.weirafricastore.com

http://dx.doi.org/10.17159/2411-9717/2017/v117n7a5

A technology map to facilitate the process of mine modernization throughout the mining cycle

by J. Jacobs* and R.C.W. Webber-Youngman*

Synopsis

It is vital for organizations and individual operations to have access to a platform with technology-related information to consider for further research and development. This paper presents a technology map that was created with the purpose of facilitating mine modernization through technological advancement throughout the mining lifecycle/cycle.

To achieve this, a platform was created to represent the mining life-cycle that incorporates each of the mining phases, *i.e.* exploration, project evaluation, mine design, operations, closure, and post-closure phases. The constituent value drivers for each phase were then investigated and included. These covered the various focus areas within the mining cycle, such as the applicable sub-phases, processes, systems, activities, or specific challenges, that impact a mine's operation.

Technologies, both physical and digital, with the potential to add value to these focus areas were then incorporated into the platform to create a technology map. This potential to add value, if applied or modified for application, was assessed on any combination of five factors, namely the ability to increase production, increase productivity, increase efficiency, improve safety, or reduce the risk of human error. The primary focus was on technologies currently classified as disruptive and/or exponential, *e.g.* internet of things, cloud computing, advanced robotics, genomics, 3D printing, and artificial Intelligence. Other emerging technologies were also investigated, such as automation, machine learning, renewable energy generation, energy storage, advanced materials, and more. Furthermore, selected innovative technologies adapted for or developed in mining were also investigated, as well as other new technologies in non-mining industries with potential to add value to mining. As such, a technology map was created that covers the entire life-cycle of a mining venture, which highlights technologies with the potential to add value to specific focus areas. This technology map may be applied to facilitate advances in technology for mine modernization.

Keywords

modernization, new technologies in mining, innovation in mining, technology map, mining cycle, mine life-cycle, mining R&D.

Introduction

The global mining industry is currently under pressure and is at the bottom of the largest mining supercycle since the Second World War (Bryant, 2011). Mining companies face ever-increasing challenges to profitability due to low commodity prices, increasingly tough mining conditions, and rising pressure from stakeholders (Deloite, 2014). In the short term, the decreased commodity prices have been straining cash flows, while in the longer term many existing mines are maturing, thereby resulting in the extraction of lower ore grades and longer haul distances from the excavation face. Orebody replacement rates are also declining and the duration of development for new mines is increasing. Added to this, worldwide mining operations are up to 28% less productive today than they were a decade ago, and that is after adjusting for declining ore grades (McKinsey, 2015a).

Depleting ore reserves and declining ore grades in existing operations also means that companies are required to mine deeper to reach new deposits, which in turn increases costs and results in reduced profits. Since the start of the 21st century, over 75% of new base metal discoveries have been at depths greater than 300 m (Deloite, 2014), highlighting both the gradual depletion of shallower reserves and the need for deeper mining. However, mining at these depths involves additional challenges, such as safety issues, flooding, gas discharges, seismic events, and ventilation problems (Deloite, 2014).

Apart from the fact that mining operations are now deeper, the geology is also more challenging and mines operate at higher risk. The result is that continuous business improvement alone is no longer sufficient for companies to survive (Deloitte, 2016). At the 2015 Johannesburg Mining Indaba in South Africa, Chris Griffith (CEO of Anglo American Platinum) stated:

> *Given the magnitude of our extraction challenges, it is quite extraordinary that the global mining industry currently spends so little on innovation and business-improvement programmes. On a revenue-to-revenue basis, the industry spends 80% less on technology and innovation compared with the petroleum sector, for example. Yet our operating costs are increasing three times faster than consumer-inflation rates and are*

* *University of Pretoria, South Africa.*
 ISSN 2225-6253. This paper was first presented at the 3rd Young Professionals Conference, *9–10 March 2017, Innovation Hub, Pretoria, South Africa.*

on their way to doubling in less than five years. With industry margins being squeezed on all fronts, we simply have to embrace innovation if we want to find more productive, efficient and sustainable ways of extracting value from the minerals we mine. We can't rely on only small, incremental changes and a business-as-usual philosophy to get us out of this predicament. Major innovation is exactly what our industry needs to solve its critical challenges. In fact, mining needs to leap forward 20 years in the next five…'

This statement is in line with the growing consensus that incremental operational improvements are no longer sufficient to sustain the mining sector as a whole. It further explains why many leading organizations are rallying behind the innovation imperative that calls for major transformation to business models and strategies (Deloitte, 2014). This is especially true with the impending technological revolution, where innovation will form a key component in making businesses sustainable. This holds true not only for the mining industry, but for all industries and individual organizations worldwide (ESPAS, 2015).

In this upcoming technological age, the lines distinguishing businesses will become increasing blurred as businesses become more technology-based (Bryant, 2011). Technology will become more integrated into all aspects of business as a tool for human assistance, with the application thereof being business-specific. As such, the silos in which various industries and sectors place themselves may disappear altogether as they experience an increased convergence towards becoming technology businesses first and foremost. In order to then draw from the knowledge and expertise of a growing business cluster, a holistic approach to innovation will be required that takes cognisance of a larger pool of potentially similar organizations.

As a result, it becomes increasingly important to improve the innovation efforts within a business by looking at technology trends across various industries. Many technologies exist (or are in the development phase) that may be applicable or may be modified for use in the mining industry. With the increase in technological advancement worldwide, it is also important for the mining industry to remain aware of cross-sectorial innovations that may have an impact in future. This is especially true when it comes to exponential and disruptive technologies. These are technologies for which the adoption curve, instead of following a linear trend with a steady rise, initially remains flat and then accelerates dramatically. Exponential technologies, such as 3D printing and artificial intelligence, often disappoint in their early years before adoption accelerates. Companies often overlook the value of such technologies in their initial stages, when they should have been exploring them (Deloitte, 2016b).

Operational performance excellence relies on the innovative use of such technologies and keeping abreast with developments that may add value to a given component within the mining value chain (Rivard, 2014), as well as in the broader mining cycle. As such, the focus should be on introducing proven technology from other industries combined with the development of new technologies. In this way the mining industry will progressively focus more on integrating all activities across the value chain. This includes the continued introduction and development of Integrated Remote Operation Centres (IROC), mechanization, and automation (MacFarlane, 2014). Such technological advances and implementations in mining form part of the modernization drive currently taking place in the South African mining industry. The Chamber of Mines of South Africa describes mine modernization as 'a process of transition and transformation of the mining industry of yesteryear and today to that of tomorrow' (COMSA, 2016). In the context of this paper, the term modernization refers to the innovative implementation, adoption, and advancement of technologies in order to create value and allow the transition towards a more technologically advanced and modernized industry.

In order to accomplish the value-added end-goals, such as mechanization, automation, and modernization as a whole, the supporting technologies need to be evaluated in detail. From these and many other technologies, mining operations can also achieve multiple other benefits and 'quick wins' (MacFarlane, 2014). It should be noted that the mining industry is often not aware of emerging technologies that could potentially add value to operations, or which may disrupt aspects of the business. The continuous assessment of technologies, in terms of impact or benefit, can then be considered as a growing business priority in order to gain an understanding of how opportunities could be exploited, or possible detrimental impacts negated or avoided. In doing so, an organization will be working towards enhancing its operational risk management strategies, minimizing negative consequences from external technological factors, and identifying potential improvements to an operation or the organization as a whole.

It is therefore vital that companies and individual operations have access to a platform that can provide technology-related information in the context of the various aspects within the mining cycle. For this reason, a technology map was created. To achieve this, it was first necessary to create a platform that represents the entire mining cycle and the underlying six mining phases, namely exploration, project evaluation, mine design, operations, closure, and post-closure. Each of these was further expanded into the focus areas that contain the value drivers impacting on a mine's operation, such as constituent sub-phases, processes, systems, activities, or specific challenges, with potential to increase or decrease value for the organization. The value drivers were then categorized under seven main value driving pillars, namely mineral resource management; production; productivity and asset efficiency; profitability and cost control; supply chain; socio-economic factors; and health, environment, safety, and legal. These seven pillars were represented throughout the six mining phases to form a seven-by-six matrix.

Numerous technologies, ranging from physical to digital, were then analysed. Analysis was based on any combination of five qualifying factors – the ability to:

- Increase production (as a measure of effectiveness, *e.g.* tons extracted)
- Increase productivity (as a measure of efficiency, *e.g.* resources, such as time and money, used to extract a specific amount of tonnages)
- Increase efficiency (as a measure distinct from

productivity, *e.g.* an increase in efficiency that may not have a direct impact on production but still adds value to the organization, such as a more efficieny payroll system)
- ➤ Improve safety (as a measure of reducing the likelihood and severity of potential causes of harm to people)
- ➤ Reduce the risk of human error (a measure of decreasing the likelihood of blunders or mishaps).

Accordingly, those technologies with potential to add value, and as such facilitate the process of mine modernization, were slotted into the applicable focus areas within the mining cycle. A technology map was thus created spanning the entire mining cycle, which highlights technologies with the potential to add value. These technologies may then be subjected to further analysis in order to identify those with sufficient potential to facilitate the modernization drive specific to that operation or organization.

Technology focus

As mining companies begin to adopt innovative practices on a larger, more all-encompassing scale, they stand to gain significant value. When they leverage new and emerging technologies for increased synergy across the entire mining value chain, organizations can alter the fundamentals of the mining sector. For example, 3D visualization tools can assist companies with real-time tracking of their people, equipment, and changing environment at each mining site. New mineral processing technologies are emerging to reduce the safety hazards associated with gold extraction and to unlock previously uneconomic mineral deposits. Social media are assisting companies in facilitating electronic bookings at mine sites and enhance employee access to information. SMS messaging platforms help foster two-way communication with employees, solicit feedback, and improve workforce engagement. New production and logistics technologies also promise to reduce both the use of natural resources and harmful gas emissions. Vale's S11D project's mine and plant in Carajás, Brazil will, for example, consume 93% less water, use 77% less fuel, and produce 50% less greenhouse gas emissions than a comparable operation using conventional methods (Deloitte, 2015a).

Mining companies are already aware of the imperative to adopt technologies to accelerate automation and reduce fatalities, and have implemented various strategies to accomplish this. Investment in innovation for better technology application is an example. These have ranged from automation and enhanced drilling systems to data analytics and mobile technologies. Mining companies that have embraced innovation are improving mining intensity while reducing labour requirements, capital requirements, and energy intensity (Deloitte, 2016b). This is why leading companies continue to look at new technologies, such as nanomaterials, robotics, 3D printing, modular design, bioengineering, and alternative haulage, in an effort to further improve operational performance (Deloitte, 2014).

Similarly, in mineral exploration, technologies such as hyperspectral imaging and interferometric synthetic aperture radar hold potential value. These technologies are already in use to monitor ground subsidence, landslides, volcanoes, and active faults (TIA, 2012). Mining companies can also leverage techniques like simulation, technical modelling, and seismic technologies borrowed from the oil and gas industry, instead of engaging in traditional drilling. This can allow companies to identify mineral-rich deposits more cost effectively, while simultaneously helping the industry to maintain a sustainable discovery pipeline (Deloitte, 2015a).

In this information age, value creation is, however, dependent on more than just physical technologies. In order to improve long-term planning and forecasting, companies must also explore emerging information technologies. Examples include cloud computing, sensors, GPS systems, embedded logic, cyber-security, 'big data', 3D visualization, and simulation modelling (Deloitte, 2014).

Underground mines can also strive to implement real-time production management systems by using the latest technologies available. Some of these include low-cost off-the-shelf wi-fi networks and inexpensive wireless radio-frequency identification (RFID) tagging for vehicle and personnel location and tracking. Other non-physical technologies include software systems for mapping, modelling, estimation, design, scheduling, simulation, and mine production management reporting. These technologies have the potential to engender a fundamental change in the way mining operations are managed (Rivard, 2014). Applying such technologies to real-time monitoring of production processes may enable faster decision-making in changing conditions (MacFarlane, 2014).

To combat rising energy costs, reduce unwanted emissions, and accelerate electrification, companies also need to investigate energy technologies. Some of these include advanced materials, smart grids, energy storage technologies, renewable energy conversion, superconductivity, non-explosive rockbreaking, and high-energy lasers (Deloitte, 2014). In the energy space alone some operations have achieved 10% to 40% energy savings. This resulted from investment in renewable energy installations, deploying innovative energy technologies, and adopting more automated mine processes to optimize energy consumption (Deloitte, 2016b).

By integrating mining, energy, and information technology into mine and process design in an innovative way, it is possible to achieve radical breakthroughs in performance. When combined, these technologies can help companies reduce capital, labour, and energy intensity, while increasing mining intensity. Companies can also improve safety standards, reduce operating costs, optimize their energy mix, and enhance operational performance by combining these three technology groups (Deloitte, 2014).

It is therefore recommended that organizations consider technologies, such as those in the technology map, in an integrated manner in order to enhance synergy across the mining value chain for existing operations and across the broader mining cycle for the entire mining venture. In this way, companies may strive towards increased operational performance improvements. Such an approach often leads to improvements that far exceed the individual benefits of the application of a single technology in isolation. In this context, it should be borne in mind that the technology map does not provide insight into such potential gains, owing to the large number of possibilities resulting from technology and system integrations. The potential benefits of technologies were

investigated individually, and these will be discussed. The resulting analysis serves as a guideline for companies or individuals that wish to extract information from the technology map. By analysing their potential value, technologies that should be considered for further research and development (R&D) can be identified and a tailor-made solution created for a specific organization, operation, environment, challenge, or problem area.

In this study, greater focus was placed on emerging technologies, such as those that have the greatest potential to be disruptive in nature or drive the largest economic impact across various industries, businesses, and countries. Recent technological advances outside of the primary scope were also investigated. These included technological innovations in mining as well as non-mining industries with potential to add value if applied (or modified for application) in the mining environment.

Mapping the mining cycle

In order to create a technology map that spans the entire mining cycle, a framework was constructed that is representative of the scope and specific needs of the study. The resulting mining cycle framework was a 7×6 matrix that covers the six mining phases, from exploration to after mine closure, and consisted of seven main value driving pillars. The pillars incorporate all aspects that impact mining and were classified as follows: mineral resource management; production; productivity and asset efficiency; profitability and cost control; supply chain; socio-economic factors; and, health, environment, safety, and legal. Figure 1 illustrates how these seven pillars form part of the general mining cycle and why they were chosen to represent the platform upon which the technology map was created. Figure 2 highlights a specific area within the mining cycle framework, namely the production pillar within the operations phase, and illustrates the various value drivers identified for this specific block in the framework.

It should be noted that no existing representations of a generic mining life-cycle were deemed sufficient in depth and/or description to be used as a basis for the technology map as per the needs of this study. For this reason, the illustrated framework was designed to address the needs and perspective of this study. As such, the classifications, definitions, groupings, level of detail, or other factors relating to the framework illustrated here may not be adequate for various other technology map designs. It is suggested that the system architecture for a technology map's platform be designed according to the requirements of each specific project or study.

After tabulating the value drivers for each corresponding pillar, the total matrix contained around 330 value drivers. All of the drivers represented potential opportunities for the investigated technologies (whether physical or digital, and for various systems and combinations of applications) to add value to a mining operation or organization as a whole. A high-level example would be increased 'digitization' of the development process, *i.e.* conversion to digital formats and the increased application of digital technologies to add value to the process. The constituent technologies to accomplish this may range from various digital to physical technologies. Applicable digital technologies may include 'big data', advanced analytics, machine learning, and various others that convert data into information and in turn into value-adding intelligence, enhancing decision-making or physical

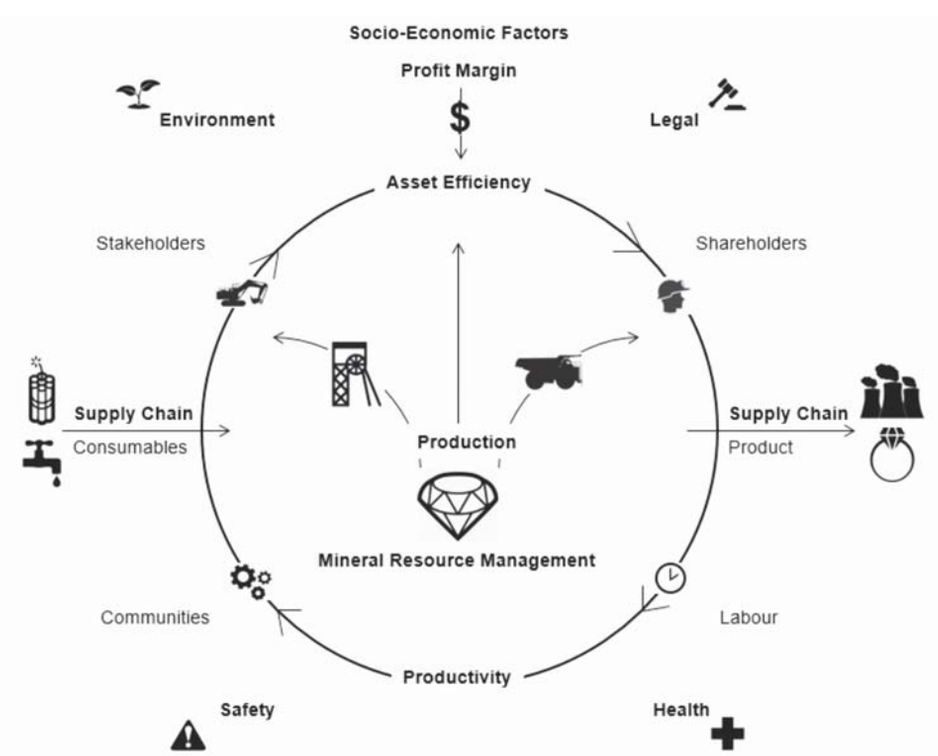

Figure 1—Visual representation for the mining cycle (Jacobs, 2016)

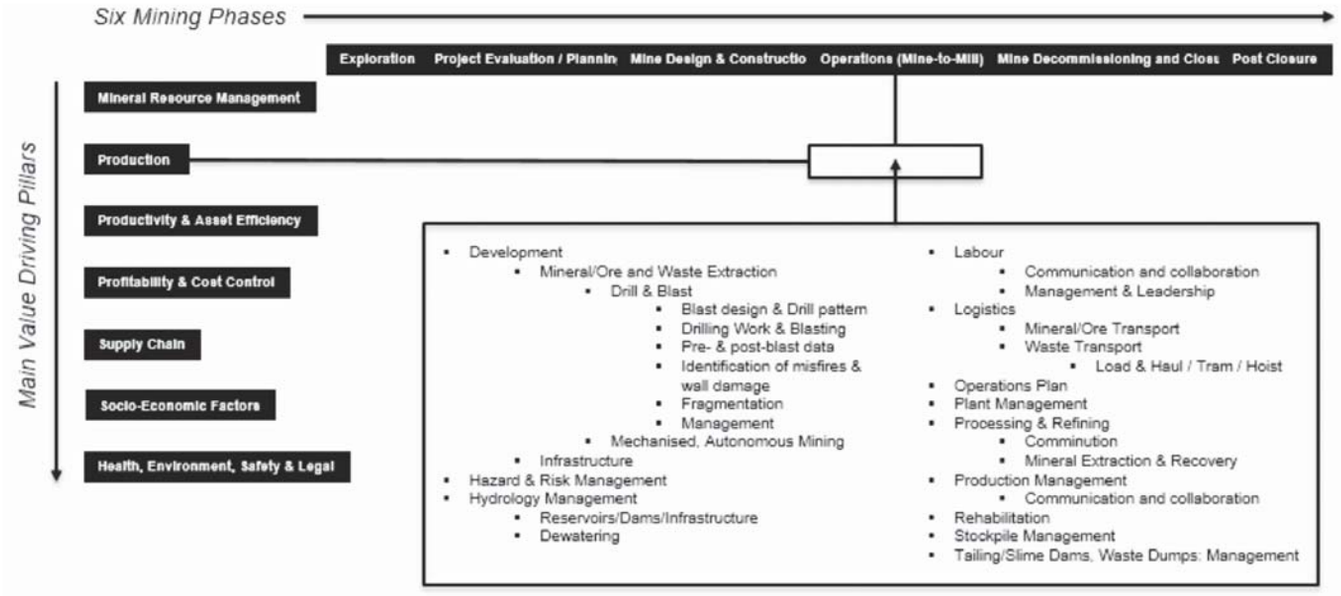

Figure 2—Mining cycle framework, indicating identified value drivers within a portion in the mining cycle (Jacobs, 2016)

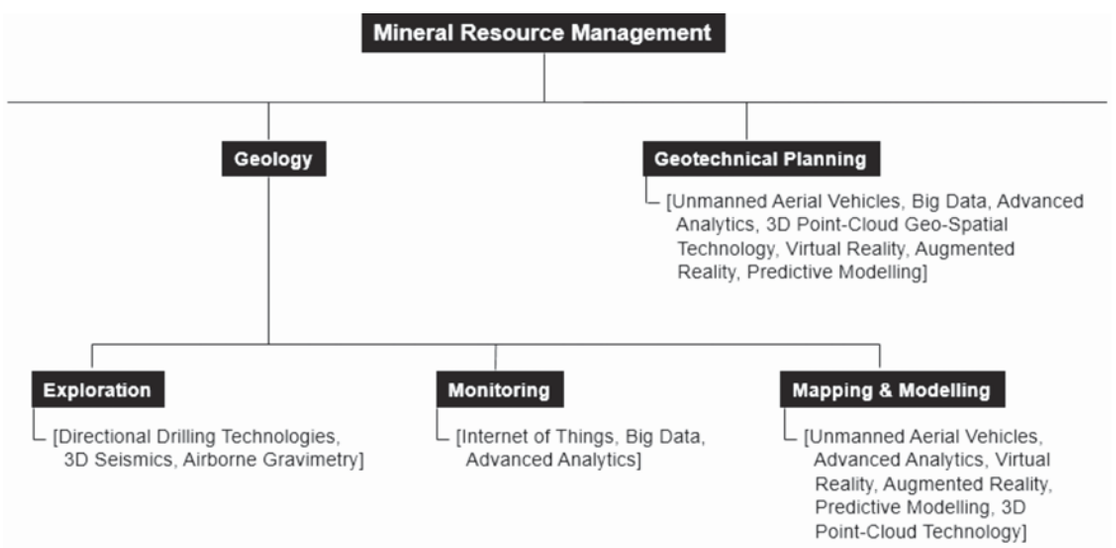

Figure 3—Technology map example 1 (Jacobs, 2016)

operation. The physical technology enablers may include the sensors for internet of things applications to extract the data, tracking technologies to monitor asset location and utilization, and robotics and ICT applications in rockbreaking or drill-and-blast-based mechanized equipment to enable remote operation.

Creating a technology map

To illustrate how the technology map was designed from the platform of the mining cycle and its constituent value drivers, consider the following examples of different sections taken from the technology map. Figure 3 displays a basic example from the operations phase under the mineral resource management pillar for the two chosen main value drivers: geology and geotechnical planning. Figure 4 is a more detailed example from the operations phase under the productivity pillar, with a specific focus on underground development as the main value driver. For this example, the chosen supporting value driver is mineral/ore and waste extraction, which in turn branches out to drill-and-blast and mechanized, autonomous mining.

Under each of these value drivers and/or constituent value drivers, the investigated technologies with potential to add value are shown in square brackets. These technologies, along with selected others from the technology map, will be discussed in relation to their potential areas of application within the mining cycle to provide context on how the technology map was designed.

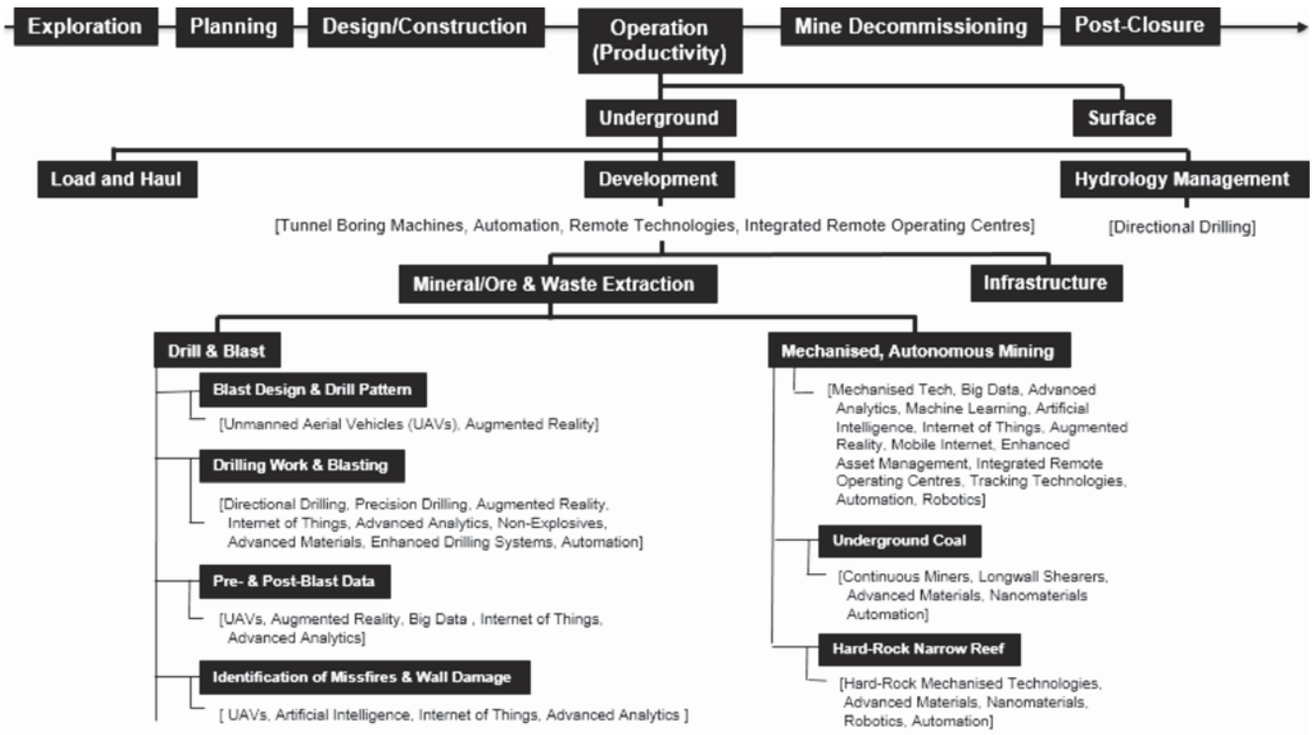

Figure 4—Technology map example 2 (Jacobs, 2016)

Advanced analytics and big data

Data is a foundational component of digital transformation. To realize the full potential that can be extracted from data, some businesses are treating data analysis as a strategic discipline and are investing in industrial-grade analytics (or advanced analytics). Advances in distributed data architecture, in-memory processing, machine learning, visualization, natural language processing, and cognitive analytics have unleashed powerful tools that can answer questions and identify valuable patterns and insights. To create value from big data through advanced analytics entails a process of information acquisition and curation, information delivery, turning information to insights, and insights to actions (Dupress, 2016a).

Analytics will become deeply, but invisibly, embedded everywhere. Organizations will face increased difficulty in managing the huge amounts of data (often termed 'big data') from the internet of things, social media, wearable devices, sensors, and other sources. Applying advanced analytics to an understanding of context could provide the preconditions for a world of smart machines. This foundation combines with advanced algorithms that allow systems to understand their environment, learn for themselves, and act autonomously (which further assists technologies such as artificial intelligence, machine learning, and deep learning). Prototype autonomous vehicles, advanced robots, virtual personal assistants, and smart advisors already exist and are evolving rapidly. This will ultimately usher in a new age of machine helpers, leading to a smart machine era that is likely to be the most disruptive in the history of information technology (Gartner, 2014).

As regards mining, global supply and demand factors lack the transparency that companies often require in order to make decisions before disaster ensues in their operations. Companies now need more flexibility than ever before, and should aim to hone their ability to scale production, labour, and other inputs and outputs up or down in response to shifting economic trends. Predictive analytics can help organizations in this regard by identifying events that may shift commodity market fundamentals (Deloitte, 2016c). Smart planning and coordination of activities are required to mitigate variability caused by external forces. Disciplined execution is needed to eliminate variability in operations. A step change in mining productivity will ensue through reducing and, where possible, eliminating the variability that has made mining unique (McKinsey, 2015a).

Mining companies continue to refine their safety programmes, but the statistics still remain unsatisfactory worldwide. Companies often turn to data analytics to pinpoint the industry risks, organizational behaviours, and internal cultures that are most likely to result in serious safety issues. As this technology becomes more intuitive and less costly, it is enabling companies to implement safety programmes focused on zero fatalities (rather than zero harm). Companies are able to better correlate the safety data they collect with other available data-sets (*e.g.* production data, employee rosters, maintenance schedules, weather forecasts, vehicle telemetry *etc.*). By correlating this data, companies can recognize safety incident patterns and employees that are particularly at risk. They are then in the position to adopt processes and procedures to minimize incidents and injuries (Deloitte, 2016c).

According to Deloitte (2014b), the use of analytics enables companies to:

- Assess the costs of entire processes in order to reveal the underlying cost base and to identify exceptions and outliers
- Improve decision-making and asset performance through the measurement of both financial and non-financial indicators that affect overall profitability
- Merge data from a wide range of different sources to deliver on-demand reports. This then enables asset utilization and reliability to be improved. It would also minimize downtime, streamline mine planning, and optimize fleet resources
- Manage operational costs, for example by quantifying the mineral content of each shovel load to determine whether it is below cut-off grade.

As data analysis becomes increasingly more sophisticated, opportunities for greater efficiency arise. From a talent management perspective, companies can leverage vast sets of employee data to make more informed workforce planning decisions. The use of real-time information on the state of equipment can improve maintenance schedules and asset performance. The consolidation of various data inputs can streamline supply chains and enhance mine planning. Continuous monitoring of mineral asset portfolios can pinpoint commodity and cost movements that affect profitability. Using predictive project analytics, companies can vastly reduce cost overruns to improve capital project outcomes. By harnessing big data in real time, some companies are also optimizing mineral processing at localities around the globe from a single location. In time, operational excellence will likely hinge on an organization's ability to effectively interpret the massive stores of data it collects (Deloitte, 2015b).

Advanced analytics can also assist production supervisors to determine the optimal material blend and schedule production to optimize mine/plant throughput. It can likewise benefit strategic procurement programmes, in that category management, strategic sourcing, supplier integration, procurement centres of excellence (COEs), and transaction optimization can all work to reduce costs and waste in the supply procurement process (IBM, 2009).

While most information technologies prove to be not only greatly beneficial, but also critical, to all levels of an organization, the integration of various technologies is both the most difficult and the most lucrative aspect. Business leaders should pay special attention to how advanced analytics, huge volumes of data, the internet of things, artificial intelligence, machine learning, and automation all tie in together. The underlying component technologies will also play a critical role in the building of a global automation and real-time analytics system that not only responds to, but also predicts and adapts to, market and operational dynamics.

By keeping these applications in mind, it becomes clear how big data and advanced analytics may play a role in the identified value drivers from Figures 3 and 4. It may assist with geotechnical and geological planning, with the optimization of outputs such as scheduling, modelling, planning, and the monitoring of data from various sensors and devices (*e.g.* through a network of sensors such as the internet of things). Similarly, advanced analytics can assist in ore or waste extraction processes. In drill-and-blast practices, for example, advanced analytics may assist with drawing up blast patterns and setting up the correct angles and hole depths to be drilled based on data inputs on geological features. It may also assist with analysing blast data and making recommendations for load-and-haul activities in order to optimize fleet efficiency by taking into account the muckpile size, shape, and fragmentation. In mechanized and autonomous mining, advanced analytics can greatly assist by providing valuable insights from data obtained by sensors and other devices regarding the state of the machinery. Real-time data can be analysed to adjust machine performance, sequence, and system or fleet integration for optimal results.

Advanced materials and nanomaterials

Scientists have discovered ways to produce materials with enhanced attributes. Some of these include smart materials that are self-healing or self-cleaning, memory metals that can revert to their original shapes, piezoelectric ceramics and crystals that turn pressure into energy, and nanomaterials. Other properties include greater reactivity, unusual electrical properties, and greater strength. These properties can lead to the development of new medical devices and treatments, 'super-slick' coatings, and stronger composites (McKinsey, 2013). Provided that such materials can be produced in large quantities, they could replace composites and other materials in a wide range of applications. These nano-altered materials would be just as strong as their conventional counterparts, but with a fraction of the weight (Bourzac, 2015). Advanced nanomaterials such as graphene and carbon nanotubes could lead to new applications and technologies, such as highly efficient batteries and solar cells. Pharmaceutical companies are also progressing research to use nanoparticles for targeted drug delivery in medical treatments (McKinsey, 2013).

Advances in technology could allow further manipulation of material properties. Enhanced material characteristics could benefit equipment exposed to tough working conditions or abrasive environments, and potentially reduce consumption of materials used for rock cutting or breaking. When the strength-to-weight ratio of materials can be improved through technology, the impact and potential benefits will extend even further. Smaller, lighter, and stronger components may eventually allow deeper and safer mining by improving rock support. Ultra-low-profile equipment could then be designed smaller and stronger to mine difficult-to-navigate deposits, reduce waste mining, and therefore mine both more economically and be able to reach previously uneconomic deposits. Advances in this field could lead to major breakthroughs in electrical equipment and vehicles if energy storage can be improved and batteries reduced in size and weight.

Advanced robotics

Robots have undergone massive improvements over the last few decades, progressing from being expensive, bulky, and inflexible to becoming much more advanced. Currently, robots are gaining enhanced senses, dexterity, and intelligence. Many of these improvements stem from advances in machine vision, artificial intelligence, machine-to-machine communication, sensors, and actuators (a component of machines that is responsible for moving or

controlling a mechanism or system). Robots are now easier to program and interact with. They may also be more compact and adaptable, making it possible to deploy them alongside workers. As a result, advanced robotics could make it practical to substitute or complement human labour with robots in a wider range of manufacturing tasks and service jobs. This technology could enable new types of surgical robots, robotic prosthetics, and 'exoskeleton' supports that help people with limited mobility to function more normally and improve and extend lives (McKinsey, 2013).

The International Federation of Robotics estimated in 2013 that these devices will create as many as 2 million additional job opportunities between 2017 and 2020. A major factor in robotics-driven job growth is the fact that the combination of humans and machines can often produce better results than neither could accomplish on their own. In dire situations, an expert may always be required to take control (Dupress, 2015). Anthropomorphic robots (robots that mimic human characteristics), on the other hand, could take over numerous repetitive production functions or other tasks that traditionally required human traits (ESPAS, 2015). As robots become cheaper, more dexterous, and safer to use, they will continue to grow as a substitute for human activities in a wider range of fields (VanderMey, 2015).

The implementation of robotics in mining constitutes further progress towards technological advancement. An example of robotic machinery in mining is the ultra-low-profile mining machines from CMTI Consulting in South Africa. These machines are currently in development and will be implemented at Sibanye Gold's Burnstone gold mine in Balfour, South Africa. The MT100, for example, has a sweeper and dozer attached and is battery-driven with a battery life of 7 hours. It is equipped with a drill rig and mechanical breaker for non-explosive mining, or a multi-drill rig that can drill four holes simultaneously for conventional blasting. It can also be equipped with a laser scanner while being operated from a gulley up to 100 m away. The machine is highly manoeuvrable, with track-based wheels, and can navigate difficult underground environments. Its multi-track concept, where four tracks are individually driven, further also allows the machine to swing around a centre point to enable it to negate vertical obstacles as high as 400 mm (Solomons, 2016).

Robotics in mining offer potential for improvements in safety, access to resources that were previously uneconomic to mine, and improvements in the larger mining cycle through the integration of different technologies. Some examples include automation, machine learning, integrated remote operating centres, the internet of things, and advanced analytics.

Airborne gravimetry

This system uses a gravimeter installed on an airborne platform such as a drone or small aircraft to measure variations in the Earth's gravitational field. In doing so, it can perform resource investigations from the air to assist with geological mapping (Förste, 2016). This can enhance geological exploration with electromagnetic surveys that provide greater coverage and depth (Holland, 2015).

Artificial intelligence and machine learning

Artificial intelligence (AI) refers to the field of study towards the creation of computers that are capable of intelligent behaviour and that could divulge answers by analysing data, as well as having the ability to learn autonomously by analysing data. Machine learning uses algorithms to analyse and learn from data and adapt the machine's behaviour accordingly. Machine learning is more specific in application, and also more accurate than AI, since it is a more mature technology(Skylads, 2015). Both fields have undergone rapid advances, with major drives from technology leaders to increase the rate of development. Due to their massive potential in all aspects of information technology systems, it is vital for business leaders to remain aware of progress within the field.

Augmented reality and virtual reality

Virtual reality (VR) makes it possible for a user to be immersed within a computer-generated environment, which can represent either an actual place or an imaginary one. In contrast, augmented reality (AR) overlays contextual information on the immediate physical environment of the user. In this way, AR blends digital components (*e.g.* virtual elements such as text or 3D models) with real life. Both of these sensory (predominantly visual) technologies allow the deployment of technology in ways that were previously impossible. As such, they open up major possibilities for training, simulation, visualization, planning, and modelling (see Figure 2), communication, and collaboration (Dupress, 2016b). AR in particular holds great potential for human assistance; some examples include on-site task assistance and guidance, navigation, re-creations of incidents, maintenance and repair, emergency management, and search and rescue operations (Jacobs, 2015).

Automation and automation of knowledge work

Automation refers to the act of making a process, activity, task, system, or even decision autonomous. With the advances in autonomous equipment, robotics, artificial intelligence, and advanced analytics, many business improvements become possible through increased automation of operations. Rio Tinto has demonstrated that driverless trucks are already changing the cost equation in the mining industry in Western Australia. Further adoption of automated drills, automatic longwall shearers, autonomous trucks and trains, and remote operating technologies will increase the efficiency of many other operations (Deloitte, 2014c).

As the 'intelligence' of these machines grows, they will be able to perform more complex tasks, including maintenance and repair activities on equipment and hazardous processing activities. This will reduce labour costs and enhance productivity. It is likely that companies will ultimately operate fully autonomous mines, concentrating labour in centralized functional hubs rather than in remote regions (Deloitte, 2016c).

Automation is not limited to robotics and autonomous equipment in physical activities. It also includes the automation of knowledge work (VanderMey, 2015). Advances in artificial intelligence, machine learning, and natural user interfaces (*e.g.* voice recognition) are making it

possible to automate many knowledge-worker tasks, many of which have long been regarded as impossible or impractical for machines to perform. For instance, some computers can answer 'unstructured' questions (those posed in ordinary language, instead of being precisely written as software queries), so employees without specialized training can obtain information on their own. This opens up possibilities for major changes in how knowledge work is organized and performed. Sophisticated analytics tools can then be used to enhance the talents of highly skilled employees. As more knowledge-worker tasks can be done by machines or computers, it is also possible that some types of jobs could eventually become fully automated (McKinsey, 2013). A few examples include administering procurement, processing payrolls, calculating materials resource needs, generating invoices, and tracking flows of material (McKinsey, 2016).

Directional drilling

Directional drilling is a mature technology, with widespread use in the oil and gas, utilities, and infrastructure industries (Dowling and Rhys-Evans, 2015). The technology, while already applied in mining (*e.g.* for in-seam exploration in coal mining), holds potential for greater adoption in various areas. One such application, for example, is dewatering well placement. Directional drilling allows the placement of permanent, high-performance dewatering wells in optimum orientations beneath an open pit, using directional drilling technology to direct the large-diameter drilling heads from outside the pit to intersect chosen geological structures. Pilot directional dewatering wells in hard-rock mining environments in the USA and Mexico have demonstrated significant benefits, such as better control of groundwater inflow, improved in-pit safety, and fewer disruptions to operations compared to conventional dewatering. Directional dewatering wells produce up to two orders of magnitude more groundwater than in-pit vertical wells (Rowland *et al.*, 2016).

Energy technologies

Technologies that increase energy efficiency

Technologies identified by McKinsey (2015b), for this purpose include energy-management systems, advanced analytics, and smart grids.

Renewables

Renewable energy sources, such as solar, wind, hydroelectric, and ocean waves, promise an endless source of power. Solar cell technology, in particular, is progressing at a rapid rate with drastic reductions in costs. (McKinsey, 2013). Many companies already employ solar, wind, hydro, and biomass power generation technologies. These are often supplemented by variable-speed backup generators capable of maximizing fuel efficiency, which is a solution that also works for companies that run power off the grid (Deloitte, 2016c). With the rate of reduction in costs relating to renewables, it makes sense for energy-intensive enterprises to critically evaluate these technologies (Davidse, 2016).

Technologies that reduce energy consumption

Technologies identified by McKinsey (2015b), for this purpose include automated mine ventilation control and air-reconditioning, high-pressure grinding rolls, in-pit crushing-conveyance and high-angle conveyance systems, low-loss conveyor belts, stirred-media mills, coarse flotation, fuel-cell-powered mine vehicles; and electro- and hydropowered drilling.

Genomics and precision agriculture

Genomics combines advances in the science of sequencing and modifying genetic material with the latest big data analytics capabilities (McKinsey, 2013). In short, genomics combines biology, genetics, and computer science (GenomeCanada, 2016). In mining, genomics solutions have already been used to bioremediate polluted soils, improve mine drainage, and mitigate threats to biological diversity through biomonitoring (Deloitte, 2016c). By understanding the way microbes function, bioleaching can be enhanced and applied more efficiently. This can improve metal recoveries by as much as 50%. Overall, this technology can help improve productivity, cut costs, and improve sustainability in the mining industry (GenomeCanada, 2016). The technology can also be used in agriculture, which may assist mining companies in their corporate social responsibility activities, or in motivating the application for a mining licence during the exploration and mine design phases. This argument also applies for precision agriculture, which is a new, site-specific farm management system that utilizes technologies and agronomic principles to optimize farm yields by collecting data on the spatial and temporal variability of the various agricultural components (such as soil, climate, seed, fertilizers, water, pests, animals, and diseases), thus enabling micromanagement of the relevant factors (Frost and Sullivan, 2016).

Internet of things

The internet of things (IoT) concerns embedded sensors and actuators in machines and other physical objects that connect them to the internet. This allows the flow of products and assets to be monitored while taking other data, such as the weather, into account. The data provided through the IoT enables assets to be better managed, performance to be optimized, and new business models may be created. With remote monitoring, the IoT has potential to improve various aspects and systems ranging from the health of patients with chronic illnesses to improved synergy between fleet equipment (McKinsey, 2013). Sensors to collect this data, for processing and control purposes, will be able to obtain information on the health of machinery, the structural integrity of bridges, and even seemingly redundant information such as temperatures in the environments surrounding different assets (VanderMey, 2015).

Tracking technologies

Tracking technologies, such as Radio-Frequency Identification (RFID), global positioning systems, Wi-Fi, unmanned aerial vehicles equipped with cameras and sensors, and thermal imaging may greatly assist various areas within the mining cycle. By using such technologies, companies can deploy sophisticated and automated identification and security management programs that can systematically track employees' access rights, location, duration, training, safety certification, permissions,

compliance, and site security from a central location. This information can then be integrated and made available to those who need it, including security and human resources personnel. Tracking of employees can also greatly assist during search-and-rescue operations, as well as enhance the effects of proximity detection and collision avoidance systems. These aspects can be integrated into a comprehensive location awareness and safety programme, with a real-time visualization engine that provides a rich graphical view of employee locations and associated metrics (IBM, 2009).

3D printing (additive manufacturing)

Additive manufacturing is the technique employed by 3D printers that allows the creation of an object by adding ultrathin layers of material on each other (LaMonica, 2013). The performance of additive manufacturing machinery is improving, the range of materials is expanding, and prices (for both printers and materials) are decreasing. These factors allow rapid adoption and open up more manufacturing uses for the technology. With 3D printing, a 3D design file can be taken directly to a finished part or product, potentially skipping many traditional manufacturing steps. The ability to achieve on-demand production has massive impacts on supply chains and the stocking of spare parts, both of which involve great costs. 3D printing can also reduce the amount of material wasted in manufacturing and create objects that are difficult, or even impossible, to produce with traditional techniques (McKinsey, 2013).

As this technology matures, the entire equipment supply chain is set to shift, driving OEMs to favour modular designs. For instance, European Truck Factory is bringing this concept to fruition with the design of modular components for use in a full array of mining trucks. As more equipment becomes modular, mining operations can also begin to rely more on new forms of heavy lifting transport, such as hybrid air vehicles, which combine blimp, helicopter, and fixed-wing aircraft designs in new types of flying machine (Els, 2016) that are capable of moving modular equipment to remote sites. This will enable operations to construct processing units in low-cost factories and transport them to where they will be used (Deloitte, 2016c). Hybrid airship technology itself is another new field with great potential for mining. These airships will be capable of carrying large loads, be easy to manoeuvre, fly at low speeds, and the transportation costs will be comparable to that of truck transport on icy roads (Shalal, 2014).

Conclusion

In the context of this paper, the sheer size of the created technology map cannot be represented in full. Due to this, a few selected examples were presented of technologies embedded in the technology map, with the potential to add value to various areas within the mining cycle. By applying some, or a combination, of the technologies in innovative ways, operations may stand to gain significant business value. This value was analysed in terms of the potential of a technology to facilitate the process of mine modernization, based on its ability to increase production, productivity, or efficiency, improve safety, or reduce the risk of human error. It should be noted that all the technologies were investigated from a holistic perspective and they do not provide 'plug-and-play' solutions for any mining operation. As such, the technology map serves to identify technologies suitable for further research and development towards creating a tailor-made solution or application specific to the needs of the user.

Suggestions for further work

It is recommended that the framework for the mining cycle should be expanded to include all subsequent functions, activities, systems, and other constituents for each of the main value drivers. As such, a blueprint could be created that is representative of all aspects related to mining, for all mining methods, geological characteristics, geographical factors, commodity types, and other variables. Such a blueprint for mining should be made publicly available to assist further research and development, academia, service providers, consulting/advisory firms, and other organizations, as it would clarify the often 'fuzzy' context of the mining industry. The mining blueprint will then provide a rigid structure that is fully representative of the mining industry and its cycles or phases along with greater detail on all the constituent value drivers that make up a mining enterprise. The blueprint should then be ported to a digital platform that can be used for various purposes. One example is the overlaying of potentially applicable technologies for the various components within the mining cycle, to create a mining technology map, as was done in this study.

In the same way in which the technology map has been created from such an overlay, so too can other applications be found that could build on the foundation of the mining cycle. Other examples may be the benchmarking of various figures, or leading practices applicable to different mining activities. The overlaying of such information on a well-structured foundation will assist both mining and non-mining experts in building the understanding required for a specific task or project. More often than not, non-mining professionals lack exposure to the mining environment and as such have difficulty in visualizing the various aspects of mining. By combining a digital mining cycle platform with visual technologies, this understanding could be enhanced in order to increase the efficiency and accuracy with which such professionals perform their work.

Another recommendation is to incorporate a wider range of technologies in the technology map, *i.e.* existing technologies that are currently in use in industry as well as all new and emerging technologies with potential to add value or have an impact. Furthermore, the level of analysis and number of factors analysed should be increased in order to gain deeper understanding of each technology's feasibility and implementability in a mining system context. The current technology map drew its information from a desktop-level analysis of the technologies, which assessed potential to add value. It would, however, be of great value to include more detailed analysis on system implications, technology maturity (or technology readiness level), and risk of adoption for each technology (both for a system application and for a component), as well as on-the-ground assessment of

suitability for mining environments where possible. Such a tool would assist companies with technology adoption timeline planning (technology roadmapping).

The proposed mining technology map should then be digitized in order to effectively create a search engine regarding technologies that are applicable to mining. It is recommended that such a digital mining technology map be made publicly available in order to reduce the resources that various organizations, institutions, and individuals spend on doing similar research. By collectively pooling R&D on general (non-proprietary) technologies instead of working in silos, the industry stands to gain value and reduce waste on R&D.

Lastly, it is suggested that a technology intelligence (TI) system framework should be created specifically for such a mining technology map. The TI system should aim to scientifically structure the gathering of intelligence along with appropriate knowledge and information management in the technology map. It should also provide a dissemination process for the technology intelligence into value-adding decision-making. The latter would serve as a decision-making tool to provide guidance in identifying applicable technologies based on inputs of variables, factors, or other criteria as provided by the user of the technology map. This would further assist with the refinement process when using the technology map. As such, it would reduce the applicable number of technologies, and potentially their desired designs and method of application, to a level applicable to the needs of the user. This decision-making tool could then be developed to include the ability to align business strategies and operational risk management strategies with the technology map. The user would then have a complete tool that is able to take inputs based on organizational and operational parameters and identify technological solutions that have the potential to add value to a component of the mining cycle. This should be followed by a well-structured and proven refinement (research and development) process.

Acknowledgements

The following persons are gratefully acknowledged for their inputs in shaping the platform for the mining cycle:

- Andre Liebenberg
- Carel Anthonissen
- Carel de Jager
- Eugene Preis
- Jan Britz
- Jannie Maritz
- Johan Hanekom
- Marinus du Plessis
- Pierre Bredell
- Tinus Pretorius
- Wolter de Graaf

References

Bourzac, K. 2015. Nano-architecture: A Caltech scientist creates tiny lattices with enormous potential. https://go.ted.com/CyGv [Accessed 5 July 2016].

Bryant, P. 2011. The Case for Innovation in the Mining Industry. Clareo Partners, Chicago.

COMSA, 2016. Modernisation: towards the mine of tomorrow. Chamber of Mines of South Africa, Johannesburg.

Davidse, A. 2016. Personal correspondence. Mining Innovation Leader, Deloitte Canada.

Deloitte. 2014. The future of mining in South Africa – Innovation imperative. Deloitte & Touche, Johannesburg.

Deloitte. 2014b. Deloitte Global Services Limited, London - Mining spotlight on: Sliding productivity and spiralling costs. http://bionanouni.wdfiles.com/local--files/teaching-im010-horario-2014i/Deloitte_14-Mining-Spotlight-On_Sliding-Productivity-and-Spiraling-Costs.pdf [Accessed 29 January 2016].

Deloitte. 2014c. Mining spotlight on: Remaking mining. http://www2.deloitte.com/content/dam/Deloitte/global/Documents/Energy-and-Resources/gx-er-remaking-mining.pdf [Accessed 26 January 2016].

Deloitte. 2015a. Tracking the trends 2015: The top 10 issues mining companies will face this year. https://www2.deloitte.com/content/dam/Deloitte/fpc/Documents/secteurs/energie-et-ressources/deloitte_etude-tracking-the-trends-2015-en.pdf [Accessed 10 February 2016].

Deloitte. 2015b. Tracking the trends 2015: The top 10 issues mining companies will face this year. https://www2.deloitte.com/content/dam/Deloitte/fpc/Documents/secteurs/energie-et-ressources/deloitte_etude-tracking-the-trends-2015-en.pdf. [Accessed 10 February 2016].

Deloitte. 2016. Innovation State of Play | Mining | Deloitte Southern Africa. Available at: http://www2.deloitte.com/za/en/pages/energy-and-resources/articles/innovation_in_mining.html [Accessed 4 May 2016].

Deloitte. 2016b. Tracking the trends 2016: The top 10 issues mining companies will face in the coming year. Deloitte Touche Tohmatsu Limited. Annual Report. United Kingdom.

Deloitte. 2016c. Tracking the trends 2016: The top 10 issues mining companies will face in the coming year. Deloitte Touche Tohmatsu Limited. Annual Report. United Kingdom.

Dowling, J. and Rhys-Evans, G. 2015. Oilfield directional well placement technology used for mine dewatering. *Mining Magazine*, May 2015. p. 28.

Dupress. 2015. Exponentials. http://dupress.com/articles/tech-trends-2015-exponential-technologies/ [Accessed 29 July 2016].

Dupress. 2016a. Industrialized analytics - Data is the new oil. Where are the refineries? http://dupress.com/articles/data-assets-and-analytics/?id=gx:2el:3dc:dup3040:awa:cons:tt16 [Accessed 28 July 2015].

Dupress. 2016b. Augmented and virtual reality go to work. http://dupress.com/articles/augmented-and-virtual-reality/?id=gx:2el:3dc:dup3036:awa:cons:tt16 [Accessed 26 July 2016].

ELS, F. 2016. Breakthrough aircraft to transform remote mining. http://www.mining.com/breakthrough-aircraft-to-transform-mining-economics/ [Accessed 4 August 2016].

ESPAS. 2015. European Strategy and Policy Analysis System (ESPAS): Global Trends to 2030: Can the EU meet the challenges ahead? http://europa.eu/espas/pdf/espas-report-2015.pdf [Accessed 3 April 2016].

FÖRSTE, C. 2016. Terrestrial and airborne gravimetry. http://www.gfz-potsdam.de/en/section/global-geomonitoring-and-gravity-field/topics/terrestrial-and-airborne-gravimetry/ [Accessed 25 October 2016].

FROST & SULLIVAN. 2016. Top 50 emerging technologies: growth opportunities of strategic imperative - Multi-billion dollar technologies ready to propel industries and transform our world. http://ww2.frost.com/news/press-releases/frost-sullivan-reveals-50-emerging-technologies-set-transform-industries-and-propel-growth-opportunities-across-globe [Accessed 19 April 2016].

GARTNER. 2014. Gartner identifies the top 10 strategic technology trends for 2015. http://www.gartner.com/newsroom/id/2867917 [Accessed 31 May 2016].

GENOMECANADA. 2016. Mining | Genome Canada. http://www.genomecanada.ca/en/why-genomics/genomics-sector/mining [Accessed 28 April 2016].

GRIFFITH, C. 2015. Modernisation – a vital step in building a sustainable mining industry in South Africa. Mining Indaba 2015 (Speech).

HOLLAND, N. 2015. Gold Fields: the gold mining company of the future. https://www.goldfields.co.za/pdf/presentations/2015/gold_fields_mine_of_the_future_28102015.pdf [Accessed 18 May 2016].

IBM. 2009. Envisioning the future of mining. https://www.ibm.com/smarterplanet/global/files/ca__en_us__oil__smarter_natural_resources_future_of_mining.pdf [Accessed 17 February 2016].

INDEXMUNDI. 2016. Commodity metals price index monthly price - index number. http://www.indexmundi.com/commodities/?commodity=metals-price-index&months=60 [Accessed 18 July 2016].

JACOBS, J. 2015. A critical investigation into the potential of augmented reality applications in the mining industry. B.Eng (Hons) (Mining Engineering) dissertation, Department of Mining Engineering, University of Pretoria, South Africa.

JACOBS, J. 2016. Creating a technology map to facilitate the process of modernisation throughout the mining cycle. M.Eng (Mining Engineering) thesis, Department of Mining Engineering, University of Pretoria, South Africa.

LAMONICA, M. 2013. Additive manufacturing: GE, the world's largest manufacturer, is on the verge of using 3-D printing to make jet parts. https://www.technologyreview.com/s/513716/additive-manufacturing/ [Accessed 26 February 2016].

MACFARLANE, M. 2014. Dassault Systemes GEOVIA: natural resources – special report on mining innovation. http://www.geovia.com/sites/default/files/campaigns/GEOVIA_SpecialReportMiningInnovation.pdf [Accessed 4 March 2016].

MCKINSEY. 2013. Disruptive technologies: Advances that will transform life, business, and the global economy. https://www.sommetinter.coop/sites/default/files/etude/files/report_mckinsey_technology_0.pdf [Accessed 28 January 2016].

MCKINSEY. 2015a. How digital innovation can improve mining productivity. http://www.mckinsey.com/industries/metals-and-mining/our-insights/how-digital-innovation-can-improve-mining-productivity [Accessed 11 March 2016].

MCKINSEY. 2015b. Greening the future: New technologies that could transform how industry uses energy. McKinsey & Company. Global Editorial Services.

MCKINSEY. 2016. Where machines could replace humans—and where they can't (yet). http://www.mckinsey.com/business-functions/business-technology/our-insights/where-machines-could-replace-humans-and-where-they-cant-yet [Accessed 25 July 2016].

RIVARD, L. 2014. Dassault Systemes GEOVIA: Special report on mining innovation: mine owners focus on technology to control costs. http://www.geovia.com/sites/default/files/campaigns/GEOVIA_SpecialReportMiningInnovation.pdf [Accessed 4 March 2016].

ROWLAND, A., BESTER, M., BOLAND, M., CINTOLESI, C., and DLOWLING, J. 2016. Adapting oil and gas drilling techniques for the mining industry with dewatering well placement technology. *Proceedings of the New Technology and Innovation in the Minerals Industry Colloquium*, Emperors Palace, Gauteng, South Africa. Southern African Institute of Mining and Metallurgy, Johannesburg.

SHALAL, A. 2014. Lockheed sees buyer for hybrid cargo airships in 2015. http://www.hybridairvehicles.com/news-and-media/lockheed-sees-buyer-for-hybridcargo-airship-in-2015 [Accessed 29 April 2016].

SKYLADS. 2015. What is the difference between machine learning and artificial intelligence? http://www.skylads.com/rtb-blog/what-is-the-difference-between-machine-learning-and-artificial-intelligence [Accessed 28 July 2016].

SOLOMONS, I. 2016. New ultralow-profile mining machine operated successfully for 500 hours at SA mines. http://www.engineeringnews.co.za/article/locally-manufactured-mining-machine-trialled-successfully-2016-02-12 [Accessed 10 July 2016].

TIA. 2012. The mining sector innovation strategies implementation plan. http://www.tia.org.za/CMS/uploaded_docs/TIA%20Mining%20and%20Minerals%20Innovation%20Strategies%20Implementation%20Plan%20(2012%20-%202016).pdf [Accessed 4 February 2016].

VANDERMEY, A. 2015. The 12 disruptive tech trends you need to know. http://fortune.com/2015/07/22/mckinsey-disruptive/ [Accessed 19 February 2016]. ◆

http://dx.doi.org/10.17159/2411-9717/2017/v117n7a6

The effect of magnesia and alumina crucible wear on the smelting characteristics of titaniferous magnetite

by M.P. Maphutha*, M. Ramaili*, M.B. Sitefane*, and X.C. Goso*

Synopsis

Test work was conducted to investigate the effect of magnesia and alumina crucible wear in laboratory-scale smelting tests on titaniferous magnetite (titanomagnetite) in terms of iron and vanadium recoveries as well as slag properties. The study was motivated by the desire to develop capacity to provide technical support to the minerals industry in the establishment and continuous optimization of industrial processes for the efficient extraction of Fe, V, and Ti from titanomagnetite. The tests were conducted using the smelting recipe used by Evraz Highveld Steel and Vanadium Corporation (EHSV); that is, the same titanomagnetite feed material and a dolomite flux to achieve a typical CaO:MgO ratio of 16:14 in the slag. The results of the test work demonstrated that chemical attack by the titania-bearing slag on the magnesia and alumina crucibles is inevitable. The crucible wear was more pronounced with magnesia crucibles than with alumina crucibles. The Fe and V recoveries to alloy in alumina crucibles were higher than those obtained in magnesia crucibles. However, the recoveries in both cases were comparable to the EHSV data. The phase chemical compositions of the best slags, in terms of Fe and V recoveries to alloy, from each crucible type were significantly different. In a magnesia crucible, the slag was composed mainly of perovskite ($CaTiO_3$), forsterite (Mg_2SiO_4), and monticellite ($CaMgSiO_4$). However, the phase chemical composition of the slag produced using an alumina crucible was similar to that of the typical EHSV titanomagnetite, comprising pseudobrookite solid solution ($MgTi_2O_5$-Al_2TiO_5), spinel [$(Mg)(Al,Ti)_2O_4$], and perovskite. The results have shown that both magnesia and alumina crucibles can be used to conduct laboratory-scale test work using the reviewed slag chemical composition. In addition, the more readily available alumina crucibles are better than magnesia crucibles in terms of Fe and V recoveries as well as the slag phase chemistry.

Keywords
smelting, titaniferous magnetite, crucible wear, slag characteristics.

Introduction

Titaniferous magnetite (titanomagnetite) deposits are found in many countries throughout the world, including Russia, China, and South Africa. In South Africa, the titanomagnetite deposits are found in the Bushveld Complex. The titanomagnetite deposits typically contain appreciable reserves of iron and vanadium with concentrations in the range of 38–58% Fe and 1.2–2.2% V_2O_5, as well as significant titanium concentrations of 12–21% TiO_2 (Gwatinetsa, 2013). Titanomagnetite is typically processed by smelting in the presence of a carbonaceous reductant and flux to produce a valuable vanadium-bearing pig iron and a slag containing significant concentrations of titanium dioxide (TiO_2, titania). The titanomagnetite slag is generally discarded on waste dumps. The metal is processed further to produce vanadium and steel products (Steinberg *et al.*, 2011). The global depression in the market and prices of metals, and increased operational expenses as a consequence of excessive electrical energy costs in some countries, including South Africa, have prompted the established titanomagnetite smelters to intensify their process technologies or close down. Furthermore, prospective smelters apply caution through comprehensive process feasibility studies before committing to an operational technology. In such cases, laboratory-scale test work is generally adopted as a cost-effective approach for testing a wide range of parameters under controlled conditions (Geldenhuys and Jones, 2011).

Mintek gained expertise and experience in titanomagnetite smelting processes as early as in the 1960s (Jochens *et al.*, 1969) and thereafter continued with innovative work on the subject (Boyd *et al.*, 1993). Substantial titanomagnetite processing work is included in numerous reports on collaborative projects conducted by Mintek and its clients over more than 45 years.

The intensification of, and likely innovation in, titanomagnetite smelting processes typically involves laboratory crucible tests to maximize vanadium and iron recoveries to metal and the deportment of titania to the slag phase. Laboratory test parameters controlled for the optimization of the extraction of vanadium, iron, and potentially titanium from titanomagnetite

* *Mintek, Randburg, South Africa.*
 ISSN 2225-6253. This paper was first presented at the 3rd Young Professionals Conference, *9–10 March 2017, Innovation Hub, Pretoria, South Africa.*

generally include reductant addition, operational temperature, and fluxing regime, which subsequently affect the characteristics of the by-product titania-bearing slag such as basicity, viscosity, activities of slag components, and liquidus temperature. The laboratory-scale smelting of titanomagnetite generally entails numerous challenges relating to test crucibles, *viz.* crucible compatibility in terms of the effects on smelting characteristics and temperature limits (Geldenhuys and Jones, 2011). Titania-bearing slag is known to be corrosive towards all refractories, hence commercial smelting furnaces operate with a freeze lining to assist with the protection of the sidewall against corrosion (Pistorius, 2004). In their study of the interaction of MgO- and Al_2O_3-based refractories with titania-bearing slag, Garbers-Craig and Pistorius (2006) showed that both refractory systems are attacked by low- and high-titania slags. At the laboratory scale, chemical attack of both the MgO- and Al_2O_3-based refractories by the titanomagnetite slag is inevitable. The crucible wear generally results in changes in the slag composition, and thus the slag characteristics and overall smelting characteristics. Magnesia crucibles are not readily available in South Africa and generally come at a high cost compared to alumina crucibles.

The focus of the current laboratory-scale study was therefore to investigate the smelting characteristics of titanomagnetite in both MgO and Al_2O_3 crucibles in terms of the vanadium and iron recoveries to metal, and slag properties such as phase chemical composition and basicity. The smelting recipe used by Evraz Highveld Steel and Vanadium Corporation (EHSV) was adopted to allow the laboratory test results to be compared with commercial plant data.

Experimental

Materials and equipment

Titanomagnetite from the Main Magnetite Layer (MML) of South Africa's Bushveld Complex deposit was supplied by EHSV. The typical bulk chemical composition of the titanomagnetite feed to the EHSV process was acquired from the literature (Steinberg *et al.*, 2011), and that of the supplied sample was determined at Mintek. These compositions are given in Table I. As desired, the chemical compositions show that the feed samples are in fact from the same orebody. The elemental compositions of the samples are also included in Table I to facilitate the determination of the elemental deportment after smelting.

A low-sulphur carbon (LS Sascarb from Sasol) was used as reductant. Commercial MgO, Al_2O_3, SiO_2, and CaO chemicals supplied by Associated Chemical Enterprise were used in synthetic fluxes to simulate the dolomite and quartz flux used by EHSV. The compositions of the reductant and synthetic fluxes are included in Table II. High-purity MgO and Al_2O_3 crucibles were purchased from Kayla Africa (South Africa) and Tateho Ozark Technical Ceramics (Germany) respectively. The smelting test work was conducted in a 100 kW induction furance that was set up by LH Power. A schematic diagram of the induction furnace is shown in Figure 1.

The bulk chemical compositions of the raw materials and smelting test products were determined by CCD simultaneous inductively coupled plasma optical emission spectrometery (ICP-OES) (Varian Vista-PRO), and the total carbon and sulphur concentrations in the metals by LECO techniques (CS–230 and CS-744). The phase chemical compositions of the slag samples were analysed by scanning electron

Table II

Composition of the reductant and synthetic fluxes (mass %)

	C	MgO	Al_2O_3	SiO_2	CaO	Ash	Loss on ignition
Sascarb	98.7				0.33	0.97	
MgO		99.0					
Al_2O_3			98.0				
SiO_2				98.5			
CaO					96.0		3.50

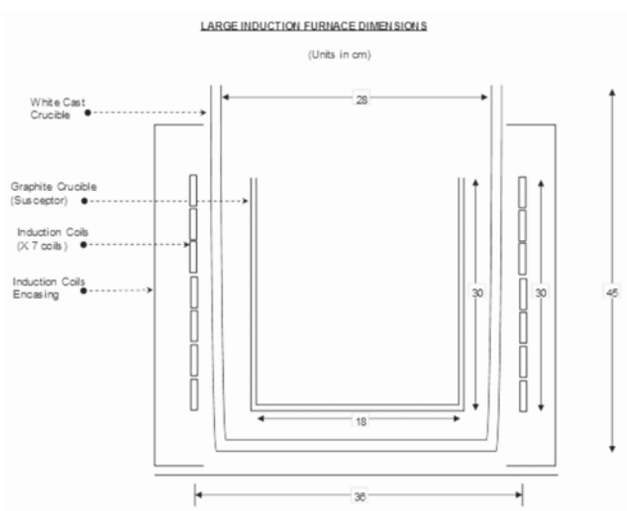

Figure 1—Schematic diagram of the 100 kW induction furnace

Table I

Bulk chemical compositions of the feed titanomagnetite materials (mass %)

	Fe_3O_4	MgO	Al_2O_3	SiO_2	CaO	TiO_2	V_2O_5	Cr_2O_3	MnO
Mintek test work	77.7	1.48	3.97	1.34	0.07	13.31	1.67	0.20	0.24
EHSV operation	76.5	1.60	4.80	2.00	0.10	12.7	1.65	0.40	0.30
	Fe	Mg	Al	Si	Ca	Ti	V	Cr	Mn
Mintek test work	55.3	0.88	2.07	0.62	0.05	7.88	0.92	0.14	0.19
EHSV operation	54.8	0.96	2.54	0.93	0.07	7.61	0.92	0.27	0.23

microscopy (SEM) (Zeiss MA15) equipped with energy dispersive spectrometry (EDS) (Bruker) and X-ray diffractometry (XRD) (Bruker D8 Advance).

Smelting recipe design

Laboratory-scale smelting tests were carried out to study the effect of wear in two crucible types (high-purity MgO and Al_2O_3) on the smelting characteristics of titanomagnetite. The principal variable in the test work was the reductant addition. Since iron is the major reduceable component in the titanomagneitite, the carbon reductant requirement was calculated based only on the stoichiometric reduction of magnetite, as shown in Equation [1]. The carbon additions in the tests were varied at 100%, 110%, and 120% of stoichiometric with the intention of studying the influence of carbon addition on the recovery of the valuable elements (Fe and V) to the alloy phase and preferential Ti deportment to the slag.

$$Fe_3O4_3 + 4C \rightarrow 3Fe + 4CO \quad [1]$$

The fluxing strategy aimed to achieve and work with a slag similar in composition to that of the EHSV operation. At EHSV, fluxing of the titanomagneite is effected by the addition of quartz and dolomite, a natural mineral with a CaO:MgO ratio of about 16:14 – this assumes that dolomite would constitute 30% of the subsequent slag as predicted by Jochens *et al.*, (1969). The liquidus temperature of the EHSV titanomagnetite slag can be predicted using the phase diagram that was developed by Jochens., *et al.* (1969) and shown in Figure 2. The concentrations of SiO_2 and Al_2O_3 as well as the overall flux slag to control the dilution of TiO_2 were controlled in order to be able to reference Jochens' phase diagram with the compositional range of CaO 30–0%, MgO 0–30%, SiO_2 19.69%, Al_2O_3 13.12%, and TiO_2 37.19% (Jochens *et al.*, 1969). As shown in the phase diagram, the slag liquidus temperature for the smelting tests with CaO and MgO contents of 16% and 14% respectively was estimated to be about 1390°C. A summary of the smelting recipes is given in Table III.

Smelting test procedure

The test recipes, shown in Table III, were prepared by mixing the respective components and subsequently milling the mixtures in a ring mill to produce a homogeneous mixture. The recipes were weighed and densely packed in MgO and Al_2O_3 crucibles. The charged crucibles were placed in the reaction chamber of the 100 kW induction furnace. As shown in Figure 1, the furnace chamber is made up of a graphite susceptor. The chamber containing the test crucibles was closed by a graphite lid equipped with three drill-holes for (1) an alumina tube used to deliver argon gas into the furnace chamber to create an inert environment throughout the duration of each test, (2) an alumina off-gas duct to avoid pressurizing the reactor, and (3) an alumina sheath for encasing the B-thermocouple used to control the heating mechanism of the furnace and monitor the sample temperature.

The smelting tests were executed in two sets (for each crucible type) of three tests to complete a total of six tests. The furnace was heated gradually by incremental power input adjustments until a target temperature of 1600°C was reached. As in commercial operations, the target smelting temperature includes a superheat of about 200°C to the predicted slag liquidus temperature of about 1390°C – this action is typically conducted in order to ensure that the viscosity of the melt is low enough to allow for efficient slag and alloy separation. The furnace operates by inductive heat generation inside a graphite suscepting crucible, created by the water-cooled induction coils around the furnace. Each test run was allowed to remain at the test temperature for 1 hour, after which the crucibles were left inside the reactor to cool overnight to room temperature under argon atmosphere. The products were then weighed and separated into alloy and slag. The alloy samples were analysed by ICP-OES and LECO techniques. The slag was analysed by ICP-OES, SEM-EDS, and XRD.

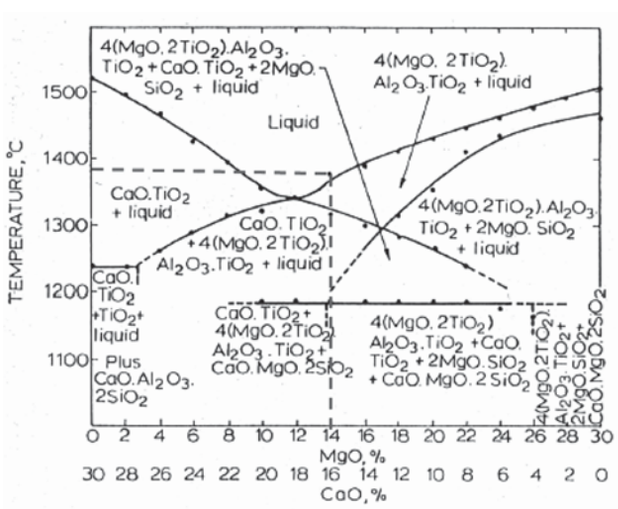

Figure 2—Phase equilibrium for the slag system: CaO 30–0%, MgO 0–30%, SiO_2 19.69%, Al_2O_3 13.12%, and TiO_2 37.19% showing the liquidus temperature of a slag with a CaO:MgO ratio of 16:14 (Jochins *et al.*, 1969)

Table III

Summary of smelting test recipes (mass %)

Test	Crucible	Stoichiometric C	Ore	CaO	MgO	Al_2O_3	SiO_2	C
1	Magnesia	100%	75.50	4.50	2.75	0.62	4.50	12.15
2		110%	74.67	4.42	2.70	0.58	4.44	13.19
3		120%	73.70	4.38	2.70	0.59	4.41	14.22
4	Alumina	100%	75.52	4.47	2.78	0.58	4.50	12.14
5		110%	74.60	4.43	2.72	0.61	4.46	13.20
6		120%	73.59	4.38	2.69	0.59	4.42	14.34

Results and discussion

Product masses

The typical appearance of the smelting products is shown in Figure 3. In general, good slag and metal separations were observed. The product alloy masses, which are calculated as the ratio of the mass of the collected alloy to the mass of the ore (without additives), expressed as a percentage, are plotted as a function of stoichiometric carbon addition in Figure 4. These results show that the mass % alloy produced was consistent at 100% and 110% stoichiometric carbon additions, but dropped significantly with 120% stoichiometric carbon addition. This was attributed to the presence of unreacted solid carbon in the molten system, which adversely affected the melt viscocity and subsequently the efficiency of slag and metal separation. Although the effects of stoichiometric carbon addition are similar, the alloy masses produced in the alumina crucibles are generally superior to those produced in magnesia crucibles.

Alloy characteristics

The chemical compositions of the alloys produced are given in Table IV. The chemical composition of the typical alloy produced by EHSV is also included for the purpose of comparison. At EHSV, the Ti and C concentrations in the alloy were used as indicators of the strength of the reducing conditions in the system. High Ti and C in the alloy indicated highly reducing conditions in the furnace, which called for the addition of a corrective material to lower the reducing conditions in the furnace (Steinberg, 2008). The results of the current test work show significant contamination of the alloys by Ti as the stoichiometric reductant addition was increased – at the respective carbon additions, Ti contamination was more severe in magnesia crucibles than in alumina crucibles. The carbon contents in alloys produced with 100% and 120% stoichiometric carbon addition in both crucible types deviate significantly from the EHSV specification of about 3.2%. This deviation may result in alloys with significantly different liquidus temperatures. The vanadium-bearing alloy is used mainly for producing vanadium and steel products, thus the characteristics of the alloy should allow for recovery of the valuable products in downstream processing. The Fe and V grades of the alloys produced in alumina crucibles are generally high compared to those produced in magnesia crucibles. It was expected that the iron and vanadium grades would improve with increased carbon addition. However, the Fe and V contents were diluted

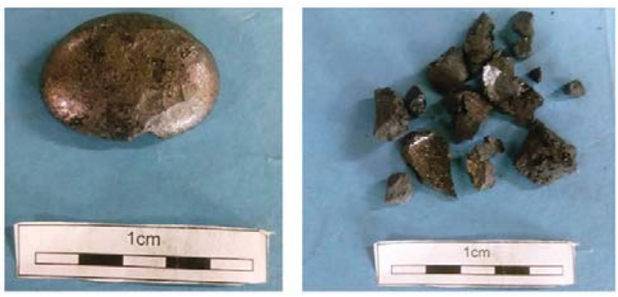

Figure 3—Typical appearance of the slag and metal produced from the smelting tests

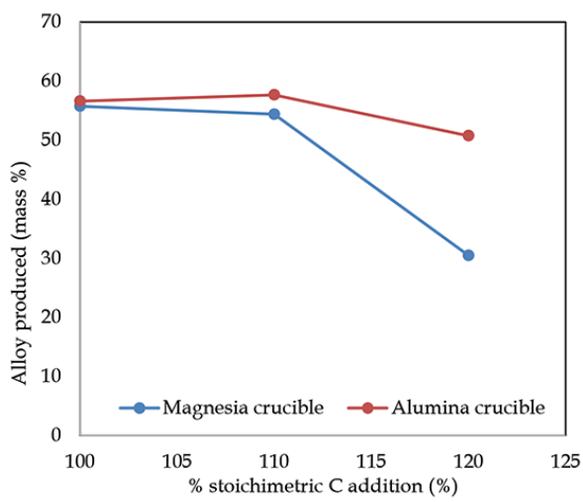

Figure 4—The mass % alloy produced plotted as a function of stoichiometric carbon addition

by undesirable elements (Ti, Si) as conditions became more reducing in both crucible types. A high deportment of Ti to the alloy is undesirable as this would require further processing of the alloy to remove the titanium prior to the recovery of the valuable products lest their quality is compromised.

It is typical in laboratory-scale investigations to evaluate or investigate the relationship between test parameters and elemental recoveries and/or alloy grades. Small-scale test work is, however, subject to large errors due to uncertainties in the analyses and masses of the products, as small quantities are collected, and a small error can easily skew the mass balance and recovery calculations.

Table IV

Bulk chemical compositions of the alloys (mass %)

Test	Al	Ca	Cr	Fe	Mg	Mn	Ni	Si	Ti	V	C	Total
1	0.22	0.14	0.44	95.5	0.15	0.18	0.11	0.48	0.17	1.24	2.27	100.96
2	0.24	0.17	0.39	95.0	0.19	0.24	0.11	0.45	0.81	1.46	3.79	102.90
3	0.22	0.19	0.39	94.6	0.21	0.24	0.10	0.32	1.23	1.37	4.67	103.57
4	<0.005	<0.005	0.42	96.8	<0.005	0.10	0.12	0.19	0.04	1.34	2.48	101.51
5	<0.005	0.008	0.46	96.2	<0.005	0.14	0.11	0.35	0.15	1.66	3.28	102.36
6	<0.005	0.332	0.41	95.8	<0.005	0.21	0.10	0.69	1.46	1.63	4.36	104.99
EHSV	-	-	0.34	94.5	-	-	-	0.20	0.20	1.29	3.20	99.73

The effect of magnesia and alumina crucible wear

In the current test work, the elemental Fe and V recoveries were calculated according to Equation [2]. Figure 5 presents the elemental recoveries of the critical elements Fe and V to the alloy phases in the magnesia and alumina crucibles. In the EHSV operation, the Fe and V recoveries to alloy were estimated, using the data in the open literature, to be about 95% and 77% respectively (Steinberg, 2008). The recovery results in the current work showed that the best smelting conditions were obtained in alumina crucibles, with the highest Fe and V recoveries (recoveries higher than 100% were attributed to measurement uncertainty) obtained at 110% stoichiometric carbon addition. However, the Fe and V recoveries with 100% stoichiometric carbon addition in both crucible types were fairly close to the typical recoveries achieved at EHSV. Although the recoveries were better in the alumina crucible tests, the Fe and V recoveries (with both 100% and 110% stoichiometric reductant additions) in magnesia crucibles are still comparable to the EHSV recoveries. In any case, commercial titanomagnetite smelting is conducted in furnaces lined with magnesia refractories.

This observation suggests that both the magnesia and alumina crucibles are suitable for studying titanomagnetite smelting characteristics for Fe and V production, It should be noted that this observation is applicable to the target smelting recipe, and thus the subsequent slag chemistry.

$$\%\ \text{Recovery of element to alloy} = (\%\ \text{Mass of element in alloy} \times \text{mass alloy}) / (\%\ \text{Mass of element in feed} \times \text{mass of feed}) \times 100 \quad [2]$$

Slag characteristics

The smelting tests targeted a slag with a melting point as identified in the phase diagram in Figure 2. Table V shows the typical chemical compositions of the EHSV slag (Steinberg *et al.*, 2011) and the slags produced in the current smelting study. The main slag components were Al_2O_3, MgO, CaO, SiO_2, and TiO_2. In the magnesia crucibles (Test 1 to Test 3) the target slag chemistry of CaO:MgO ratio of 16:14 was not attained due to the wear of magnesia crucible, which resulted in the dilution of other slag components by the increased

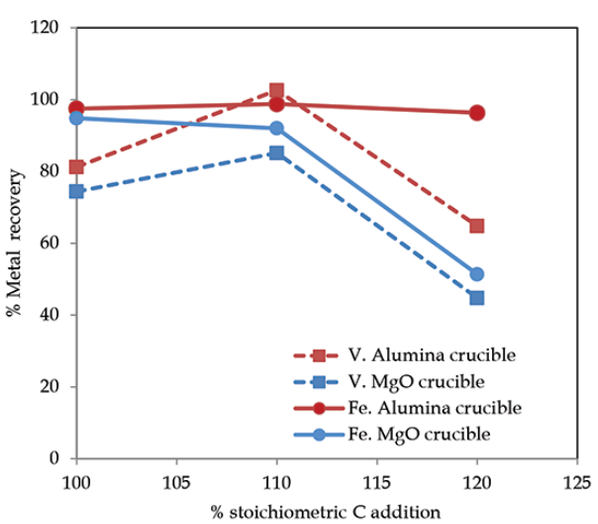

Figure 5—Relationship between stoichiometric carbon addition and recoveries of Fe and V to alloy

MgO content in the slag. Crucible wear also resulted in an increase in the basicity of the slags. However, at 120% stoichiometric reductant addition (Test 3), the concentrations of the slag components, including CaO and MgO, were severely diluted by high iron in the slag. The high iron in the Test 3 slag is attributed to the possible increase in the viscocity of the melt due to the presence of unreacted solids, resulting in the entrainment of Fe metal in the slag. The extent of metal entrainment in the slag was, however, not investigated. As shown by the generally good recoveries of Fe and V in the alloys produced with 100% and 110% stoichiometric reductant addition, the increased basicity of the slag did not appear to adversely affect the Fe and V recoveries in the reviewed slag composition.

In the alumina crucible tests (Test 4 to Test 6), the crucible wear was still severe and resulted in the dilution of slag components. However, as the current definition of basicity (explained in Table V) does not include Al_2O_3 as a component, the alumina crucible wear did not affect the basicity. The basicity with alumina crucibles was consistent and comparable to the targeted basicity of about 1.5 (CaO 16%, MgO 14%, and SiO_2 19.69%). The slag from Test 6, which was conducted with 120% stoichiometric reductant addition, contained relatively high iron due to the increase in the viscocity of the melt, which was due to the presence of high unreacted carbon in the melt, which resulted in the entrainment of Fe metal in the slag.

In general, the residual iron and vanadium with specific reductant additions was relatively high in magnesia crucible tests compared to alumina crucible tests. The dilution of the slag components in alumina crucible tests was slightly less prominent compared to that in MgO crucibles. In particular, the TiO_2 slag concentrations in magnesia crucible tests were significantly lower than in alumina crucibles, due to the dilution of the TiO_2 by the relatively high Fe alloy entrainment in the magnesia crucible slags.

It is evident from the results that dissolution of the MgO and Al_2O_3 from the respective crucibles had occurred, resulting in higher concentrations of MgO and Al_2O_3 in the slags than anticipated.

The phase chemical compositions of the slags obtained from the best conditions (high recoveries) in both crucibles were subjected to SEM-EDS analysis for comparison with EHSV slag. Figures 6–8 show the backscattered electron images and EDS and XRD results. As reported by Goso *et al.* (2015), the EHSV slag is composed primarily of pseudobrookite ($MgTi_2O_5$-Al_2TiO_5) or spinel [$(Mg)(Al,Ti)O_4$] phases; it is not clear which of the two phases forms first. The perovskite in this slag crystallized as a ternary phase.

Figure 7 shows the microstructure of the best slag produced in magnesia crucibles (110% stoichiometric carbon addition). The slag is composed mainly of perovskite and forsterite, with monticellite forming as a finer-grained ternary phase. A significant portion of the slag that occurs in the Mg-Al-Ti-O system was not confirmed by XRD – the phase could be either pseudobrookite or spinel. Although this slag and the EHSV plant slag were produced using basic refractories, they have different phase compositions, but the reason for this is not well understood. It is unlikely that the difference in phase composition resulted from different cooling regimes, as neither of the slags was subjected to quenching.

Table V

Bulk chemical composition of the slags (mass %)

Test	Al_2O_3	CaO	Cr_2O_3	FeO	MgO	MnO	SiO_2	TiO_2	V_2O_5	Total	#Basicity
1	10.30	13.13	0.16	10.98	20.50	0.2.	15.85	24.80	0.88	+96.82	2.12
2	10.70	14.70	0.08	5.03	20.60	0.19	17.60	25.70	0.37	+94.96	2.01
3	6.52	8.04	0.31	55.97	13.70	0.24	9.50	16.90	1.49	*112.66	2.28
4	22.00	16.03	0.10	1.01	11.05	0.41	18.45	30.75	0.39	100.19	1.47
5	21.70	16.66	0.08	1.21	11.90	0.36	18.30	31.00	0.27	101.48	1.56
6	19.30	16.24	0.09	10.97	11.90	0.25	17.00	29.20	0.43	*105.38	1.66
EHSV	18.00	14.10	0.20	1.00	14.10	0.40	16.20	35.60	0.90	100.50	1.74

Basicity = (%CaO+%MgO)/%SiO_2
* High totals due to Fe entrainment in the slag
+ Deviation from 100% attributed to measurement uncertainty

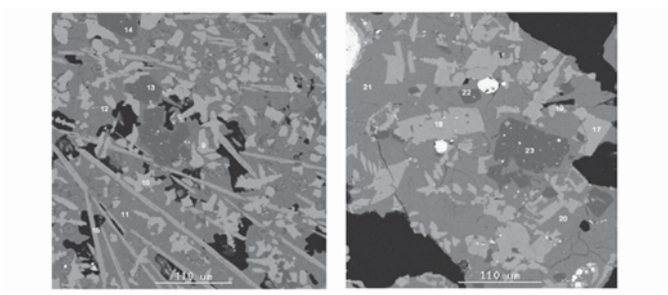

Point	MgO	Al_2O_3	SiO_2	CaO	TiO_2	V_2O_5	FeO	Phases
9,10	0.1	0.2	0.1	39.6	55.8	0.1	0	Perovskite
11	18	11.3	30.5	18.5	15.3	0.3	0.3	*
12	13.9	8.2	38.7	22.1	12.6	0.1	0.2	*
13, 14	28	60.6	0.1	0	11.3	1.7	0.3	Spinel
15, 16	8.9	2.1	0.3	0.7	82.3	1.1	0.2	Pseudobrookite
17, 18	5.8	2.7	0.1	0.2	90.3	0.2	0.1	Pseudobrookite
19	0.2	0.3	0.1	39.5	56.1	0	0.1	Perovskite
20, 21	10.5	9.7	34.8	23.4	16.7	0.1	0.2	*
22, 23	28.1	65.2	0.3	0.1	7.9	0.7	0.4	Spinel

* Phase not detected by XRD

Figure 6—Microstructure, chemical composition (mass %, by EDS), and phase composition (by XRD) of the EHSV slag

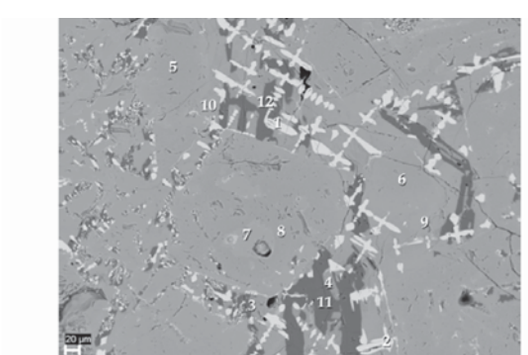

Point	MgO	Al_2O_3	SiO_2	CaO	TiO_2	Phase
1, 2		0.45		39.46	60.09	Perovskite
3, 4	27.97		33.8	38.22		Monticellite
5	35.58	18.71			45.71	MgAlTiO
6	33.44	15.49			51.07	MgAlTiO
7	22.34	17.35	16.9	15.42	27.99	*
8	32.11	17.72			50.17	MgAlTiO
9	10.83	11.61	34.1	26.92	16.58	*
10	11.14	15.55	32	25.96	15.35	*
11, 12	58.77		37.4	2.622	1.18	Forsterite

* Phase not detected by XRD

Figure 7—Backscattered electron image, chemical composition (mass %, by EDS), and phase composition (by XRD) of the slag produced with 110% stoichiometric C addition in a magnesia crucible

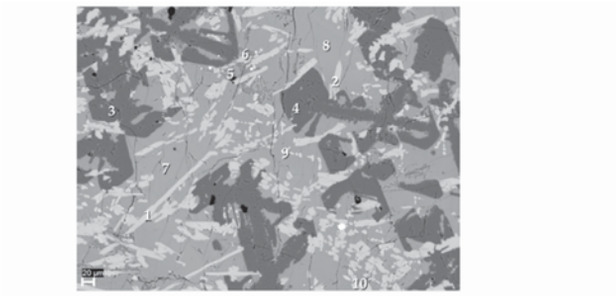

Point	MgO	Al_2O_3	SiO_2	CaO	TiO_2	MnO	FeO	Phase
1, 2	6.62	3.86		0.84	88.14		0.54	Pseudobrookite
3, 4	28.50	65.60			5.90			Spinel
5, 6	2.03	27.18	47.61	11.06	2.93	2.63		x
7, 8	7.90	19.29	26.28	23.71	22.81			x
9, 10		0.84	1.12	38.99	59.05			Perovskite

[x] Phase not detected by XRD

Figure 8—Backscattered electron image, chemical composition (mass %, by EDS), and phase composition (by XRD) data of the slag produced with 110% stoichiometric C addition in an alumina crucible

The slag that resulted in highest Fe and V recoveries in the alumina crucible tests (Figure 8) consisted of pseudobrookite as the primary phase, spinel as the secondary phase, and perovskite as the ternary phase. This phase composition is similar to that of the EHSV slag, though in this case inclusions of pseudobrookite were observed in the spinel, suggesting that the pseudobrookite crystallized first.

As detailed above, the difference in the phase compositions of the slags produced using magnesia and alumina crucibles did not adversely affect the Fe and V recoveries, as in both cases the recoveries were comparable to those in the commercial EHSV process. Based on the phase chemical compositions, the titanomagnetite slag produced in alumina crucibles is similar to the EHSV slag. Hence, for the studied slag composition the alumina crucible appears to be the best type to use in laboratory-scale test work.

Conclusion

Laboratory-scale carbothermic reduction smelting tests on titanomagnetite have demonstrated that chemical attack of the magnesia and alumina crucibles by the titania-bearing slag is inevitable. The aggressiveness of the titania-bearing slag led to dissolution of the respective crucible components into the slag phase. The crucible wear was more pronounced with magnesia crucibles than with alumina crucibles. The Fe and V recoveries to the alloy were higher in alumina crucibles than those in magnesia crucibles, but the recoveries in both cases were comparable to the EHSV data. The phase chemical compositions of the best slags in terms of Fe and V recoveries were significantly different for each crucible type. The slag produced using an alumina crucible had a similar phase chemical composition to that of the commercial EHSV titanomagnetite slag. The results of the test work have shown that both the magnesia and alumina crucibles can be used to conduct laboratory-scale test work with slags in the reviewed chemical composition range. However, since alumina crucibles are relatively easily obtainable, it is preferable to use alumina crucibles.

Further work is recommended to investigate the effect of magnesia and alumina crucibles on the smelting characteristics of titanomagnetite at various CaO to MgO ratios in the compositional range covered in the available phase diagram, and to study the changes in liquid phase formation as a function of MgO and Al_2O_3 addition.

Acknowledgement

The paper is published by permission of Mintek. The authors wish to thank Mintek for financial support. The input of Mr Archie Corfield and Mintek's Analytical Services Division is greatly appreciated.

References

Boyd, M.D., Schoukens, A.F., and Denton, G.M. 1993. The recovery of titanium from titanomagnetite. South African patent. P11756 MVS/mdg.

Garbers-Craig, A.M. and Pistorius, P.C. 2006. Slag-refractory interaction during smelting of ilmenite. *South African Journal of Science*. pp. 576–580.

Geldenhuys, I.J. and Jones, R.T. 2011. What scale should your smelting testwork be done at, and what do you get for the money you spend? *Proceedings of the 6th Southern African Base Metals Conference*, Phalaborwa, 18-20 July 2011. Southern African Institute of Mining and Metallurgy, Johannesburg. pp. 477–490.

Goso, X.C., Nell, J., and Petersen, J. 2015. Review of liquidus surface and phase equilibria in the TiO_2-SiO_2-Al_2O_3-MgO-CaO slag system at pO_2 applicable in fluxed titaniferous magnetite smelting. *Advances in Molten Slags, Fluxes, and Salts: Proceedings of the 10th International Conference on Molten Slags, Fluxes and Salts*, Seattle. The Minerals, Metals and Materials Society. pp. 105–114.

Gwatinetsa, D. 2013. Distribution of iron-titanium oxides in the vanadium main magnetite seam of the upper zone: nothern limb, Bushveld Complex. MSc thesis, Department of Geology, Rhodes University, Grahamstown, South Africa.

Jochens, P.R., Sommer, G., and Howat, D.D. 1969. Preliminary equilibrium and non-equilibrium phase studies of titaniferous slags. *Journal of the Iron and Steel Institute*. pp. 187–192.

Pistorius, P.C. 2004. Equilibrium interaction between freeze lining and slag from ilmenite smelting. *Journal of the South African Institute of Mining and Metallurgy*, vol. 104, August. pp. 237–242.

Steinberg, W.S. 2008. Development of a control strategy for the open slag bath furnaces at Highveld Steel and Vanadium Corporation Ltd. MEng thesis, University of Pretoria. http://repository.up.ac.za/bitstream/handle/2263/26090/dissertation.pdf;sequence=1[accessed 10 October 2016].

Steinberg, W.S., Geyser, W., and Nell, J. 2011. The history and development of the pyrometallurgical processes at Evraz Highveld Steel and Vanadium. *Journal of the Southern African Institute of Mining and Metallurgy*, vol. 111, no. 10. pp. 705–710. ◆

Comment on the paper: 'Financial analysis of the impact of increasing mining rate in underground mining, using simulation and mixed integer programming'

by A. Salama, M. Nehring, and J. Greberg

which was published in the April 2017 issue of the *Journal*

It should come as no surprise that a model can show increased profitability with increasing mining rate. However, models are based on assumptions, and sometimes those assumptions are hidden or even overlooked.
This may have happened in the present paper. There is an implicit assumption that grade control was maintained at all rates of mining. I know of several cases in which this was not true.

In one classic mining experiment on the Witwatersrand, the rate of face advance was increased from 3 m to 25 m per month at very little direct cost. However, a fault was encountered.

Because of the interest in the experiment, all available geological resources were brought to bear on the problem. Finally it was agreed that this was a downthrust. A small development revealed what looked like a continuation of the reef lower down, the plane of mining was lowered and we continues at 25 m/month face advance.

Slowly the news broke that grade control had been lost over the whole mine. Slowly the sampling results for our rapid-mining section came in. Slowly we discovered we were mining waste - very efficiently, but at huge cost, because we were undercutting pay-grade material and effectively immobilising it. After two months our experiment was forcefully halted.

So this is a plea to all who use simulation and modelling in an attempt to improve their mining methods. Check the implicit assumptions. It is all to easy to overlook them. When you try to implement the improvement, it fails because of an assumption you made without even realizing you had done so.

Professor P. Lloyd

* *Cape Peninsula University of Technology, Cape Town, South Africa.*

http://dx.doi.org/10.17159/2411-9717/2017/v117n7a7

Entrained defects in light metal cast alloys

by M.A. El-Sayed* and M. Ghazy*

Synopsis

The properties of light alloy castings are strongly affected by their inclusion content, particularly double oxide film defects (bifilms), which not only decrease the tensile and fatigue properties, but also increase their scatter. Recent research has suggested that oxide film defects may alter with time, as the air inside the bifilm would react with the surrounding melt. In this work, the effect of time on double oxide film defects is studied for different Al alloys. The results suggest that bifilm defects, once entrained, experience changes in their internal atmospheres which significantly affect their morphology and their influence on the alloy's mechanical properties. These changes involve the consumption of both oxygen and nitrogen inside the defect (with the former occurring first), which enhances the mechanical properties, but this is followed by hydrogen diffusion into the bifilms with a corresponding adverse effect on the properties.

Keywords
double oxide film defects, aluminium, casting, hydrogen.

Introduction

As the use of cast aluminium has increased, so have the mechanical property requirements (El-Sayed, 2015; Youssef and El-Sayed, 2016). Since the mechanical properties of Al castings are greatly affected by their inclusion content, it is important to study these inclusions, their types, causes, and harmful influences. One of the most significant inclusions is the double oxide film defect, which has been reported to have very detrimental effects on the reliability and reproducibility of Al castings (Campbell, 2003).

During the casting of aluminium alloys, the molten surface is exposed to air, which results in the formation of a surface oxide film. As the liquid metal is transferred or poured, its surface can experience disturbances or breaking waves (known as surface turbulence), resulting in the surface of the liquid metal folding over onto itself. This causes the upper and lower oxidized surfaces to come together and trap a layer of the mould atmosphere between them, creating a double oxide film defect or 'bifilm'. This defect can be incorporated into the bulk liquid by entrainment as shown in Figure 1 (Campbell, 2003, 2006).

Entrained double oxide film defects represent the easiest possible initiating sites for cracks, hot tears, or pores, as their unbonded dry inner surfaces can be separated with minimal effort because of the presence of an internal atmosphere. In a study of the fatigue properties of Al-7Si-0.4Mg alloy castings, Nyahumwa, Green, and Campbell (1998a) reported that in about 98% of all fatigue fractures, bifilms were the initiators of cracks. The remaining 2% of samples that did not contain bifilms exhibited up to 100 times greater fatigue lives.

Campbell (2006) suggested that after entrainment and due to internal turbulence in the bulk liquid, the entrained bifilm could become compacted into a convoluted form. Afterwards, the bifilm might unfurl in the quiescent conditions of the mould cavity and then re-establish its shape as a planar crack. Moreover, during solidification, the solubility of hydrogen in the alloy decreases significantly, and it may diffuse into the bifilm gap, causing it to expand into a crack or pore. It has also been shown that double oxide films could be favourable sites for the nucleation and growth of a wide variety of intermetallic compounds (Cao and Campbell, 2003), as shown in Figure 2.

Bifilms, either acting as cracks or helping in the nucleation of porosity or intermetallic phases, can therefore be detrimental to the mechanical properties of Al castings. They not only reduce the elongation, tensile strength, and fatigue limit of the castings, but also increase the variability of these properties (El-Sayed, 2016; El-Sayed and Griffiths, 2014).

Nyahumwa, Green, and Campbell (1998b) suggested that, after entrainment, the oxide layer might transform from γ-Al_2O_3 to α-Al_2O_3, a process that might take about 5 hours. This transformation is associated with a

* *Arab Academy for Science and Technology and Maritime Transport, Abu Qir, Egypt.*
 ISSN 2225-6253. Paper received Apr. 2016; revised paper received Nov. 2016.

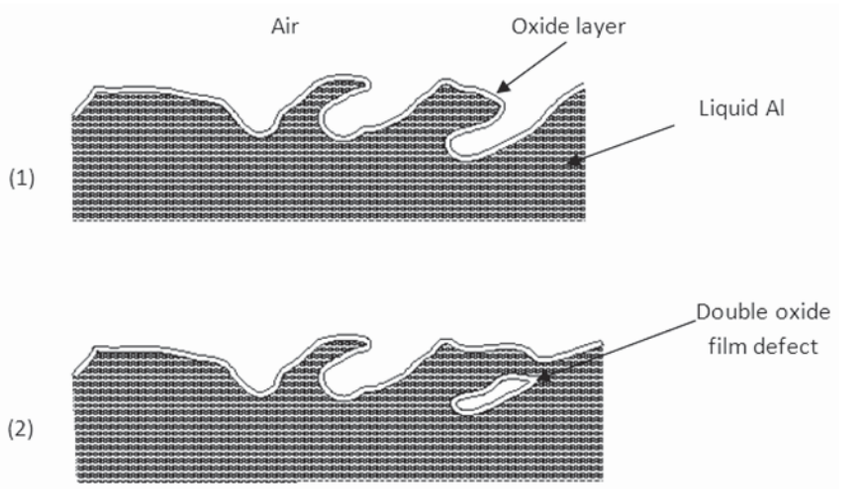

Figure 1—Schematic diagram illustrating the formation of a double oxide film defect (Basuny *et al*., 2016)

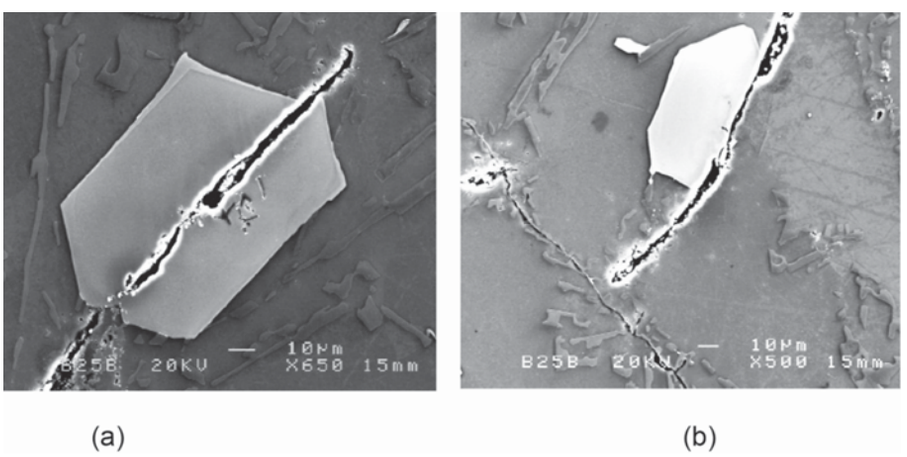

Figure 2—Secondary electron SEM images of Al-11.5Si-0.4Mg alloy castings showing cracks in (a) an iron-rich intermetallic phase and (b) the interface between an intermetallic phase and the Al matrix (Cao and Campbell, 2003)

volume decrease of about 24%, which would create stresses in the oxide skin, resulting in cracking. This would allow the oxygen and nitrogen inside the defect to react with the surrounding melt. With time, all the bifilm atmosphere would be consumed, possibly allowing other processes to operate that might lead to the deactivation of the defect.

Raiszadeh and Griffiths (2006) established a methodology to study the history of oxide films in an Al melt. Their results showed that, because of the higher free energy of formation of Al_2O_3, the oxygen in the trapped air inside a double oxide film defect would be consumed, first to form Al_2O_3, then the nitrogen would react to form AIN. These reactions would reduce the volume of the trapped air bubble. Also, if the initial hydrogen content of the melt was higher than the equilibrium associated with the ambient atmosphere, hydrogen would diffuse into the trapped air bubble and increase its volume. The reaction rates of the trapped air within the defect were utilized to build a semi-empirical mathematical model to predict the duration of the atmosphere inside a double oxide film defect. The results suggested that the consumption of oxygen and nitrogen inside the defect would not take more than about three minutes (Raiszadeh and Griffiths, 2008).

The aim of the current work was to study the effect of holding an Al alloy melt in the liquid state on the shape of the entrained oxide film defects, and hence on the mechanical properties of the resulting castings. The main objective was to learn whether oxide film defects could be eliminated, or at least whether their deleterious effects could be reduced.

Experimental procedure

The effect of holding an Al alloy melt under a vacuum

In order to determine the effect of holding an Al alloy melt under a vacuum on the oxide film content, 6 kg of Al-7Si-0.3Mg (wt%) (2L99) alloy was melted in an induction furnace and then allowed to solidify under a reduced pressure of 80 mbar. The solidified casting was sectioned into two halves, and the internal surfaces of the pores were investigated using scanning electron microscopy (SEM) (Philips XL-30 instrument) with energy dispersive spectroscopy (Oxford Inca) to determine their relationship to double oxide film defects.

Investigation of the effect of holding time before solidification on double oxide film defects

Castings were produced by the investment casting technique, and contained oxide films which were nominally of different ages; 0, 10, and 20 minutes, by holdup at these times. Three different aluminium alloys were considered: commercial-purity Al, Al-7Si-0.3Mg (wt%), and Al-5Mg (wt%) to involve different oxide films that might have different behaviours. The three oxide species expected to form in each alloy were Al_2O_3, $MgAl_2O_4$, and MgO.

In each experiment, about 10 kg of the given alloy was melted and held at about 800°C under a vacuum of about 80 mbar for one hour. This was intended to remove previously introduced oxide films from the melt (Raiszadeh and Griffiths, 2010; El-Sayed, Hassanin, and Essa, 2016). The liquid metal was then poured into preheated investment shell moulds, which were placed in an induction furnace and stirred using a power setting of 7.5 kW and frequency of 2350 Hz for one minute. This led to splashing of the liquid metal surface, and the creation of new double oxide film defects and their entrainment into the melt.

One casting was then allowed to solidify immediately, while two further castings were maintained in the liquid state by placing the filled ceramic shell mould in a furnace for 10 and 20 minutes, respectively, then removing it and allowing the melt to solidify. The change in hydrogen content of each melt during holding was also determined. After solidification, each of the castings was machined into 15 tensile test bars for determination of the ultimate tensile strength and percentage elongation at failure, using a cross-head speed of 0.17 $mm.s^{-1}$. The tensile results were evaluated using a Weibull statistical analysis approach (Weibull, 1951) to assess the influence of the holding period on the variability of the mechanical properties of the castings. Finally, the fracture surfaces of the test bars were examined using SEM.

The effect of holding time on the composition of an air bubble

In order to follow the changes in gas composition of the internal atmosphere of a double oxide film defect within an Al melt, a series of analogue experiments was carried out to determine the changes in composition of a trapped air bubble held in a melt of commercial-purity Al. The air bubble was formed by immersing a blind hole of 6 mm diameter and 5 mm depth, drilled into the centre of a steel piece, into an Al melt. This was then rotated at a speed of 540 r/min, corresponding to an angular velocity of 1.4 $m.s^{-1}$. The air bubble inside the hole was therefore in direct contact with the Al melt, allowing its interior (initially air) to react with the surrounding liquid Al and hydrogen to diffuse between the melt and air bubble. Two such experiments were carried out, of 5 and 20 minutes duration, before allowing the melt to solidify. After solidification, a section containing the remaining air bubble was machined out of the casting, without piercing the bubble. This section was placed in a pore gas analyser (constructed by Hyden Ltd), in which the contents of the bubble were extracted under a vacuum, and the gas obtained analysed using mass spectrometry. A reference air bubble containing ambient atmosphere was created by soldering and sealing the bottom of a blind hole of the same dimensions, which was also analysed to provide a calibration sample that should comprise the normal composition of the atmosphere.

Results

The effect of holding liquid Al under a vacuum

Figure 3 shows an example of an SEM image from within a pore that was allowed to solidify under a vacuum of about 80 mbar. Oxide fragments were visible inside the pore and were confirmed by energy-dispersive X-ray (EDX) analysis, which indicated the presence of $MgAl_2O_4$ spinel. This suggests that the origin of the pore lay with a double oxide film defect. Holding the melt under vacuum would be expected to cause the expansion of any atmosphere within the entrained double oxide films, increasing their buoyancy and causing them to float to the surface of the melt, thus reducing their harmful effects on the mechanical properties of the casting. In this experiment, the holding process was interrupted and the liquid metal was allowed to solidify under vacuum in order to determine the character of the porosity inside the casting. The analysis of these pores confirmed a relationship with oxide films. Subsequently, the melts used to make the castings for investigation of the effect of holding time on their scatter of properties were subjected to a vacuum for 1 hour before casting, in order to minimize the effect of prior oxide film defects.

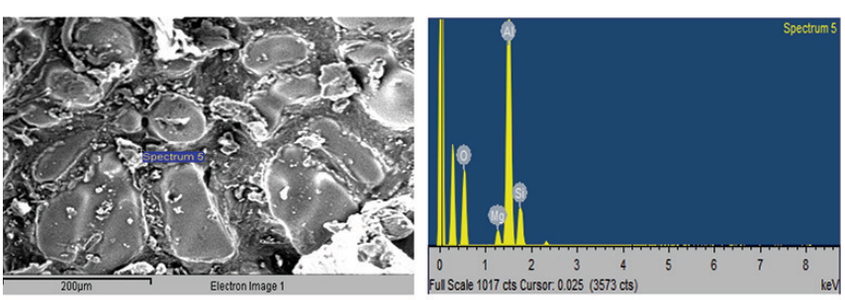

(a) (b)

Figure 3—(a) Secondary electron SEM image of oxide fragments within a pore on the machined surface of a 2L99 alloy casting solidified under vacuum, (b) EDX spectrum at the location shown in (a)

Table I

Results of the Weibull analysis for the test bars of different Al alloys containing oxide films of age 0, 10, and 20 minutes

Alloy type	Commercial-purity Al alloy			Al-7Si-0.3Mg alloy			Al-5Mg alloy		
Holding time	0 min.	10 min.	20 min.	0 min	10 min.	20 min.	0 min.	10 min.	20 min.
H (cm^3/100 g)	0.10	0.15	0.28	0.08	0.10	0.15	0.91	1.0	1.22
Weibull modulus of UTS (MPa)	33	36	30	37	39	34	22	31	24

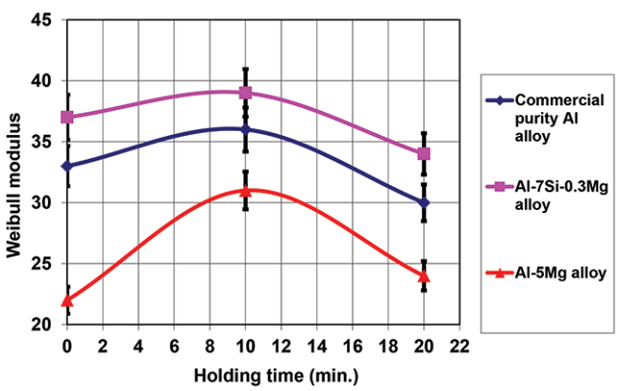

Figure 4—Effect of holding time on Weibull modulus of the UTS for the different Al alloys

The effect of holding time before solidification on mechanical properties

Table I shows the Weibull analysis of the mechanical property results of the three different alloys, as well as measurements of the melt hydrogen content. The Weibull moduli of the UTS are also shown in Figure 4. In all three alloys, the Weibull moduli were maximum for the castings held for 10 minutes before solidification, although for the pure aluminium and Al-7Si-0.3Mg alloys the maximum values were only slightly higher than the Weibull moduli at 0 and 20 minutes. The hydrogen content of the castings increased with holding time, with this being particularly marked for Al-5Mg, due to the greater solubility of hydrogen in this alloy (Anyalebechi, 1995).

Figures 5a and 5b show whisker-like oxides found within some pores of the commercial-purity Al and the Al-5Mg alloy castings held for 20 minutes before solidification. The pores are suggested to be associated with oxide films, as shown by EDX analysis which indicated the presence of Al_2O_3 and/or MgO inside the pores. Although the interconnections were too small to influence the mechanical properties, their presence perhaps suggests that chemical reactions were occurring within the pore atmosphere, resulting in the deposition of ceramic whiskers. No whiskers were found on the fracture surfaces of samples, either when solidified immediately or when held in the liquid state for 10 minutes before solidification. This is shown in Figure 5c, which illustrates a casting from Al-5Mg alloy held for 10 minutes before solidification.

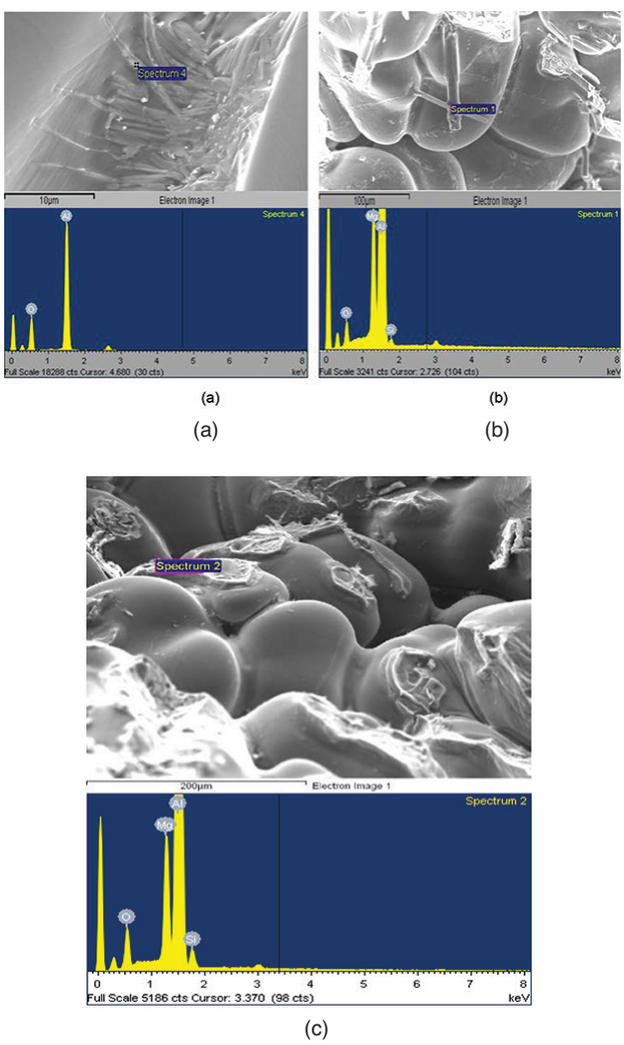

Figure 5—Secondary electron SEM micrographs and corresponding EDX spectra showing (a) whiskers between adjacent oxide layers in castings from commercially-pure Al held for 20 minutes, (b) whiskers growing from the dendrite tips in a pore inside a casting from Al-5Mg alloy held for 20 minutes, and (c) the inside of a pore from a casting from Al-5Mg alloy held for 10 minutes, in which no whiskers were detected

Results of the pore gas analysis experiments

Figure 6 depicts the initial results from the pore gas analysis experiment, showing the composition of gas bubbles held for different times in liquid metal subjected to stirring at

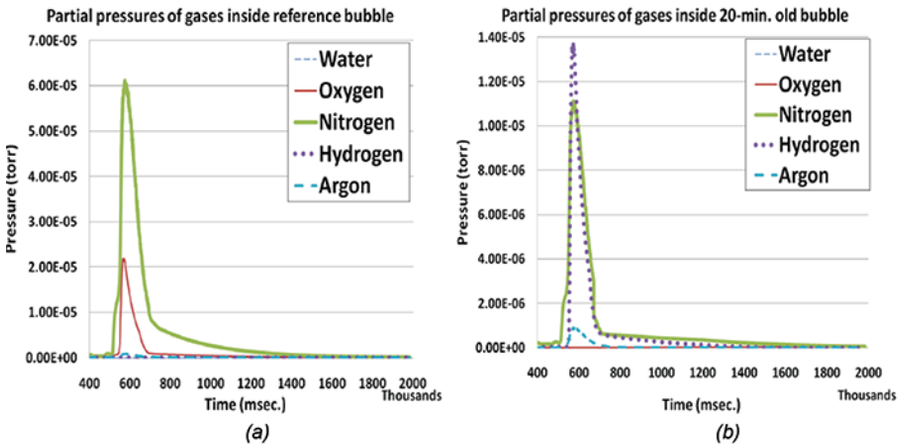

Figure 6—Results of the pore gas analysis for bubbles of (a) zero minutes and (b) 20 minutes holding time

540 r/min. The change in composition with time is given in Table II, and shown in Figure 7. The data suggests that the first 5 minutes of the experiment were characterized by a rapid loss of oxygen (causing the air bubbles to lose most of their oxygen content within this holding period) and a slight increase in hydrogen content. The slight increase in nitrogen content was presumably due mostly to the reduction in bubble volume as the oxygen reacted with the liquid Al. After 20 minutes' holding, the bubble volume was reduced to about one-quarter of its original size, as shown by the increase in argon content, which is unreactive and insoluble in liquid Al, but by this time almost all of the initial oxygen content had been consumed. The nitrogen content was also reduced to about 20% of its initial amount, but the hydrogen concentration had increased markedly, to represent about 40% of the volume of the bubble. The the bubble in the melt held for 20 minutes therefore consisted mainly of nitrogen and hydrogen with trace amounts of oxygen, argon, and water vapour.

Discussion

Previous research suggested that holding liquid metal under vacuum may cause its entrained bifilms to expand (Dispinar and Campbell, 2004; Fox and Campbell, 2000). The SEM investigation accompanied by EDX analysis (Figure 3) detected many oxide fragments inside the pores in the casting solidified under vacuum. The fragments were determined to be spinel, suggesting that such pores were initially double oxide film defects that expanded due to the application of the vacuum. If the liquid aluminium is held under vacuum for a sufficient time, this might allow double oxide film defects to expand and float to the melt surface. In the experiment performed here, the holding treatment was suspended at an intermediate stage to allow investigation of the defects. The significance of this experiment is that, since the experiments involving the holding of castings in the liquid state were made with melts previously held under a vacuum, the oxide film defects seen in the mechanical property test bars were probably created during casting of the bars, rather than the result of prior casting processes.

The mechanical property data shown in Table I indicates a peak in properties in the casting held for 10 minutes before solidification. This could be an indication of two competing mechanisms, each influencing the morphology of the double oxide film defects, (*i.e.,* their size and shape), and hence their effect on mechanical properties. Initially, the internal atmosphere of the double oxide film defects may have been reduced by reaction of their oxygen content with the surrounding melt, and as the volume of the internal atmosphere decreased, the size of the defects, and their effect on mechanical properties, was correspondingly reduced, resulting in an increase in the Weibull modulus to reach a maximum at 10 minutes. The second effect may be the diffusion of hydrogen from the melt into the defect interiors, increasing their size and the effect on mechanical properties, and so decreasing the Weibull modulus.

The whisker-like structures found within pores, shown in Figure 5 and confirmed by EDX to be oxides, occurred mostly at holding periods of 20 minutes. The whisker-like growths are indicative of ceramic structures grown from a vapour phase (Edwards and Happel, 1962; Hayashi and Saito, 1974), which might be evidence that they formed within porosity containing an atmosphere. The occurrence of whiskers in the pores in the castings, (which were themselves related to oxides) is suggestive of double oxide film defects retaining an atmosphere for tens of minutes after their formation, and perhaps an atmosphere consisting mostly of hydrogen. DeVries and Sears (1959) reported that heating of alumina to 2000°C in the presence of hydrogen caused the vaporization of alumina to produce Al_2O and water vapour, both in the gaseous form. When the temperature was lowered, the reaction was reversed and alumina was deposited in the form of whiskers. It is speculated that, during holding of the melt, reaction between the bifilm atmosphere and the surrounding melt may produce sufficient heat energy to locally increase the temperature of the double oxide film defect to such an extent that could cause the partial reduction of the alumina forming the bifilm to Al_2O (which would be expected to occur as a vapour phase at these temperatures) and water vapour. During solidification, if all of the O_2 and N_2 had been consumed, the temperature would begin to decrease, perhaps resulting in the reaction of Al_2O with water vapour to produce the alumina in whisker form.

Table II

Change in composition (volume %) in an air bubble with time

Time	0 minutes	5 minutes	20 minutes
Argon	1.0	1.3	3.7
Hydrogen	0.7	4.9	39
Nitrogen	80	90	53
Oxygen	18	2.9	1.9
Water	0.6	0.8	2.2
Relative volume	1.0	0.77	0.27

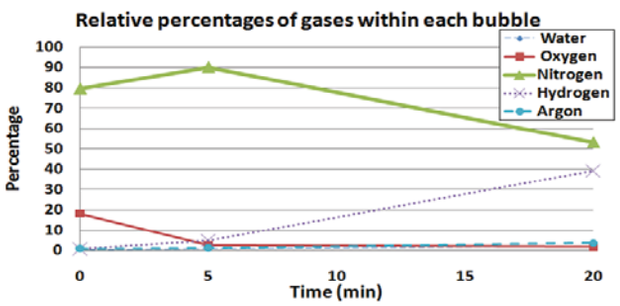

Figure 7—Change in the percentages of gases inside the bubble at different holding periods

The effect of holding time on the composition of the internal atmosphere of a double oxide film defect is supported by the initial results of the pore gas analyses shown in Table II and Figure 7. The most marked changes in the bubble composition were the loss of oxygen during the early stages of holding, and the subsequent increase in hydrogen content.

To summarize, the change in mechanical properties, the occurrence of oxide whiskers, and the pore gas analysis results suggest that double oxide films, once formed, quickly undergo changes in their internal atmosphere which affect the mechanical properties by influencing the size and shape of the double oxide films. These changes comprise the rapid consumption of oxygen and a slower accumulation of hydrogen, with the latter dependent on the hydrogen content of the melt. The consumption of nitrogen was also a slower process, occurring subsequent to the reaction of oxygen, although complete oxygen consumption did not appear to be required before the formation of AlN.

Conclusions

- Holding Al castings in the liquid state for up to 20 minutes before solidification resulted in peak values of the Weibull modulus occurring at a nominal holding period of 10 minutes
- Whisker-like structures of oxides were found in pores in castings solidified after holding for 20 minutes in the liquid state
- Pore gas analysis showed that a trapped air bubble held in stirred liquid Al alloy lost most of its oxygen content within around 5 minutes, and subsequently gained hydrogen by diffusion from the melt
- These results suggest that double oxide film defects in liquid Al alloys may have variable effects on casting properties, depending on their morphology. This morphology is influenced by the composition of the interior atmospheres of the defects, which is influenced by reaction with the surrounding melt and diffusion of hydrogen into the defect.

References

Anyalebechi, P.N. 1995. Analysis of the effects of alloying elements on hydrogen solubility in liquid aluminum alloys. *Scripta Metallurgica et Materialia*, vol. 33. pp. 1209–1216.

Basuny, F.H., Ghazy, M., Kandeil, A.-R.Y., and El-Sayed, M.A. 2016. Effect of casting conditions on the fracture strength of Al-5 Mg alloy castings. *Advances in Materials Science and Engineering*. DOI: 10.1155/2016/6496348

Campbell, J. 2003. Castings. Butterworth-Heinemann.

Campbell, J. 2006. Entrainment defects. *Materials Science and Technology*, vol. 22. pp. 127–145.

Cao, X. and Campbell, J. 2003. The nucleation of Fe-rich phases on oxide films in Al-11.5Si-0.4Mg cast alloys. *Metallurgical and Materials Transactions*, vol. 34A. pp. 1409–1420.

Deveries, R.C. and Sears, G.W. 1959. Growth of aluminum oxide whiskers by vapor deposition. *Journal of Chemical Physics*, vol. 31. pp. 1256–1257.

Dispinar, D. and Campbell, J. 2004. Critical assessment of reduced pressure test. Part 1: porosity phenomena. *International Journal of Cast Metals Research*, vol. 17. pp. 280–286.

Edwards, P.L. and Happel, J.R.J. 1962. Alumina whisker growth on a single-crystal alumina substrate. *Journal of Applied Physics*, vol. 33. pp. 826–827.

El-Sayed, M.A. 2015. Effect of welding conditions on the mechanical properties of friction stir welded 1050 aluminum alloy. *International Review of Mechanical Engineering*, vol. 9. pp. 252–256.

El-Sayed, M.A. 2016. The behaviour of bifilm defects in cast Al-7Si-Mg alloy. *PloS one,* vol. 11, no. 8. e0160633. DOI: 10.1371/journal.pone.0160633

El-Sayed, M.A. and Griffiths, W.D. 2014. Hydrogen, bifilms and mechanical properties of Al castings. *International Journal of Cast Metals Research*, vol. 27. pp. 282–287.

El-Sayed, M.A., Hassanin, H., and Essa, K. 2016. Effect of casting practice on the reliability of Al cast alloys. *International Journal of Cast Metals Research*, pp. 1-5. DOI: 10.1080/13640461.2016.1145966

Fox, S. and Campbell, J. 2000. Visualisation of oxide film defects during solidification of aluminium alloys. *Scripta Materialia*, vol. 43. pp. 881–886.

Hayashi, S. and Saito, H. 1974. Growth of magnesia whiskers by vapor phase reactions. *Journal of Crystal Growth*, vol. 24-25. pp. 345–349.

Nyahumwa, C., Green, N.R., and Campbell, J. 1998a. The concept of the fatigue potential of cast alloys. *Journal of the Mechanical Behavior of Materials*, vol. 9. pp. 227–235.

Nyahumwa, C., Green, N.R., and Campbell, J. 1998b. Effect of mold-filling turbulence on fatigue properties of cast aluminum alloys. *AFS Transactions*, vol. 106. pp. 215–223.

Raiszadeh, R. and Griffiths, W.D. 2006. A method to study the history of a double oxide film defect in liquid aluminum alloys. *Metallurgical and Materials Transactions B*, vol. 37. pp. 865–871.

Raiszadeh, R. and Griffiths, W.D. 2008. A semi-empirical mathematical model to estimate the duration of the atmosphere within a double oxide film defect in pure aluminum alloy. *Metallurgical and Materials Transactions B*, vol. 39. pp. 298–303.

Raiszadeh, R. and Griffiths, W.D. 2010. The behaviour of double oxide film defects in liquid Al alloys under atmospheric and reduced pressures. *Journal of Alloys and Compounds*, vol. 491. pp. 575–580.

Weibull, W. 1951. A statistical distribution function of wide applicability. *Journal of Applied Mechanics*, vol. 13. pp. 293–297.

Youssef, Y. and El-Sayed, M. 2016. Effect of reinforcement particle size and weight fraction on the mechanical properties of SiC particle reinforced Al metal matrix composites. *International Review of Mechanical Engineering*, vol. 10, no. 4. pp. 261–265. DOI: 10.15866/ireme.v10i4.9509 ◆

http://dx.doi.org/10.17159/2411-9717/2017/v117n7a8

Health risk posed by enriched heavy metals (As, Cd, and Cr) in airborne particles from Witwatersrand gold tailings

by J. Maseki*, H.J. Annegarn*†, and G. Spiers‡

Synopsis

Severe episodes of windblown dust from mine tailings storage facilities (TSFs) are a common phenomenon on the Witwatersrand, especially during the spring windy season. For communities around TSFs, such events pose health and environmental challenges. This paper reports on health risk assessment using US Environmental Protection Agency (US EPA) risk assessment methods for heavy metal elements in windblown dust from TSFs on the central and east Witwatersrand. Samples of surface material from these TSFs were analysed for heavy metal content using inductively coupled plasma-mass spectrometry (ICP-MS). From a range of 30 heavy metals analysed, only As, Cd, Cr, Pb, and U were enriched by a factor of two or more above the average crustal composition and at concentrations that could be of possible health concern—elements present in the range of a few parts per billion (ppb) or lower were ignored. As, Cd, Cr, Pb and U were selected for a comprehensive risk assessment from exposure through airborne routes, mainly considering inhalation and ingestion. Ambient exposures were based on a worst-case measured episode of 540 µg m^{-3} (24-hour average), which was projected over each day of an annual exposure for the hours for which the wind speed was above the threshold for dust generation.

US EPA risk assessment methods were used to determine the inhalation and ingestion hazard quotients and hazard indices for adults and children. The sum of the hazard indices was assessed to be below the non-cancer benchmark (hazard indices 1.0) considered to be acceptable for a lifetime exposure. The total risk for both exposures (inhalation and the ingestion) was within the range of 1 per 1 000 000 to 100 per 1 000 000—taken as 'acceptable risk' by the US EPA for adults and children. These results represent the first quantitative health risk assessment of the hazard posed by heavy metals in windblown mine tailings dust on the Witwatersrand goldfield.

Keywords

mine tailings, dust, airborne particles, health risk, inhalation, ingestion heavy metals, arsenic, cadmium, chromium.

Introduction

Dust fallout from tailings storage facilities (TSFs) is a major contributor to ambient air pollution on the Witwatersrand, especially during dust storm episodes in the spring season when ambient PM10 aerosol concentrations (particles smaller than 10 µm) can reach 2 000 µg m^{-3} (24-hour average) (Annegarn, Scorgie, and Sithole, 2002; Annegarn *et al.*, 1990; Blight and Caldwell, 1984; Ojelede, Annegarn, and Kneen, 2012). Numerous public statements and claims have been made by individuals and organizations about the dust fallout from tailings affecting public health through several routes of exposure (Bega, 2011a, 2011b; Federation for a Sustainable Environment, 2010). Inhalation or ingestion of particulate matter (PM) has been shown to have adverse impacts on human health (Valavanidis, Fiotakis, and Vlachogianni, 2008; Wilson and Suh, 1997). Furthermore, several studies have confirmed a strong link between the inhalation of fine aerosols in ambient environments and the occurrence of cardiopulmonary mortality and respiratory diseases (Berico, Luciani, and Formignani, 1997; Dockery, 2001; Harrison and Yin, 2000; Fubini and Fenoglio, 2007; Griffin, Kellogg, and Shinn, 2001; Park *et al.*, 2004; Pope and Dockery, 2006; Schwartz, 1994; Wilson and Suh, 1997). According to Schwartz (1992) and the World Health Organization (2006), for human health, there is 'no safe threshold' level of PM exposure. The toxicity of particulate matter is a result of on the particle size, which allows the smaller particle to be transported deeper in the respiratory track (Bakand and Hayes, 2010; Harrison and Yin, 2000) and is exacerbated by metals and metalloids that adhere to the surfaces of such particles (Berico, Luciani, and Formignani, 1997; Ghio and Devlin, 2001; Soukup, Ghio, and Becker, 2000; World Health Organization, 2003).

This study comprises a health risk assessment on the inhalation and ingestion of heavy-metals enriched particles generated by wind erosion (dust fractions ≤ 20 µm) from gold tailings storage facilities in the central Witwatersrand Basin. Despite the known hazards of inhaled fine particle and public concern, we could find no prior quantitative health risk assessment of windblown dust from gold mine tailings of the Witwatersrand.

* *University of Johannesburg, Johannesburg, South Africa.*

† *Cape Peninsula University of Technology, Cape Town, South Africa.*

‡ *Laurentian University, Ontario, Canada.*

 ISSN 2225-6253. Paper received May 2016; revised paper received Sept. 2016.

The key objectives are as follows:

- To sample and separate the inhalable fraction of a representative suite of source materials from gold mine TSFs
- To determine the elemental compositions of the separated inhalable fractions of the samples
- To identify dominant heavy metals that are present at concentrations above crustal averages
- To calculate the non-cancer and the cancer risks for adults and children, considering the inhalation and ingestion exposures associated with seasonal wind storms on the Witwatersrand.

Materials and methods

Study area, sample collection, and sample treatment

The study area and sampling sites extended over the central and eastern Witwatersrand Basin. The sampling sites included the following tailings storage facilities (coordinates are for the centre points of the facilities): Central Witwatersrand (CWJH) E 27°57′, S 26°14′; Central Witwatersrand Roodepoort (CWRD) E 27°50′ S 26°12′; Eastern Witwatersrand Springs (ERSP) E 28°18′, S 26°21′, and Eastern Witwatersrand Boksburg (ERBK) E 28°12′ , S 26°14′.

Undisturbed bulk samples (approx. 5 kg) were collected at source from a depth of 15 cm to avoid material already exposed to water and aeolian erosion. Samples taken from the top level of the TSFs represented the core deposited material as original material. Samples from the side slopes and bottom represented material eroded from the top layers by wind or water, and redeposited. After drying at room temperature, bulk material was separated by particle size using an AS 200 Jet Sieve Shaker® and the ≤ 20 µm fractions were retained for analysis. Each separated sample of ≤ 20 m dust obtained from the shaker, comprising 5 g or less, was labelled and stored in a clean glass bottle. All the separated sub-samples were stored at room temperature until needed for further analysis.

Sample preparation and analysis

For each sample, 0.2 g of sieved tailings material (diameter ≤ 20 µm), the digestion procedure was as follows

Step 1: 10 ml of 10:1 HF:HCl was added to the sample, which was then heated to 110°C for 210 minutes—until dry (this step repeated three times to ensure dissolution of quartz and oxides)

Step 2: 7.5 ml HCl + 7.5 ml HNO3 were added to the dry residue, followed by heating to 110°C for 230 minutes—until dry

Step 3: 0.5 ml HF, 2 ml HCL, and 10 mL HNO3 were added to the sample residue, which was then heated to 110°C for 60 minutes—not dry

Step 4: The sample was diluted to 50 ml with deionized water.

Over 30 elements were measured using inductively coupled plasma-mass spectrometry (ICP-MS, using a Varian 810 instrument in standard resolution mode). A solution of Ru, Re was used as a constant bleed into the uptake stream as an internal standard. To correct for mass bias and calibration drift during sample analysis by ICP-MS, an internal standard solution containing 10 µg/L of Be, Re, Ru, was bled into the sample uptake line using a glass T-shaped mixing chamber (Glass Expansion TM). As part of the quality assurance procedures, a series of certified reference materials (CRMs), reagents, procedural blanks, and many duplicates (both procedural and analytical) were analysed with every batch of 20 samples.

Heavy metal identification and enrichment factors

From the range of 30 elements analysed, a selection was made of elements in the parts per million (ppm) and higher concentration range. This sub-set included the heavy metals As, Pb, U, Zn, Ni, Au, Cr, Cd, K, Fe, and Mn. Of these, only metals that were enriched in the tailings with respect to average crustal composition were selected for the health risk assessment. For the purposes of this study, *enriched* was taken as any element with an enrichment factor (EF) greater than 2. Elements with concentrations less than 1 ppm were not considered, as these are unlikely to constitute a health hazard, even if they were enriched relative to average crustal composition.

Si (the major metal present in the tailings) in the form of quartz is known to constitute a health hazard greater than when present in silicon-aluminium-potassium minerals (Hnizdo, 1995, 1994; Hnizdo, Sluis-Cremer, and Thomass, 1993); however, the health risk posed by quartz in either the micrometre or nanoparticle size ranges is outside the scope of this paper.

For the calculation of the EF, iron was used as the reference element (Taylor and McLennan, 1995). The average crustal abundance of Fe is 43 200 ppm (Rudnick and Presper, 1990; Shaw, Dostal, and Keays, 1976). Equation [1] was used for the EF enrichment factor calculation.

$$FM = (M_x * Fe_b) / (M_b * Fe_x) \quad [1]$$

where M_x and Fe_x are the concentrations of element M and Fe in the sample x, and M_b and Fe_b are the mean concentrations of element M and Fe in the continental crust (Wedepohl, 1995). All concentrations are in ppm. Although it would be preferable to use the most abundant element, silicon, as the reference element, silicon cannot be determined by ICP-MS.

Aerosol concentration determination

Onset of saltation (movement of sand grains) occurs at a wind speed of approximately 4 m s^{-1}, and increases with wind speed proportional to the square of the velocity. Significant generation of dust resulting in visible plumes begins only above about 6 m s^{-1}. Dust generation is dependent further on the exposure of dry, unvegetated soil or sand surfaces. The frequency of such winds is seasonally dependent; on the South African highveld the dusty season is from the onset of spring winds at the beginning of August through mid-October, by which time, spring rainfall suppresses further windblown dust generation. Measurements of ambient aerosol (dust) concentrations were made with Grimm® aerosol monitor during three weeks in September 2010. During this monitoring period, high-dust episodes occurred, associated with short-duration convective thunderstorms. These episodes were selected as worst-case scenarios of extreme dust storm days. The worst-case scenario assumed that the highest 24-hour concentration (540 µg m^{-3}) (Ojelede, Annegarn, and Kneen, 2012) persisted for the entire three-month windy season (August, September, and October). This scenario was used in the calculation of the exposure concentration of airborne aerosol for the risk assessment.

Exposure assessment

Inhalation and ingestion exposure

Two routes of exposure, inhalation and ingestion, were considered for the potential health risk posed by heavy metals in airborne particles to the population living around the TSFs. Intake of each element was calculated according the current standard risk assessment procedures of the US EPA (2011a, b). For the risk calculation formula, the exposure duration is required to be expressed as the average exposure in units of hours per day. Mean exposure duration (time) (ET) to the windblown dust from the TSFs was derived using the wind speed and direction record from the meteorological station at OR Tambo International Airport (courtesy of the South African Weather Service). A ten-year record from 2000 to 2009 was used to extract the number of hourly wind speeds above the threshold of 6 m s^{-1} for the onset of dust generation. This process yielded an annual average exposure time ET = 2.5 h d^{-1}.

Default exposure parameter values used for the dose calculation for inhalation and ingestion pathways are taken from the US EPA (2011b). Equations [2] and [3] were used for calculation of the exposure concentration for inhalation and chemical daily intake for the ingestion as developed by the US EPA (2011b):

$$EC_{inh} = C^{*}(ET^{*}EF^{*}ED)/AT_{n} \quad [2]$$

where EC_{inh} is the exposure concentration for inhalation, C the metal concentrations in 24 hours for worst-day dust concentration (540 mg kg-1 or µg m^{-3}), ET the exposure time (2.5 h d^{-1}), EF the exposure frequency (350 d a^{-1}), ED theexposure duration (6 years for children and 24 years for adults), AT*n* the averaging time: for non-carcinogens, AT = ED × 365 d × 24 hours; for carcinogens, AT = 70 × 365 d × 24 hours).

$$CDI_{ingest} = (C^{*}IngR)/BW^{*}(EF^{*}ED)/AT^{*}CF \quad [3]$$

where CDI_{ingest} is the chemical daily intake from soil ingestion (mg kg^{-1} d^{-1}), C the chemical concentration in soil (mg kg^{-1}), IngR the soil ingestion rate (mg d^{-1}), BW the body weight (kg); CF the unit conversion factor (10^{-6} kg mg^{-1}), EF the exposure frequency (350 d^{-1}), ED the exposure duration (6 years for children and 24 years for adults), AT the averaging time (for non-carcinogens, AT= ED × 365 d; for carcinogens, AT = 70 × 365 =25 550 d).

Risk characterization

Risk characterization for selected heavy metals was assessed for adults and children in calculating the non-cancer and cancer risk adopting the equations described in the EPA Methods (US EPA, 2011a, b, 2005a, b, c). The non-cancer risk was calculated by assessing the hazard quotient and hazard indices only for the selected enriched elements. The hazard quotient was derived by assessing each heavy element encountered and computing the results for the concentration inhaled or dose ingested using exposure duration (Equations [4] and [5]).

The reference dose (RfD) is 'an estimate (with uncertainty spanning perhaps an order of magnitude) of a daily oral exposure to the human population (including sensitive subgroups) that is likely to be without an appreciable risk of deleterious effects during a lifetime' (US EPA, 2011a). Reference concentration is 'an estimated daily concentration of a chemical in air, the exposure to which over a specific exposure duration poses no appreciable risk of adverse health effects, even to sensitive populations' (US EPA, 2011a).

RfC and RfD were from the US EPA (2012). An assumption on the toxic values (RfC and RfD) of Cr VI as total Cr was made in the risk assessment based on previous risk assessment studies on dust (Hu *et al.*, 2011, 2012; Kurt-Karakus, 2012). Although Cr VI is the identified carcinogenic chemical form of Cr, for screening purposes in this study the risk factor was calculated as though all Cr present was in the form of Cr VI. If the calculated risk for the total amount of Cr was within the acceptable limit, then any lesser fraction of Cr VI would similarly be within the limits, and the need for separate chemical speciation of the Cr components could be avoided.

A hazard index (HI) was obtained by summing the results from hazard quotient (Equation [6]) taking into account both routes of exposure (US EPA, 2011b).

$$HQ\ inhalation = EC^{*}0.001/RfC \quad [4]$$

$$HQ\ ingestion = CDI/RfD \quad [5]$$

CDI is the daily intake (mg $kg^{-1}d^{-1}$); RfC is the reference concentration inhaled material (mg m^{-3} per day).

RfD is the reference dose of ingested material (mg kg^{-1} d^{-1}).

$$HI = \Sigma HQ_{i} \quad [6]$$

where HQ_i is the hazard quotient for $COPC_i$

$$HI_{ingestion} = \Sigma_{I}\{DI_{1}/RfD_{1} + DI_{2}/RfD_{2}\ldots\ldots DI_{I}/RfD_{i}\} \quad [7]$$

where DI_i is the daily intake for i^{th} toxicant in (mg kg^{-1} d^{-1}) and RfD_i is the reference dose for i^{th} toxicant in mg kg^{-1} d^{-1}.

$$\text{Total HI} = \Sigma_{j} HI_{j} \quad [8]$$

where HIj is the hazard index for exposure pathway *j*.

The cancer risk was computed for both routes of exposure (inhalation and ingestion). To calculate the excess lifetime cancer risk due to inhalation and ingestion of particulate matter, Equations [9] and [10] were used (US EPA, 2011b). The cancer inhalation unit risk factor (IURF) [(mg m^{-3})$^{-1}$] and slope factor (SF) [mg^{-1} kg d] values were taken from US EPA (2012) for As and Cr, while the SF for Cd was from the Agency for Toxic Substances and Disease Registry (2008).

$$CR_{inhalation} = EC \times IURF \quad [9]$$

where CR is the cancer risk, EC is the chronic daily exposure concentration (averaged over a 70-year lifetime) for inhalation of particulate matter [mg kg^{-1}], and IURF is the inhalation unit risk factor [(mg m^{-3})$^{-1}$].

$$CR_{ingestion} = CDI \times SF \quad [10]$$

where CDI is chemical daily intake, and SF is the slope factor.

Total risks were calculated by summing the CR values for both routes of exposure, for the inhalation and ingestion risks (Equation [11]) (US EPA, 2011b):

$$\text{Total cancer} = CR_{inhalation} + CR_{ingestion} \quad [11]$$

Statistical analysis

Descriptive statistics (means and standard deviations) of the elemental concentrations for samples from each TSF were calculated using the Statistical Package for the Social Sciences (SPSS®) software.

Table I

Measured mean concentration of heavy metals in the gold mine tailings storage facilities (TSFs) compared to Earth crustal averages (bold indicates above crustal average) (ppm)

Element	Mean concentration in each TSF				Mean concentration across the four TSFs	Concentration in continental crust #
	ERSP	ERBK	CWJB	CWRD		
Fe	40 500	42 200	**44 800**	21 300	37 100	43 200
K	19 700	21 000	10 670	22 00	11 700	21 400
Mn	205	220	325	160	240	716
Cr	**410**	**550**	**230**	120	**290**	126
Zn	40	30	**70**	30	46	65
Ni	**106**	**60**	**76**	16	**60**	56
As	**150**	**140**	**90**	**110**	**116**	1.7
U	**8**	7	**16**	**16**	**13**	1.7
Pb	**16**	11	**27**	**24**	**21**	14.8
Cd	0.10	0.08	**1.52**	**5.67**	**2.42**	0.10
Au	**0.52**	**0.72**	**3.91**	**1.30**	**2.09**	0.0025

Adopted from Wedepohl, 1995

Results and discussion

Mean concentrations of elements around TSFs are presented in Table I and are compared to average concentrations in the continental crust as proposed by Wedepohl (1995).

Mean concentrations of As, Au, and U were above the Earth crustal average in the four tailings; Pb concentration was higher at CWRD, CWJB, and ERSP. Cr and Ni concentrations were above the crustal average at CWJB, ERBK, and ERSP. Mean concentrations across the four TSF complexes showed that As, Au, U, Pb, Cd, Cr, and Ni were all above the crustal average.

The elevated concentration of these metals may be explained by the mineralogical features of the Witwatersrand Basin gold deposits. Concentrations of elements below the Earth crustal average, including K, Mn, Zn, Fe, are not surprising for the gold tailings material (a silica-rich mineral matrix) (Frimmel and Minter, 2002; Robb and Meyer, 1995).

Results on the elemental enrichment with respect to average crustal composition in the sub-20 µm tailings fraction were derived using Equation [1] and were broken down into two ranges. The first range included elements with EF >2, which were Au (78 500), Cd (18 800), As (64), U (8), Cr (2), and Pb (2); while in the second range K (0.90), Ni (0.80), Zn (0.70), Fe (1), and Mn (0.25) presented an EF <2. The EF of elements in the tailings occurs in the order: Au>Cd>As>U>Cr>Pb>Fe>K>Ni>Zn>Mn.

Cd, Au, and As had the highest enrichment factors, falling in the class of extremely high enrichment (EF >40). Similar results on Au enrichment factors (20–400) in the sediments have been documented by Roychoudhury and Starke (2006), and the presence of arsernopyrite has been previously demonstrated (Genkin *et al.*, 1998). The enrichment of metals (*e.g.* As and Cd) in pyrite tailings is explained by adsorption onto the pyrite or by Fe-oxyhydroxides generated by the oxidation of pyrite (Öhlander *et al.*, 2007). Cd is found in sulphide minerals such as greenockite (CdS) which are among the minerals associated with gold in the Witwatersrand. The enrichment of Cr is due to the fact that its composition is made up of 30% of phyllosilicates (Feather and Koen, 1975). Cr is hosted in phyllosilicates, and a similar moderate enrichment has been recorded by Craw, Windle, and Angus (1999). U enrichment in tailings dumps may be explained by the enhanced uranium content of the Dominion Reef (one of the gold-bearing horizons mined on the Witwatersrand) (Robb and Meyer, 1995). Pb indicates a moderate enrichment, which can be explained by the fact that galena (PbS) is one of minerals associated with gold ore. Pb occurs also as the end-member of the uranium radioactive decay series. Fe, K, Mn, Zn, and Ni are not enriched, with values EF < 2. The acidification occurring in tailings could justify these results as long as those elements are dissolved in the solution (Espana *et al.*, 2005; Tutu, McCarthy, and Cukrowska, 2008). Tutu, McCarthy, and Cukrowska (2008) reported the occurrence of acidification in tailings in which oxidation reactions contribute to the dissolution of elements such as U, As, Cu, Ni, Co, and Zn.

The risk assessment includes non-cancer and cancer risk. Enriched elements (Cr, Cd, and As) with EF >2 were used for risk assessment. However, Pb was not assessed due to the lack of data on the exposure concentration for inhalation or reference dose (Integrated Risk Information System, 2005) and might require a particular method of risk assessment which considers several sources of intake (US EPA, 2002). Although Au was enriched, it was not considered for further analysis because it is biologically inert (Walker, 2007).

Results on non-cancer risk are summarized in Table II, indicating the hazard quotient and hazard indices via inhalation and ingestion for the adults and children. HI shows values of less than unity, which is considered as a threshold. The interpretation of risk assessment (extrapolated from recorded values for the inhalation or ingestion of enriched elements of critical concern (*i.e.* As, Cr, and Cd) revealed that there was no evidence of negative health impacts for either children or adults according to benchmarks established by the US EPA (1986).

The results in Table II on the total of hazard indices show values less than unity for all four TSFs, indicating that the concentrations are within acceptable limits.

The cancer risk was assessed on the enriched elements (As, Cd, and Cr) classified as carcinogenic (Fishbein, 1984; Kyle *et al.*, 2011; US EPA, 1998; Smith and Steinmaus, 2009; Wang *et al.*, 2011).

Table II

Summary of HI values via inhalation and ingestion for children and adults

Tailings	Element	HQ inhalation		HI inhalation		HQ ingestion		HI ingestion		HI ingestion + inhalation	
		Children	Adults	Children	Adults	Children	Adults	Children	Adults	Children	Adults
ERSP	Cr	2.34E-01	2.34E-01	0.85	0.85	1.85E-03	1.98E-04	9.2E-03	2.0E-04	0.86	0.86
	As	6.17E-01	6.17E-01			7.31E-03	7.83E-04				
	Cd	3.38E-04	3.38E-04			1.60E-06	1.71E-07				
ERBK	Cr	2.98E-01	2.98E-01	0.79	0.79	2.35E-03	2.52E-04	8.2E-03	8.8E-04	0.80	0.80
	As	4.97E-01	4.97E-01			5.89E-03	6.31E-04				
	Cd	1.41E-04	1.41E-04			6.67E-07	7.14E-08				
CWJB	Cr	1.15E-01	1.15E-01	0.45	0.45	9.11E-04	9.76E-05	4.9E-03	9.8E-05	0.46	0.45
	As	3.35E-01	3.35E-01			3.96E-03	4.25E-04				
	Cd	4.36E-03	4.36E-03			2.07E-05	2.21E-06				
CWRD	Cr	7.05E-02	7.05E-02	0.58	0.58	5.57E-04	5.97E-05	6.5E-03	7.0E-04	0.59	0.58
	As	4.95E-01	4.95E-01			5.87E-03	6.29E-04				
	Cd	1.49E-02	1.49E-02			7.05E-05	7.56E-06				

Table III

Total risk of selected heavy metals Cr, Cd, and As via inhalation and ingestion exposure routes

Tailings	Element	CR inhalation		CR inhalation		CR ingestion		CR ingestion		CR ingestion + inhalation	
		Children	Adults	Children	Adults	Children	Adults	Children	Adults	Children	Adults
ERSP	Cr	3.46E-06	8.01E-07	6.24E-05	1.44E-05	2.69E-07	1.15E-07	5.9E-07	2.5E-07	6.30E-05	1.47E-05
	As	5.89E-05	1.36E-05			3.20E-07	1.37E-07				
	Cd	2.00E-10	4.63E-11			9.48E-10	4.06E-10				
ERBK	Cr	4.41E-06	1.02E-06	5.19E-05	1.20E-05	3.43E-07	1.47E-07	6.0E-07	2.6E-07	5.25E-05	1.23E-05
	As	4.75E-05	1.10E-05			2.57E-07	1.10E-07				
	Cd	8.33E-11	1.93E-11			3.95E-10	1.69E-10				
CWJB	Cr	1.71E-06	3.95E-07	3.37E-05	7.79E-06	1.33E-07	5.69E-08	3.2E-07	1.4E-07	3.40E-05	7.93E-06
	As	3.20E-05	7.40E-06			1.73E-07	7.43E-08				
	Cd	2.58E-09	5.98E-10			1.22E-08	5.25E-09				
CWRD	Cr	1.04E-06	2.42E-07	4.84E-05	1.12E-05	8.11E-08	3.48E-08	3.8E-07	1.6E-07	4.88E-05	1.14E-05
	As	4.73E-05	1.10E-05			2.57E-07	1.10E-07				
	Cd	8.82E-09	2.04E-09			4.18E-08	1.79E-08				

U fell into the criteria of risk assessment, but naturally occurring U contains three isotopes, ^{238}U, ^{235}U, and ^{234}U so the carcinogenic risk depends on the different radiological properties of these isotopes (Eisenbud and Gesell, 1997). It was outside the scope of this work to assess the excess lifetime cancer risk for uranium.

Equations [9] and [10] were applied for calculating the cancer risk via inhalation and ingestion, respectively. The total cancer risk for Cd, Cr (VI), and As via inhalation and ingestion (Equation [11]) showed values between 1.0E-05 and 1.0E-06 for adults, and from 3.0E-05 to 6.0E-05 among children (Table III). The total cancer risk fell within the tolerable risk range of 10^{-4} to 10^{-6} (US EPA, 1991).

However, the full health effects of inhaled mineral dust need to include factors other than the heavy metal content dealt with in this contribution—the crystalline habit of minerals such as quartz and the possible aggravating effects of particles in the nanoparticle size range present additional hazards (Bakand, Hayes, and Dechsakulthorn, 2012, Davies and Mundalamo, 2010; Oberdörster, 2005, Hoet *et al.*, 2004). Within mixed dust, mineral particles can interact synergistically to increase or attenuate the toxicity (Fubini and Otero Areàn, 1999).

Conclusions

Chemical analysis of sub-20 µm dust fractions collected from four gold TSFs at Witwatersrand basin revealed elements such As, U, Cd, Pb, and Cr with EF>2. This enrichment is due to the fact that those elements occur in the gold-bearing ores.

Health risk assessment, including non-carcinogenic risk estimation via inhalation and ingestion of As, Cd, and Cr (VI) presented hazard indices of less than unity for children and adults. The total cancer risk level fell within the range of acceptable risk (10^{-4} to 10^{-6}) suggested by US EPA. Non-

carcinogenic and carcinogenic risks were found to be below the thresholds for public health and permissible for ambient exposures.

However, continued mitigation of airborne dust emissions and enforcement of current national dust fallout standards are important to maintain ambient dust levels within the risk levels reported in this work.

Acknowledgements

The project 'Adverse health impacts associated with dust emissions from gold mine tailings', under the leadership of Professor Mary Gulumian, was supported by a Mine Health Safety and Council grant under project no. SIM100801, and by the University of Johannesburg grant to the SeTAR Centre. Thanks to the National Institute for Occupational Health, the University of Johannesburg, and Elliot Lake Research Field Station (Laurentian University, Sudbury, Ontario, Canada) for the use of laboratory facilities and elemental analysis of the samples.

References

Agency for toxic substances and disease registry. 2008. Draft toxicological profile for cadmium. http//www.atsdr.cdc.gov./toxprofiles/tp5.pdf [Accessed 5 September 2011].

Annegarn, H.J., Scorgie, Y., and Sithole. J. 2002. Dust monitoring and mitigation on surface gold tailings reclamation. *Proceedings of Surface Mining 2002 – Modern Developments for the New Millennium*. South African Institute for Mining and Metallurgy, Johannesburg. pp. 103–109.

Annegarn, H., Zucchiatti, A., Sellschop, J.P.F., and Booth-Jones, P.A. 1990. Time variations of dust concentration and elemental composition in a gold mine. *Mining Science and Technology*. vol. 10. pp. 1–14.

Bakand, S., Hayes, A., and Dechsakulthorn, F. 2012. Nanoparticles: a review of particle toxicology following inhalation exposure. *Inhalation Toxicology*, vol. 24, no. 2. pp. 125–135.

Bakand, S. and Hayes, A. 2010. Troubleshooting methods for toxicity testing of airborne chemicals in vitro. *Journal of Pharmacological and Toxicological Methods*, vol. 61. pp.76–85.

Bega, S. 2011a. Living in S.A.'s own Chernobyl. *Saturday Star*, 8 January 2011. p. 13.

Bega, S. 2011b. Toxic mine dump time bomb threatens. *Saturday Star*, 5 November 2011. p. 15.

Berico, M., Luciani, A., and Formignani, M. 1997. Atmospheric aerosol in an urban area – measurements of TSP and PM10 standards and pulmonary deposition assessments. *Atmospheric Environment*, vol. 31. pp. 3659–3665.

Blight, G.E. and Caldwell, J.A. 1984. The abatement of pollution from abandoned gold residue dams. *Journal of the South African Institute of Mining and Metallurgy*, vol.84, no. 1. pp.1–9.

Craw, D., Windle, S.J., and Angus, P.V. 1999. Gold mineralization without quartz veins in a ductile – brittle shear zone, Macraes Mine, Otago Schist, New Zealand. *Mineralium Deposita*, vol. 34. pp. 382–394.

Davies, T.C. and Mundalamo, H.R. 2010. Environmental health impacts of dispersed mineralization in South Africa. *Journal of African Earth Sciences*, vol. 58. pp. 652–666.

Dockery, D.W. 2001. Epidemiological evidence of cardiovascular effects of particulate air pollution. *Environmental Health Perspective,* vol. 109. pp. 483–486.

Eisenbud, M. and Gesell, T. 1997. Environmental Radioactivity; from Natural Industrial, and Military Sources. 4th edn. Academic Press Elsevier, San Diego.

Espana, S.J., Pamo, E.L., Santofimia, E., Aduvire, O., Reyes, J., and Barettino, D. 2005. Acid mine drainage in the Iberian Pyrite Belt (Odiel River Watershed, Huelva, SW Spain): geochemistry, mineralogy and environmental implications. *Applied Geochemistry*, vol. 20. pp. 1320–1356.

Feather, C.E., and Koen, G.M. 1975. The mineralogy of the Witwatersrand reefs. *Mineral Science and Engineering*, vol. 7, pp. 89–224.

Federation for a Sustainable Environment. 2010. Annual report on the past year's activities. Rivonia, Johannesburg. 51 pp.

Fishbein, L. 1984. Overview of analysis of carcinogenic and/or mutagenic metals in biological and environmental samples – arsenic, beryllium, cadmium, chromium and selenium. *International Journal of Environmental Analytical Chemistry*, vol. 17. pp. 113–170.

Frimmel, H.E. and Minter W.E.L. 2002. Recent developments concerning the geological history and genesis of the Witwatersrand gold deposits, South Africa. *Integrated Methods for Discovery: Global Exploration in the Twenty-First Century*. Goldfarb, R.J. and Nielsen, R.L. (eds). *Special Publication*, vol. 9. Society of Economic Geologists. pp. 17–45.

Fubini, B. and Fenoglio, I. 2007. Toxic potential of mineral dusts. *Elements*, vol. 3. pp. 407–414.

Fubini, B. and Otero Areàn, C. 1999. Chemical aspects of the toxicity of inhaled mineral dust. *Chemical Society Reviews*, vol.28. pp. 373–381.

Genkin, A.D., Bortnikov, N.S., Cabri, L.J., Wagner, F.E., Stanley, C.J., Safonov, Y.G., Mcmahon, G., Freidl, J., Kerzin, A.L., and Gamyanin, G.N. 1998. A multidisciplinary study of invisible gold in arsenopyrite from four deposits in Siberia, Russian Federation. *Economic Geology*, vol. 93. pp. 463–487.

Ghio A. J. and Devlin, R.B. 2001. Inflammatory lung injury after bronchial instillation of air pollution particles. *American Journal of Respiratory and Critical Care Medicine*, vol. 164. pp. 704–708.

Griffin, D., Kellogg, C. and Shinn, E. 2001. Dust in the wind: long-range transport of dust in the atmosphere and its implications for global public and ecosystem health. *Global Change and Human Health*, vol. 2. pp. 20–33.

Harrison, R.M. and Yin, J. 2000. Particle matter in the atmosphere: which particle properties are important for its effects on health? *Science of the Total Environment*, vol. 249. pp. 85–101.

Hoet, P.H.M., Brüske-Hohlfeld, I., and Salata, O.V. 2004. Nanoparticles – known and unknown health risks. *Journal of Nanobiotechnology*, vol. 2, no. 12. 15 pp. DOI:10.1186/1477-3155-2-12

Hnizdo, E. 1995. Risk of silicosis in relation to fraction of respirable quartz. *American Journal of Industrial Medicine*, vol. 27. pp. 619–622.

Hnizdo, E. 1994. Risk of silicosis: Comparison of South African and Canadian miners. *American Journal of Industrial Medicine*, vol. 25. pp. 771–772.

Hnizdo, E., Sluis-Cremer, G., and Thomas, G.K. 1993. Correlation between radiological and pathological diagnosis of silicosis: An autopsy population based study. *American Journal of Industrial Medicine*, vol. 24. pp. 427–445.

Hu, X., Zhang, Y., Luo, J.U., Wang, T., Lian, H., and Ding, Z. 2011. Bioaccessibility and health risk of arsenic, mercury and other metals in urban street dusts from a mega-city, Nanjing, China. *Environmental Pollution*, vol. 159. pp. 1215–1221.

Hu, X., Zhang, Y., Ding, Z., Wang, T., Lian, H., Sun, Y. and Wu, J. 2012. Bioaccessibility and health risk of arsenic and heavy metals (Cd, Co, Cr, Cu, Ni, Pb, Zn and Mn) in TSP and PM2.5 in Nanjing, China. *Atmospheric Environment*, vol. 57. pp. 146–152.

Integrated Risk Information System, 2005. Lead and compounds (inorganic) (CASRN 7439-92-1) | IRIS | USEPA. https://cfpub.epa.gov/ncea/iris/iris_documents/documents/subst/0277_summary.pdf [Accessed 10 August 2016].

Kurt-Karakus, P.B. 2012. Determination of heavy metals in indoor dust from Istanbul, Turkey: estimation of the health risk. *Environment International*, vol. 50. pp.47–55.

Kyle, J.H., Breuer, P.L., Bunney, K.G., Pleysier R., and May, P.M. 2011. Review of trace toxic elements (Pb, Cd, Hg, As, Sb, Bi, Se, Te) and their deportment in gold processing. Part 1: Mineralogy, aqueous chemistry and toxicity. *Hydrometallurgy*, vol. 107. pp. 91–100.

Oberdörster, G. 2005. Inhaled nano-sized particles: potential effects and mechanisms. *Proceedings of the First International Symposium on Occupational Health Implications of Nanomaterials*, Buxton, UK. Health and Safety Executive, Great Britain and the National Institute for Occupational Safety and Health, United States.

Öhlander, B., Müller, B., Axelsson, M., and Alakangas, L. 2007. An attempt to use LA-ICP-SMS to quantify enrichment of trace elements on pyrite surfaces in oxidizing mine tailings. *Journal of Geochemical Exploration*, vol. 92. pp. 1–12.

Ojelede M.E., Annegarn, H.J., and Kneen, M.A. 2012. Evaluation of aeolian emissions from gold mine tailings on the Witwatersrand. *Aeolian Research*, vol. 3. pp. 477–486.

Ojelede, M.E. 2012. Risk assessment of atmospheric emissions from gold mine tailings on the Witwatersrand. PhD thesis, University of Johannesburg, South Africa.

Park, R.J., Jacob, D.J., Field, B.D., Yantosca, R.M., and Chin, M. 2004. Natural and transboundary pollution influences on sulfate–nitrate–ammonium aerosols in the United States: implications for policy. *Journal of Geophysical Research*, vol. 109, D15204. DOI:10.1029/2003JD004473

Pope III, C.A. and Dockery, D. W. 2006. Health effects of fine particulate air pollution: lines that connect. J*ournal of Air and Waste Management Association*, vol. 56. pp. 709–742.

Robb, L.J. and Meyer, F.M. 1995. The Witwatersrand basin, South Africa, geological framework and mineralization processes. *Ore Geology Reviews*, vol. 10, no. 2. pp. 67–94.

Roychoudhury, A.N. and Starke, M.F. 2006. Partitioning and mobility of trace metals in the Blesbokspruit: Impact assessment of dewatering of mine waters in the East Rand, South Africa. *Applied Geochemistry*, vol. 21. pp. 1044–1063.

Rudnick, R.L. and Presper, T. 1990. Geochemistry of intermediate/- to high-pressure granulites. *Granulites and Crustal Evolution*. Vielzeuf, D. and Vidal, P. (eds). Kluwer, Dordrecht. pp. 523–550,

Schwartz, J. 1994. Particulate air pollution and respiratory disease. *Environmental Research*, vol. 62. pp. 7–13.

Schwartz, J. 1992. Particulate air pollution and daily mortality: a synthesis. *Public Health Reviews*, vol. 19. pp. 39–60.

Shaw, D.M., Dostal, J., and Keays, R.R. 1976. Additional estimates of continental surface Precambrian shield composition in Canada. *Geochimica et Cosmochimica Acta*, vol. 40. pp. 73–84.

Smith, A.H. and Steinmaus, C.M. 2009. Health effects of arsenic and chromium in drinking water: recent human findings. *Annual Review of Public Health*, vol. 30. pp. 107–120.

Soukup, J.M., Ghio, A.J., and Becker, S. 2000. Soluble components of Utah Valley particulate pollution alter alveolar macrophage function in vivo and in vitro. *Inhalation Toxicology*, vol. 12. pp. 401–414.

Taylor, S.R. and Mclennan, S. M. 1995. The geochemical evolution of the continental crust. *Reviews in Geophysics*, vol. 33. pp. 241–265.

Tutu, H., McCarthy, T.S., and Cukrowska, E. 2008. The chemical characteristics of acid mine drainage with particular reference to sources, distribution and remediation: The Witwatersrand Basin, South Africa as a case study. *Applied Geochemistry*, vol. 23. pp. 3666–3684.

Us Epa. 2012. Regional screening levels (RSL) tables (Last updated November 2012). United States Environmental Protection Agency, Washington DC http://www.epa.gov/PacificSouthwest/Superfund [Accessed 9 August 2016].

Us Epa. 2011a. Exposure factors handbook (final edition). United States Environmental Protection Agency, Washington, DC. EPA/600/R-09/052F. https://cfpub.epa.gov/ncea/risk/recordisplay.cfm?deid=236252 [Accessed 29 October 2016].

Us Epa. 2011b. Risk assessment guidance for superfund. Part A: Human health evaluation manual; Part F, Supplemental guidance for inhalation risk assessment, vol. I. United States Environmental Protection Agency, Washington, DC. https://www.epa.gov/risk/risk-assessment-guidance-superfund-rags-part-f [Accessed 9 August 2016].

Us Epa. 2005a. Guidelines for carcinogen risk assessment. Risk Assessment Forum, United States Environmental Protection Agency, Washington, DC. EPA/630/P-03/001F. https://www.epa.gov/risk/guidelines-carcinogen-risk-assessment [Accessed 10 August. 2016].

Us Epa. 2005b. Human health risk assessment protocol. Appendix C. Risk characterization equations. United States Environmental Protection Agency, Washington, DC. https://archive.epa.gov/epawaste/hazard/tsd/td/web/pdf/05hhrapapc.pdf [Accessed 10 August 2016].

Us Epa. 2005c. Human health risk assessment protocol hazardous waste combustion facilities. United States Environmental Protection Agency, Washington, DC. http:// https://nepis.epa.gov/Exe/ [Accessed 10 August 2016].

Us Epa. 2002. A review of the reference dose and reference concentration processes EPA/630/P-02/002F. United States Environmental Protection Agency, Washington, DC. https://www.epa.gov/sites/production/files/2014-12/documents/rfd-final.pdf [Accessed 10 August 2016].

Us Epa. 1991. Guidelines for developmental toxicity risk assessment. 56 FR 63798-63826. United States Environmental Protection Agency, Washington, DC. https://cfpub.epa.gov/ncea/risk/recordisplay.cfm?deid=23162 [Accessed 10 August 2016].

Us Epa. 1998. Toxicological review of hexavalent chromium. https://ofmpub.epa.gov/eims/eimscomm.getfile?p_download_id=498828 [Accessed 24 August 2016].

Us Epa. 1986. Guidelines for the health risk assessment of chemical mixtures. 51 Federal Register 34014. United States Environmental Protection Agency, Washington, DC. https://ofmpub.epa.gov/eims/eimscomm.getfile?p_download_id=4487 [Accessed 10 August 2016].

Valavanidis, A., Fiotakis, K., and Vlachogianni, T. 2008. Airborne particulate matter and human health: toxicological assessment and importance of size and composition of particles for oxidative damage and carcinogenic mechanisms. *Journal of Environmental Science and Health, Part C, Environmental Carcinogenesis and Ecotoxicology Reviews*, vol. 26, no. 4. pp. 339–362.

Walker, N. 2007. Research concept: Nano-scale gold. http//ntp.niehs.nih.gov/ntp/.../6_walker_Nanogold_for_BSC_120607.pdf [Accessed 23 June 2012].

Wang, Z.X., Chen, J.Q., Chai, L.Y., Yang, Z.H., Huang, S.H., and Zheng, Y. 2011. Environmental impact and site-specific human health risks of chromium in the vicinity of a ferro-alloy manufactory, China. *Journal of Hazardous Materials*, vol. 190. pp. 980–985.

Wedepohl, K.H. 1995. The composition of the continental crust. *Geochimica et Cosmochimica Acta*, vol. 59, no. 7. pp. 1217–1232.

Wilson, W.E. and Suh, H.H. 1997. Fine particles and coarse particles: concentration relationships relevant to epidemiologic studies. *Journal of Air and Waste Management Association*, vol. 47. pp. 1238–1249.

World Health Organization. 2006. Air quality guidelines for particulate matter, ozone, nitrogen dioxide and sulfur dioxide: Global update 2005. Summary of risk assessment. WHO/SDE/PHE/OEH/06.02. Geneva http://whqlibdoc.who.int/hq/2006/WHO_SDE_PHE_OEH_06.02_eng.pdf [Accessed 10 March 2013].

World Health Organization. 2003. Health aspects of air pollution with particulate matter, ozone and nitrogen dioxide. Report on a WHO working group, Bonn, EUR/03/5042688, Geneva. http://ec.europa.eu/environment/archives/cafe/activities/pdf/1st_report.pdf [Accessed 30 August 2012]. ◆

MINESAFE 2017

Striving for Zero Harm

Driving Excellence through Compliance

Emperors Palace, Hotel Casino Convention Resort, Johannesburg

Technical Conference and Industry day

30–31 August 2017—Conference
1 September 2017—Industry day

OBJECTIVES

The conference will focus on improving health, safety and the environmental impact in the mining and metallurgy industry and highlight actions to be taken. It will act as a platform for learning and allow people to share ideas on safety, health and the environment.

This conference aims to bring together management, DMR, Chamber of Mines, Unions and health and safety practitioners at all levels from the industry to share best practice and successful strategies for zero harm and a value-based approach to health and safety. It will address the main challenges in the mining industry such as logistics, energy and safety of employees, contractors and the communities.

SPONSORSHIP

Sponsorship opportunities are available. Companies wishing to sponsor or exhibit should contact the Conference Co-ordinator.

WHO SHOULD ATTEND

The conference should be of value to:

- Safety practitioners
- Mine management
- Mine health and safety officials
- Engineering managers
- Underground production supervisors
- Surface production supervisors
- Environmental scientists
- Minimizing of waste
- Operations manager
- Processing manager
- Contractors (mining)
- Including mining consultants, suppliers and manufacturers
- Education and training
- Energy solving projects
- Water solving projects
- Unions
- Academics and students
- DMR.

SAIMM
THE SOUTHERN AFRICAN INSTITUTE OF MINING AND METALLURGY

Association of Mine Managers of South Africa

MMMA

The S.A. Colliery Managers' Association

SUPPORTED BY:

Chamber of Mines of South Africa
Putting South Africa First

Mine Health & Safety Council
MHSC

mineral resources
Department: Mineral Resources
REPUBLIC OF SOUTH AFRICA

NUM
National Union of Mine Workers

Solidariteit
Solidarity

UASA
THE UNION

SPONSORS

ADVANCED COMMS
KUTTA

LANXESS
Energizing Chemistry
LANXESS Chrome Mining (Pty) Ltd.

SHAFT SINKERS

BOOYCO ELECTRONICS

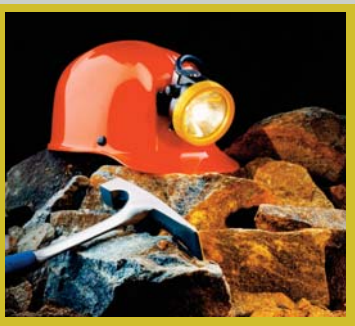

For further information contact:

Head of Conferencing
Camielah Jardine, SAIMM,
Tel: +27 11 834-1273/7
Fax: +27 11 833-8156 or +27 11 838-5923
E-mail: camielah@saimm.co.za
Website: http://www.saimm.co.za

Conference Announcement

http://dx.doi.org/10.17159/2411-9717/2017/v117n7a9

A analytical model for cover stress re-establishment in the goaf after longwall caving mining

by W. Wang*, T. Jiang*†, Z. Wang*, and M. Ren*

Synopsis

Cover stress re-establishment has a significant influence on the deformation and development of permeability in the fractured rock mass, which control the surface subsidence and water inflow after longwall caving mining. This paper reviews previous studies on cover stress re-establishment in the goaf after coal mining, and proposes a new analytical model based on the stress-strain characteristics of the caved rock mass and the voussoir beam theory. A scale model test is also conducted to study the cover stress re-establishment based on a coal mining case. A function was derived for cover stress re-establishment in the goaf, which can be approximately described as a logarithmic function and which agreed well with two completely re-established monitoring sites from the scale model test. The scale model test also indicated that cover stress re-establishment presents a hysteresis phenomenon. A 'stress balance' model was built for calculating the distance of cover stress re-establishment in the goaf, and the result from the model was lower than the results from the previous two methods. The cover stress re-establishment function and the 'stress balance' model will be of great significance for a better understanding of the stress distribution in the goaf.

Keywords
longwall mining, goaf, caving, fracturing, cover stress re-establishment, calculation model.

Introduction

The excavation of an underground coal seam by longwall caving or longwall top caving coal mining (LTCC) causes strata movement and fracture, and forms caving, fractured, and continuous deformation zones (Peng and Chiang,1984; Sui *et al.*, 2015). The voids and fractures in the caved and fractured rock mass provide seepage channels for water and coalbed gas. Cover stress re-establishment has a significant influence on the deformation and development of permeability in the fractured rock mass, which control the surface subsidence and minewater inflow after longwall caving mining. The groundwater level always subsides due to the fractures that develop after coal mining; however, stress re-establishment in the cover can reduce the size of the fractures, which reduces the flow rate and helps the groundwater level to recover (Zhang *et al.*, 2010; Wang *et al.*, 2016). The stress increment distribution on pillars, which is also affected by the destressed zone distribution in the goaf, is also the primary factor for coal pillar design. Thus, an understanding of the cover stress re-establishment characteristics in the goaf is required.

The original stress equilibrium conditions in the rock strata are disturbed after longwall caving mining (Figure 1). The load previously supported by the extracted material is transferred to the surrounding gates and pillars (abutments). This creates zones of increased stress on the surrounding coal and rock mass, and zones of decreased stress in the goaf, so that the stress balance is maintained (Yavuz, 2004). As the extracted distance and the subsidence of the upper fractured rock mass increase, the caved material in the goaf is re-loaded by the weight of the overburden and undergoes compaction, which causes the supported load in the caved roof rock strata to be re-established to almost the original cover stress within a certain mining distance (X_a, as shown in Figure 1).

Much research has been done in previous studies on the zone of increased stress. Seventy-five *in-situ* monitoring data points show that the load transfer distance generally increases with cover depth (Figure 2). There is no obvious relationship between excavation height and load transfer distance (Abel, 1988; Singh *et al.*, 2011; Zhang *et al.*, 2012; Ouyang *et al.*, 2009; Karacan and Goodman, 2009; Shen, King, and Guo, 2008). The maximum stress increases with decreasing mining thickness according to an elastic foundation approach (Majumder and Chakrabarty, 1991). The maximum stress decreases with increasing excavation thickness, and the distance of the maximum stress to the mining face increases, based on numerical simulation and analytical modelling (Xie, Yang, and Liu, 2006; Xie, Yang, and Chan, 2007). The stress concentration factors around a longwall panel change in different conditions, ranging from

* *North China University of Water Resources and Electric Powetr, Zhengzhou, China .*
† *Corresponding Author.*

 ISSN 2225-6253. Paper received Dec. 2015; revised paper received Mar. 2017.

An analytical model for cover stress re-establishment in the goaf

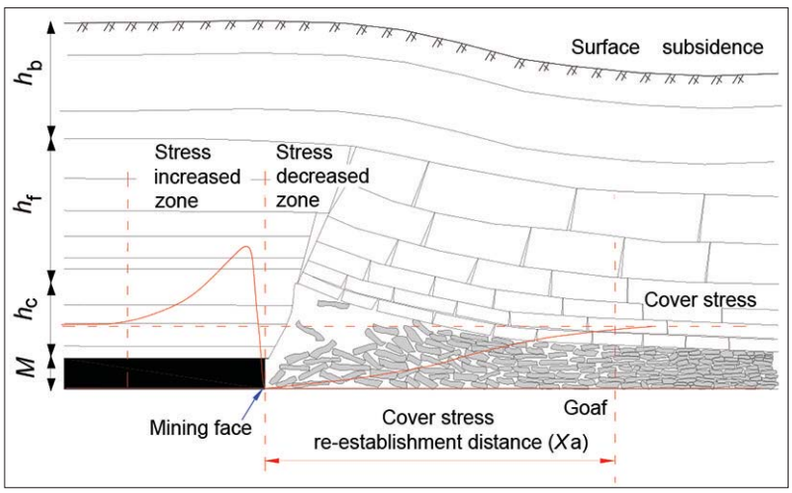

Figure 1—Disturbed zones and stress zone distributions around the mining face (adapted from Yavuz, 2004)

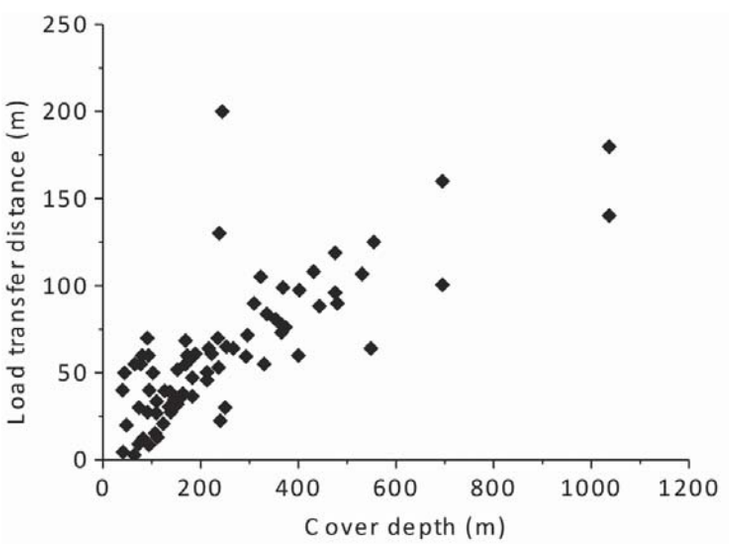

Figure 2—Load transfer distance versus depth (adapted from Abel, 1988; Singh, 2011; Zhang, 2012; Ouyang, 2009; Karacan, 2009; Shen, 2008)

1.08 to 6 (Sheorey, 1993; Xie *et al.*, 2011; Khanal, Adhikary, and Balusu, 2012). After considerable effort to determine the coal pillar strength, some important formulae for calculating the abutment stress distribution were proposed and are listed in Table I.

Little research has been done on the zone of decreased stress in the goaf due to the inaccessibility of the goaf and potential danger (Wilson 1983; Yavuz, 2004; Suchowerska, Merifield, and Carter, 2013). An estimation method based on the concept of a shear angle, which is the angle between the vertical line at the panel edge and the inclined line to the strata over the caved zone, proposed by King and Whittaker (1970) and modified by Choi and McCain (1980) was considered. The shear angle might be equal to the angle of draw used in subsidence analysis as accepted by King and Whittaker (1970), who also suggested the value of the angle as 31° for British conditions. Choi and McCain (1971) proposed that the shear angle was between the vertical line at the panel edge and the line connecting the panel edge to the starting point of the complete vertical displacement zone. A value of 18° was accepted by Choi and McCain (1971), while Mark (1990) modified this value to 21°. Wilson (1983) proposed that the roof sagging in the goaf behind the mining face usually fitted a logarithmic or exponential type of equation. Furthermore, the compaction of broken material in the caved waste also fitted a logarithmic-type equation. Through comprehensive analysis, Wilson proposed that the relationship between the cover stress re-establishment and the distance from the mining face fits a linear form. A value of 0.3H was adopted as the cover stress re-establishment distance, where H is the working depth. Based on the investigations, the stress-strain relationship of the broken material in the goaf was assumed to be the same as a very large stone-built pack, and the cover stress would be reached

Table I

Some important formulae for calculation the abutment stress

No.	Calculation formulae	Remark	References
(1)	$\begin{cases}\sigma_v(x')=\dfrac{3L_s}{(D_s-P)^3}(D_s-x')^2\\ D_s=P+9.3\sqrt{0.3048H}\end{cases}$		(Mark, 1990 and Peng and Chiang, 1984)
(2)	$\begin{cases}\sigma_v(x')=\dfrac{x'q}{\sqrt{x'^2-P^2}}\\ q=\gamma H\end{cases}$	For $x'>P$	(Salamon, 1963)
(3)	$\begin{cases}\sigma_v(x')=qP\sqrt{\dfrac{2E_c}{E_s\lambda M}}e^{-\sqrt{\frac{2E_c}{\psi E_s M}}(x'-P)}\\ \psi=\sqrt{\dfrac{t^2}{12(1-\nu^2)}}\end{cases}$	For $x'>P$	(Heasley, 1998)
(4)	$\begin{cases}\sigma_v(x)=\tau_0\cot\varphi\dfrac{1+\sin\varphi}{1-\sin\varphi}e^{\frac{2\zeta x}{M}(\frac{1-\sin\varphi}{1+\sin\varphi})} \quad (a)\\ \sigma_v(x)=K\gamma He^{\frac{2\zeta}{M\lambda}(x_0-x)} \quad (b)\end{cases}$ where, $\begin{cases}x_0=\chi\dfrac{M}{2\zeta}\dfrac{(1+\sin\varphi)}{(1-\sin\varphi)}\ln\left(\dfrac{K\gamma H}{\tau_0\cot\varphi}\dfrac{(1-\sin\varphi)}{(1+\sin\varphi)}\right)\\ x_1=\dfrac{M\lambda}{2\zeta}\ln K\end{cases}$	(a) For $x\leq x_0$, elastic zone (b) For $x_0<x<x_0+x_1$, plastic zone	(Chen et al., 1994)
(5)	$\begin{cases}\sigma_v(x)=\left[\dfrac{1}{\lambda}\cdot(P_x+\gamma_0 x_0\sin\alpha)+\dfrac{2c_0-M\gamma_0\sin\alpha}{2\tan\varphi_0}\right]\\ \cdot e^{\frac{M\lambda\gamma_0\cos\alpha-2\tan\varphi_0}{2\lambda}+\frac{2\tan\varphi_0}{M\lambda}x+(\frac{2\tan^2\varphi_0}{M\lambda}-\gamma_0\cos\alpha)\frac{M}{2}}\\ x_0=\dfrac{M\lambda}{2\tan\varphi_0}\ln\left[\dfrac{\lambda(K\gamma H\cos\alpha\tan\varphi_0+2c_0-M\gamma_0\sin\alpha)}{\lambda(2c_0-M\gamma\sin\alpha)+2P_x\tan\varphi_0}\right]\end{cases}$	For plastic zone	(Xie et al., 2006)

Notes: (1), (2), (3) are for stress distribution on pillars, (4) and (5) for stress distribution in front of the mining face.

x' is the distance from the centre of the panel
P is the half-width of the panel
L_S is the total side abutment load
D_S is the maximum horizontal extent of the abutment stress from the panel edge ($x'>L$ and $x'<D_S$)
$\sigma_V(x')$ is the vertical stress distribution on pillars
$\sigma_V(x)$ is the vertical stress distribution in front of mining face
q is the original *in-situ* stress
H is the depth of cover
γ is the unit weight of the overburden
E_C is the elastic modulus of the coal seam
E_S is the elastic modulus of the overburden
M is the extraction thickness
ψ is the lamination constant
t is the lamination thickness
ν is Poisson's ratio
ζ is the coefficient of friction between the layers
φ is angle of internal friction in the coalbed
$\tau_0\cot\varphi$ is the supporting force of the coalbed
K is stress concentration factor
x is the distance to the mining face
x_0 is the range of the plastic zone
x_1 is the range of the elastic zone
λ is the lateral pressure coefficient
P_X is the constraining force from the tunnel support to the coal bed in the x direction,
φ_0 is the friction angle in the interface between the coal bed and the floor
α is the dip angle of coal bed
C_0 is the cohesive force between the coal bed and the floor
γ_0 is the average volume force of the coal bed
χ is disturbance factor due to coal mining.

at a distance of 0.12*H* (Smart and Haley, 1987). These researchers mostly assumed that the stress in the goaf increased linearly. Wade and Conroy (1980) conducted *in-situ* measurements of cover stress re-establishment in the goaf and subsidence of the ground surface above the goaf. The results indicated that the surface subsidence shows a good corresponding relationship with cover stress re-establishment in the goaf. An estimation function for cover stress re-establishment with the independent variables of depth, excavation height, bulking factor, and compressive strength of the rock fragments was proposed by Yavuz (2004) based on previous field and laboratory investigations. Considering the broken materials in the goaf with a strain-hardening characteristic (Pappas and Mark, 1993), 'double-yield' elements were applied to numerical simulation to analyse the characteristics of the cover stress re-establishment and stress-strain in the goaf, and some effective results were obtained (Yavuz, 2004; Esterhuizen, Mark, and Murphy, 2010; Saeedi *et al.*, 2010; Shabanimashcool and Li, 2012).

According to the above summaries, two available analytical methods for estimation the re-establishment of cover stress in the goaf can be concluded, as follows.

Abutment angle model

In this concept, the abutment load is the weight of the wedge of the overburden material defined by the abutment angle β and a vertical line at the edge of the panel (see Figure 3). This weight, which should load on the goaf, is carried by the coal bed in front of the mining face, thus causing a zone of decreased stress in the goaf. This angle is almost equal to the angle of draw used in subsidence analysis, as shown in Figure 3.

The weight of the wedge of the overburden can be expressed as Equation [1].

$$L_S = H^2 \tan\beta\gamma / 2 \qquad [1]$$

The re-establishment of cover stress following a linear function is assumed in this model, so the cover stress re-establishment distance is presented by Equation [2]:

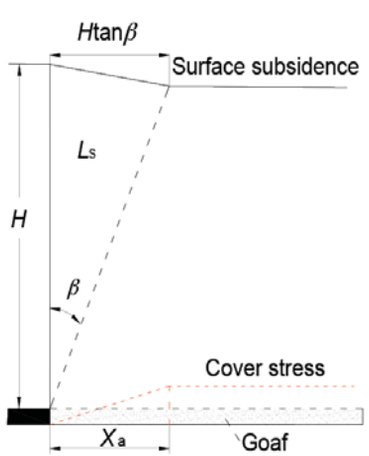

Figure 3—The conceptualization of a side abutment load angle (adapted from Mark, 1992)

$$X_a = \frac{2L_S}{\gamma H} = \frac{2H^2 \tan\beta\gamma}{2\gamma H} = H\tan\beta \qquad [2]$$

where L_S is the weight of the wedge of the overburden, β is the abutment angle, γ is the unit weight of the overburden, H is the depth of the coal bed, and X_a is the cover stress re-establishment distance.

Estimation method (Yavuz, 2004)

Yavuz (2004) discussed the stress-strain behaviour of the caved rock pile, bending of the lowest strata without caving depending on seam thickness, and residual expansion of fractured strata vertically over the caved zone from previous field and laboratory investigations, and established the relationships between these parameters and surface subsidence. Finally, Yavuz (2004) proposed two functions, one being a three-parameter power function for the distance of cover stress re-establishment, and the other an estimation with a six-parameter Taylor series polynomial function for the development of cover stress in sufficiently wide panels, as shown in Equation [3]:

$$\begin{cases} X_a = 0.2H^{0.96^{S_m/M}}, R^2 = 0.993 \\ \sigma_v(X) = \sigma_V \left[1.02 - 1.76\left[\frac{S_m}{M}\right] - 0.14\left[\frac{X}{X_a}\right] + 0.44\left[\frac{S_m}{M}\right]^2 \right. \\ \qquad \left. + 0.6\left[\frac{X}{X_a}\right]^2 + \left[\frac{S_m}{M}\right]\left[\frac{X}{X_a}\right]\right], R^2 = 0.98 \end{cases} \qquad [3]$$

where S_m is the surface subsidence above the cover stress re-establishment position in the goaf, M is the mining thickness, X_a is the distance of cover stress re-establishment, X is the distance to the mining face in the goaf, $\sigma_v(X)$ is the cover stress re-establishment at the distance of X, and σ_v is the cover stress when the original stress is totally re-established.

Much more work has been done on the stress increase zone than on the stress decrease zone (cover stress re-establishment). It is an appropriate method to study factors governing cover stress re-establishment based on the results of existing research on the stress increased zone, through establishing the relationship between them.

Methodology

In most cases, the distribution of cover stress re-establishment in the goaf is assumed to follow a linear function in order to simplify the calculation. The corresponding distance of cover stress re-establishment is generally described in terms of the cover depth of the coalbed modified with a coefficient (King and Whittaker, 1970; Choi and McCain, 1980; Wilson, 1983; Smart and Haley, 1987; Mark, 1990). However, due to the complex process of compression deformation of the caved materials in the goaf, it is proposed here that the cover stress re-establishment may follow a more complex rule than that of a linear function.

Theoretical analysis

The sagging function of the fractured rock mass

An analytical model for cover stress re-establishment in the goaf

The stress increment characteristics depend on the characteristics of the roof sagging and the stress-strain relationship of the broken material in the goaf. Wilson (1983) proposed that the roof sagging curve usually fits a logarithmic- or exponential-type equation according to the *in-situ* measurements. The curve can be described by Equation [4]:

$$X = \eta \ln \frac{w_0}{w_0 - w} \quad [4]$$

where X is the distance from the mining face, w is the amount of roof sagging, η is a constant required to give a close approximation to the measured values, and w_0 is the ultimate amount of roof sagging.

From Equation [4], the parameter w can be expressed as:

$$w = w_0\left(1 - e^{-\frac{X}{\eta}}\right) \quad [5]$$

The model of voussoir beam theory was proposed by Qian, Shi, and Xu (2003) based on a previous study and a large number of results from *in-situ* observations and laboratory experiments. This theory was widely used in China to interpret the deformation and stress distribution in the rock strata above the extracted coal bed. The voussoir beam structure is always formed in the key stratum, which controls the overall deformation of the overburden. Failure of the key stratum will cause failure of the superincumbent overburden and generate subsidence of the ground surface. The voussior beam structure is illustrated in Figure 4. The key stratum breaks at a periodic fracture length L, and several broken rock blocks comprise the voussior structure, which supports the load from the overburden temporarily. These broken rock blocks remain stable for a short time, due to the frictional force between them, which is caused by the horizontal compression force. As the mining distance increases, the broken block in the key stratum (block *C*) tends to be stable, with a new broken block being generated (block *O*), and block *C* is supported by the caved rock mass in the goaf. The development of fracture between rock blocks and the rotational deformations of rock blocks are shown in Figure 4. The distance of the stable process of the broken rock blocks in the key stratum is equal to the distance of cover stress re-establishment in the goaf.

Miao and Qian (1995) proposed that the sagging curve of the broken key stratum approximately fitted an exponential function based on this mechanical analysis model, as shown in Equations [6] to [8]:

$$W_X = W_0\left(1 - e^{-\frac{X}{2L}}\right) \quad [6]$$

$$W_0 = M - h_p\left(B_p - 1\right) \quad [7]$$

$$L = \frac{h}{1-\nu^2}\sqrt{\frac{2R_T}{q}} \quad \text{(Jiang, Dai, and Wang, 2014)} \quad [8]$$

where W_X is the sagging displacement at the distance X from the mining face, W_0 is the maximum sagging displacement when the voussoir beam tends to be stable, X is the distance from the mining face, L is the periodic fracture length, h and R_T are the thickness and tensile strength of the key stratum respectively, q is the total weight of the key stratum and superincumbent strata. B_p is the remnant bulking factor of the broken strata below the key stratum, h_p is the distance from the key stratum to the coalbed, and ν is the Poisson's ratio.

It is seen that Equations [5] and [6] are of the same form in describing the sagging curve of the roof above the caved zone. Here, Equation [6] is chosen as the function of the roof sagging form.

The stress-strain characteristics of the broken materials in the goaf

Pappas and Mark (1993) investigated strain hardening behaviour in the goaf as the material becomes stiffer and the elastic modulus increases under increasing compaction. With the increase in the size of fragments, the strain decreases under high-stress conditions. They also found that the stress-strain characteristics have little relation to the rock type.

According to the characteristics of the caved rocks, Salamon (1990) suggested the following equation for the backfill material to describe the stress-strain behaviour of goaf material:

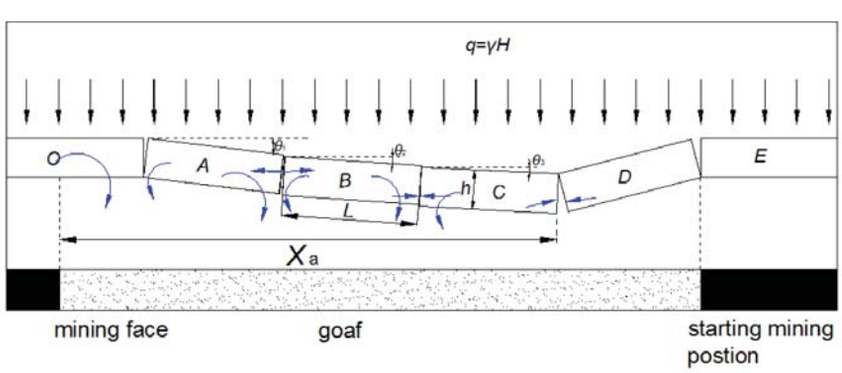

Figure 4—Analysis of the breakage deformation process under voussoir beam structure

$$\sigma = \frac{E_0 \varepsilon}{1 - \varepsilon / \varepsilon_m} \quad [9]$$

where

$$\varepsilon_m = \frac{B-1}{B} \quad [10]$$

$$B = \frac{h_c + M}{h_c} \quad [11]$$

According to Equations [9] to [11], B_p in Equation [7] can be calculated by:

$$B_p = B - \varepsilon(h_c + M) = B - \frac{\sigma \varepsilon_m}{\sigma + E_0 \varepsilon_m}(h_c + M) \quad [12]$$

Yavuz (2004) proposed the following formula for E_0:

$$E_0 = \frac{10.39 \sigma_c^{1.042}}{B^{7.7}} \quad [13]$$

where

- σ_c is the uniaxial compressive strength of the rock
- ε is the strain occurring under the applied stress
- E_0 is the initial tangent modulus σ is the applied stress
- ε_m is the maximum possible strain of bulked rock material
- h_c is the height of the caved zone
- m is the excavation thickness
- B is the bulking factor of the caved zone.

By substituting Equations [10], [11], and [13] into Equation [9], we obtain Equation [14]:

$$\sigma = \frac{10.39 \sigma_c^{1.042} \varepsilon}{B^{7.7}[1 - \varepsilon(h_c + M)/M]} \quad [14]$$

According to Equation [14], if the strain of caved rock in the cover stress re-establishment range was obtained, the stress change (cover stress re-establishment) can be calculated.

The sagging of the fractured rock mass will compress the caved rock mass, and the amount of sagging is equal to the vertical compression displacement of the caved rock mass.

The sagging amount of the fractured rock mass can be calculated using Equation [6], thus the corresponding strain can be calculated using Equation [15]:

$$\varepsilon = \frac{W_0\left(1 - e^{-\frac{X}{2L}}\right)}{h_c + M} \quad [15]$$

Scale model test

Scale model testing is one of the common methods used in investigations of cover stress re-establishment in the goaf. A scale model test was conducted based on the Taiping coal mine.

Background geology and mining environment of scale model test

The Taiping coal mine is located in the southwestern part of the Yanzhou Coalfield, Shangdong, China, in the margin of the Western Shandong Block of the North China Platform.

The thickness of the primary coal seam, No. 3, is approximately 8.85 m with the overburden bedrock consisting of clayey sandstone, siltstone, and fine- and medium-grained sandstones. The coal measure stratum dips at an angle of 5° to 15°. The strike directions of normal faults are usually in a north-south direction, while those of reverse faults are usually east-to-west. One of the geological dip sections is shown in Figure 5. The surface elevation is about 41.0 m; however, only the elevation from -40.0 m to -160.0 m is shown in this figure. Panel S03, with a width of 67.8 m and length of 428.7 m, belongs to the southern part of the 6th district in the Taiping coal mine. This area is located in the rising end of a syncline, as the coal measure stratum has a dip angle of 8° on average. A large area of the coal seam is directly covered by the Quaternary unconsolidated formations with a thickness from 133.0 m to 194.0 m and an average thickness of about 160.0 m. According to the exploration borehole results, the overburden bedrock thickness is from 20.0 to 32.6 m. The coal seam is designed to be excavated in four slices, each with a thickness of 2.2 m. When the top slice is excavated, the roof strata behind the longwall face are allowed to collapse, forming a water-flowing fractured zone

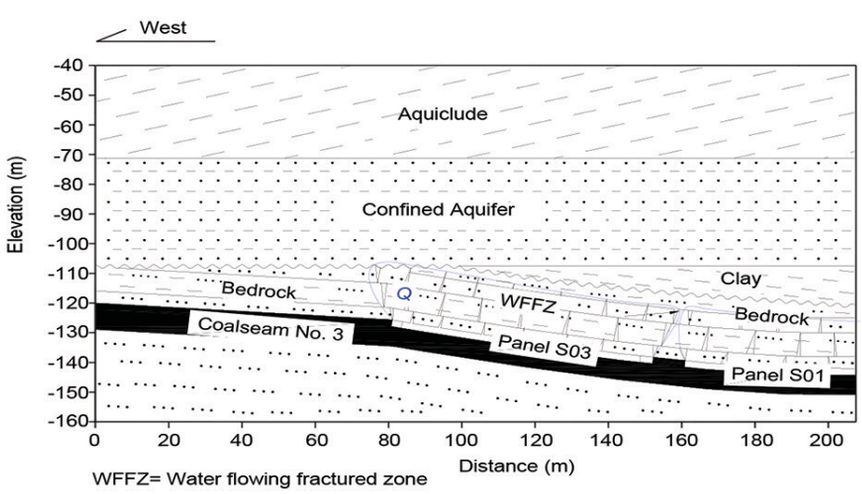

Figure 5—Geological dip section of panel 03

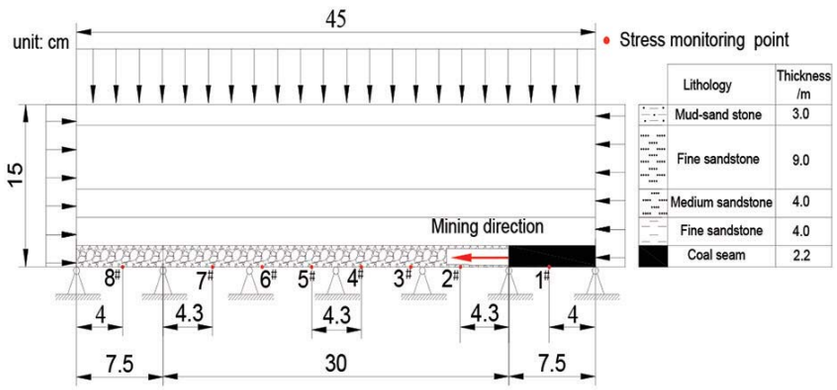

Figure 6—Schematic of scale mechanical model test (Wang *et al.*, 2016a)

Table II

Engineering geological types and mechanical properties of the coal measures

Engineering geological type	h (m)	σ_c (MPa)	τ (MPa)	E ($\times 10^3$MPa)	ν	c (MPa)	ϕ (°)
Mudstone	3.0	2.23	0.33	0.285	0.351	1.65	38
Fine sandstone	9.0	30.60	1.60	1.87	0.23	5.5	36
Medium sandstone	4.0	22.40	1.46	2.15	0.208	4.76	37.8
Fine sandstone	4.0	10.80	0.54	1.15	0.288	2.34	38
Coal seam no.3	8.8	8.45	0.51	1.31	0.293	2.0	36
Fine sandstone	>10.0	29.90	1.49	4.01	0.261	7.45	33.5

Note: h = thickness; σ_c = uniaxial compressive strength; τ = tensile strength; E = Young's modulus; ν = Poisson's ratio; c = cohesion; ϕ = angle of internal friction

(WFFZ) with a maximum height of 20.8 m, as shown in Figure 5. The lower three slices are excavated using backfilling methods. The cover stress re-establishment rule in the goaf when the top slice is excavated was studied by a scale model test.

Model building and stress monitoring

The dimensions of the scale model test rig are 45 × 15 × 10 cm (length × height × thickness). The model parameter scales are as follows:

- 1:200 for geometry (was set based on scale model frame size)
- 1:1.8 for gravity (according to the density ratio of the similar material to the real rock)
- 1:360 for uniaxial compressive strength (UCS) (calculated based on the similarity ratios of geometry and gravity).

Materials used for modelling comprised a combination of quartz powder (particle size < 0.075 mm) and gypsum. Mica powder was well distributed between the rock layers to simulate bedding. This model included only the bedrock parts and 2.2 m coalbed, and the weight of upper unconsolidated formations was compensated for by a uniformly distributed load from above. Corresponding compensatory horizontal stresses calculated according to lateral pressure coefficient were applied on both sides of this model. The schematic mechanical scale model is shown in Figure 6, indicating the mining direction, the starting cut, and the positions of stress monitoring. The stratigraphic column of the proximate geology is also shown in Figure 6, and the mechanical properties of the coal measures and bedrock strata are listed in Table II. Some model test equipment, distribution of the film stress sensors, and the installation process of the scale model are shown in Figure 7. The toughened glasses were installed in the front and back sides for monitoring fracture evolution during the mining process. Airbags were installed above and on both sides for adding compensative load. On both sides of this model, 7.5 cm pillars were set. The coal bed was excavated at a distance of 7.5 cm from the right-hand side in the model in steps of 1 cm, and the time interval between succeeding steps was 20 minutes. The stress changes at the bottom of the coal-bed were monitored using eight film stress sensors, the positions of which can be seen in Figure 6 and Figure 7b.

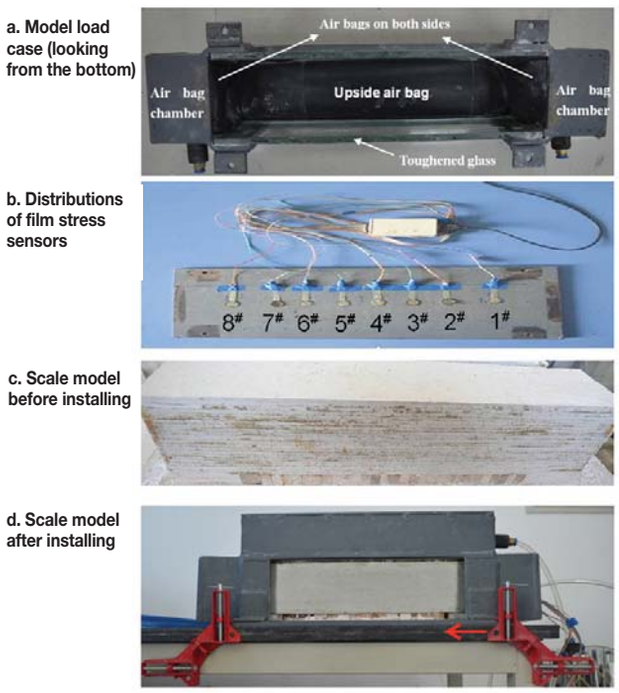

Figure 7—Installation process for scale model

Results and analysis

Cover stress re-establishment function in the goaf

By substituting Equation [15] into Equation [14], the cover stress re-establishment function $g(x)$ can be expressed as:

$$g(x)=\sigma=\frac{W_0\left(1-e^{-\frac{X}{2L}}\right)\cdot 10.39\sigma_c^{1.042}}{B^{7.7}\left[1-\frac{W_0\left(1-e^{-\frac{X}{2L}}\right)}{M}\right](h_c+M)} \quad [16]$$

In order to better understand the shape of the cover stress re-establishment curve, the parameters from the Taiping coal mine, which are listed in Table III, were substituted into Equation [16].

Figure 8 is the cover stress re-establishment curve as the distance from the mining face increases in the goaf. The cover stress re-establishment rate decreases as the distance from the mining face increases. A logarithmic function was used to fit the curve to simplify the expression, and is well

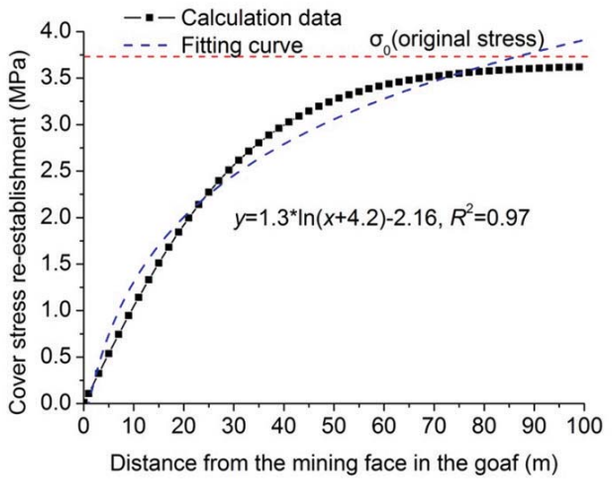

Figure 8—Cover stress re-establishment with increasing distance from the mining face

matched with R^2 = 0.97 at a distance of 100.0 m. It can be seen that the fitting curve fits well in the early stage of cover stress reestablishment, however, the fitting curve presenting a discrete phenomenon in the later stage because the cover stress keeps stable in this stage. A logarithmic function with a form like $y = a^*\ln(x+b)-c$ can be used to describe most of the cover stress re-establishment process generally.

Stress monitoring results from scale model test

In order to simulate a complete stress re-establishment process, the left 7.5 cm pillar was excavated at the end. The stress monitoring (Figure 9) indicate that excavation of the coal bed caused the stress in front of the mining face and in the back pillar to increase. The nearer the monitoring site to the mining face, the greater the stress increase. However, the stress under the excavated coal bed decreased to nearly zero immediately, until the key stratum failed and compressed the broken materials, upon which the stress began to increase generally. This indicates that the cover stress re-establishment presents a hysteresis phenomenon due to the periodic fracture of the key stratum. The maximum stress in front of the mining face increases with mining distance before the key stratum generates the initial breakage. When the key stratum generates the periodic breakage, the maximum stress in front of mining face is a little lower than the maximum stress at the initial breakage, as shown in Figure 10. It is also seen that the mining influence distance is

Table III

Parameters for cover stress re-establishment calculation

M (m)	R_T (MPa)	h (m)	σ_c (MPa)	h_c (m)	B	ν	q (MPa)	W_0 (m)	L (m)
2.2	1.6	9	11.3	7.3	1.3	0.23	3.72	1.05	8.8

Note: W_0 and L are calculated using Equations [7] and [8] respectively, with other parameters in Table I, and σ_c is an average value.

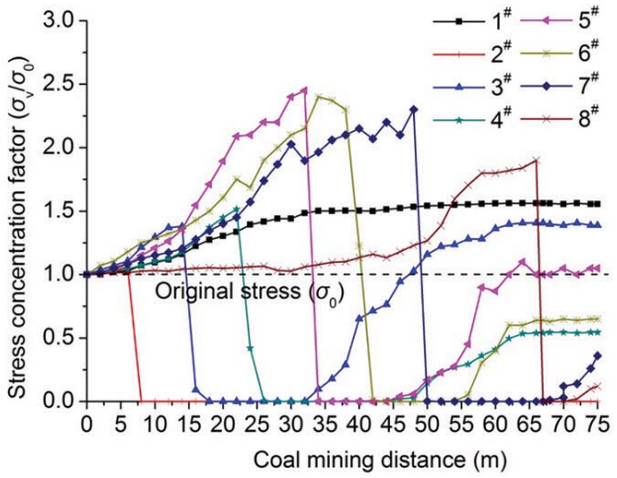

Figure 9—Vertical stress changes at the bottom of coal bed with increasing mining distance (Wang *et al*, 2016a)

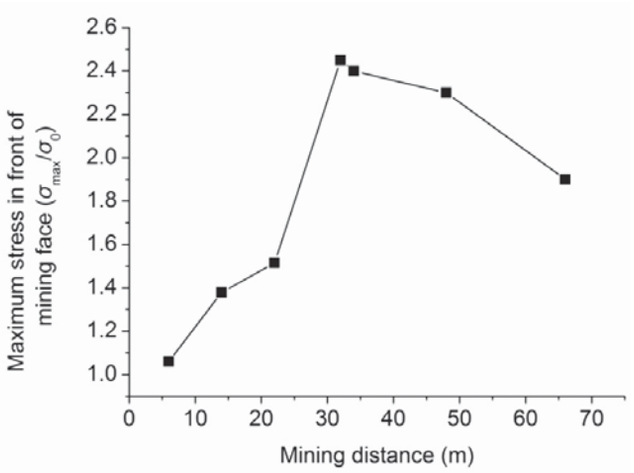

Figure 10—Variation in maximum stress in front of mining face with mining distance

about 35 m (from stress monitoring points 1 and 8), the initial and periodic roof weighting lengths are about 30 m and 12 m respectively, and the cover stress re-establishment distance is about 40 m (including the periodic roof weighting length).

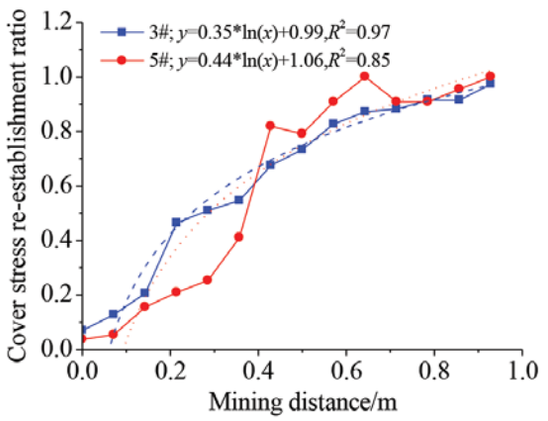

Figure 11—Relationship between cover stress re-establishment and mining distance

From the results of the scale model test in Figure 9, it can be seen that the extent of cover stress re-establishment differs greatly between different monitoring sites. The cover stress re-establishes in most of the stress monitoring sites, except at site 2. In some positions, the re-established cover stress is greater than the original stress; however, at some monitoring sites the re-established stress is lower than the original stress, or there may even be no re-establishment. However, on the whole, the cover stresses generally re-establish to the original stress. The size of the film stress sensors and the small inner structures of the broken rock mass in the goaf are the main reasons for this phenomenon. Some film stress sensors do not load the weight of the overburden, or do so only partly, although some sensors load a greater weight. Despite the differences in the weight of the overburden registered by the film stress sensors, the cover stress re-establishment processes are nearly the same. In this investigation, we assumed that the stress re-establishment processes at monitoring points 3 and 5, which are comparatively complete, could represent the cover stress re-establishment rule in the goaf after mining. In order to analyse the cover stress re-establishment rule, the relationships between the normalization results of cover stress and mining distance at these stress monitoring points are shown in Figure 11. A logarithmic function is used to fit these curves, which matched well with the R^2 values of 0.97

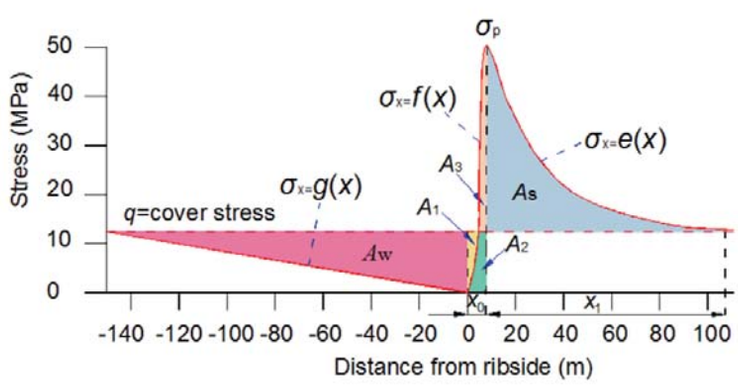

Figure 12—Stress distribution around the coal mining face (adapted from Wilson, 1983)

and 0.85 respectively. These results show that the cover stress re-establishment in the goaf can be expressed using a logarithmic function with the form of $y = a^*\ln(x)-c$. These two results coincide well with theoretical results presented previously.

Calculation of the distance of cover stress re-establishment based on the 'stress balance' model

'Stress balance' model

A hypothesis on the vertical stress distribution after a longwall panel mined was first proposed by Whittaker and Potts (1974), who presented the redistribution of stress in the form of 'high' and 'low' pressure zones. Wilson (1983) proposed that since the total downward force remains that of the cover load, any increase in stress over the rib-side must be compensated for by an equivalent stress reduction over the waste, and *vice versa*. Knowledge of one enables an estimate of the other, hence the term 'stress balance' for this approach, as shown in Figure 12. Compoli *et al.* (1993) conducted *in-situ* monitoring of stress changes in a coal-bed pillar and floor rock using a stainless steel borehole platened flat jack (BPF). They found that the measured stress was almost exactly equal to the original equilibrium pressure distribution as a result of the load being applied symmetrically in three dimensions, which confirmed the reliability of the 'stress balance' method.

According to the 'stress balance' and referring to Figure 12:

$$A_w+A_1=A_3+A_s \quad [17]$$

By adding A_2 to both sides of Equation [17]:

$$A_w+(A_1+A_2)=(A_2+A_3)+A_s \quad [18]$$

Therefore

$$A_w+qx_b=A_b+A_s \quad [19]$$

$$\int_0^{x_s} g(x)\mathrm{d}x+qx_0=\int_0^{x_0} f(x)\mathrm{d}x+\left(\int_{x_0}^{x_b} e(x)\mathrm{d}x-qx_1\right) \quad [20]$$

where x_0 is the width of yield zone, x_1 is the width of elastic zone, $X_b = x_0+x_1$; $g(x)$ is the function of cover stress re-establishment, $f(x)$ is the function of stress distribution in the yield zone, $e(x)$ is the function of stress distribution in the elastic zone, σ_p is the peak stress, A_1, A_2, A_3, A_W, A_S are stress increased or decreased areas in different parts of the stress distribution, and $A_b= A_2+A_3$.

From Equation [20], if any side of the stress distribution function is known, the other side can be estimated.

The existing data on the zone of increased stress in front of the mining face is more abundant than that on the stress-decreased zone in the goaf, whether acquired by *in-situ* measurements or by analytical modelling. Figure 2 shows that there are abundant results from *in-situ* monitoring of the stress influence distance in front of the mining face, which increases with increasing mining depth. Thus, based on the *in-situ* measurements of stress distribution in front of the mining face, the distance of cover stress re-establishment in the goaf can be calculated from Equation [20].

Cover stress re-establishment distance

The functions describing stress distribution in front of the mining face are necessary for using the 'stress balance' model to calculate the cover stress re-establishment distance. The formulae from Xie, Yang, and Liu (2006) for the plastic zone and from Chen and Qian (1994) for the elastic zone, listed in Table I are substituted into Equation [20]:

$$\begin{cases} f(x)=\left[\frac{1}{\lambda}\cdot(P_x+\gamma_0 x_0\sin\alpha)+\frac{2c_0-M\gamma_0\sin\alpha}{2\tan\varphi_0}\right]\cdot e^{\frac{M\lambda\gamma_0\cos\alpha-2\tan\varphi_0}{2\lambda}x+(\frac{2\tan^2\varphi_0}{M\lambda}-\gamma_0\cos\alpha)\frac{M}{2}} \\ e(x)=K\gamma H e^{\frac{2\xi}{M\lambda}(x_0-x)} \end{cases} \quad [21]$$

We applied this model to the Taiping coal mine to calculate the distance of cover stress re-establishment in panel S03. Some parameters for this calculation are listed in Table IV, and x_0 can be calculated using Equation[22]. (x_1+x_0) is always obtained from *in-situ* monitoring results.

$$x_0=\chi\frac{M\lambda}{2\tan\varphi_0}\ln\left[\frac{\lambda(K\gamma H\cos\alpha\tan\varphi_0+2c_0-M\gamma_0\sin\alpha)}{\lambda(2c_0-M\gamma\sin\alpha)+2P_x\tan\varphi_0}\right] \quad [22]$$

The value of x is equal to the stress concentration factor K.

The maximum stress in front of the mining face can be calculated by Equation [23] (Xie, Yang, and Liu 2006)

$$\sigma_{max}=2.729(\varpi\sigma_c)^{0.729} \quad [23]$$

The maximum stress concentration factor K can be calculated using Equation [24]:

$$K=\frac{\sigma_{max}}{\sigma_0} \quad [24]$$

where ϖ is the rheological coefficient of the coal bed, σ_c is the uniaxial compressive strength of the coalbed, and σ_0 is the original stress.

Taking the parameters in Table IV into Equations [23] and [24], we obtain:

$$\sigma_{max}=7.8\ \text{MPa},\ K=2.1\ \text{and}\ x_0=1.1\ \text{m}.$$

The deformation of the tunnels on both sides of the panel

Table IV

Parameters for calculation of the stress distribution

M (m)	λ	α (°)	φ (°)	ζ	c_0 (MPa)	γH (MPa)	P_x	γ_0 (MPa)	ϖ	σ_c (MPa)
2.2	0.45	8	32	0.01	2	3.72	0	0.014	0.5	8.45

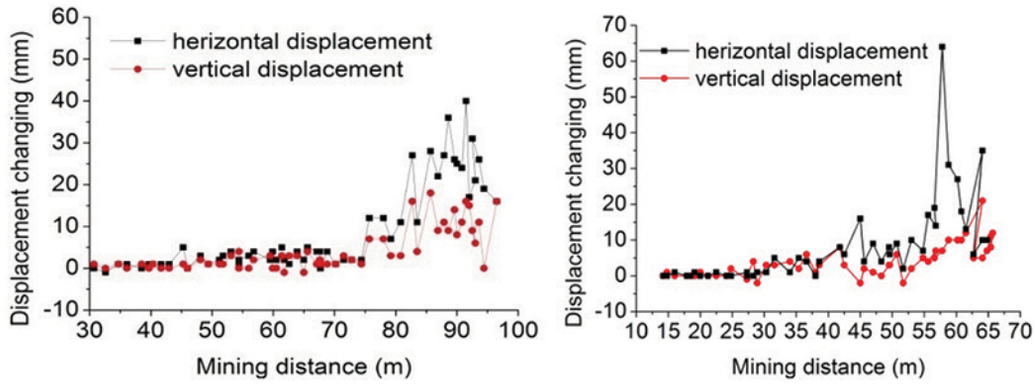

Figure 13—Deformation of the tunnels with mining face advancing

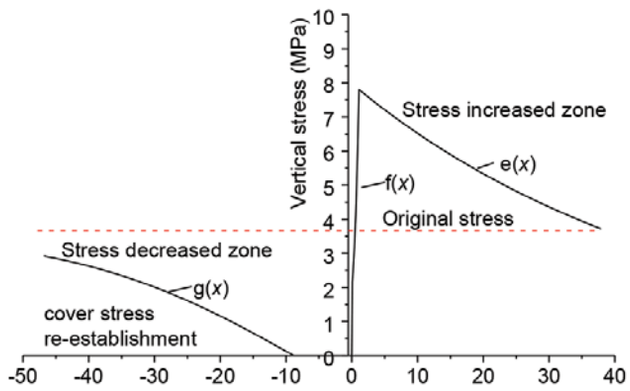

Figure 14—Stress distribution around mining face

can be monitored by displacement sensors. The deformation increases with increasing stress, thus the deformation monitoring results can also be used to determine the zone of increased stress in front of the mining face. When the coal bed was excavated in panel S03, the deformation of the surrounding rock was monitored at two sites (67 m and 95 m from the starting position) in the tunnels in front of the mining face. The results indicate that the tunnel displacements are close to zero when the mining face is far from the monitored sites; however, when the mining face advances to about 35 m from the monitoring sites, the displacement begins to increase markedly, as shown in Figure 13. The values in the vertical coordinate represent the relative displacement: positive numbers represent an increase and negative numbers a decrease. These results indicate that the stress increase influence range is about 35 m in front of mining face, thus, $x_0+x_1 = 35$ m.

From x_0, x_0+x_1, and the parameters listed in Tables II and IV, by substituting Equation [16] and Equation [21] into Equation [20], the cover stress re-establishment distance was calculated as 39 m. According to the hysteresis phenomenon of the cover stress re-establishment in the goaf, a periodic fracture length (L = 8.8 m) should be added for the whole distance of cover stress re-establishment, thus the total cover stress re-establishment distance should be 47.8 m. The stress distribution around the mining face in panel S03, based on 'stress balance' model, is shown in Figure 14.

Discussion

The scale model test results show that the maximum height of the water flowing fractured zone is 19.0 m, and the initial and periodic roof weighting lengths are about 30.0 m and 12.0 m respectively. These results are similar to the *in-situ* monitoring values of 20.8 m, 28.0 m, and 10.8 m respectively. This indicates that this scale model test results are valid.

Cover stress re-establishment can also be calculated using the 'abutment angle' model and estimation method from Yavuz (2004). During the excavation of panel S03 at the Taiping coal mine, the surface subsidence was monitored along the vertical in the middle of the panel. As shown in Figure 15, the maximum surface subsidence ratio of 0.73 corresponds to the coal mining thickness of 2.2 m. Using the data shown in Figure 15, we calculated that the shear angle was 14.5°. The coal seam cover depth was 180 m, and the cover stress re-establishment distance was estimated to be 46.5 m using Equation [2] based on the 'abutment angle' model.

According to the estimation method from Yavuz (2004), the cover stress re-establishment distance was calculated to be 50.4 m using Equation [3]. However, the stress re-establishment function is applicable for X/X_a ratios between 0.2 and 0.8, since the data points between these ratios were used for the regression analysis. For X/X_a ratios of 0 and 1, σ_x/σ_v ratios should be assigned as 0 and 1 respectively.

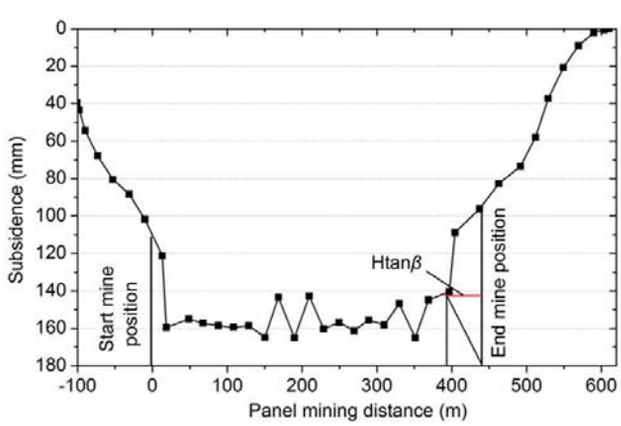

Figure 15—Surface subsidence monitoring curve above panel S03 of the Taiping coal mine

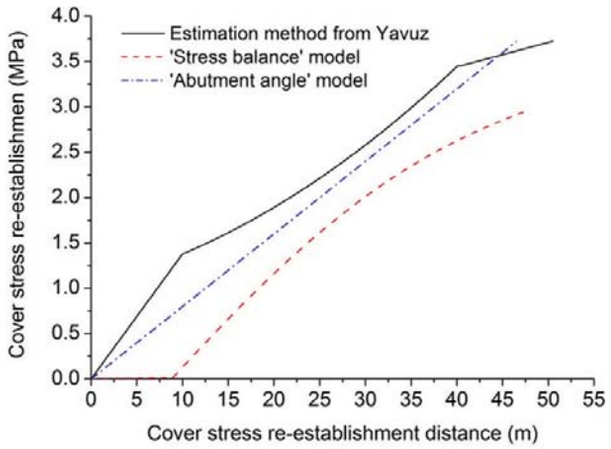

Figure 16—Cover stress re-establishment using different methods

Combined with the 'stress balance' model, the results from the other two methods for calculating the cover stress re-establishment in the goaf are shown in Figure 16, from which it can be seen that the cover stress re-establishment distance calculated from the 'stress balance' model is similar to that obtained by the other two methods. However, the cover stress is assumed to re-establish from the mining face with consideration of the hysteresis phenomenon. The value of cover stress re-establishment at different distances, as calculated from 'stress balance' model, is lower than the results from the other two methods, which consider the hysteresis phenomenon. According to the stress balance conditions, the cover stress re-establishment results calculated from the 'abutment angle' model and estimation method from Yavuz (2004) are too large. The cover stress re-establishment generally decreases with increasing distance in the 'stress balance' model. The cover stresses obtained by the 'abutment angle' model and the estimation method from Yavuz (2004) are both assumed to re-establish to the original stress level. However, it is noted that the cover stress is re-established to only 80% of the original stress based on the 'stress balance' model in this case. The main reasons for this are the stress-strain relationship of the caved materials in the goaf applied in Equation [14] and the stress distribution in front of the mining face. Actually, the increasing stress in the initial stage plays the primary role in control of deformation and permeability of the fractured rock mass, so the cover stress re-establishment calculated from the 'stress balance' model will be of great significance.

Conclusions

Previous studies of cover stress re-establishment in the goaf after underground coal mining suffer from weakness in that cover stress re-establishment calculation methods are generally simplified as linear functions. The voussoir beam theory, 'stress balance' model, and a scale model test were applied in this study of the cover stress re-establishment rule. The main results are as follows:

- The cover stress re-establishment rule in the goaf was derived as Equation [16], which can be approximatively described as a logarithmic function with a form like $y = a^*\ln(x+b)-c$
- The scale model test results indicate that cover stress re-establishment in the goaf presents a hysteresis phenomenon due to periodic fracture of the key stratum. The monitoring results of cover stress re-establishment from the scale model test agree well with the analytical result
- The cover stress re-establishment distance was calculated using the 'stress balance' model. This method was applied to the Taiping coal mine together with the other two previous methods, and a similar result was obtained by adding the hysteresis length (periodic fracture length). This method provides a new analytical technique for calculating the cover stress re-establishment distance.

Acknowledgements

The National Natural Science Foundation of China under Grant No. 41602298, and the Henan Institution of higher Education Key Scientific Research project (16A410004) are acknowledged. The authors also sincerely thank Gregory Weissmann at the University of the Pacific for his editorial help.

References

Abel, J.F. 1988. Soft rock pillars. *Geotechnical and Geological Engineering*, vol. 6, no. 3. pp. 215–248.

Chen, Y. and Qian, M. 1994. China's Coal Mining Strata Control. Coal Industry Press, Beijing (in Chinese).

Choi, D.S. and McCain, D.L. 1980. Design of longwall systems. *Transactions of the Society of Mining Engineers of AIME*, vol. 268. pp. 1761–1764.

Compoli, A.A., Barton, T.M., Vandyke, F.C., and Gauna, M. 1993. Gob and gate road reaction to longwall mining in bump-prone strata. US Department of the Interior, Bureau of Mines.

Esterhuizen E., Mark, C., and Murphy, M.M. 2010. Numerical model calibration for simulating coal pillars, gob and overburden response. *Proceedings of the 29th International Conference on Ground Control in Mining*, Morgantown, WV. pp. 46–57.

Heasley, K.A. 1998. Numerical modeling of coal mines with a laminated displacement-discontinuity code. PhD thesis, Department. of Mining Engineering, Colorado School of Mines.

Jiang, J.Q., Dai J., and Wang, P. 2014. Overlying hard and thick strata breaking movement and broken-roof control. *Rock and Soil Mechanics*, vol. 35, supp.1. pp. 264–270 (in Chinese).

Karacan, C.Ö. and Goodman, G. 2009. Hydraulic conductivity changes and influencing factors in longwall overburden determined by slug tests in gob gas ventholes. *International Journal of Rock Mechanics and Mining Sciences*, vol. 46, no. 7. pp. 1162–1174.

Khanal, M., Adhikary, D., and Balusu, R. 2012. Numerical analysis and geotechnical assessment of mine scale model. *International Journal of Mining Science and Technology*, vol. 22, no. 5. pp. 693–698.

King, H.J. and Whittaker, B.N. 1970. A review of current knowledge on roadway behaviour, especially the problems on which further information is required. *Proceedings of the Symposium on Strata Control in Roadways*, Nottingham, UK. Institution of Mining Engineers, London. pp. 73–90.

Majumder, S. and Chakrabarty, S. 1991. The vertical stress distribution in a coal side of a roadway-an elastic foundation approach. *Mining Science and Technology,* vol. 12, no. 3. pp. 233–240.

Mark, C. 1990. Pillar design methods for longwall mining. US Department of the Interior, Bureau of Mines.

Miao, X.X. and Qian, M.G. 1995. Solid structure and model of voussoir beam of face surrounding rock. *Ground Pressure and Strata Control*, vol. 3. pp. 3–12 (in Chinese).

Ouyang, Z., Li, C., Xu, W., and Li, H.J. 2009. Measurements of in situ stress and mining-induced stress in Beiminghe Iron Mine of China. *Journal of Central South University of Technology*, vol. 16. pp. 85–90.

Pappas, D.M. and Mark, C. 1993. Behavior of simulated longwall gob material. US Department of the Interior, Bureau of Mines.

Peng, S.S. and Chiang, H.S. 1984. Longwall Mining. Wiley, New York.

Qian, M.G., Shi, P.W., and Xu, J.L. 2003. Rock pressure and strata control. China University of Mining and Technology Press, Xuzhou (in Chinese).

Saeedi G., Shahriar, K., Rrezai, B., and Karpuz, C. 2010. Numerical modelling of out-of-seam dilution in longwall retreat mining. *International Journal of Rock Mechanics and Mining Sciences*, vol. 47, no. 4. pp. 533–543.

Salamon, M.D.G. 1963. Elastic analysis of displacements and stresses induced by the mining of seam or reef deposits Part 1: fundamental principles and basic solutions as derived from idealized models. *Journal of the South African Institute of Mining Metallurgy*, vol. 64. pp. 128–149.

Salamon, M.D.G.. 1990. Mechanism of caving in longwall coal mining. *Rock Mechanics Contribution and Challenges: Proceedings of the 31st US Symposium on Rock Mechanics*, Golden, CO. CRC Press, Boca Raton, FL. pp. 161–168.

Shabanimashcool, M. and Li, C.C. 2012. Numerical modelling of longwall mining and stability analysis of the gates in a coal mine. *International Journal of Rock Mechanics and Mining Sciences*, vol. 51. pp. 24–34.

Shen, B., King A., and Guo, H. 2008. Displacement, stress and seismicity in roadway roofs during mining-induced failure. *International Journal of Rock Mechanics and Mining Sciences*, vol. 45, no. 5. pp. 672–688.

Sheorey, P.R. 1993. Design of coal pillar arrays and chain pillars. *Comprehensive Rock Engineering*. Pergamon Press, Oxford, vol. 2. pp. 631–70.

Singh A.K., Singh, R., Maitj J, Kumar, R., and Mandal, P. K. 2011. Assessment of mining induced stress development over coal pillars during depillaring. *International Journal of Rock Mechanics and Mining Sciences*, vol. 48, no. 5. pp. 805–818.

Singh, R., Singh, T.N., and Dhar, B.B. 1996. Coal pillar loading in shallow mining conditions. *International Journal of Rock Mechanics and Mining Sciences & Geomechanics Abstracts*, vol. 33, no. 8. pp. 757–768.

Smart, B. and Haley, S.M. 1987. Further development of the roof strata tilt concept for pack design and the estimation of stress development in a caved waste. *Mining Science and Technology*, vol. 5, no. 2. pp. 121–130.

Suchowerska, A.M., Merifield, R.S., Carter, J.P., and Clausen, J. 2012. Prediction of underground cavity roof collapse using the Hoek–Brown failure criterion. *Computers and Geotechnics*, vol. 44. pp. 93–103

Suchowerska, A.M., Merifield, R.S., Carter, J.P. 2013.Vertical stress changes in multi-seam mining under supercritical longwall panels. *International Journal of Rock Mechanics and Mining Sciences*, vol. 61. pp. 306–320.

Sui, W.H., Hang Y., Ma, L.X., Zhou, Y. J., Long, G.Q., and Wei, L.B. 2015. Interactions of overburden failure zones due to multiple-seam mining using longwall caving. *Bulletin of Engineering Geology and the Environment*, vol. 74, no. 3. pp. 1019–1035.

Wang, W.X., Jiang T., Faybishenko, B., Wang, Z.F., Hu W., and Zhao, Q.J. 2016a. Closure of fracture due to cover stress re-establishment after coal mining. *Geotechnical and Geological Engineering,* vol. 34, no. 5. pp. 1525–1537.

Wang, W.X., Sui, W.H., Faybishenko, B., and William, T.S. 2016b. Permeability variations within mining-induced fractured rock mass and its influence on groundwater inrush. *Environmental Earth Sciences*, vol. 75, no. 4. pp. 1–15.

Whittaker, B.N. and Potts, E.L. 1974. Appraisal of strata control practice: Discussion on by B.N. Whittaker, and authors' reply. 22F, 19R. *Transactions of the Institution of Mining and Metallurgy*, vol. 83. pp. A95–A109. *International Journal of Rock Mechanics and Mining Sciences & Geomechanics Abstracts*, vol. 11, no. 11. p. A225.

Wilson, A.H. 1983. The stability of underground workings in the soft rocks of the coal measures. *International Journal of Mining Engineering*, vol. 1, no. 2. pp. 91–187.

Xie, G.X., Yang, K., and Liu Q.M. 2006. Study on distribution laws of stress in inclined coal pillar for fully-mechanized top-coal caving face. *Chinese Journal of Rock Mechanics and Engineering*, vol. 25, no. 3. pp. 545–549 (in Chinese).

Xie, G.X., Yang, K., and Chang, J. 2007. Study on distribution characteristics of 3D stress and thickness effects of coal-seam in unsymmetrical disposal and fully-mechanized top-coal caving. *Chinese Journal of Rock Mechanics and Engineering*, vol. 26, no. 4. pp. 775–779 (in Chinese).

Xie, X.Z., Fan, Z.Z., Huang, Z.Z., and Xu G. 2011. Research on unsymmetrical loading effect induced by the secondary mining in the coal pillar. *Procedia Engineering*, vol. 26. pp. 725–730.

Yavuz. H. 2004. An estimation method for cover pressure re-establishment distance and pressure distribution in the goaf of longwall coal mines. *International Journal of Rock Mechanics and Mining Sciences*, vol. 41, no. 2. pp. 193–205.

Zhang, D.S., Fan, G.W., Liu, Y.D., and Ma, L.Q. 2010. Field trials of aquifer protection in longwall mining of shallow coal seams in China. *International Journal of Rock Mechanics and Mining Sciences,* vol. 47, no. 6. pp. 908–914.

Zhang, R., Wang, Z., and Chen, J. 2012. Experimental research on the variational characteristics of vertical stress of soft coal seam in front of mining face. *Safety Science*, vol. 50, no. 4. pp. 723–727. ◆

SAIMM
THE SOUTHERN AFRICAN INSTITUTE OF MINING AND METALLURGY

4 August 2017—CULLINAN TECHNICAL TOUR
7–8 August 2017—CONFERENCE | 9 August 2017—TECHNICAL VISIT
EMPERORS PALACE, GAUTENG

RAPID UNDERGROUND MINE and CIVIL ACCESS CONFERENCE 2017

ANNOUNCEMENT

BACKGROUND

This conference is in response to the industry being under immense pressure to sink shafts and develop tunnels in safer and more efficient ways. The global call for no harm has been taken very seriously. The advance rates and daily production has come under immense pressure to improve and shorten the entire project period to make it financially viable. We can sink shafts and develop tunnels without hurting people, however to repeatedly achieve this while achieving the productivity targets has proven to be a challenge. We need to critically examine all aspects related to the sinking process. The way in which we conduct the entire project, right from mine concept study through to commissioning and handover all needs to be considered. Shaft sinking and tunnelling is not only about the sinking cycle. There are many diverse factors that influence the sinking process including: business drivers in the concept phase, mining methodologies and technology alternatives in the pre-feasibility stages, cost and timing parameters in the feasibility as well as partner selection, technical criteria and management systems during the execution phase. Mechanisation attempts to remove people from the hazards of sinking and to provide a continuous consistent advance rate has made great strides in the past five years.

OBJECTIVES

The objective of this conference is to demonstrate an understanding from mining companies, sinking contractors, EPCM organizations and investors on their perception of the current process. The idea is to look at current best practice, Research and Development that is in process and to raise suggestions on how to improve the process using experiences collectively gained worldwide. At the very least the conference must identify areas of action in order to plan for improvements going forward. Otherwise, deeper ore resources may remain beyond our reach for the foreseeable future (and mining of asteroids may become a reality).

WHO SHOULD ATTEND

The Conference will be of value to:

- All stakeholders involved in the shaft sinking arena for mine access and heavy underground civil projects
- Mine owners, executives and management
- Underground civil construction companies
- Engineering design and consulting companies
- Project management practitioners
- Mining entrepreneurs
- Hydropower experts and other underground civil experts
- Technology suppliers and consumers
- Health, safety and risk management, personnel and officials
- Governmental minerals and energy personnel
- Research and academic personnel
- Rock engineers
- All engineering disciplines
- Consultants
- Contractors
- Financiers

Supported by

South African National Committee on Tunnelling

Sponsored by

AVENG SHAFTS & UNDERGROUND
HERRENKNECHT Tunnelling Systems
MASTER DRILLING
Murray & Roberts
Murray & Roberts Cementation
PALMIERI GROUP
WorleyParsons resources & energy

FOR FURTHER INFORMATION CONTACT:
Head of Conferencing: Camielah Jardine **E-mail:** camielah@saimm.co.za **Tel:** +27 11 834 1273/7 **www.saimm.co.za**

http://dx.doi.org/10.17159/2411-9717/2017/v117n7a10

Application of fuzzy linear programming for short-term planning and quality control in mine complexes

by M. Rahmanpour and M. Osanloo

Synopsis

Production planning in a mine complex aims to determine the amount of material that should be mined from each site, and can be modelled as a linear programming problem. Deterministic production plans are optimized based on the estimated quantity and quality of the *in-situ* material. These estimations always have a level of uncertainty and impreciseness due to the insufficiency of exploration data in the planning phase. In this paper, based on the gathered data, the uncertainties of grades, recovery, and mining costs are modelled using bounded fuzzy numbers. Due to the quality variation of the material, mine planning and blending optimizations are in fact uncertainty-based optimization problems. Thus, a fuzzy linear programming model is formulated to optimize short-term production planning. The results provide a comprehensive set of solutions with a corresponding degree of membership. As an illustration, the model is applied to a limestone mine complex, and a conservative and an optimistic plan are provided.

Keywords

mine complex planning, fuzzy linear programming, blend optimization, short-term planning.

Introduction

A strategic mine plan sets the overall objectives of a mining project. Mine planning is a multidisciplinary process and its aim is to develop the life-of-mine extraction plan to meet some predefined goals (Dagdelen, 2007; Henderson and Turek, 2013). Mine plans are classified into long-, medium-, and short-term plans. Normally, these plans are organized such that the mining operations achieve the highest cash flow or net present value (Heureux, Gamache, and Soumis, 2013; Juarez *et al.*, 2014; King, 2014). These plans should consider capacities, blending requirements, block sequencing, reclamation requirements, pit slope, and any other constraints that may exist in each particular mine site (Caccetta and Hill, 2003).However, many problems in the field of mining engineering are characterized by insufficient and incomplete data. The stochastic and uncertain nature of geological, technological, market, political, and ecological factors are inherent in the context of mining engineering. For example, the dynamic change of ore and waste material due to the presence of spatial grade uncertainty makes predictions of the optimal mining sequence a challenging task (Godoy and Dimitrakopoulos, 2004; Azimi, Osanloo, and Esfahanipour, 2013; Rahmanpour and Osanloo, 2016a). These uncertainties highlight the importance of careful and risk-based mine planning through the development of new production planning models (Osanloo, Gholamnejad, and Karimi, 2008; Newman *et al.*, 2010).

Long-term plans outline the strategies to achieve a company's goals (the highest net present value, for instance). Short-term plans are aimed at following the strategies of the long-term plan, and the other objective of short-term plans is to minimize operating costs as much as possible. For this purpose, engineers try to find a reliable system with minimal cost (Levitin and Lisnianski, 2001; Rahmanpour and Osanloo, 2016b). Modern and successful production systems are characterized by high productivity, full utilization of resources, flexibility, and reliability. These characteristics enable an operating system to adapt to changing conditions. In any mining operation, ore is mined from different blocks and is hauled to predetermined destinations based on its chemical or mineralogical properties. Mining operations obtain the desired quality of the plant feed by blending ore of different qualities. The same practice is applied in a mine complex where the ore is sourced from different mines and has different chemical and physical characteristics (Figure 1).

Since ore properties can vary considerably, blending is a prerequisite in order to obtain a consistent feed to the processing plant. The run-of-mine quality depends on the quality and quantity of ore mined from each face. Uncertainty is the state of having limited knowledge to perform a task. During feasibility studies, the precise values of all the input parameters are not known. Normally,

* *Amirkabir University of Technology, Tehran, Iran.*
 ISSN 2225-6253. Paper received Sept. 2015; revised paper received Jan. 2017.

Application of fuzzy linear programming for short-term planning

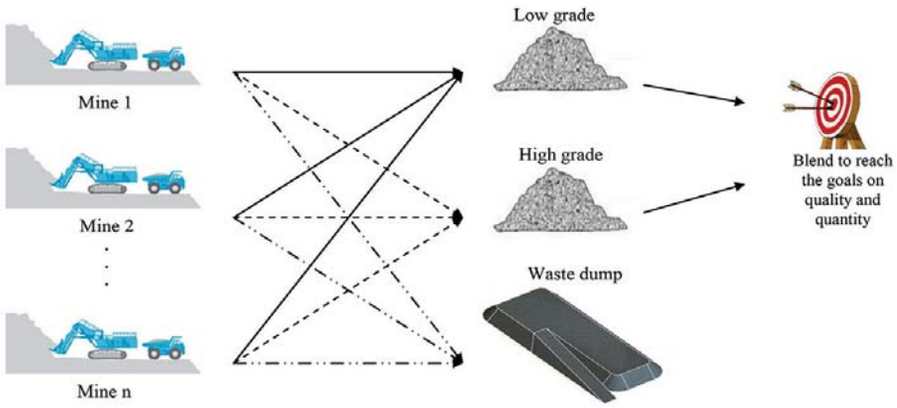

Figure 1—The scheme of operation in a mining complex

parameters such as the grades, operating costs, commodity prices, recoveries, and operational constraints are all estimated using the data available at the time of planning, based on the assessments of the mining engineers. Hence blending and quality control plans are determined based on some *in-situ* and estimated characteristics of a deposit. Therefore, the optimum blending plan is affected by the uncertainties of geological and chemical properties of the ore. Short-term planning in open pit mines has been studied by many researchers (Splaine *et al.*, 1972; Wilke and Reimer, 1979; Zhang *et al.*, 1992). Some researchers have incorporated the effect of uncertainties in short-term planning (Smith and Dimitrakopoulos, 1999; Kumral and Dowd, 2002; Fioroni, Bianchi, and Luiz, 2008; Gamache, Hébert, and Desaulniers, 2009; Jewbali and Dimitrakopoulos, 2009; Asad, 2010; Gholamnejad, 2008; Souza *et al.*, 2010; Askari-Nasab *et al.*, 2011; Eivazy and Askari-Nasab, 2012; Montiel and Dimitrakopoulos, 2015; Osanloo and Rahmanpour, 2017). They applied a variety of mixed integer linear programming models, Lagrangian parameterization, simulation, linear programming (LP), and heuristic models.

It is obvious that as planning parameters change, production plans should be re-optimized using the updated data. Therefore, a simple and deterministic LP model is not an appropriate tool for these types of problem, where planning parameters are uncertain. Moreover, there is always an acceptable limit (guarantee limit) for each mining constraint. For example, a thermal power plant may require coal with a maximum sulphur limit of 0.9%. It should be noted that coal with a sulphur content of 0.91% is also acceptable for the plant (Pendharker, 1997). In typical LP models, the constraints ignore this option. In such circumstances, fuzzy linear programming (FLP) seems to be a suitable tool. An FLP model considers the possible uncertainties by using fuzzy numbers. In addition, small deviations from the acceptable limits are allowed in FLP models, which leads to the determination of practical plans. FLP has been applied in a coal mine and in a bauxite mine for production scheduling (Pendharker, 1997; Vujic *et al.*, 2011). These studies carried out a procedure based on sensitivity analysis and shadow prices to determine a reliable production schedule.

This paper addresses short-term production planning in open pit mines in an uncertain environment. The objective is to provide a set of scenarios that represent the optimistic and the pessimistic options for short-term planning. Further, these scenarios enable the mine planner to incorporate some extra information based on his/her experiences to conduct a risk-based approach to select a suitable mining schedule. The optimized plan would present a protective strategy against unknown or highly uncertain events. For the purpose of this paper, short-term planning is investigated using a procedure based on FLP models. As an illustration, the model is applied in a limestone mine complex.

Fuzzy linear programming

An FLP model is a form of LP model where some or all of the parameters are fuzzy numbers. FLP has many applications in real-world problems, including production planning and scheduling, transportation, finance, engineering design, environmental management, and assignment (Rommelfanger, 1996; Sahinidis, 2004; Ko and Chen, 2014). This concept can be applied to optimize the mining schedule and production planning in open pit mines. Consider the general form of LP models (Equation [1]) where the objective function's coefficient ($\tilde{c}$), resources ($\tilde{b}$), and coefficients of the constraints ($\tilde{A}$) are all fuzzy numbers (Lie and Hwang, 1992; Wang, 1997; Sakawa, Yano, and Nishizaki, 2013; Luhandjula, 2014).

$$\begin{aligned} &\text{Max} \quad \tilde{c}x \\ &\text{s.t}: \quad \tilde{A}x \le \tilde{b} \\ &\qquad x \ge 0 \end{aligned} \qquad [1]$$

It should be noted that the non-fuzzy version of the model in Equation [1] should be feasible and an increasing function of the model parameters. Assume that $\tilde{c}=[c_0,c_1)$, and $(\tilde{b})=[b_0,b_1)$are defined as bounded fuzzy numbers (BFNs). The lower bounds of these BFNs represent the risk-free values that are conservative and implementable, and the upper bounds represent the optimistic values of the parameters (Figure 2).

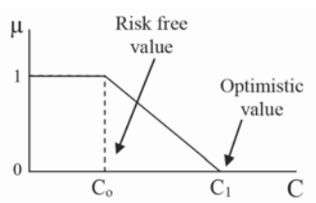

Figure 2—Representation of bounded fuzzy numbers (BFNs)

These parameters could also be represented as triangular fuzzy numbers. The fuzzy interval or the fuzzy membership function of each parameter must be specified initially. For this purpose, the decision-maker, according to his experiences and the mine conditions, specifies a membership function for each parameter. After formulating the model, a procedure similar to that presented by Carlsson and Korhonen (1986) is used to determine the optimum solution of the FLP model. This procedure is similar to a grid search algorithm. It provides a set of solutions to the decision-maker, who can select his/her preferred solution. The optimum solution of the problem is a trade-off among the degree of memberships (Lie and Hwang 1992). The full trade-off exists where the membership degrees of all the parameters in the model are equal (*i.e.* $\mu = \mu_c = \mu_A = \mu_b$ and $\mu \in [0,1]$). Therefore, the following equations are obtained, $c = g_c(\mu)$, $A = g_A(\mu)$, $b = g_b(\mu)$

where g_c, g_A, and g_b are the inverse functions of μ_c, μ_A, and μ_b respectively. This converts Equation [1] into Equation [2].

$$\begin{aligned} \text{Max} \quad & g_c(\mu)x \\ \text{s.t:} \quad & g_A(\mu)x \le g_b(\mu) \\ & x \ge 0 \end{aligned} \qquad [2]$$

This model (Equation [2]) is nonlinear but can easily be converted into an LP model for any given value of membership degree (*i.e.* μ). Thus, for any given value of μ, an optimum solution (z^*) can be determined. Finally, the pairs of solutions (*i.e.* (z^*,μ)) provide a guide for the decision-makers to determine the suitable strategy. Each pair of solutions represents the contribution of each mine site to the run-of-mine. The procedure required to obtain the optimum solution is as follows:

Step 1: Develop a scheduling model based on FLP models
Step 2: Determine the membership function of each fuzzy parameter
Step 3: Determine a membership degree or the level of uncertainty, or start with $\mu = 0$
Step 4: Assuming a membership degree, convert the nonlinear model into its LP equivalent, and solve the LP format of the model
Step 5: Plot the optimized solution of the model against the membership degree
Step 6: Let $\mu = \mu + \delta$, $\delta \in [0,1]$ and if $\mu > 1$ go to step 7, else go to step 4
Step 7: The plot in step 5 shows the relationship between the optimal schedule and the corresponding membership degree.

These steps are summarized in Figure 3. Considering the optimized solutions and their membership degrees, the decision-maker will select the optimal solution from among the calculated solutions. The selected solution indicates the optimum production plan.

Developing the fuzzy scheduling model

As shown in Figure 1, the aim of mine planners is to determine the optimum amount of material that should be mined from each specific mine site such that the customer (or the processing plant) is provided with a suitable and consistent quantity and quality of raw material. Therefore, the mined material is blended to provide a consistent feed with the required quality. Objectives are set at strategic and long-term planning; then the short-term objective chiefly concerns implementation to achieve those long-term goals. Short-term plans are normally optimized to achieve high productivity and full utilization of resources, which in turn minimizes operating costs. In this paper, the objective function of the short-term planning model is to minimize the total mining costs by determining the minimum amount of material that should be mined from each mine site. This is obtained through determining the optimal blending plan.

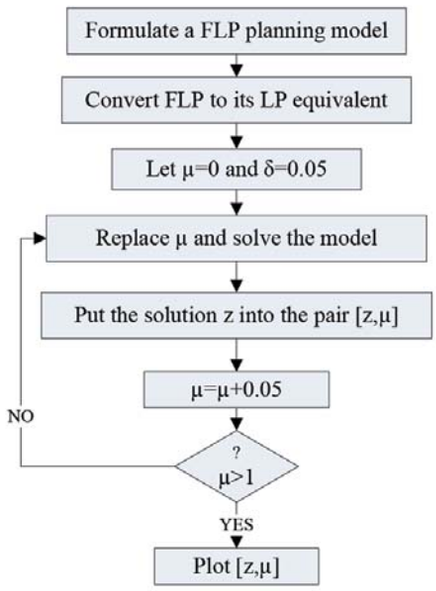

Figure 3—The procedure for solving the production scheduling model

Uncertainty is a problem that all mining operations are faced with. The most important factors that affect the mining schedule and are associated with uncertainty are the *in-situ* quality of mineable reserves, mining and processing capacities, mining costs, and commodity price. Mining and processing recoveries are functions of the chemical, physical, and mechanical properties of the material at each mine site and the type of mining operation. To analyse the effect of ore quality, mining and processing recoveries, and mining cost uncertainties on the optimum mining schedule and blending plan, an LP model is formulated (Equation [3]). Considering the mine characteristics and the requirements of the customer or the plant, the constraints of the mine planning model are recognized (Equation [3]). The notation used in the model is as follow:

N	The set of mines in the mining complex
c_i	The average operating cost at site i
x_i	The decision variable which is the amount of material that should be mined from site i
r_i	The recovery of material from site i
M_c	The minimum mining rate
M_i	The maximum possible mining rate at site i
PC	The feed rate required by the plant or the customer
g_i	The average grade of economic material at site i
$q_{i,k}$	The average grade of penalty element of impurity k at site i

G_{min} The minimum acceptable grade of economic material
$Q_{i,max}$ The maximum acceptable grade of impurity k
K The number of impurities or the penalty elements

The objective function is:

$$\text{Min} \sum_{i \in N} \tilde{c}_i \; x_i \qquad [3a]$$

subject to:

$$\sum_{i \in N} x_i \geq M_C \qquad [3b]$$

$$x_i \leq M_i, \forall i \in N \qquad [3c]$$

$$\sum_{i \in N} (\tilde{q}_{k,i} - \tilde{Q}_{k,\max}) x_i \leq \tilde{0}, \forall k \in K \qquad [3d]$$

$$\sum_{i \in N} (-\tilde{g}_i + \tilde{G}_{\min}) x_i \leq \tilde{0} \qquad [3e]$$

$$\sum_{i \in N} \tilde{r}_i x_i \geq \tilde{P}_C \qquad [3f]$$

$$x_i \geq 0, \; \forall i \in N \qquad [3g]$$

The objective function of the model (Equation [3a]) is defined as the minimization of the total mining costs of the production system. Equation [3b] ensures that the summation of the mined material is equal to or greater than the amount required by the plant or customer. Equation [3c] restricts the mining capacity of each mine site considering a possible and implementable mining capacity. Equations [3d] and [3e] are quality control constraints. Equation [3d] ensures that the total amount of penalty elements in the feed does not exceed the prescribed upper bounds. For example, in limestone mining, the presence of dolomite and silica is not tolerated. These constituents are considered as impurities or penalty constituents and they are modelled using Equation [3d]. Equation [3e] ensures that the total amount of economic material in the feed is always greater than the prescribed lower bounds. Equation [3f] ensures that the total amount of the final product produced in the mining complex is greater than the quantity required by the plant or customers. Finally, the logical constraints are embedded into the model as represented by Equation [3g].

The FLP model defined in Equation [3] is capable of determining the optimum blending plan. The symbol ~ indicates the fuzzy parameters in the model, which are assumed to be BFNs. As stated, for each BFN the lower bounds represent a possible and risk-free value and the upper bounds represent an optimistic value. Considering the fuzzy numbers and their membership functions, the FLP model in Equation [3] is then converted into a nonlinear programming model (Equation [4]).

The objective function becomes:

$$\text{Min} \sum_{i \in N} g_{c(i)}(\mu) x_i \qquad [4a]$$

subject to:

$$\sum_{i \in N} x_i \geq M_C \qquad [4b]$$

$$x_i \leq M_i, \forall i \in N \qquad [4c]$$

$$\sum_{i \in N} g_{y(k,i)}(\mu) x_i \leq g_{pe(k)}(\mu), \forall k \in K \qquad [4d]$$

$$\sum_{i \in N} g_{u(i)}(\mu) x_i \leq g_{ue}(\mu) \qquad [4e]$$

$$\sum_{i \in N} g_{r(i)}(\mu) x_i \geq g_{PC}(\mu) \qquad [4f]$$

$$x_i \geq 0, \; \forall i \in N \qquad [4g]$$

where $y(k,i) = q_{k,i} - Q_{k,\max}$ and $\mu_i = -g_i + G_{\min}$ are substituted in the model to simplify the formulation. The inverse membership functions of mining costs, grade of economic material, grade of penalty elements, and ore recovery are defined by $g_{c(i)}(\mu)$, $g_{y(j,i)}(\mu)$, $g_{u(i)}(\mu)$, and $g_{r(i)}(\mu)$, respectively. Also, the inverse membership functions of the right-hand side parameters corresponding to the quality and quantity constraints in Equations [4d], [4e], and [4f] are shown as $g_{pe(k)}(\mu)$, $g_{ue}(\mu)$, and $g_{PC}(\mu)$, respectively. After formulating the nonlinear model in Equation [4], steps 3 to 7 described in the previous section should be carried out to convert the model into a linear one and to obtain the optimum mining schedule and blending plan.

Model verification

The model (Equation [4]) was applied to a limestone mine complex in Iran. The mine is located in Semnan province about 230 km east of Tehran (Figure 4A). There are five distinct mining areas in the complex and the quantity and quality of the mineable limestone in each mine is different. In these mines, the limestone and dolomite beds are accompanied by cherty lenses. The limestone beds are Triassic light-gray, regular bedded limestone. The limestone bed is located beneath a siliceous or cherty limestone. This formation is covered by a dark-coloured basaltic and some ferruginous layers. The beds have a dip of 50 to 65 degrees (Figure 4B) and the thickness the of limestone layers varies from 30 to 65 m.

According to the long-term plan, the amount of mineable reserve in each mine is determined. For the purpose of short-term planning (within a one-month horizon), it is also assumed that the entire amount of materials scheduled is mineable within the short time periods. The limestone is supplied to a soda ash plant for the production of sodium carbonate, which has many uses in industrial processes. The quality control (QC) office of the plant specifies the required quality of the feed. The grade of $CaCO_3$ in the feed should be more than 93.5%, and the grades of $MgCO_3$ and SiO_2 should be less than 3.5% and 3% respectively.

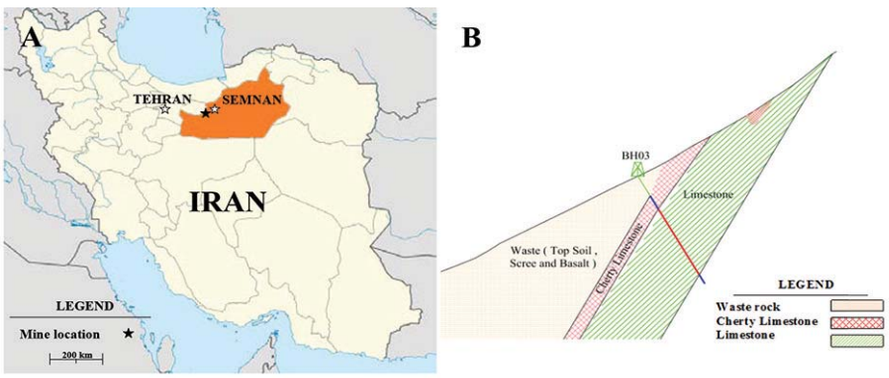

Figure 4—Location map of the mine

According to the data gathered from the mine sites during the year 2014, the characteristics of the limestone mined from each mine site are modelled as BFNs. As the lower bound of each BFN represents a possible and implementable value, the minimum value of the gathered data is selected as the lower bound. In case of positive parameters, such as ore grade (the percentage of $CaCO_3$), the upper bound is selected as the expected grade of the gathered data. However, in case of negative parameters such as the grade of penalty elements (the percentage of SiO_2 and $MgCO_3$) the opposite applies (Table I).

The other parameter that governs the scheduling of the mine is the possible production capacities of each mine site. In this case, the lower bound of fuzzy representation indicates the current mining capacity of each site. These values are determined based on local factors, including pit geometry and the thickness of limestone beds. The upper bound is an optimistic possible mining rate for each site. This value is determined based on the maximum mining rate that was reported from each mine site during the year 2014, as shown in Table I.

Table I

Characteristics of material from each mine

Mine	$CaCO_3$ (%)	$MgCO_3$ (%)	SiO_2 (%)	Mining capacity (t/month)	Recovery (%)
1	[88–93)	[5.5–4.8)	[3–2)	[9 500–10 000)	[50–55)
2	[89.8–93)	[6.5–5.8)	[3.8–1.5)	[9 500–10 000)	[50–55)
3	[93.5–96)	[3.8–2.8)	[3.5–1.4)	[32 000–33 000)	[55–62)
4	[90 –96)	[4.8–3)	[1.9–0.5)	[6 500–8 000)	[65–75)
5	[89.7–95)	[5.8-4)	[3–2.2)	[40 000–41 000)	[60–70)

Figure 5—Map of the mines and the blending plant

Table II

Quality requirements of the plant

Item	Allowable grade (%)	Description
$CaCO_3$	>93.5	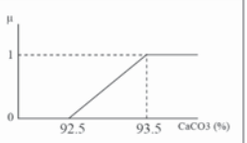
$MgCO_3$	<3.5	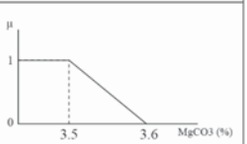
SiO_2	<3	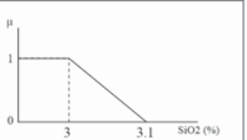

The plant requires limestone with a size distribution of 5–12 mm. The overall recovery of the material in the crushing unit depends on the mining operation itself and the mechanical characteristics of the limestone from each mine. After blasting, the blasted material is moved to a loading area by dozers and then loaded onto trucks by excavators. The material is hauled from each mine site to a crushing and blending unit. The fragmentation of the limestone feed to the plant from each mine site is a function of blasting and dozing operations. The relative location of each mine site with respect to the crushing and blending unit is shown in Figure 5. According to the data and experience of the mining crew, the overall recovery of the limestone mined from each mine site is also modelled using BFNs (Table I).

The crushed material with the prescribed size distribution is fed into the soda ash plant. The current capacity of the plant is 1500 t of crushed limestone per day, and the nominal quality required by the plant is given in Table II. This data is fuzzified considering a deviation of 1% for the ore grade and 2% for the penalty elements from the nominal quality requirements.

After fuzzification of the planning parameters, the model in Equation [4] is applied to determine the mining schedule and the blending plan for the mining system. The steps described in Figure 3 are applied to solve the planning model. The procedure was programmed in MatLab and was solved using the Simplex method.

Results and discussion

The membership degrees of the planning parameters are varied from risk-free or conservative values to optimistic values. Following the steps described in Figure 3, the optimum pairs of solutions are obtained. Each pair defines a scheduling scenario for the mine for each particular degree of membership. According to the results (Table III), as the membership degree of the planning parameters increases (*i.e.* it changes from optimistic values to risk-free values), the mines should exploit and process more material in order to fulfil the predetermined goals on limestone quality and quantity. The plant requires 45 000 t of crushed limestone monthly (equals 1500 t/d). As stated earlier, BFNs are used to represent the uncertainty of the planning parameters, where the lower and upper bounds define the conservative and optimistic values of each parameter. Considering the concept of BFNs, one could define the optimistic and conservative strategies for mine scheduling. In Table III, the schedule corresponding to a membership degree of 100% is regarded as the conservative schedule, and that with a membership degree of zero as the optimistic schedule. When the membership degree of the planning parameters decreases, it means that the optimistic values of the parameters are considered in the model and the results are optimistic as well.

According to the results, Mine 2, Mine 3, and Mine 4 are operating at their maximum nominal production rates in all the cases. When the inherited positive error of the planning parameters increases (*i.e.* the membership degree of the parameters decreases), the value of these parameters tends to improve to the optimistic values, then the production rate at Mine 5 decreases as shown in Figure 6. According to the results, Mine 5 should produce 30 708 t and 18 629 t of limestone per month based on the conservative and the optimistic mining schedules, respectively. Considering the reserve characteristics at each mine site (Table I), the reserve of Mine 1 is low in quality compared to the others, and according to the results, mining should be halted at this site. However, the costs at Mine 1 and Mine 2 are low compared to the other mines and the model tends to exploit from these sites to decrease the total mining costs. The amount of material mined from these two sites is controlled by the blending requirements. In other words, the limestone available at Mine 1 and Mine 2 is a balancing reserve for the production system in order to obtain the required output and to lower the mining costs.

By analysing the results and the given scheduling scenarios, the mine planner is able to determine the best mining schedule. Based on the experiences in this mine, and considering the selected membership degree, which indicates the strategy of the decision-maker, the mining schedule is selected from among the generated scenarios. According to Table III, selection of a membership degree of 20% for the planning parameters indicates that the mine planner is somewhat optimistic (80%) about the mine condition. At

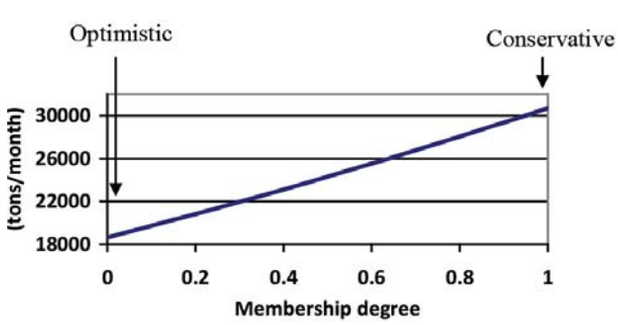

Figure 6—The membership function of optimal schedule at Mine 5

20%, the optimum mining schedule for the system is to produce 71 218 t of limestone per month. This is a decrease of 10% in the total mining rate compared with the most conservative case. This will decrease the total mining costs by 18% (Figure 7A). This is true for the rest of the cases as well.

The results show that the operation should produce less limestone when the mine planner is optimistic about the precise value of the planning parameters. This will reduce the total amount of mined material by about 12% compared to the case where the planning parameters are determined conservatively (Figure 7B). The difference in total mining costs between the optimistic and the conservative schedules is about 22% (Figure 7A). This shows that there is a chance of a considerable saving in costs.

Table III

The optimal solutions (t/month)

Membership degree of the planning parameters (%)	Mining schedule					Feed rate	Description
	x1	x2	x3	x4	x5		
100	0	9 500	32 000	6 500	30 708	78 708	Conservative schedule
95	0	9 525	32 050	6 575	30 029	78 179	
90	0	9 550	32 100	6 650	29 358	77 658	
85	0	9 575	32 150	6 725	28 697	77 147	
80	0	9 600	32 200	6 800	28 044	76 644	
75	0	9 625	32 250	6 875	27 400	76 149	
70	0	9 650	32 300	6 950	26 763	75 663	
65	0	9 675	32 350	7 025	26 135	75 185	
60	0	9 700	32 400	7 100	25 515	74 715	
55	0	9 725	32 450	7 175	24 903	74 253	
50	0	9 750	32 500	7 250	24 298	73 798	
45	0	9 775	32 550	7 325	23 701	73 351	
40	0	9 800	32 600	7 400	23 110	72 910	
35	0	9 825	32 650	7 475	22 527	72 477	
30	0	9 850	32 700	7 550	21 951	72 051	
25	0	9 875	32 750	7 625	21 381	71 631	
20	0	9 900	32 800	7 700	20 818	71 218	
15	0	9 925	32 850	7 775	20 261	70 811	
10	0	9 950	32 900	7 850	19 711	70 411	
5	0	9 975	32 950	7 925	19 167	70 017	
0	0	10 000	33 000	8 000	18 629	69 629	Optimistic schedule

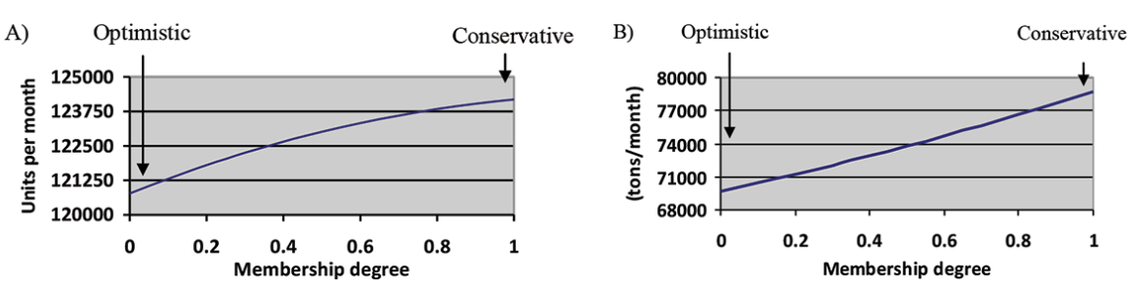

Figure 7—The membership functions of (A) total production costs and (B) total production

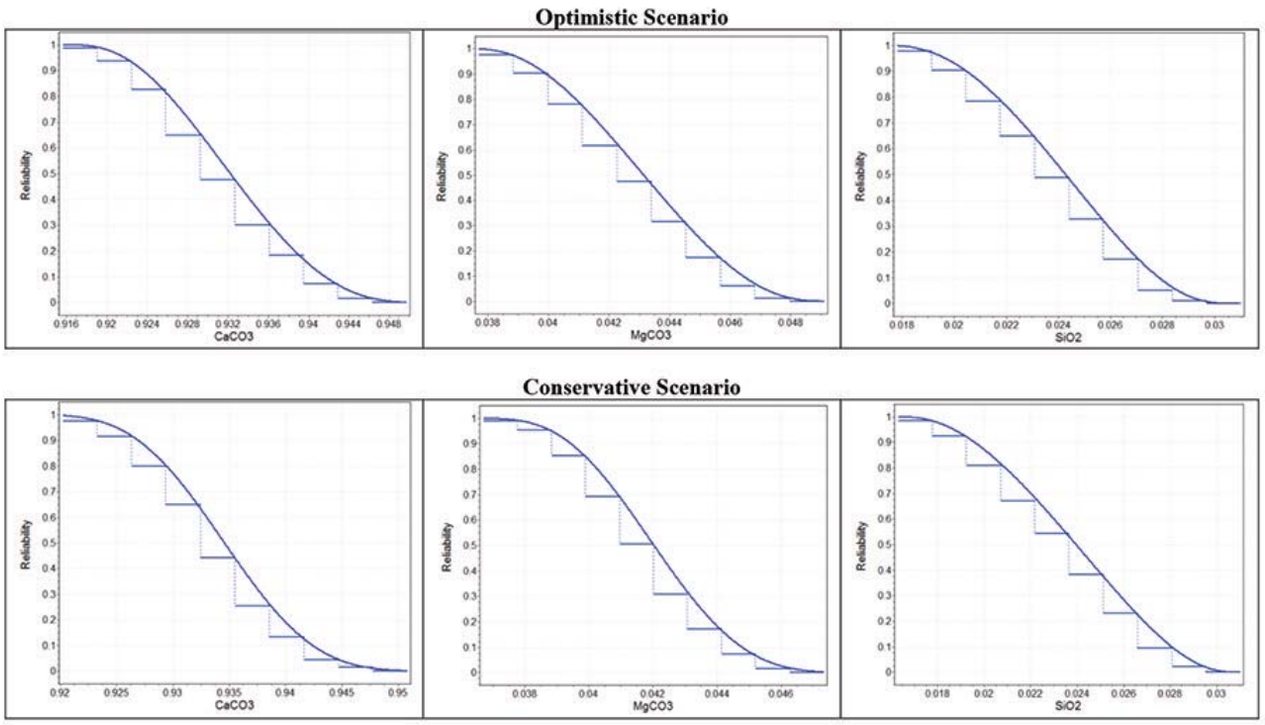

Figure 8—Reliability functions of the conservative and the optimistic scenarios with respect to variations in planning parameters

The blending plan could be analysed based on the reliability of the production system. From a reliability point of view, as shown in Figure 7, in the conservative mining schedule the mine system must produce extra limestone in order to increase the probability of obtaining the required quality. To check the validity of this statement, a Monte Carlo simulation was conducted on the conservative and optimistic schedules. For this purpose, a beta distribution function was fitted to the data. The general form of a beta distribution function (i.e. f(x, α, β)) is as follows:

$$f(x,\alpha,\beta)=\begin{cases}\dfrac{x^{\alpha-1}(1-x)^{\beta-1}}{B(\alpha,\beta)} & 0\le x\le 1\\ 0 & else\end{cases}$$

where α and β are the shape parameters of the beta distribution, and β is a normalization constant to ensure that the total probability integrates to unity.

The simulation results provide the distribution function of the conservative and the optimistic schedules with respect to $CaCO_3$, $MgCO_3$, and SiO_2 variations. If the grade of the mined material is not within the predetermined range, it is defined as failure for the mine schedule. The distribution functions are used to predict the reliability function of the conservative and the optimistic scenarios as shown in Figure 8. Here, reliability of quality (RQ) is defined as the probability that the average grade of the mined limestone is within the range dictated by the QC as represented by Equation [5].

$$RQ(g)=\Pr\{G>g\}=\int_{g}^{UB} f(x,\alpha,\beta)\,dx \qquad [5]$$

where g represents the minimum grade required by the quality control, G is the average grade of the mined limestone, and UB is the upper bound of the beta distribution function.

According to the results, the likelihood of attaining the required quality by implementing the optimistic and the conservative schedules is about 88%, and the probability of failure is 12% in both cases. This means that there is no bottleneck on attaining the required quality. In the next step, the plans are analysed to evaluate the overall tonnage of material produced by the plant. The reliability of tonnage (RT) is defined as the probability that the tonnage of the crushed and sized limestone is within the range dictated by the quality control as represented by Equation [6].

$$RT(t)=\Pr\{T>t\}=\int_{t}^{UB} f(x,\alpha,\beta)\,dx \qquad [6]$$

where t represents the tonnage required by the plant (in this case t is equal to 45 000 t/month), T is the tonnage of mined limestone, and UB is the upper bound of the beta distribution function.

The reliability in this case is a function of recovery in the plant. The result shows that the reliability of the conservative schedule is 100% and the reliability of the optimistic schedule is almost zero, as shown in Figure 9. Based on the results, the conservative option is the most reliable schedule. However, decision-making about the scheduling option depends on the utility function of the decision-maker and his/her knowledge and experience at the mine site.

Conclusions

A mine production-scheduling model based on fuzzy linear

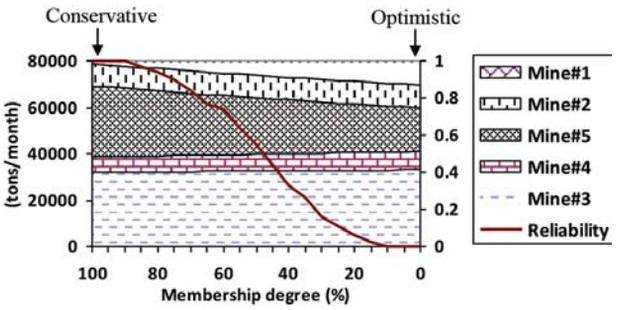

Figure 9—The relationship between mine production and the reliability of the mining system

programming has been developed and applied to optimize the mining schedule and blending plan in the presence of uncertainty. Fuzzy linear programming is a useful tool for modelling and optimizing mine production planning. Due to the fact that at the time of mine planning the precise values of all input data are not known in advance, the uncertainty of the input parameters (or simply planning parameters) should be considered in any mine planning optimization. The input data was fuzzified (into bounded fuzzy numbers) according to the data gathered from the mine during the year 2014. In addition, the 'right-hand side' values of the constraints were fuzzified with a deviation of 2% from the nominal values.

The procedure presented is capable of determining variable scenarios for the mining schedule. Therefore the mine planner, considering a degree of preciseness and optimism about the planning parameters, will be able to select the optimum mining schedule from among the presented options. Introducing uncertainty into the production planning model has increased the total amount of material that should be mined. This means that the mining operation pays for the cost of uncertainty by excess production. Mining and processing extra material would increase the reliability of the mining operation (Figure 9). In case of full uncertainty (the conservative option), the mine system should produce about 78 708 t of limestone in each month in order to satisfy the quality and quantity requirements of the blending plant. In the optimistic case, however, the operation should be producing about 69 629 t/month, which is 12% less than the conservative option.

References

Asad, M.W.A. 2010. Implementing a blending optimization model for short-range production planning of cement quarry operation. *Journal of Mining Science*, vol. 46, no. 5. pp. 525–535. DOI: 10.1007/s10913-010-0066-x

Askari-Nasab, H., Eivazy, H., Tabesh, M., and Badiozamani, M.M. 2011. A mathematical programming model for open pit short-term production scheduling. *Proceedings of the SME Annual Meeting*, Denver, Colorado, USA, 28 February - 2 March. pp. 1–8

Azimi, Y., Osanloo, M., and Esfahanipour, A. 2013. An uncertainty based multi-criteria ranking system for open pit mining cut-off grade strategy selection. *Resources Policy*, vol. 38. pp. 212–223. DOI:10.1016/j.resourpol.2013.01.004

Caccetta, L, and Hill, S.P. 2003. An application of branch and cut to open pit mine scheduling. *Journal of Global Optimization*, vol. 27. pp. 349–365. DOI: 10.1023/A:1024835022186

Carlsson, C. and Korhonen, P. 1986. A parametric approach to fuzzy linear programming, *Fuzzy Sets and Systems*, vol. 20. pp. 17–30. DOI: 10.1016/S0165-0114(86)80028-8

Dagdelen, K. 2007. Open pit optimization - strategies for improving economics of mining projects through mine planning. *Orebody Modeling and Stochastic Mine Planning*. 2nd edn. Dimitrakopoulos R. (ed.). *Spectrum Series* no. 14. Australasian Institute of Mining and Metallurgy, Melbourne. pp. 145–148.

Eivazy, H. and Askari-Nasab, H. 2012. A mixed integer linear programming model for short-term open pit mine production scheduling. *Mining Technology*, vol. 121, no. 2. pp. 97–108. DOI: 10.1179/1743286312Y.0000000006

Fioroni, M.M., Bianchi, T.J., and Luiz, R.P. 2008. Concurrent simulation and optimization models for mining planning. *Proceedings of the 2008 Winter Simulation Conference*, Miami, Florida, USA, 7-10 December. IEEE. pp. 759–767.

Gamache, M., Hébert, D.L., and Desaulniers, G. 2009. A generic linear program for an optimal mine production plan. *Proceedings of the 18th International Symposium on Mine Planning and Equipment Selection* (MPES), Banff, Alberta, Canada, 16-19 November. Singhal, R.K. (ed.). The Reading Matrix. pp. 326–334.

Gholamnejad, J. 2008. A zero-one integer programming model for open pit mining sequences. *Journal of the Southern African Institute of Mining and Metallurgy*, vol. 108. pp. 759–762.

Gholamnejad, J. and Osanloo, M. 2007. Incorporation of ore grade uncertainty into the push back design process. *Journal of the Southern African Institute of Mining and Metallurgy*, vol. 107, March. pp. 177–185.

Godoy, M. and Dimitrakopoulos, R. 2004. Managing risk and waste mining in long-term production scheduling of open-pit mines. *SME Transactions*, vol. 316. pp. 43–50.

Henderson, R. and Turek, C. 2013. Mine planning best practice at Kinross Gold. *Mining Technology*, vol. 122, no. 2. pp. 86–93. DOI: 10.1179/1743286313Y.0000000041

Heureux, G.L., Gamache, M., and Soumis, F. 2013. Mixed integer programming model for short term planning in open-pit mines. *Mining Technology*, vol. 122, no. 2. pp. 101–109. DOI: 10.1179/1743286313Y.0000000037

Jewbali, A. and Dimitrakopoulos, R. 2009. Stochastic mine planning – example and value from integrating long and short-term mine planning through simulated grade control. *Proceedings of Orebody Modelling and Stochastic Mine Planning*. Australasian Institute of Mining and Metallurgy, Melbourne. pp. 16–8.

Juarez, G., Dodds, R., Echeverria, A., Guzman, J.I., Recabarren, M., Ronda, J., and Vila-Echague, E. 2014. Open pit strategic mine planning with automatic phase generation. *Proceedings of the Orebody Modeling and Strategic Mine Planning Symposium*, Perth, WA, 24-26 November. Dimitrakopoulos, R. (ed.). Australasian Institute of Mining and Metallurgy, Melbourne. pp. 147–153.

King, B. 2014. Modelling open pit and underground production scheduling in concert. *Proceedings of the Orebody Modeling and Strategic Mine Planning Symposium*, Perth, WA, 24-26 November. Dimitrakopoulos, R. (ed.). Australasian Institute of Mining and Metallurgy, Melbourne. pp. 369–373.

Ko, W.C. and Chen, L.H. 2014. An approach of new product planning using quality function deployment and fuzzy linear programming model. *International Journal of Production Research*, vol. 52, no. 6. pp. 1728–1743.

Kumral, M. and Dowd, P.A. 2002. Short term mine production scheduling for industrial mineral using multi objective simulated annealing. *Proceedings of the 30th International Symposium on the Application of Computers and Operations Research in the Mineral Industry (APCOM)*, University of Alaska. Society for Mining, Metallurgy, and Exploration, Littleton, CO. pp. 731–737.

Levitin, G. and Lisnianski, A. 2001. A new approach to solving problems of multi-state system reliability optimization. *Quality and Reliability Engineering International*, vol. 17. pp. 93–104. DOI: 10.1002/qre.388

Lie, Y.J. and Hwang, C.L. 1992. Fuzzy Mathematical Programming, Methods and Applications. Springer-Verlag. pp. 74-127. DOI: 10.1080/00207543.2013.848479

Luhandjula, M.K. 2014. Fuzzy optimization: milestones and perspectives. *Fuzzy Sets and Systems*, vol. 274. pp. 4–11. DOI:10.1016/j.fss.2014.01.004

Montiel, L. and Dimitrakopoulos, R. 2015. Optimizing mining complexes with multiple processing and transportation alternatives - an uncertainty-based approach. *European Journal of Operational Research*, vol. 247, no. 1. pp. 166–178. DOI: doi:10.1016/j.ejor.2015.05.002

Newman, A.M., Rubio, E., Caro, R., Weintraub, A., and Eurek, K. 2010. A review of operations research in mine planning. *Interfaces*, vol. 40, no. 3. pp. 222–245. DOI: 10.1287/inte.1090.0492

Osanloo, M., Gholamnejad, J., and Karimi, B. 2008. Long-term open pit mine production planning: a review of models and algorithms. *International Journal of Mining, Reclamation, and Environment*, vol. 22, no. 1. pp. 3–35.

Osanloo, M. and Rahmanpour, M. 2017. Optimizing short-term production plan using a portfolio optimization model. *Revista Escola de Minas*, vol. 70, no. 1. pp. 109–116. DOI: 10.1590/0370-44672016700071

Pendharker, P.C. 1997. A fuzzy linear programming model for production planning in coal mines. *Computers and Operations Research*, vol. 24, no. 12. pp. 1141-1149. DOI: 10.1016/S0305-0548(97)00024-5

Rahmanpour, M. and Osanloo, M. 2016a. Determination of value at risk for long-term production planning in open pit mines in the presence of price uncertainty. *Journal of the Southern African Institute of Mining and Metallurgy*, vol. 116, no. 3. pp. 229–236.

Rahmanpour, M. and Osanloo, M. 2016b. Resilient decision making in open pit short-term production planning in presence of geologic uncertainty. *IJE Transactions A: Basics*, vol. 29, no. 7. pp. 1022–1028. DOI: 10.5829/idosi.ije.2016.29.07a.00

Rommelfanger, H. 1996. Fuzzy linear programming and applications. *European Journal of Operational Research*, vol. 92. pp. 512–527.

Sahinidis, N.V. 2004. Optimization under uncertainty: state-of-the-art and opportunities. *Computers and Chemical Engineering*, vol. 28. pp. 971–983. DOI:10.1016/j.compchemeng.2003.09.017

Sakawa, M., Yano, H., and Nishizaki, I. 2013. Linear and Multi-Objective Programming with Fuzzy Stochastic Extensions. Springer. pp. 104–148.

Smith, M.L., and Dimitrakopoulos, R. 1999. The influence of deposit uncertainty on mine production scheduling. *International Journal of Surface Mining, Reclamation and Environment*, vol. 13. pp. 173–178. DOI: 10.1080/09208119908944244

Souza, M.J.F., Coelho, I.M., Ribas, S., Santos, H.G., and Merschmann, L.H.C. 2010. A hybrid heuristic algorithm for the open-pit-mining operational planning problem. *European Journal of Operational Research*, vol. 207, no. 2. pp. 1041–1051. DOI: 10.1016/j.ejor.2010.05.031

Splaine, M. Atklnson, D.C., Davidson, W., and Smith, M.L. 1972. Optimizing medium-term operational plans for a group of copper mines. *Journal of the South African Institute of Mining and Metallurgy*, vol. 72. pp. 225–230.

Vujic, S., Benovic, T., Miljanovic, I., Hudej, M., Milutinovic, A., and Pavlovic, P. 2011. Fuzzy linear model for production optimization of mining systems with multiple entities. *International Journal of Minerals, Metallurgy, and Materials*, vol. 18, no. 6. pp. 633–637.

Wang, L.X. 1997. Fuzzy linear programming. *A Course in Fuzzy Systems and Control*. Prentice Hall Chapter 30. pp. 381–392.

Wilke, F.L., and Reimer, T. 1979. Optimizing the short term production schedule for an open pit iron ore mining operation. *Computer Methods for the 80's in the Mineral Industry*. Society of Mining Engineers of the American Institute of Mining, Metallurgical, and Petroleum Engineers, New York. pp. 642–646

Zhang, Y., Cai, Q., Wu, L., and Zhang, D. 1992. Combined approach for surface mine short term planning optimization. *Proceedings of the 23rd APCOM Symposium*, Tucson, AZ. Kim, Y.C. (ed.). SME, Littleton, CO. pp. 499–506. ◆

http://dx.doi.org/10.17159/2411-9717/2017/v117n7a11

Laboratory-scale smelting of limonitic laterite ore from Central Anatolia

by S. Pournaderi*, E. Keskinkılıç†, A. Geveci‡, and Y.A. Topkaya‡

Synopsis

The feasibility of ferronickel production from a low-grade limonitic laterite ore was investigated. The ore was first calcined and then prereduced in the solid state. The reduced ore was then smelted to produce ferronickel. The effects of coal addition, smelting temperature, and retention time on the process were investigated. Chemical and physical losses in the slag were separately quantified. Coal addition was the main parameter that controlled the ferronickel grade and losses in the slag. The melting point of the slag was well below that of the ferronickel, which enhanced metal-slag separation and minimized physical losses in the slag. A microstructural study of an industrial slag revealed that Cr-rich particulates, which were suspended in the slag, were mainly responsible for the physical losses in the slag.

Keywords
ferronickel, limonite, physical loss, chemical loss, slag.

Introduction

Nickel laterites are classified into three main types; saprolite, nontronite, and limonite. Of these, limonitic ores possess the lowest nickel content, ranging from 0.8 to 1.5 wt%. It is generally accepted that limonitic laterites are suitable for hydrometallurgical treatment while saprolitic laterites are suitable for pyrometallurgical treatment, *i.e.* ferronickel smelting. However, this perception is changing and new projects (Reinecke and Lagendijk, 2007) are aiming to treat low-grade limonitic ores by pyrometallurgical routes (Mudd, 2010) to produce ferronickel. The simplicity of the process, the nickel market, and new advances in furnace technology, as briefly discussed below, are the main incentives for smelting of limonitic laterites.

Nickel in limonitic laterites is incorporated in minerals containing elements such as Fe, Co, Si, and Mg. Hydrometallurgical methods basically handle the separation of nickel from these elements through a complex process to obtain nickel in pure form (Canterford, 1975). Pyrometallurgical processing is simpler and shorter as the product contains Ni, Fe, Co, and Cu.

The nickel market is the other incentive for ferronickel smelting from limonitic laterites. About 70% of this nickel output is used in iron-nickel based alloys such as stainless steels (Zevgolis, 2004), where Ni is added to the bath of molten alloy as ferronickel rather than high-priced metallic nickel. Hence separation of nickel from iron through the longer and more complicated hydrometallurgical processes is not necessary. In addition, the growing demand for ferronickel and the gradual decline in high-grade saprolitic reserves will inevitably shift the industry towards the smelting of low-grade limonitic ores in the future.

Furthermore, recent advances in furnace technology (Walker *et al.*, 2009; Voermann *et al.*, 2004) have overcome, to a great extent, difficulties related to the smelting of limonitic ores, such as unfavourable slag composition and high CO_2 emissions. Energy costs per ton of metal have decreased, thus compensating for the low grades of limonitic ores. With current technology and nickel market conditions, ores with a nickel content of more than 1% can be treated economically (Norgate, 2010). In the future, however, higher Ni prices and new advances could lower the cut-off grades.

This study investigated the feasibility of ferronickel production from a low-grade limonitic laterite ore. At the same time, it focused on the nickel losses in the slag, which is one of the major problems in ferronickel smelting. Ferronickel slags typically contain 0.1–0.2% Ni and the nickel partition ratio (percentage Ni in the ferronickel divided by percentage Ni in the slag) is about 200 or

* *Department of Metallurgical and Materials Engineering, Karadeniz Technical University, Trabzon, Turkey.*
† *Department of Metallurgical and Materials Engineering, Atılım University, Incek, Ankara, Turkey.*
‡ *Department of Metallurgical and Materials Engineering, Middle East Technical University, Ankara, Turkey.*

 ISSN 2225-6253. Paper received Jul 2016; revised paper received Nov. 2016.

greater (Warner, *et al.*, 2006). Nonetheless, the Ni recovery does not exceed 95% at best because of the high volumes of ferronickel slags. Laterites are not amenable to concentration and all the ore, consisting of mainly gangue minerals, has to be processed. Therefore, regardless of laterite type, ferronickel smelting generates large volumes of slag (10–5 t of slag per ton ferronickel). Although many studies have been conducted on the smelting of laterites, nickel losses in the slag have not been adequately addressed and remain a challenge for the industry. An innovative method was used in this study for the first time to separately quantify the chemical and physical losses in the slag.

Experimental

Raw materials

Limonitic laterite ore from the Sivrihisar region in Turkey was used in the study. The run-of-mine (ROM) ore was screened at 50 mm to reject large Ni-deficient rocks. The undersize fraction was crushed to -1 mm, which was used in the experiments. The chemical composition of the -50 mm ore, determined by inductively coupled plasma–atomic emission spectrometry (ICP-AES), is given in Table I.

Ukrainian coal was used as reductant. The particle size of the coal was reduced to -1mm in accord with that of the ore. The net calorific value and chemical analysis of the coal are given in Table II.

Experimental procedure

The ore was calcined and prereduced prior to smelting. An externally controlled muffle furnace was used for calcination. The sample was heated at 700°C for 40 minutes in air to completely remove chemically bound water and other volatiles. A vertical tube furnace was used for prereduction. Forty grams of calcined ore was mixed with a specified amount of coal and charged into a cylindrical alumina crucible. The sample was reduced at 1000°C for 40 minutes. A gas mixture consisting of 70%N_2–20%CO_2–10%CO was passed through the furnace at a flow rate of 50 ml/min. Further information on the calcination and prereduction behaviour of the ore has been published previously (Keskinkılıç *et al.*, 2012; Pournaderi *et al.*, 2014).

The prereduced ore was then smelted at a desired temperature to obtain ferronickel, using the same furnace and crucible as used in the prereduction stage. The sample was retained at the smelting temperature for a predetermined time and then cooled to room temperature. No further coal was added in the smelting step and the reduction process was completed by the remaining (unreacted) coal from the prereduction stage. During smelting, a gas mixture consisting of CO (20 ml/min) plus CO_2 (10 ml/min) was passed through the furnace. Details of the gas supply system and the vertical tube furnace are given in the following section. At the end of each experiment, the crucible was broken to remove slag and metal. Various views of a typical smelted sample are shown in Figure 1.

Experimental set-up

The gas supply system is schematically presented in Figure 2a. The system consisted of three manometers and capillary tubes. A manometer is shown in detail in Figure 2b. The height of the coloured liquid (an aqueous solution of $KMnO_4$) in the column controlled the gas flow through the capillary tube; the greater the height of liquid in the column, the higher the gas flow rate through the capillary tube. The gas mixture was sent to the vertical tube furnace, which is schematically shown in Figure 3.

High-purity nitrogen (99.99%) and carbon dioxide (99.5%) gases were used. Carbon monoxide gas was purified by passing it over copper chips at 500°C.

Chemical analysis

The ferronickel button (see Figure 1) was readily obtained after breaking the crucible. The sample was prepared by standard metallographic methods and analysed by X-ray fluorescence (XRF). The carbon and sulphur contents were determined using a carbon/sulphur combustion analyser. Slag was obtained as lumps which were crushed and ground for X-ray diffraction (XRD) and chemical analyses. Prior to the grinding, metallographic sections of some slag lumps were prepared and investigated using scanning electron microscopy (SEM).

Table I

Chemical composition of the -50 mm ore (wt%)

Ni	Co	Fe	SiO_2	MgO	Cr	CaO	Al_2O_3
1.405	0.093	33.7	25.8	1.29	1.26	1.65	3.23
MnO	**As**	**P_2O_5**	**S**	**Cu**	**TiO_2**	**Zn**	**K**
0.74	0.04	0.04	0.03	0.006	0.08	0.03	0.2

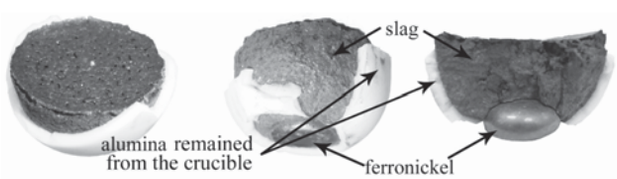

Figure 1—Photographs of a typical metal-slag sample obtained at the end of the smelting experiments

Table II

Net calorific value and chemical analysis (wt%) of the Ukrainian coal used in the study

Ash (mainly SiO_2)	Volatile matter	Sulphur	Moisture	Fixed carbon	Net calorific value (kcal/kg)
ASTM D3174 4.2	ASTM D3175 17.64	ASTM D4239 0.33	ASTM D3302 1.77	- balance	ASTM D5865 7752

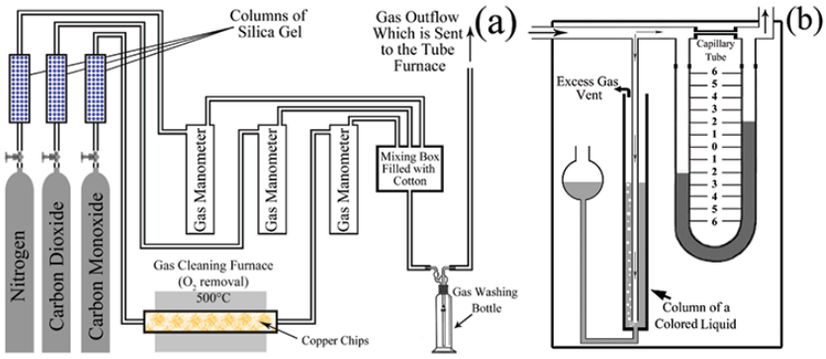

Figure 2—(a) General view of the gas supply, (b) detail of gas manometer

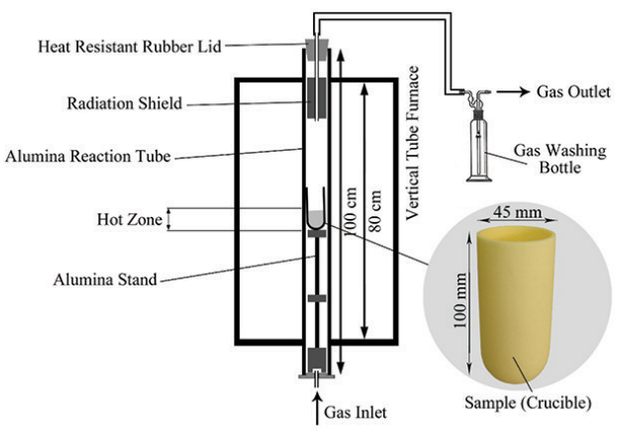

Figure 3—Schematic diagram of the vertical tube furnace and the crucible used in the smelting experiments

The chemical composition of the slag was determined by XRF. However, it was not possible to distinguish between different oxidation states of the same elements (*e.g.* Fe^{3+} and Fe^{2+}) by XRF. This is particularly crucial in the current study, since it is required to separately measure physical (Ni^0) and chemical (Ni^{2+}) losses of nickel in the slag.

A unique two-step wet chemical technique was used to separately measure the physical and chemical losses of nickel in the slag. In the first step, physical losses were determined by extraction of the metallic phases with bromine-methanol solution (Pournaderi *et al.*, 2014; Kinson, Dickeson, and Belcher, 1968) and measurement of the dissolved metals by atomic absorption spectrophotometry (AAS). In the second step, the residue from the first step was dissolved in an acid mixture (HNO_3+HCl+HF) and the solution was analysed by AAS to determine the chemical losses in the slag.

Results and discussion

Effect of coal addition

The effect of coal addition on the ferronickel grade and losses in the slag was investigated using 0, 7.5, 12.5, and 17.5% in excess of the theoretical amount of coal required in the prereduction stage to reduce all of the ferric iron (haematite) to the ferrous state (wüstite) and all of the Ni and Co oxides to the metallic form. The aim was to maximize Ni+Co metallization while limiting the metallization of iron, thereby ensuring a high-grade ferronickel product in the subsequent smelting step. Chemical analysis of the prereduced samples revealed that, depending on the coal amount, about 50–60% of nickel and cobalt, and 5–10% of iron, was reduced to the metallic form. The prereduced samples were smelted at 1500°C and retained for 30 minutes at this temperature.

The chemical compositions of the ferronickel products are given in Table III. The major constituents were Fe, Ni, and Co, with low amounts of C and impurities (mainly As and S). Trace amounts of Cu, Si, Al, and P were also detected but are not included in the analyses. The reduction of Cr, Al, and Si oxides during ferronickel smelting is very limited because ferronickel slags contain significant amounts of a less stable oxide, *i.e.* iron oxide. Only P, S, Cu, and As can be readily reduced and thus are expected to enter ferronickel. P and S are eliminated in the refining step in the industrial process. Copper does not cause any problems, but a high As (> 0.15%) content is not acceptable in the stainless steel industry (Zevgolis, 2004). Arsenic may be effectively

Table III

Chemical composition of the ferronickel products

Exp. no.	Experimental conditions			Ferronickel composition (wt.%)						
	Temperature (°C)	Retention time (min)	Excess coal (%)	Ni	Co	As	Cr	S	C	Fe
1	1500	30	0	16.63	1.02	0.33	0.08	0.0690	0.0830	Balance
2	1500	30	7.5	15.58	0.94	0.31	0.08	0.0766	0.0731	Balance
3	1500	30	12.5	13.45	0.85	0.23	0.06	0.0691	0.0756	Balance
4	1500	30	17.5	12.28	0.71	0.27	0.08	0.0671	0.0712	Balance

removed by volatilization in the oxide or metallic form during the calcination or prereduction processes, but more experimental work is required to address the issue.

Figure 4 shows the variations in weight and grade of the ferronickel product with excess coal addition. Iron was reduced more extensively with higher coal additions, which increased the mass of the ferronickel but also diluted the nickel grade of the product.

The slags were composed mainly of Fe and Si oxides (Table IV). A rough calculation revealed that only about 30% of the Fe entered the ferronickel at best (experiment no. 4), while the rest remained in the slag. As mentioned before, the low levels of impurities in the alloy were ascribed to the high FeO content of the slag.

The alumina contents of the slags were 2–3 times higher than expected. The excess alumina entered from the crucible. CaO, Cr_2O_3, MgO, and MnO were the other minor oxides in the slag. In addition, TiO_2, K_2O, Sc_2O_3, ZnO, and NiO were present in small quantities. Of these, Sc_2O_3 is valuable and commercially important, but was lost in the slag.

Low- and high-magnification SEM micrographs of the solidified slag are shown in Figures 5a and 5b, respectively. The slag contained three phases; a dark grey matrix, light grey strips, and a dendritic phase (labelled 1, 2, and 3, respectively on Figure 5b). It can be seen that the dendritic phase was mostly composed of fine particles of regular shape. In addition, there were some entrapped ferronickel particles, as seen in Figure 5c. The size of the ferronickel particles rarely exceeded 25 μm and was mostly in the 10–20 μm range.

Energy-dispersive spectrometry (EDS) analysis indicated that the matrix was a Si-Fe-Al-rich oxide. Calcium was also incorporated in this phase. The strip-like phase was a Si-Fe-rich oxide with minor Mg. The dendritic phase was a Cr-Al-Fe-rich oxide. From the EDS and XRD analyses of the slag, the strip-like phase was found to be a kind of fayalite with the formula $Mg_{0.26}Fe_{1.74}SiO_4$. The background was probably ferrosilite with the general formula $FeSiO_3$. The Cr-Al-Fe-rich phase could not be identified.

Losses in the slag

Metal losses in the slag comprise two types: physical (or mechanical) loss, which is the loss as entrapped ferronickel in the slag (see Figure 5c), and chemical loss, which is the loss as dissolved metal oxide in the slag. Physical and chemical losses of Fe, Ni, and Co are discussed below.

Physical losses

Although the physical losses of Fe, Ni, and Co were determined individually, these elements were lost in the slag as ferronickel rather than in the pure form. Therefore, consideration of the entrapped ferronickel in the slag, which can be regarded as the sum of Fe, Ni, and Co physical losses, can be helpful in understanding how the physical loss of each element was affected by the process.

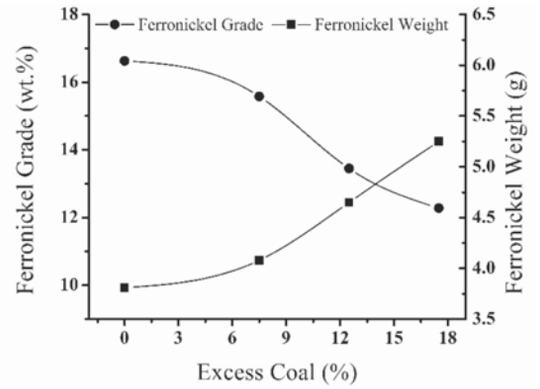

Figure 4—Effect of excess coal on the grade and weight of the ferronickel product

Variations of the physical loss of iron and entrapped ferronickel with excess coal addition are plotted in Figure 6. It is seen that the physical loss of iron increased when more excess coal was added. The total metal (ferronickel) loss in the slag followed the same pattern because iron formed the majority of the physical losses. Hence the effect of coal addition on the ferronickel loss also accounts for the physical loss of iron.

As shown in Figure 7, ferronickel nucleated and grew during the solid-state reduction (prereduction). These nuclei joined together, coalesced, and settled during the subsequent smelting to form a ferronickel pool. Nevertheless, some fine and individual particles, which did not succeed in coalescing with the other nuclei, remained suspended in the silicate matrix and were physically lost in the slag. As the number of nuclei increases, more individual particles are likely to remain in the slag. In addition, the total number of nuclei is directly proportional to the reduction potential during the process, *i.e.* the coal amount. This could lead to increased physical losses in the slag and could explain why entrapped ferronickel (and physical loss of iron) increased with higher coal additions.

The effect of coal addition on the physical loss of nickel in the slag is shown in Figure 8. The effect may be explained better by considering the average grade of the entrapped ferronickel particles, which is also plotted. The average grade of the entrapped ferronickel can be calculated as follows:

Table IV

XRF analyses of the slags

Exp. no.	Experimental conditions			Slag weight	Chemical composition of slag (wt%)						
	Temperature (°C)	Retention time (min)	Excess coal (%)	(g)	FeO	SiO_2	Al_2O_3	CaO	Cr_2O_3	MgO	MnO
1	1500	30	0	32.12	45.46	33.82	14.26	2.46	1.43	1.28	1.05
2	1500	30	7.5	31.69	45.57	33.68	14.32	2.48	1.42	1.33	0.96
3	1500	30	12.5	31.06	45.44	33.85	13.73	2.65	1.58	1.45	1.06
4	1500	30	17.5	30.28	43.64	35.41	13.85	2.7	1.64	1.46	1.08

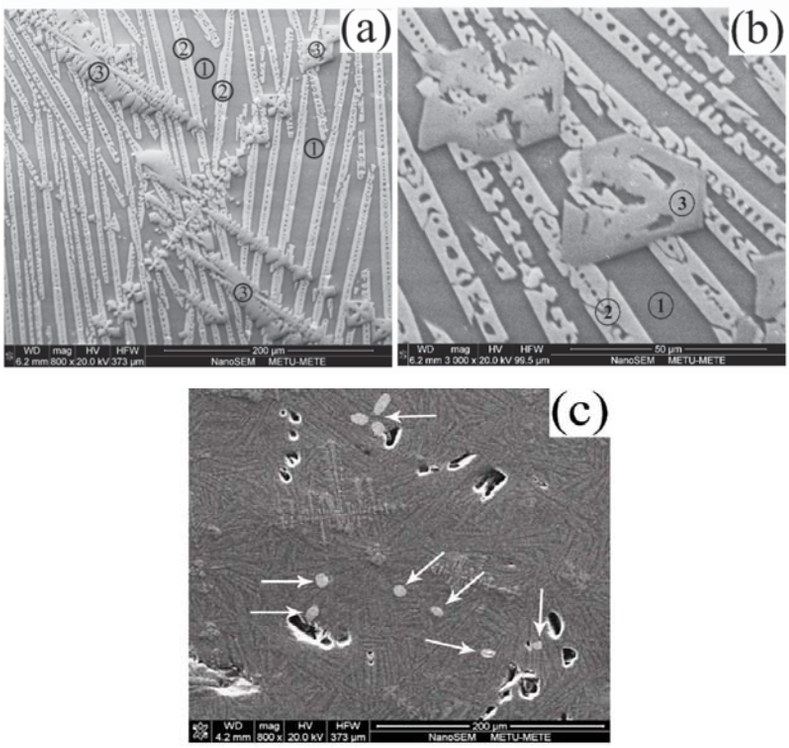

Figure 5—SEM micrographs of the slag; (a) low magnification, (b) high magnification, and (c) entrapped metal particles in slag

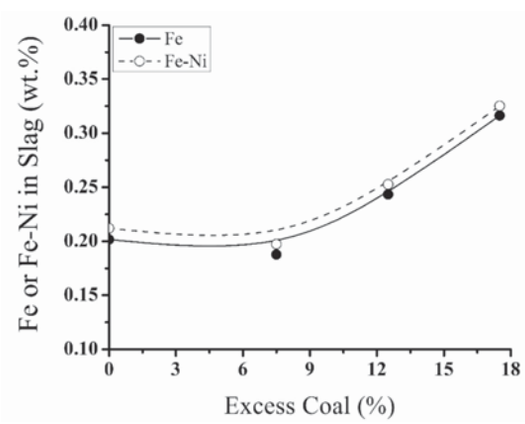

Figure 6—Variation of physical loss of iron and entrapped ferronickel in slag with excess coal addition

$$\text{Average grade of entrapped particles (wt\%)} = \frac{(Entrapped\ Ni\ (wt\%)}{(Entrapped\ (Fe+Ni+Co)(wt\%))} \times 100$$

Comparison of Figure 8 with Figure 4 shows that the grade of the ferronickel product and the average grade of the entrapped ferronickel changed in the same manner, both decreasing with increasing coal additions. A decrease in the grade of the ferronickel product was accompanied by a corresponding decrease in the average grade of the entrapped ferronickel and physical loss of nickel. It was concluded that physical loss of nickel was directly proportional to the grade of the ferronickel.

Physical loss of cobalt was very low (15–18 ppm) and was not affected significantly by the coal addition. This was attributed to the low cobalt concentration in the ferronickel.

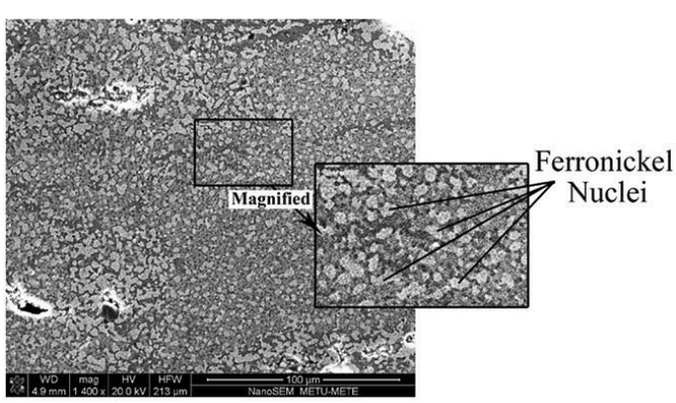

Figure 7—Ferronickel nuclei in a particle prereduced at 1100°C

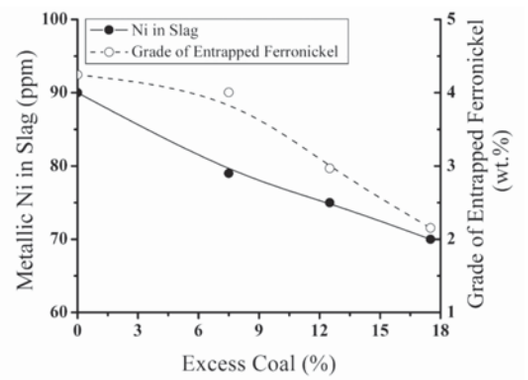

Figure 8—Variation of physical loss of nickel and grade of entrapped ferronickel in slag with excess coal addition

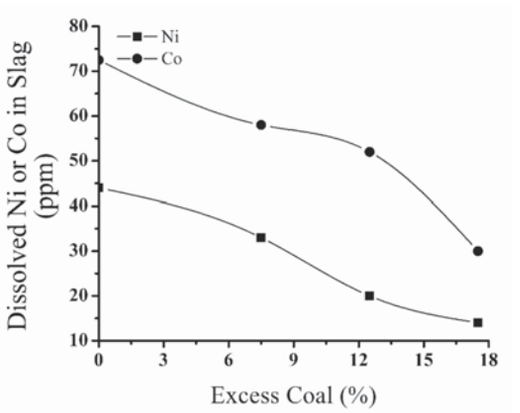

Figure 9—Chemical losses of nickel and cobalt in the slag with excess coal addition

Chemical losses

Chemical loss of iron, which is in fact the FeO content of the slag, was discussed previously (see Table IV). This section deals with the chemical losses of nickel and cobalt. Chemical losses of nickel and cobalt decreased with increasing coal addition, as illustrated in Figure 9. The effect may be explained as follows. Ferronickel was assumed to be in chemical equilibrium with the slag. Therefore, the activity of a component (Ni, Co) in the slag should be related to its activity in the ferronickel. In addition, the activity of a component in a solution (slag, ferronickel) is proportional to the concentration of that component in the solution. Consequently, the decreased Ni and Co chemical losses with increasing coal addition can be ascribed to the lower Ni and Co concentrations in the corresponding ferronickel product.

Effect of smelting temperature and retention time

In these experiments, the aim was to determine the minimum required retention time and temperature for the process. The coal addition was chosen to be 12.5% in excess of the theoretically calculated amount. This coal addition yielded a ferronickel containing about 14.5 wt% (Ni+Co), which can be commercially upgraded to 15–20 wt% (Ni+Co) after refining.

Two experiments were conducted at 1500°C with retention times of 10 minutes and 1 minute. The results (experiments no. 5 and 6, respectively) are summarized in Table V. In comparison with the previous results (experiment 3), decreasing the retention time from 30 minutes to 10 minutes and even to 1 minute had no effect on the process, and the same products with the same level of losses were obtained.

In another test, the smelting temperature was lowered to find the minimum required temperature. An experiment was carried out at 1450°C with 5 minutes' retention time, but the sample did not melt completely and metal-slag separation was not achieved. The second attempt was made at 1480°C, but again the sample did not melt completely. Another experiment (experiment 7) was carried out at the mid-point between 1480 and 1500°C, *i.e.* 1490°C. The sample was kept at this temperature for 5 minutes. This time, the sample completely melted and ferronickel was obtained. Therefore, a temperature between 1480 and 1490°C was the minimum required temperature for complete smelting of the ore. The results of this experiment are also included in Table V.

There was no meaningful difference between the results of previous experiments at 1500°C and the experiment at 1490°C with 5 minutes' retention time, particularly in terms of losses in the slag. This showed that separation of the metal from the slag was achieved soon after the temperature reached 1490°C. Complete metal-slag separation was achieved at 1490°C, while 1480°C was not high enough for complete smelting. The full separation of the metal from the slag was therefore achieved in a relatively short period of time and in a restricted temperature range between 1480 and 1490°C.

In order to understand what was happening during the course of smelting, the microstructures of the samples which were treated at 1450 and 1480°C were examined under SEM.

Table V

Chemical composition of the ferronickel and slag samples

Exp. no.	Experimental conditions			Ferronickel composition* (wt%)		Slag composition (wt%)				Loss in slag (ppm)				
	Temp. (°C)	Retention time (min.)	Excess coal (%)							Physical			Chemical	
				Ni	Co	FeO	SiO_2	Al_2O_3	CaO	Ni	Co	Fe	Ni	Co
5	1500	10	12.5	13.26	0.71	44.3	35.4	13.5	2.5	75	19	2339	17	25
6	1500	1	12.5	13.18	0.66	45.0	35.6	12.4	2.6	74	18	2927	20	26
7	1490	5	12.5	12.89	0.73	46.1	34.5	12.0	2.7	92	21	2458	12	27

* The balance is iron and minor elements

Their microstructures (Figure 10) were composed of ferronickel aggregates within a slag matrix. The microstructure of the slag matrix was very similar to that observed in the completely melted samples (see Figure 5a), indicating that the slag was molten at these temperatures (1450 and 1480°C). These results suggested that the incomplete metal-slag separation at 1450 and 1480°C stemmed from the high melting point of the ferronickel relative to that of the slag. In fact, the slag was molten but the ferronickel was not.

The impact of the low-melting slag on the process was twofold. Since the slag melted before the ferronickel, ferronickel particles (nuclei) could move freely in the liquid slag and easily coalesce during heating. The second impact was that the slag should be heated to well above its liquidus temperature on order to melt the ferronickel as well. The high superheat resulted in an adequately fluid slag. This enabled a quick and complete metal-slag separation within a restricted temperature range between 1480 and 1490°C.

Nickel recovery

Nickel losses can simply be calculated as follows:

$$Nickel\ losses\ (\%) = \frac{(W_{slag} \times (L_{ch}^{Ni} + L_{ph}^{Ni}))}{Nickel\ input} \times 100$$

where L_{ch}^{Ni} and L_{ph}^{Ni} are weight percentages of the dissolved (chemical loss) and the metallic nickel (physical loss) in slag, respectively. In the current study, the nickel concentration of the slags was about 0.01%. Under these circumstances, 0.4–0.7% of the nickel was lost in the slag, implying that recoveries of about 99.5% were achieved. The nickel concentration of industrial slags, however, is typically 0.1–0.2 wt% and the nickel recovery thus lies between 90–95%. That is, 5–10% of the nickel is lost in industrial slags.

For further studies, a few kilograms of industrial ferronickel and slag were obtained from the Larco smelter in Greece. Sivrihisar laterite and Greek laterites (Halikia, Skartados, and Neou-Syngouna, 2002; Zevgolis *et al.*, 2010) are alike in mineralogical and compositional terms.

The chemical composition of the Larco ferronickel and slag, as given in Table VI, was similar to those obtained experimentally. The main difference was the higher alumina content of the experimental slags, which was ascribed to the slag-crucible interaction in the experiments.

SEM micrographs of the Larco slag are shown in Figure 11. Being analogous to the experimental slags (see Figure 5), the Larco slag was also composed of three phases: a Si-Al-Fe-Ca-rich matrix, Si-Fe-Mg-rich stripes, and Cr-Al-Fe-rich particulates of regular shape. Entrapped ferronickel particles were also observed in the slag (Figure 11b). They varied from only a few micrometres to more than 350 μm in size. Physical and chemical losses in the industrial slag are given in Table VII. The chemical losses were in the same range as the experimental results, but the physical losses were much greater in the industrial slag. The difference arose from conditions prevailing in arc furnaces where, in contrast to the experimental set-up, the ore is smelted on a very large scale and the system is dynamic. Slag movements do not provide the quiescent conditions required for metal particles to coalesce.

A microstructural study of the Larco slag further revealed that the Cr-rich particles may, to a large extent, have been responsible for the physical losses of fine Fe-Ni particles in the slag. With the exception of some large entrapped ferronickel particles, in most of the cases fine particles were entrapped among the Cr-rich particles (Figure 12). Some of the ferronickel particles were deformed between the Cr-rich particles and some, semicircular in shape, adhered to these particles, indicating that the Cr-rich particles were solid when

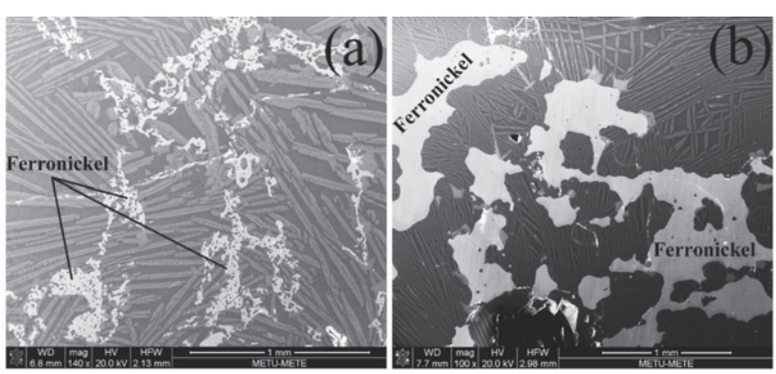

Figure 10—SEM micrographs of the sample heated at (a) 1450°C and (b) 1480°C

Table VI

Chemical composition of the Larco ferronickel and slag

	Ferronickel*				Slag					
Ni	Co	As	S	C	FeO	SiO_2	Al_2O_3	CaO	Cr_2O_3	MgO
14.8	0.47	0.06	0.21	0.05	43.7	33.5	8.8	4.4	4.3	3.7

* The balance is iron and traces of *e.g.* P, Al, Cu, Si

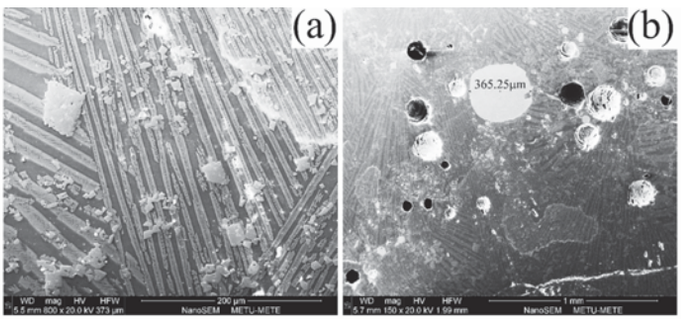

Figure 11—SEM micrographs of the Larco slag

Table VII

Physical and chemical losses in industrial slag from Larco smelter

Physical loss in slag (ppm)			Chemical loss in slag (ppm)	
Fe	Ni	Co	Ni	Co
4699	760*	32	60	58

* Higher nickel losses (1920 ppm) were reported by the smelter. The difference may be related to sampling.

they came into contact with the liquid ferronickel droplets. The high-melting-point Cr-rich particles were suspended throughout the slag and acted as traps for fine ferronickel particles.

Conclusions

The pyrometallurgical extraction of nickel from a Turkish laterite ore was investigated. The main findings of this research work are as follows.

- A ferronickel of acceptable grade was smelted from low-grade limonitic laterite ore. However, more experimental work is required to address the arsenic content in the product
- During the smelting, almost all of the nickel, 90–95% of the cobalt, and 30–40% of the iron in the ore were reduced to yield a ferronickel containing from 12–18% (Ni+Co)
- Coal addition was the key parameter that controlled the grade of the product ferronickel. Increased coal additions encouraged iron reduction, which in turn diluted the product ferronickel and lowered its grade
- Coal addition also controlled the physical loss of ferronickel. The higher the coal addition, the higher the physical loss
- Smelting of limonitic laterite ore resulted in a slag with a lower melting temperature than that of the ferronickel. Accordingly, the melting point of the ferronickel determined the minimum processing temperature. The minimum temperature for successful smelting was found to be in the range 1480–1490°C. A short retention time (5 minutes) was sufficient to achieve complete metal-slag separation at this temperature
- The physical loss of iron was proportional to the coal addition, whereas the physical losses of nickel and cobalt were directly proportional to the ferronickel grade. Chemical losses of Fe, Ni, and Co decreased when more coal was added to the charge.
- The high-melting-point Cr-rich particles suspended in the slag were the main source of the physical losses in the industrial slag.

Acknowledgement

The authors would like to thank the Scientific Research Projects (BAP) Department of the Middle East Technical University for the financial support under project no. BAP-03-08-2012-002. The authors also wish to express their thanks to the META Nickel Cobalt Company of Turkey for supplying the lateritic ore. The LARCO smelter in Greece is acknowledged for supplying the ferronickel slag.

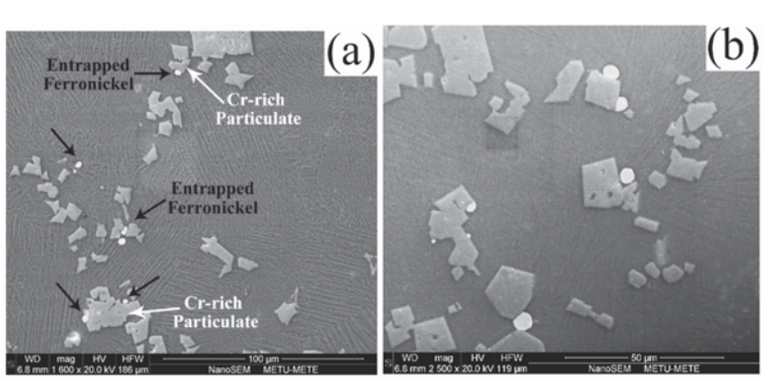

Figure 12—(a) Low- and (b) high-magnification SEM micrographs of ferronickel particles entrapped among the Cr-rich particulate phase

References

CANTERFORD, J.H. 1975. The treatment of nickeliferous laterites. *Minerals Science and Engineering*. vol. 7, no. 1. pp. 3–17.

HALIKIA, I., SKARTADOS, K., and NEOU-SYNGOUNA, P. 2002. Effect of reductive roasting on smelting characteristics of Greek nickel laterites. *Mineral Processing and Extractive Metallurgy*, vol. 111, no. 3. pp. 135–142.

KESKINKILIÇ, E., POURNADERI, S., GEVECI, A., and TOPKAYA, Y. 2012. Calcination characteristics of laterite ores from the central region of Anatolia. *Journal of the Southern African Institute of Mining and Metallurgy*, vol. 112, no. 10. pp. 877–882.

KINSON, K., DICKESON, J.E., and BELCHER, C.B. 1968. The determination of metallic iron, nickel and cobalt in reduced ores and oxides. *Analytica Chimica Acta*, vol. 41. pp. 107–112.

MUDD, G.M. 2010. Global trends and environmental issues in nickel mining: Sulfides versus laterites. *Ore Geology Reviews*, vol. 38, no. 1. p. 9–26.

POURNADERI, S., KESKINKILIÇ, E., GEVECI, A., and TOPKAYA, Y. 2014. Reducibility of nickeliferous limonitic laterite ore from Central Anatolia. *Canadian Metallurgical Quarterly*, vol. 53, no. 1. pp. 26–37.

REINECKE, I.J. and LAGENDIJK, H. 2007. A twin-cathode dc arc smelting test at Mintek to demonstrate the feasibility of smelting FeNi from calcine prepared from siliceous laterite ores from Kazakhstan for Oriel Resources plc. *Infacon XI, Proceedings of the 11th International Ferroalloys Congress*, New Delhi, India, 18-21 February 2007. Indian Ferro Alloy Producers' Association. pp. 781–797. http://www.mintek.co.za/Pyromet/Files/2007Reinecke.pdf

NORGATE, T. and JAHANSHAHI, S. 2010. Low grade ores – smelt, leach or concentrate? *Minerals Engineering*, vol. 23, no. 2. pp. 65–73.

VOERMANN, N.T., GERRITSEN, T., CANDY, I., STOBER, F., and MATYAS, A. 2004. Developments in furnace technology for ferronickel production. *Infacon X, Proceedings of the Tenth International Ferroalloys Congress*, Cape Town, South Africa, 1–4 February 2004. pp. 455–465. http:// http://www.pyro.co.za/InfaconX/069.pdf

WALKER, C., VOERMANN, N., CANDY, I.M., and WASMUND, B. 2009. Nickel laterite rotary kiln - electric furnace plant of the future. *Proceedings of Pyrometallugy of Nickel and Cobalt*, Sudbury, Ontario, Canada, August 2009. CIM, Montreal. pp 33–50.

WARNER, A. E. M.. DÍAZ, C.M., DALVI, A.D., MACKEY, P.J., and TARASOV, A.V. 2006. JOM world nonferrous smelter survey, part III: nickel: laterite. *JOM*, vol. 8, no. 4. pp. 11–20.

ZEVGOLIS, E.N. 2004. The evolution of the Greek ferronickel production process. *Proceedings of the International Laterite Nickel Symposium,* Charlotte, NC, USA. Imrie, W.P., Lane, D.M., and Barnett, S.C.C. (eds.).Wiley, New York. pp. 619–632.

ZEVGOLIS, E.N., ZOGRAFIDIS, C., PERRAKI, T., AND DELVIN, E. 2010. Phase transformations of nickeliferous laterites during preheating and reduction with carbon monoxide. *Journal of Thermal Analysis and Calorimetry*, vol. 100, no. 1. p. 133–139. ◆

Conference Announcement

science & technology
Department:
Science and Technology
REPUBLIC OF SOUTH AFRICA

advanced metals initiative

SAIMM
THE SOUTHERN AFRICAN INSTITUTE OF MINING AND METALLURGY

AMI Precious Metals 2017

THE PRECIOUS METALS DEVELOPMENT NETWORK (PMDN)

3 ECSA CPD points will be allocated to all attending delegates

In Association with **Platinum 2017**

17–19 October 2017 —Conference
20 October 2017— Technical Visits

Protea Hotel Ranch Resort, Polokwane, South Africa

BACKGROUND

The Precious metals Development Network (PMDN) of the DST's advanced metals initiative (AMI) programme will host the AMI's annual conference in 2017.

The AMI Precious Metals 2017 Conference will be held in association with the Platinum 2017 Conference. The Platinum conference series has covered a range of themes since inception in 2004, and traditionally addresses the opportunities and challenges facing the platinum Industry.

This AMI Precious Metals 2017 Conference will present a forum where scientists and technologists can come together to learn and discuss the latest advances in precious metals (platinum group metals and gold) science and technology, under the broad themes of:

- Catalysis
- Materials
- Chemistry

OBJECTIVES

- To bring together researchers, industry and government stakeholders to share and debate the latest trends, research and innovtion in the precious metals field.
- To provide a forum for researchers and industry to present progress made over the past few years on precious metal R&D and applications.
- To promote the activities of the AMI's PMDN.
- To network and share information.

WHO SHOULD ATTEND

- Platinum group metals and gold mining houses
- Precious metal industrial players
- Government departments
- Science Councils
- Higher Educational Institutes
- Anyone involved or interested in precious metals' R&D

EXHIBITION/SPONSORSHIP

Sponsorship opportunities are available. Companies wishing to sponsor or exhibit should contact the Conference Co-ordinator.

For further information contact:
Head of Conferencing, Camielah Jardine
SAIMM, P O Box 61127, Marshalltown 2107
Tel: +27 11 834-1273/7 ·Fax: +27 11 833-8156 or +27 11 838-5923
E-mail: camielah@saimm.co.za · Website: http://www.saimm.co.za

MINTEK
Specialists in mineral and metallurgical technology

necsa
We're in your world

CSIR
our future through science

http://dx.doi.org/10.17159/2411-9717/2017/v117n7a12

Calibration of a numerical model for bore-and-fill mining

by D. Roberts

Synopsis

Bore-and-fill mining was implemented at a pilot site in Tau Tona mine's shaft pillar on 97 level. Observations, scan data, and measurements from this site were used to calibrate an inelastic numerical model of bore-and-fill mining within the Carbon Leader Reef (CLR).

Borehole breakout was found to occur around holes at the site as they were bored. A strike-parallel exposure showed that fracturing within the Carbon Leader stratum extended far beyond the breakout (up to 1.2 m from the hole sidewall). This was confirmed by borehole camera observations in a hole drilled on-reef through a bored-and-filled hole.

A Mohr-Coulomb strain-softening model was calibrated against the observed fracturing. It was found that it was necessary to include interfaces corresponding with CLR contacts to replicate the extent of fracturing that was observed. The effect of hole position on breakout was quantified by analysing hole scan data. Models with holes at various positions, together with this data, were used to calibrate the upper and lower CLR contact properties. A novel displacement-based method for simulating breakout was developed for use on Carbon Leader models. Although the breakout distributions were not precisely matched, the modelled values lay within the extremes that were observed. Trends and other features observed underground were also replicated.

Modelled stresses and measured stress histories showed similar responses to the boring of nearby holes, but the magnitudes differed by varying degrees in each stress component. The modelled subvertical stress changes were generally lower than those measured, though both were greater than those obtained from a virgin stress measurement in the fill. It was noted that either measured value could be obtained by simply shifting the measurement position in the model. The strike stresses correlated reasonably well. Dip stresses were very different: measured tensile stresses greater than the fill strength suggest that these measurements were erroneous.

The result of this work is a calibrated plane strain model that can be used to study the effects of geology, mining sequence, and fill properties on the rock mass response to bore-and-fill mining.

Keywords
bore-and-fill mining, borehole breakout, strain-softening model, stress changes.

Introduction

Tau Tona mine has historically experienced damaging seismicity during attempts to extract its high-grade, highly stressed shaft pillar (Murphy, 2012). In an attempt to reduce the potential for seismic events a new mining method that involves the boring of large-diameter holes on-reef has been trialled. The rationale behind reef boring is that it reduces the effective stoping height, thus limiting the influence of the excavation on the surrounding rock mass. This is particularly important in the shaft pillar, as high deformation and closure are associated with increased seismic hazard.

Optimization of the boring sequence and in-hole support enable the extraction of as much of the reef as possible, while minimizing waste rock mining. Support must be installed in such a way that workers are never required to enter the holes. Filling the holes with a stiff, strong material will achieve these goals. Concrete, for example, has low porosity, can be engineered to have high strength and stiffness, and is easily poured or pumped into the holes from service excavations.

This paper describes how observations and measurements at a reef-boring pilot site were used to calibrate nonlinear numerical models. Initial models were calibrated based on observations of breakout and additional fracturing that was exposed when a raise was mined along the axis of an existing hole. A novel criterion for simulating breakout was developed, based on displacement into the hole and parallel to the minor stress axis. This criterion was used with the calibrated model to simulate the drilling and filling of a sequence of five holes. Some of these holes were instrumented with stress-change gauges and some were scanned and surveyed. The *in situ* data was compared with modelled outcomes.

Reef boring background

The feasibility of reef boring was considered by Jager, Westcott, and Cook (1975). They analysed various reefs in terms of deviation from planarity, presenting charts and tables to indicate optimal hole diameters in different mining areas. Adams (1978) describes stoping using a raiseboring machine on the Carbon Leader Reef (CLR) at West Driefontein mine. Holes were drilled adjacent to each other to create a continuous slot between reef drives. Pilot holes were bored and then used to guide a raisebore reamer from the upper reef drive. The completed slot is shown in Figure 1.

* *CSIR, Johannesburg, South Africa.*
 ISSN 2225-6253. Paper received Apr. 2016; revised paper received Jan. 2017.

Figure 1—The completed slot bored by sequential raisebore holes at West Driefontein (Adams, 1978)

It was observed that the first and last 0.5 m of each hole showed very little damage. Spalling did not occur when holes were bored into fractured (de-stressed) ground, while extensive spalling occurred when holes were bored into highly stressed, unfractured ground adjacent to the fractured material. Breakout occurred while the holes were being bored. Without filling, falls of ground (FOGs) occurred in the slot and time-dependent damage was observed after completing the slot.

It was concluded that fracturing was inevitable and that no fill could prevent breakout. Simple calculations showed that over 164 holes needed to be drilled before the fill would start to take the full overburden load. Jager, Westcott, and Cook (1975) commented that it would be necessary to fill the holes with 'a relatively incompressible material' not more than 2 m away from the hole being bored.

In the current work, it is acknowledged that the fill cannot prevent fracturing, but it is emphasized that this is not the intended purpose of the fill. The effectiveness of the fill is not in sustaining the 'full overburden load', but in reducing closure and limiting the stress transferred to the abutments of the extracted reef zone. By doing this, the occurrence of large-scale fractures at the edge of the extracted zone will be prevented, and bed separation will be limited to the extent that fallout does not occur in nearby service excavations.

Underground observations

Pilot site description

The pilot site for the boring and filling operations is on Tau Tona mine within the shaft pillar on 97 level. The location of the site is shown in Figure 2. The site is a 30 × 50 m pillar created between two reef drives on strike and raises on dip. The reef drives and raises are nominally 3.5 m × 3.5 m, though the lower reef drive was up to 5 m wide, as the northern sidewalls were sliped and the southern sidewalls cut away to accommodate the boring machine.

The CLR is exposed in all these service excavations. The average channel width exposed in the western raise is 24.9 cm, although scans from holes bored within the pillar indicated thicknesses greater than 40 cm. The reef dips at 23°. The footwall is a medium- to coarse-grained, slightly argillaceous quartzite containing footwall pebble bands. The hangingwall is a medium-grained, slightly argillaceous quartzite with occasional milky white quartz veins. Quartz veins tend to be oriented NE-SW and either terminate on the reef's bottom contact or cut through the reef. No major geological structures were observed. The Green Bar argillite (Ryder and Jager, 2002) lies approximately 2.0 m above the top reef contact. The basal Green Bar contact is not exposed, so ground control problems associated with it were not expected at the pilot site.

Map3D boundary element modelling was employed to estimate the stress state. The stress gradient was specified to correspond with previous virgin stress measurements at Tau Tona (Hofmann, Scheepers, and Ogasawara, 2013). A model of the shaft pillar area was analysed with interrogation grids around the 97 level pillar. The following stress state was obtained:

Reef-perpendicular stress:	107.5 MPa
Strike-parallel stress:	0.44 × σ_{yy} = 47.3 MPa
Dip-parallel stress:	0.74 × σ_{yy} = 79.6 MPa

Since the holes are drilled on-reef, the stress field is oriented so that the major principal stress is perpendicular to the hole axis and perpendicular to the Carbon Leader contacts. For a section perpendicular to the hole axis, the effective stress field is shown in Figure 3.

Breakout observations

Initial holes were drilled at least five diameters apart, resulting in no stress interaction between the holes. The resulting breakout damage was consistent with observations at West Driefontein, that is:

- The first and last 1.0–1.5 m of the hole were undamaged
- Breakout was oriented along the minor principal stress axis (*i.e.* in the horizontally opposed sidewalls)

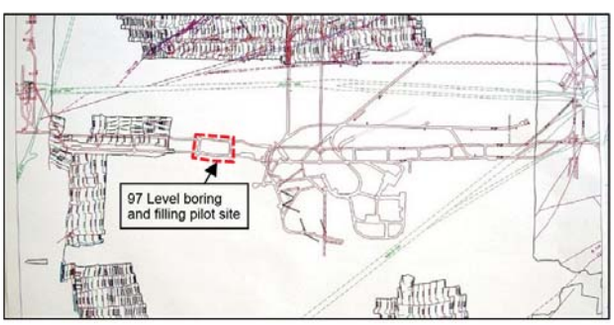

Figure 2—Tau Tona shaft pillar area, indicating the location of the pilot site

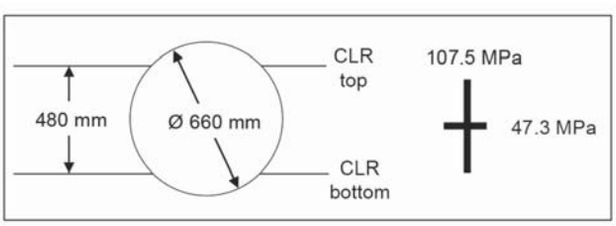

Figure 3—Geometry of a typical bored hole relative to the CLR contacts and the orientation of the stress field in the plane perpendicular to the hole axis

- Breakout occurred during drilling, with almost no time-dependent failure being observed.

It was also noted that the fractures tended to break out against the upper CLR contact. This was particularly evident in hole 12 (Figure 4). The extent of breakout was found to vary considerably between holes, and even along the length of some holes. Many of the holes were scanned to quantify the extent, shape, and volume of the breakout. In the following discussions the breakout volume for a given section is expressed in m^3/m, that is, volume broken out per metre of hole length. This is equivalent to the broken out area (in m^2) for that section.

Figure 5 shows the condition of hole 10 as is viewed from the southern reef drive. The hole profiles generated for the southernmost 6 m of the hole are also shown.

Figure 6 shows a photograph of the same hole taken from the northern reef drive, along with the topmost hole profiles. It was found that this hole was drilled, initially, where the CLR package was relatively thick, resulting in significant breakout extending all the way to the CLR contacts (up to 0.18 m^3/m). The hole then deflected upwards, so much so that the upper part of the hole was drilled entirely into hangingwall quartzite. In this region the breakout was less than was typically observed in holes drilled entirely in CLR (0.025 to 0.045 m^3/m).

Figure 4—Photograph of hole 12 from the southern reef drive. Intersections and exposures of the CLR top and bottom contact are shown in red and blue, respectively

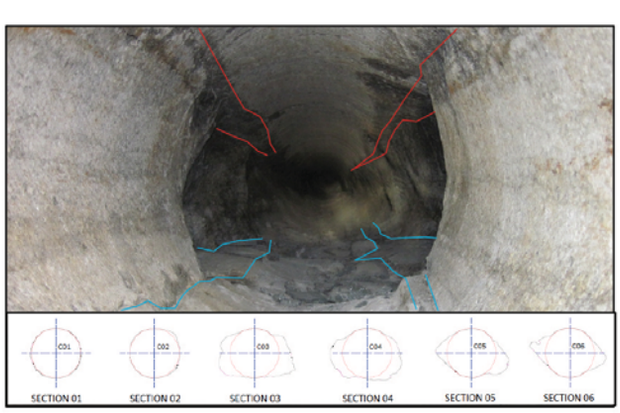

Figure 5—Photograph of hole 10 from the southern reef drive and scan profiles for the lower 6 m of the hole. Intersections and exposures of the CLR top and bottom contact are shown in red and blue, respectively

The breakout volumes, cumulated from the start of each hole, for a selection of the scanned 660 mm diameter holes are presented in Figure 7. Holes 17 and 18 show very different levels of breakout to all the other holes. Hole 17 was drilled between holes 14 and 11, which were so closely spaced that the concrete in these holes was exposed in the sides of hole 17. At this point not enough stress had been regenerated in the fill for breakout to occur. Only towards the top of the hole, where the hourglass pillar was larger and the rock mass was exposed, was there breakout around hole 17. Hole 18 was drilled adjacent to hole 10, effectively in the abutment created by the 11-17-14-10 sequence. This region was highly stressed, as reflected by the high volume that was broken out. The geometry of the holes in this sequence is shown in Figure 8.

The lateral (horizontal) extent of the breakout was also measured in each of the scanned holes. The maximum breakout length was measured on both sides of the hole. This data was revealing, particularly for holes that were drilled close to previously drilled and filled holes.

Figure 9 shows the distribution of the breakout extent on either side of hole 18, which was drilled adjacent to hole 11. Initially the damage was concentrated on the western side of the hole, with almost no damage occurring in the small pillar separating holes 18 and 11. This is consistent with the observation of Adams (1978), indicating that the pillar had

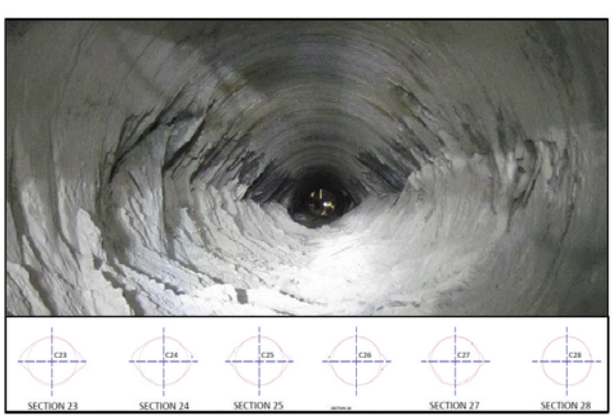

Figure 6—Photograph of hole 10 from the northern reef drive and scan profiles for the upper 6 m of the hole

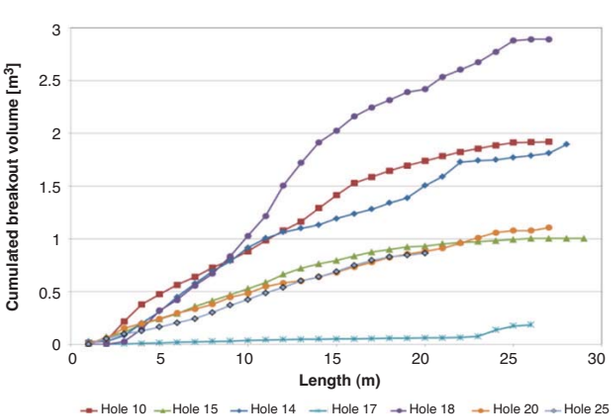

Figure 7—Breakout volume cumulated from the start of each hole

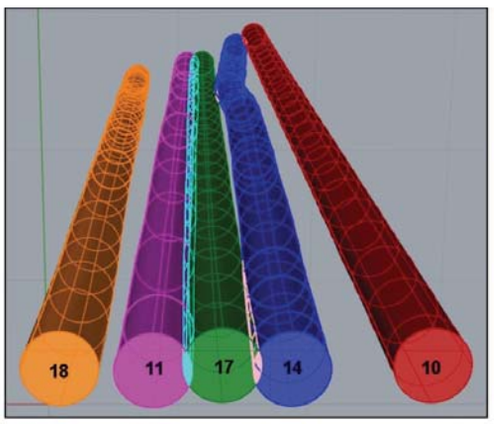

Figure 8—Geometry of the region encompassing holes 10, 11, 14, 17, and 18, viewed from the southern reef drive

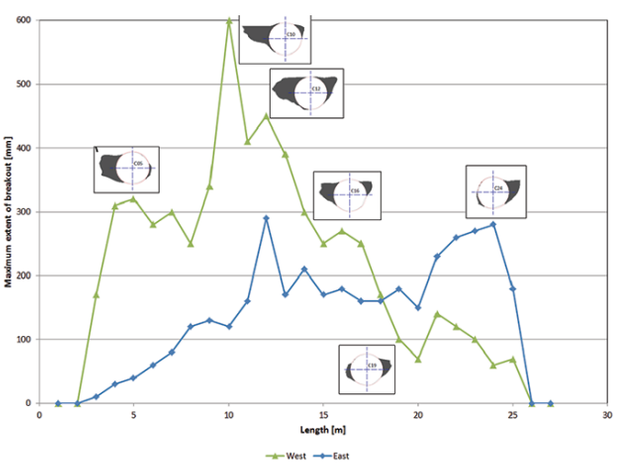

Figure 9—Maximum extent of lateral breakout on the east and west sides of hole 18 for each metre of hole length. Insets – breakout shape as seen from the southern reef drive

failed and was de-stressed, and that the adjacent rock mass was highly stressed. As Figure 8 shows, the distance between the two holes (and therefore the pillar width) gradually increased. In response to this, damage on the western side decreased, while damage in the pillar increased. At a distance of 18 m from the southern hole collar the breakout was symmetrical, indicating that the stress was evenly distributed between the pillar and the abutment. From this point onwards the pillar was wide enough to sustain significant stress and the extent of breakout was greater here than in the abutment.

The effect of the hole position relative to the reef was examined. Holes 10 and 18, both of which deviated significantly from the reef position, were evaluated in more detail. The extent of breakout for these holes is plotted against the approximate vertical position of the hole (relative to the centreline of the reef package) in Figure 10. Since these holes were drilled in different stress regimes, the breakout volume is normalized to the average breakout along the length of each hole. The general trend is a decrease in failure volume as the hole position moves away from the reef; however, there is also an increase when the bottom of the hole approaches the upper reef contact (from 550 to 620 mm). It also appears that the breakout is greater when the top of the hole coincides with the upper contact (around -90 mm). The breakout is lower than average when the hole centreline coincides with the upper and lower reef contacts (-240 and 240 mm), and when the hole is located entirely outside of the reef package ($y > 560$ mm).

This data indicates that damage is increased when the top or bottom of the hole coincides with the reef contacts, in particular the upper reef plane. The breakout shape (Figure 11) show that damage extends from the sidewalls of the hole all the way up to the reef contact.

Subsequent investigation revealed that the extent of fracturing greatly exceeded that indicated by breakout alone. A hole was bored in the planned position of a reef raise in an attempt to de-stress this region. Given the high stresses in the area the risk of strain-bursting, particularly in tunnel sidewalls, was considered a potential hazard. When the reef raise was created using conventional drill-and-blast methods the full extent of fracturing around the hole was revealed (Figure 12). 'Onion-skin' fracturing was observed within the reef package up to one hole diameter (660 mm) distant from the sidewall of the hole. The extent of breakout (material detaching from the rock mass and falling into the hole) was limited compared to the extent of fracturing.

It was suggested that the extra fracturing around the hole could have been caused by stress induced by the advancing face of the raise. To confirm that these fractures were present prior to mining of the raise, an exploration hole was drilled on-reef through a bored-and-filled hole. The discontinuity distribution inferred from borehole camera videos is shown in Figure 13. Fractures in the sidewall of the raise dominate

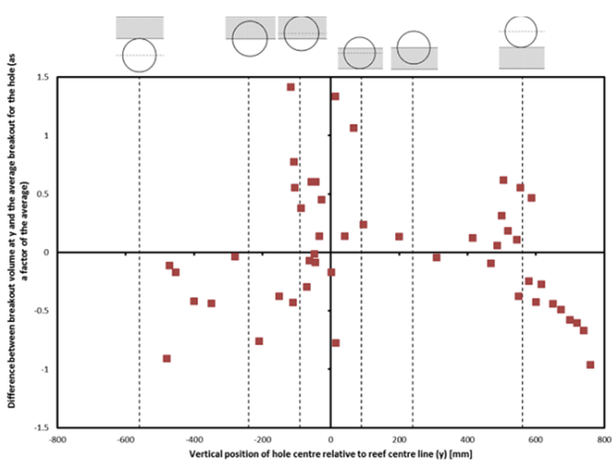

Figure 10—The effect of vertical position of the hole relative to the reef centreline for holes 10 and 18, expressed as a factor of the average breakout along each hole

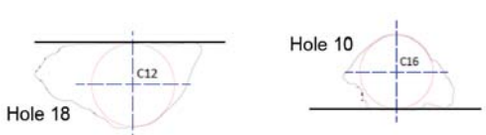

Figure 11—Breakout shapes for holes 18 and 10 where the top and bottom of the hole coincides with the upper reef contact

Figure 12—Photograph of exposed reef raise face, revealing extensive fracturing beyond the extent of breakout around the hole

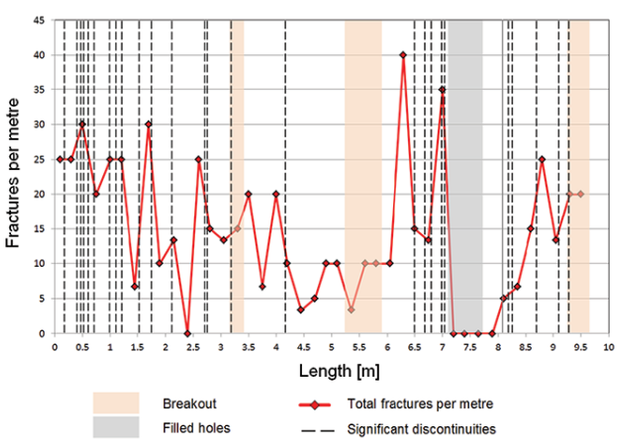

Figure 13—Discontinuity distribution inferred from borehole camera videos of an on-reef exploration hole. The length axis begins at the raise from which the hole was drilled

up to 3.2 m. A high-stress region (breakout with few discontinuities) is evident from 3.2 to 6 m. The region (6 to 7.2 m) adjacent to the hole (7.2 to 7.7 m) is highly fractured, as is the region from 8.6 to 9.3 m, which is adjacent to another hole. This confirms that the fracture zone extends up to 1.2 m away from the edges of bored holes.

Sequence and observations for holes 10 to 18

A sequence of holes that were drilled close to each other was modelled.

Figure 14 shows the geometry of the holes as viewed from the lower reef drive towards the west side of the test site. The five 660 mm diameter holes 10 to 18 were modelled. The larger diameter holes 5 and 1 are far enough from this sequence to be ignored in the modelling. The 'VWSG' labels indicate that vibrating wire stress gauges were installed in holes 10 and 14.

In addition to the stress measurements, holes 10, 14, 17, and 18 were scanned along their entire lengths, allowing quantification of the damage in each hole, and providing accurate geometries of these holes. Hole 17 was filled for only half its length, allowing observation of the hole condition after the drilling of hole 18 from the top drive. After hole 18 was drilled, some spalling was observed in the western sidewall of hole 17 (Figure 15).

Stress measurements

Vibrating wire stress gauges were installed in holes 10 and 14 when they were filled. These instruments show stress changes in a single plane. Two sets were installed in each hole. One set was mounted such that the subvertical and dip stresses were recorded (XZ) and the other in the plane of the subvertical and strike stresses (YZ). In this layout the following conventions apply: X is parallel to dip (parallel to hole axis, pointing down the hole); Y is parallel to the strike direction (horizontal, pointing east); and Z is 23° down-dip of vertical (*i.e.* perpendicular to the hole axis and the horizontal strike direction).

The readings were processed so that the major (P) and minor (Q) principal stresses were calculated in the XZ and YZ planes. The measurement histories up to the boring of hole 19 are shown in Figure 16 (hole 10) and Figure 17 (hole 14).

The instruments show reasonable reactions to the drilling of nearby holes. Hole 10 shows a significant reaction to the drilling of the hole 14 pilot, and a similar reaction to the reaming of the hole. The boring of hole 17 had a small influence, while hole 18 caused significant stress change. Hole 14 also showed a relatively small reaction to hole 17, and a significant change when hole 10 was bored. A portion of the XZ record from hole 14 was corrupted and not used in the analysis of this data. The high tensile stresses recorded in the XZ plane of hole 10 are also questionable.

A hole was drilled into the fill emplaced in hole 10 around four months after the completion of hole 18 (hole 24 was being bored at the time). Absolute stress measurements were done using the compact conical borehole overcore (CCBO) stress measurement method (Sugawara and Obara, 1999). The concrete core often broke up during overcoring, requiring repeated measurements. The measured strain changes were averaged to provide a complete stress tensor (Figure 18). The major principal stress is very close to strata-perpendicular, the intermediate stress (54% of σ_1) is oriented approximately east-west (*i.e.* parallel to strike), and

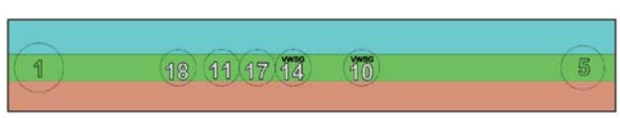

Figure 14—Detail of the holes at the west end of the test site

Figure 15—Photograph of hole 17 taken from the upper reef drive, showing spalling on the western (right) sidewall that occurred only after the hole 18 was drilled

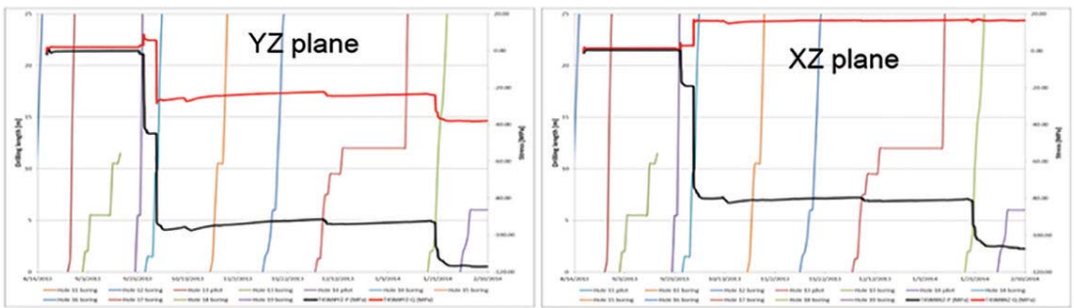

Figure 16—Stress change measurement history for hole 10

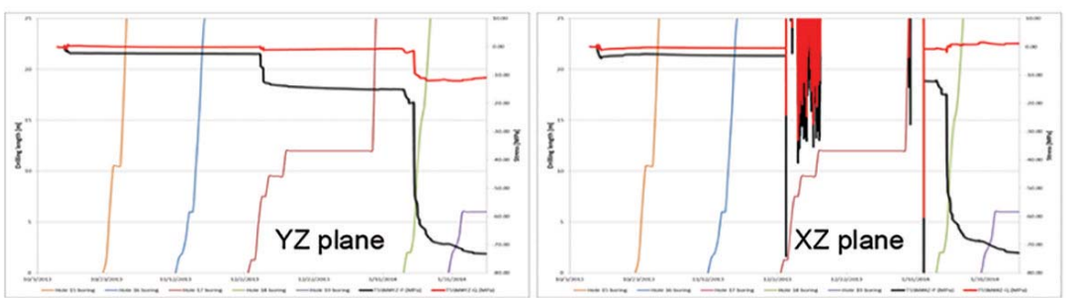

Figure 17—Stress change measurement history for hole 14

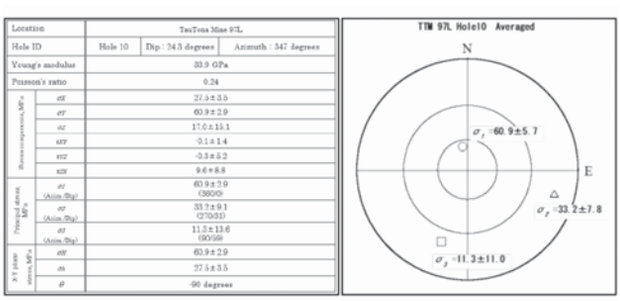

Figure 18—Averaged results from the 3D CCBO absolute stress measurements in hole 10

the minor stress is roughly parallel to dip. The minor stress has a particularly high uncertainty, ranging from 0.3 to 22.3 MPa.

The CCBO and VWSG measurements are discussed and compared with the model results in a later section.

Virgin stress conditions were estimated from the results of Map3D modelling of the shaft pillar area.

Numerical modelling

Background

Borehole breakout occurs when cylindrical holes are drilled in a pre-stressed rock mass. In an idealized triaxial stress field, where the intermediate principal stress is oriented parallel to the hole axis, high tangential shear stresses are developed along the borehole sidewalls oriented parallel to the minor principal stress axis. Failure will either take the form of conjugate fracture zones which intersect at some distance from the borehole wall (Haimson and Song, 1993), or extensile fracturing sub-parallel to the borehole wall and parallel to the major compressive stress direction (Ewy and Cook, 1990; Lee and Haimson, 1993; Sellers and Klerck, 2000). The former results in wedge-shaped fallout bounded by shear fractures, and generally occurs in weak sedimentary rocks. The latter is typical in strong brittle rocks, and has the appearance of buckled slabs that spall away from the free face. This type of extensile fracturing is typically observed around deep-level gold mining excavations (Ortlepp, 1997). Tensile and 'remote' fractures may also occur, depending on the magnitude of the confining stress (Carter, Lajtai, and Yuan, 1992), although these are not expected for isolated holes at depth (Roberts, 2001).

Breakout around a large-scale underground excavation was studied in detail at the AECL Mine-by experimental tunnel (Read, 1994; Martin and Read, 1996; Martin, 1997). Hajiabdolmajid, Kaiser, and Martin (2002) successfully simulated damage around the Mine-by tunnel using a cohesion-weakening and frictional-strengthening strain-softening (CWFS) model implemented in the FLAC program (Figure 19). The model was implemented using user-defined FISH functions. This model has subsequently been implemented in the main FLAC and FLAC3D codes.

Sellers and Klerck (2000) performed tests on cubes of quartzite and norite containing a cylindrical hole drilled halfway through the samples. Solid and layered samples were tested. They were able to replicate the fractures observed in the tests using a Mohr-Coulomb strain-softening discrete fracture algorithm implemented in the Elfen finite/discrete element code. It was found that the presence of layers significantly altered the fracture patterns, resulted in more fracturing than was observed in the solid blocks (Figure 20). The fracturing also tended to be constrained by the layers, that is, fractures did not penetrate through the layer boundaries.

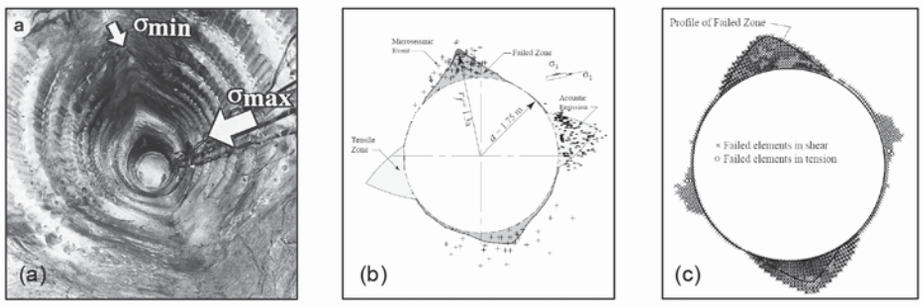

Figure 19—(a) Photograph of the shape of the failed zone observed around the circular test tunnel (after Martin, 1997), (b) schematic showing micro-seismic events locations in the notch area (+), and acoustic emission locations (-) in the tensile failure zone, and (c) damage predicted by the CWFS model (after Hajiabdolmajid, Kaiser, and Martin, 2002)

The literature suggests that a Mohr-Coulomb strain-softening (CWFS) model will accurately model the extent of damage around circular holes in a biaxial stress field. Sellers and Klerck (2000) showed that the presence of contact planes influences the fracturing, tending to constrain the damage between these planes. This was also observed between CLR contacts at the pilot site. The model should be able to replicate this trend.

Modelling approach

Initial modelling with FLAC did not produce satisfactory results. The fracture patterns around the hole tended to follow the rectilinear mesh (Figure 21) and did not resemble the natural breakout patterns shown above (Figure 19 and Figure 20). The mesh structure, command syntax, and FISH implementation of FLAC and FLAC3D differ significantly. Since the intention was ultimately to extend the modelling work into three dimensions, it was decided that it would be more efficient to use FLAC3D to construct and analyse all the models.

Plane strain modelling was done in FLAC3D by extruding 2D meshes made up of triangular zones into 3D prism-shaped zones. The result is a model that is one element thick, with the zone thickness corresponding to the 2D zone edge length in the area of interest. Plane strain conditions were imposed by constraining all grid-points in the out-of-plane (z) direction. The CWFS (Mohr-Coulomb with strain-softening) material model was used to simulate the failure around the holes. Interfaces were used to represent the CLR contacts.

All models are constructed on the same basic template. A solid square block of sufficient size is defined and a fine mesh zone (FMZ) is specified where failure is expected to occur. The block is meshed uniformly in the FMZ and the zone sizes gradually increased towards the boundaries. The model is assigned sliding constraints along three boundaries. A pressure load is applied along the top boundary corresponding to the major principal stress. The x (horizontal) axis in these models corresponds with the strike of the reef. The y axis is the upwards normal to the strata. This axis is offset from vertical by an angle equal to the dip of the strata. Initial stresses that correspond to the major and minor principal stresses are applied throughout the model. Gravity loading is not applied. Geometry features are included in a number of these models. Most commonly, a pair of horizontal lines representing the Carbon Leader contacts are specified. In other models, strata are defined in a similar way at regular spacings above and below the reef. In some of these models the hole profiles are also defined. Strain-softening materials are specified in the FMZ and elastic materials elsewhere. The zones on either side of contact planes are separated and the planes are assigned Mohr-Coulomb strain-softening properties.

It was noted above that the extent of fracturing greatly exceeds the observed breakout volume. The model needs to replicate this observation. Fracturing in the CWFS model is expressed as the accumulation of so much plastic strain that the affected zones reach 'zero' (very low) cohesion. While it is intuitively attractive to remove and replace these failed zones with fill, such an approach will over-estimate the extent of breakout. A novel criterion is required to determine which zones should be removed to replicate the observed breakout.

As failure occurs around the periphery of the hole, the damaged material moves into the hole. The extent of this movement will decrease with distance from the surface of the hole. Examination of various displacement parameters indicated that the displacement contours resemble the shape of breakout observed underground. The magnitude of the displacement vector pointing into the hole and the displacement in a direction parallel to the minor stress (towards the hole centre) were examined as potential candidate criteria. It was found that the x-displacement contours quite closely mimic the typical breakout shape.

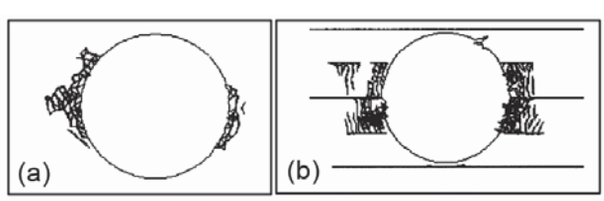

Figure 20—Modelled fractures for (a) solid and (b) layered blocks

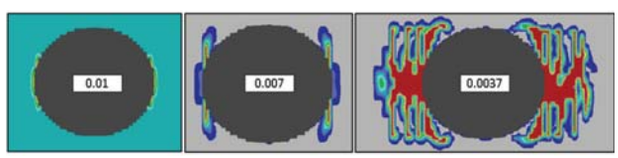

Figure 21—Plastic strain distributions for FLAC models assigned various values of strain-to-failure

Experimentation with these criteria and various other permutations (for example, zone deactivated if plastic strain and displacement criterion are exceeded) showed that the displacement perpendicular to the major stress, expressed as a ratio of the distance to the centre of the hole, provided the best approximation of the breakout volume and shape. Absolute displacement in the same direction gave similar results, but the displacement ratio criterion allowed greater control, particularly at higher criterion values.

Table I shows how the breakout shape and volume vary with the value of the displacement ratio criterion. For a displacement ratio of 10^{-4}, zones not involved in the breakout process are deactivated, which is not realistic. At a ratio of 5×10^{-4}, the breakout resembles the extreme cases observed underground. This value represents a practical maximum value of breakout (0.42 m^3/m). The maximum observed breakout of 0.63 m^3/m cannot be achieved with this material set or deactivation criterion. For ratios greater than 0.15 less breakout occurs than was observed, so this serves as an upper limit for this criterion. At a value of 0.29 no zones are deactivated. The criterion needs to be recalibrated for different property sets. The deactivation criterion is not, strictly speaking, a material property since its ideal value depends on the deformation mechanics of the model. It is nevertheless reasonable to assign different critical values to different materials.

The deactivation procedure is initiated after a stable solution is obtained by the FLAC3D 'unbalanced force ratio' criterion. After the zones are deactivated they are re-initialized and assigned the properties of the fill material in a single step. No timestepping occurs between deactivating the zones and reactivating them as fill.

It is essential that the filling procedure does not significantly alter the stress distribution around the hole, or induce significantly more damage during subsequent cycling. An algorithm was developed that averages the stress components in the zones that are to be deactivated. These averaged stresses are applied as initial stresses in all fill zones when these zones are reactivated. This algorithm resulted in a less disturbed stress distribution than applying zero stress in the fill zones. Further experimentation revealed that applying a factor to the averaged stresses was even more effective in reducing the stress disturbance. The optimal factor for the models discussed in this paper was –0.1. This equates to the application of a small tensile stress within the fill.

Calibration

The unknown parameters in this study include the internal cohesion, internal friction angle, and plastic strain-to-failure of the hangingwall, footwall, and CLR strata. The properties of the contacts between the CLR and surrounding quartzites will also affect the extent of failure and breakout. The initial assumed rock mass material properties were obtained from back-analysis of laboratory experiments by Roberts (2012). The strength (cohesion) was reduced to between 48 and 58% of laboratory values, in accordance with York (1998), to represent *in situ* rock mass properties. For the contact planes, Sellers and Klerck (2000) used a friction angle of 30° (and zero cohesion) between rock layers to simulate laboratory experiments.

Table I

Breakout shapes and volumes for various critical displacement ratios using material property set S1

Displacement ratio	0.0001	0.005	0.008	0.015
Removed volume (m^3/m)	0.52	0.215	0.136	0.044
Breakout shape	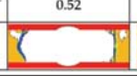	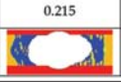	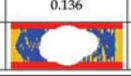	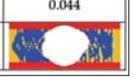

The deviation of some of the holes into the surrounding quartzites provided valuable data that could be used to calibrate material properties and contact parameters. Based on the measured breakouts and observed fracturing the calibration criteria in Table II are used.

For the geology shown in Figure 12, fracturing extending one hole diameter away from the edge of the borehole is expected. The breakout volume for this hole is not known, but is assumed to be typical (0.08 to 0.12 m^3/m). A model was created to simulate the damage around this hole. The photographs were digitized and the strata positions traced to replicate these contacts as accurately as possible.

The resulting cohesion distribution using set xR model parameters is shown in Figure 22. The extent of fracturing is similar to that observed underground. Penetration of the fractures into the stratum below the CLR is also replicated, particularly further away from the hole. The 'onion-skin' nature of the fractures is not replicated in the model. Fractures form a lattice that we would more typically expect to see in 2D models of pillar fracturing. This is a feature of this implementation of Mohr-Coulomb strain softening. As noted above, the intention here is not to precisely replicate the shape of the fracturing, but to match the extent of fracturing so that the resulting stress redistribution and deformation are simulated.

Modelling the strata around this hole with various material and contact property sets provided simple guidelines for further calibration. It was found necessary to reduce the

Table II

Calibration criteria

Scenario	Minimum breakout (m^3/m)	Maximum breakout (m^3/m)
Isolated hole in a single material (hangingwall or footwall)	0.02	0.06
Isolated hole in centre of reef	0.04	0.18
Isolated hole with top contact coinciding with top of hole	0.04	0.20
Isolated hole with top contact coinciding with bottom of hole	0.05	0.13
Elsewhere, including locations where the bottom contact coincides with bottom of hole	0.02	0.10

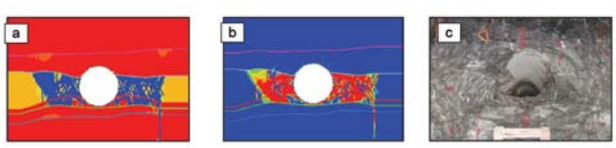

Figure 22—Internal cohesion (a) and maximum plastic shear strain (b) for the 'exact' model using set xR parameters, compared to fracturing observed underground (c)

CLR internal friction angle from that of the host rock (from 48° to 40°) to obtain the extent of fracturing observed. The damage could not be matched by reducing UCS, tensile strength, or plastic strain-to-failure. It was necessary to include contacts. Without contacts, even greatly weakening the CLR material properties did not result in a degree of fracturing similar to that observed. It was found that a minimal value of contact cohesion (0.5 MPa) on all contacts produced the best approximation to the observed fracturing. Appropriate values for contact friction were generally quite low (15–30°) relative to those previously employed in the literature.

With these basic features of the fracturing and breakout successfully approximated, more detailed features observed at the pilot site were used to fully calibrate the model.

The effect of the vertical hole position was examined by varying the hole position relative to the CLR stratum in a standard model. The intention was to match the trends evident in Figure 10. In this model, only the top and bottom CLR contacts were modelled. Experiments with multiple strata contacts in the footwall and hangingwall showed that excessive breakout and failure occurred unless the contacts were exceptionally strong (Ø>45°, C_0>5 MPa). They are therefore treated as 'welded' and not modelled as interfaces. Given the asymmetry in the response when the hole approaches the upper and lower CLR contacts, different properties are assigned to these, with the upper contact expected to be weaker or to have a lower friction angle.

In this model the hole is not predefined and can be bored at any position in the model FMZ. To assess the variability imposed by the underlying mesh geometry, the model was run with the hole placed randomly. The resulting distribution of breakout volume as a function of vertical (y) position is shown in Figure 23. The expected envelope of breakout volumes observed underground is included in the vertical position graph.

Most of the breakout values fall within the expected envelope for the vertical position graph. The breakout where the hole bottom coincides with the upper contact slightly exceeds the expected maximum, and the lowest values tend to be lower than the expected minimum of 0.02 m^3/m. Some variability is evident, as holes with similar elevations show different breakout levels. In the 'typical' range (0–0.06 m^3/m) this variability can be as high as 0.02 m^3/m.

The material models and contact properties given for property set S8 (upper CLR: Ø=40°, C_0=0.5 MPa, lower CLR: Ø=30°, C_0=0.5 MPa) were used in the subsequent modelling.

Fill properties

The fill material was extensively tested using specimens prepared in a laboratory setting and core obtained from fill emplaced in holes at the pilot site. The resulting average material properties are given in Table III.

The plastic strain at which the minimum cohesion is attained (plastic strain-to-failure) was set to the same value as the rock mass.

Modelling of the 10-11-14-17-18 hole sequence at Tau Tona

Model set-up

The holes in this sequence are shown in Figure 24. It is evident that the holes deviate significantly from the reef package, and are not consistently parallel. Cross-sections (along strike) at different positions result in very different geometries along the length of the holes.

The 3D model in Figure 24 was cut through by a series of planes oriented approximately perpendicular to the hole axes and spaced 1.5 m apart over the length of the hole. The individual slice geometries were meshed in two dimensions and analysed using the calibrated properties obtained above. Recall that hole 17 was half-filled from the southern (lower) reef drive. The hole was therefore not filled in the models representing the upper half of the hole profiles.

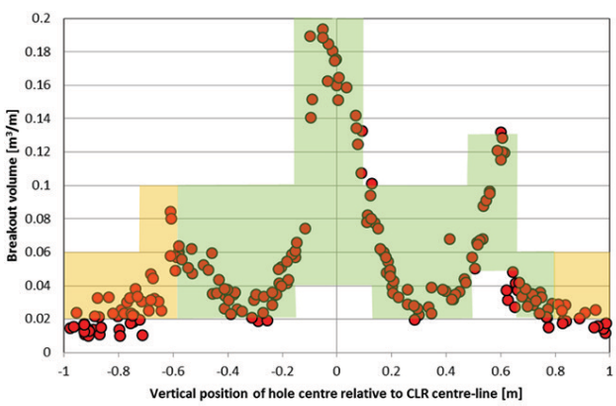

Figure 23—Effect of vertical position on the breakout volume for property set S8

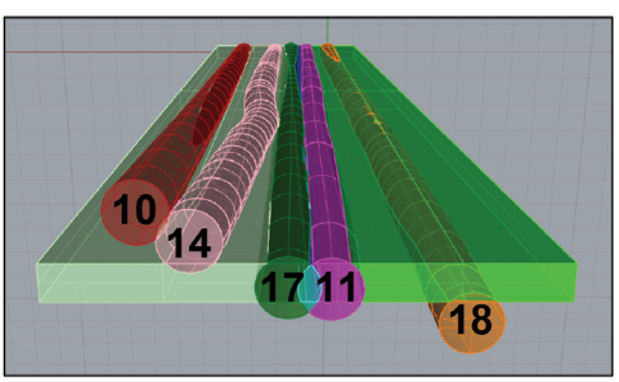

Figure 24—Perspective view of holes 10, 11, 14, 17, and 18 relative to the reef package, viewed from the northern reef drive

Table III

Fill material properties

Property	Value
Young's modulus	34.6 GPa
Poisson's ratio	0.24
Density	2160 kg/m^3
Initial cohesion	30 MPa
Minimum cohesion	0.1 MPa
Initial friction angle	35°
Maximum friction angle	40.4° (at one-tenth of maximum plastic strain)
Maximum dilation angle	10°
Tensile strength	9.9 MPa

Results

The distribution of breakout and damage along the length of the holes is now examined in detail. In the following discussion, 'length' refers to distance from the southern reef drive. The coloured regions indicate material that has been replaced with fill at the end of the relevant stage and correspond with the hole profile plus the expected breakout. The colours in each stratum (CLR, hangingwall, and footwall) also vary as the filling algorithm assigns filled groups according to the rock mass group to which the material originally belonged.

Hole 10

Hole 10 is an isolated hole that deviates upwards so that it lies entirely in the hangingwall at the northern reef drive. At this point the bottom of the hole is around 200 mm above the upper reef contact. The modelled and observed distributions of breakout volume are compared in Figure 25. Table IV compares the breakout shapes. The largest modelled breakouts occur when the hole is in the centre of the reef and the upper contact coincides with hole bottom. This conforms to expected behaviour (Figure 23) but appears to be offset (in terms of the length axis) from the underground scan data. Lower modelled breakouts occur when the hole is located in the hangingwall, as observed in the scans. The breakout shapes show similar trends, but there is a mismatch at 12 to 18 m. It appears that the actual hole is no longer influenced by the reef contact, while the modelled breakout is clearly affected and reaches a maximum at this point. This is due to the positions of the actual and modelled holes (relative to the CLR contact) being slightly different. Shifting the model result to the left gives much better parity.

Hole 11

Hole 11 is far enough from hole 10 to ensure that induced stresses will be low, and therefore little additional breakout is expected. The hole is located in the reef package for its entire length, so a reasonably uniform distribution of breakout is expected. This is confirmed in Figure 26. The average breakout is 0.10 m^3/m. This hole was not scanned, so no data is available for comparison.

Hole 14

Hole 14 is bored initially between holes 10 and 11 and then deviates upwards and towards hole 10. The hole follows an S-curve as it moves slightly away from hole 10 and then abruptly curves towards it and deviates sharply upwards. The modelled and observed distributions of breakout volume are compared in Figure 27. Breakout shapes are compared in Table V. The observed breakout is quite variable initially, and tends to become limited to the western sidewall when the distance to hole 14 reduces. The model shows the opposite trend, with more breakout in the damaged eastern sidewall. It appears that the deactivation algorithm is allowing too much breakout in the hangingwall layer. The critical displacements in the different material layers are not well calibrated for this particular situation.

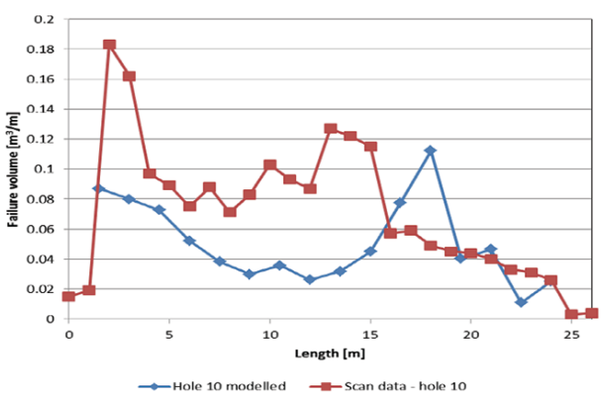

Figure 25—Observed and modelled distribution of breakout volume along the length of hole 10

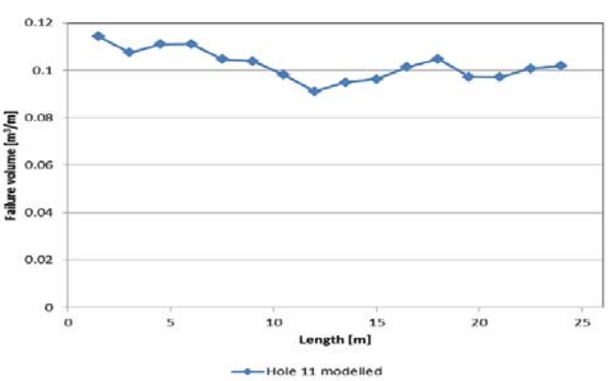

Figure 26—Modelled distribution of breakout volume along the length of hole 11

Table IV

Comparison of observed and modelled breakouts around hole 10

Length	4.5 – 5 m	9 m	12 m	15 m	18 m	20 - 21 m
Scan	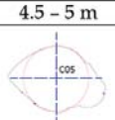	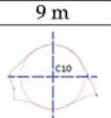	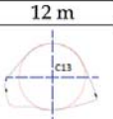	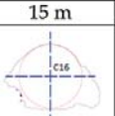	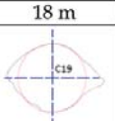	
	0.097 m^2	0.083 m^2	0.087 m^2	0.12 m^2	0.049 m^2	0.044 m^2
Model	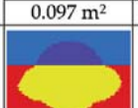	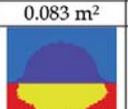	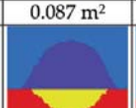	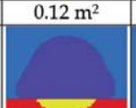	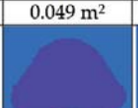	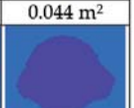
	0.073 m^2	0.03 m^2	0.026 m^2	0.045 m^2	0.11 m^2	0.046 m^2

Hole 17

In reality and in the models, hole 17 shows breakout only towards the top of the hole, where the distance between holes 17 and 14 increases sufficiently for breakout to occur.

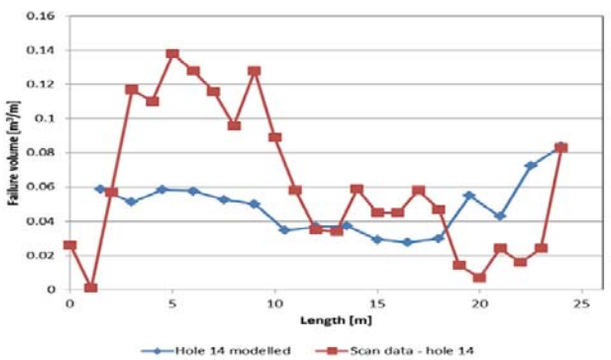

Figure 27—Observed and modelled distribution of breakout volume along the length of hole 14

Figure 28 shows that damage occurs in the western side of the unfilled hole 17 when hole 18 is drilled, as was observed on site (Figure 15).

Hole 18

Hole 18 is bored in the highly stressed region adjacent to hole 11. The hole dips into the footwall, gradually at first and then, from around 21 m length, quite abruptly. The gap to hole 11 increases from zero to about 0.8 m at the northern reef drive.

Figure 9 shows the distribution of breakout extents and the breakout shapes along the length of the hole. Breakouts are compared in Table VI and Figure 29.

Breakout around hole 18 shows a general increase from the southern drive up to a maximum at 12 m by observation, and at 22 m in the model. As the distance between the holes increases, the breakout volume increases up to the point where the hole dips down rather abruptly into the footwall, whereupon the hole straddles the lower reef contact and breakout volume decreases. The observed and modelled

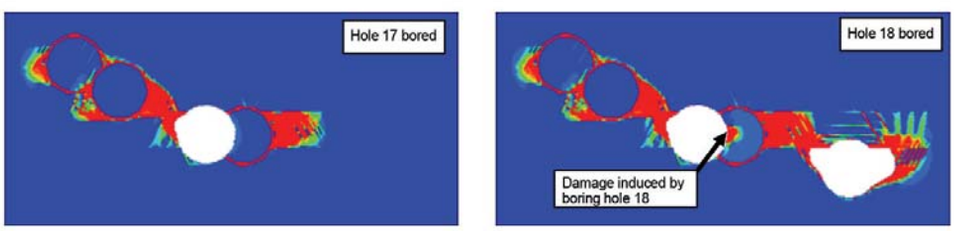

Figure 28—The appearance of damage in the fill in the sidewall of hole 17 after hole 18 is bored (northernmost model)

Table V

Comparison of observed and modelled breakouts around hole 14

Length	4.5–5 m	9 m	12 m	15 m	18 m	24 m
Scan	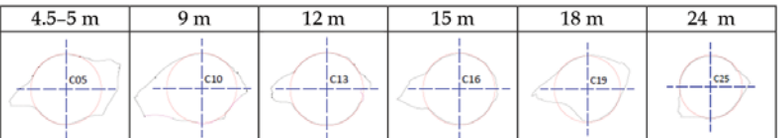					
	0.11 m²	0.13 m²	0.035 m²	0.045 m²	0.047 m²	0.024 m²
Model	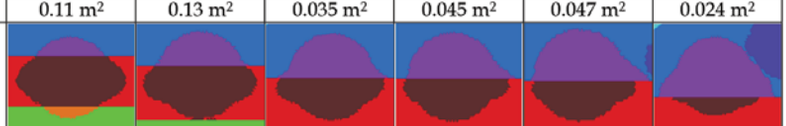					
	0.058 m²	0.05 m²	0.03 m²	0.03 m²	0.03 m²	0.072 m²

Table VI

Comparison of observed and modelled breakouts around hole 18

Length	4.5 – 5 m	9 - 10 m	12 m	15 m	18 m
Scan	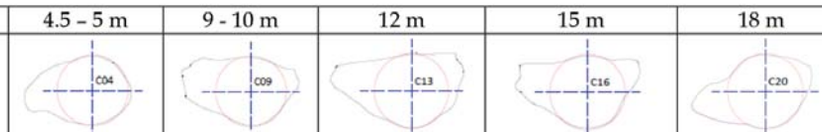				
	0.12 m²	0.17 m²	0.29 m²	0.11 m²	0.07 m²
Model	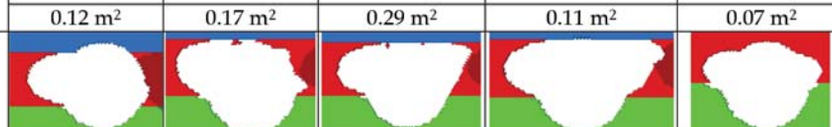				
	0.087 m²	0.11 m²	0.11 m²	0.14 m²	0.07 m²

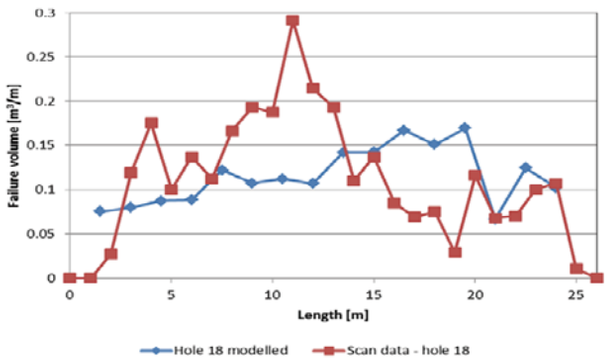

Figure 29—Observed and modelled distribution of breakout volume along the length of hole 18

breakout shapes are generally very similar, but the magnitudes differ, particularly when the hole dips.

Stress measurement comparison

The stresses measured by the VWSGs are compared with modelled stresses in Figure 30. In these graphs the major measured stresses from each VWSG pair are averaged. The principal measured stresses were oriented approximately on dip, on strike, and perpendicular to the reef plane, which allows us to compare the *xx*, *yy*, and *zz* stresses directly with the measured stresses. CCBO measurements are shown in the graph for hole 10.

In hole 10, the measured subvertical (reef-perpendicular: *yy*) stresses are up to 35 MPa higher than those modelled. Both the model and VWSGs give higher stresses than the CCBO measurement: the CCBO reading is around half that of the VWSG. The strike stresses (*xx*) show better correlation, differing by only 3.7 MPa in the final stage. These values approximately correspond with the lower error bracket of the CCBO reading. The dip stress (*zz*) according to the VWSG is tensile, while the CCBO and model results indicate compressive stresses of up to 22.3 MPa and 25.4 MPa, respectively. All components in hole 14 are reasonably well matched, but the subvertical (*yy*) stress measured in response to the boring of hole 18 is much greater than that modelled.

Closure

The deformation in response to the boring of holes is expressed as closure. Closure provides a measure of the extent to which the surrounding rock mass is disturbed by the mining operation and, as a relative measure, indicates the potential for seismic energy release. Closure in this instance is measured as the change in *y* displacement at horizons 1.5 m above and below the reef centreline. This envelope was chosen as it corresponds to the height of the reef drives at either end of the holes. The closures at the southern and northern reef drives were extracted from the model results and are presented in Figure 31. Both histories show the greatest increases in closure over stages where significant failure occurs. For example, after boring hole 14 the rock mass spanning all holes (plus the fractured zone around holes 10 and 11) has failed.

Discussion

The extent of simulated breakout is generally consistent with that observed underground; however, the distribution of breakout along the length of the hole is not faithfully replicated. The effect of the vertical position of the hole is clearly discernible in the results, as is the increased fallout volume and asymmetric breakout around the more highly stressed hole (hole 18). The absence of fallout in the hole bored between filled holes (hole 17) is also replicated, with damage occurring later when the adjacent hole was bored. The differences in breakout volume are partially explained by the variability of the geology and differences in the relative positioning of the holes.

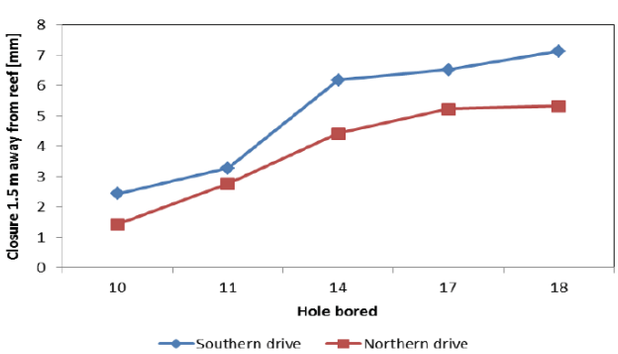

Figure 31—Maximum closure measured between horizons 1.5 m above and below the reef drive

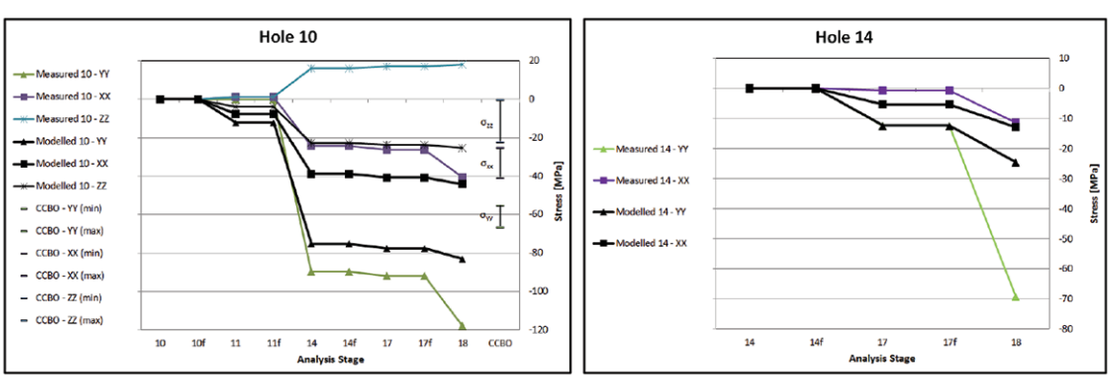

Figure 30—Comparison between modelled and measured stress readings in holes 10 and 14. Error bars show the range of values obtained by CCBO measurements for each component

The correlation between measured and simulated stresses was inconsistent. The VWSG-measured dip stresses were tensile, which does not correspond with the modelled stresses or those measured by CCBO. The strike stresses were in reasonable agreement with the measured stresses. Strata-perpendicular stresses measured by VWSG were higher than those modelled, and both were higher than those measured using CCBO. The measured subvertical and strike stress changes correspond well with the boring of nearby holes, but the measured magnitude of the subvertical changes appears to be higher than the modelled value. Stresses within the models varied considerably: from 131 MPa to 47 MPa in hole 10. Shifting the position of the measurement to the west in the model would give values much closer to those measured with the VWSGs, while shifting the position to the east would give values closer to the CCBO measurements. For the purposes of forward modelling it is sufficient that the stress gradient captures both the maximum and minimum values indicated by the instruments.

Closure histories showed that closure increases with the effective excavated span. The closure increases most abruptly when large volumes of rock mass fail. The decreasing closure increments indicate that the system is becoming more stable. Even when a hole (18) is drilled outside of the filled region, the closure increment is small compared to the increments recorded while creating the initial span (10-11-14).

The correlations obtained here are believed to be sufficient for forward modelling. It is re-emphasized that the breakout deactivation algorithm is not suitable for general use, and needs to be calibrated according to the context in which it is to be used.

Conclusions

A pseudo-3D model for simulating drill-and-fill operations on the Carbon Leader Reef was calibrated against underground data and used to successfully replicate the damage and observations around a selected sequence of holes at the 97 level test site. Sequencing of the holes, the resulting geometry of the holes and pillars, and the local geological and material characteristics, had a significant influence on the occurrence of damage and stress redistribution.

A novel displacement-based method for simulating breakout was developed for use on Carbon Leader models. Although the breakout distributions were not precisely matched, the modelled values lay within the extremes that were observed. Other features, such as the additional damage that occurred in the fill around hole 17 after boring hole 18, were replicated. Asymmetrical breakout was replicated around hole 18, but not around hole 14, where the critical displacement values appeared not to be well calibrated.

Modelled stresses and measured stress histories showed similar trends, but the magnitudes differed by varying degrees in each stress component. The modelled subvertical stresses were generally lower than those measured by vibrating wire stress gauge (VWSG), although both were greater than that obtained from a compact conical borehole overcore (CCBO) measurement. Either measured value could be obtained by simply shifting the measurement position in the model. The strike stresses correlated reasonably well. Dip stresses were very different: tensile stresses were indicated by the VWSGs, and comparable compressive stresses by CCBO and by the model. Since there is no obvious mechanism for generating tensile stresses in this situation, it is suggested that the VWSG reading for this component be discounted.

Further work will focus on implementing the systems described here in a fully three-dimensional model. Variations in the out-of-plane (dip) stress and geometry can then be accounted for. A more thorough set of sensitivity analyses will be done and forward modelling will be employed (in 2D and 3D) to determine the optimal extraction sequence and fill parameters.

Acknowledgements

The authors wish to thank the Tau Tona reef-boring team, rock engineering staff, surveyors, and management for their assistance. Thanks to Willie Timmerman, Johann de Wett, and Henry Klopper at African Consulting Surveyors for their diligence in creating and processing the scans; to Chris Stander and Willie Janse van Rensburg for their assistance underground; to the ATIC team for their assistance and support; to George Kgori for drilling a special hole; to Gerhard Hofmann for assisting with stress measurements and interpretations; to Roelize Nel for assistance with seismic interpretation; to Lourens Scheepers for his guidance and leadership; and to Shaun Newberry and AngloGold Ashanti for permitting publication of this information.

References

Adams, G.R. 1978. A study of the fractures forms in the rock around openings made by a reef boring machine. *Research report* no. 60/78. Chamber of Mines Research Organisation, Johannesburg.

Carter, B.J., Lajtai, E.Z., and Yuan, Y. 1992. Tensile fracture from circular cavities loaded in compression. *International Journal of Fracturing*, no. 57. pp. 221–236.

Ewy, R.T. and Cook, N.G.W. 1990a. Deformation and fracture around cylindrical openings in rock – I: Observations and analysis of deformations. *International Journal of Rock Mechanics and Mining Sciences & Geomechanics Abstracts*, vol. 27. no. 5. pp. 387–407.

Ewy, R.T. and Cook, N.G.W. 1990b. Deformation and fracture around cylindrical openings in rock – II: Initiation, growth and interaction of fractures. *International Journal of Rock Mechanics and Mining Sciences & Geomechanics Abstracts*, vol. 27. no. 5. pp. 409–427.

Haimson, B. and Song, I. 1993. Laboratory study of borehole breakouts in cordova cream: a case of shear failure mechanism. *International Journal of Rock Mechanics and Mining Sciences & Geomechanics Abstracts*, vol. 30, no. 7. pp. 1047–1056.

Hajiabdolmajid, V., Kaiser, P.K., and Martin, C.D. 2002. Modelling brittle failure of rock. *International Journal of Rock Mechanics and Mining Sciences*, vol. 39. pp. 731–741.

Hofmann, G., Scheepers, L., and Ogasawara, H. 2013. Loading conditions of geological faults in deep level tabular mines. *Proceedings of the 6th International Symposium on In Situ Rock Stress*, Sendai. Japan, 20–22 August, 2013. International Society for Rock Mechanics.

Jager, A.J., Westcott, M., and Cook, N.G.W. 1975. A geological assessment of the applicability of reef boring to mining the Basal, Carbon Leader and Vaal Reefs. *Research report* no. 20/75. Chamber of Mines Research Organisation, Johannesburg.

KLERCK, P.A. 2000. The finite element modelling of discrete fracture in quasi-brittle materials. PhD thesis, University of Wales. Swansea.

LEE, M. and HAIMSON, B. 1993. Laboratory study of borehole breakouts in Lac du Bonnet granite: a case of extensile failure mechanism, *International Journal of Rock Mechanics and Mining Sciences & Geomechanics Abstracts*, vol. 30, no. 7. pp. 1039–1045.

MARTIN, C.D. 1997. The effect of cohesion loss and stress path on brittle rock strength. *Canadian Geotechnical Journal*, vol. 34. pp. 698–725

MARTIN, C.D. and READ R.S. 1996. AECL's Mine-by experiment: a test tunnel in brittle rock. *Proceedings of the 2nd North American Rock Mechanics Symposium*, Montreal. Vol. 1.. Aubertin, M., Hassani, F., and Mitri, H. (eds). A.A. Balkema, Rotterdam. pp. 13–24.

MURPHY, S.K. 2012. Linear elastic numerical modelling for failure prediction – an assessment. *Journal of the Southern African Institute of Mining and Metallurgy*, vol. 112, no. 8. pp. 737–748.

ORTLEPP, W.D. 1997. Rock Fracture and Rockbursts: an Illustrative Study. *Monograph Series* M9. South African Institute of Mining and Metallurgy, Johannesburg.

READ, R.S. (1994). Characterizing excavation damage in highly stressed granite at AECL's Underground Research Laboratory. *Proceedings of the International Conference on Deep Geological Disposal of Radioactive Waste*. Winnipeg, Toronto. Martino, J.B. and Martin, C.D. (eds). Canadian Nuclear Society. pp. 35–46.

ROBERTS, D.P. 2001. The influence of tunnel shape on damage and fracture propagation at ultra-depth. *Proceedings of the Fourth International Conference of Discontinuous Deformation*, University of Glasgow, June 2001. University of Glascow. pp 35–46.

ROBERTS, D.P. 2012. Numerical simulation of shear fracture evolution in laboratory-scale samples. *Journal of the Southern African Institute of Mining and Metallurgy*, vol. 112, no. 8. pp. 685–695.

SELLERS, E.J. and KLERCK, P.A. 2000. Modelling of the effect of discontinuities on the extent of the fracture zone surrounding deep tunnels under pressure. *Proceedings of the World Congress of International Tunnelling Association (ITA 2000)*, Durban, South Africa, 13–18 May 2000. Stacey, T.R. (ed.). Southern African Institute of Mining and Metallurgy, Johannesburg.

SUGAWARA, K. and OBARA, Y. 1999. Draft ISRM suggested method for *in situ* stress measurement using the compact conical-ended borehole overcoring (CCBO) technique. *International Journal of Rock Mechanics and Mining Sciences*, vol. 36. pp. 307–322.

YORK, G. 1998. Numerical modelling of the yielding of a stabilizing pillar/foundation system and a new design consideration for stabilizing pillar foundations. *Journal of the South African Institute of Mining and Metallurgy*, vol. 98, October. pp. 281–297. ◆

APPENDIX

MATERIAL AND CONTACT PROPERTY SETS.

Material	Property	Set 1	Set 3	Set S8	Set xR	Set 9d
Quartzites	Young's modulus [GPa]	70	70	70	70	70
	Poisson's ratio	0.25	0.25	0.25	0.25	0.25
	Density [kg/m³]	2700	2700	2700	2700	2700
	Initial cohesion [MPa]	28	28	28	28	28
	Minimum cohesion [MPa]	0.1	0.1	0.1	0.1	0.1
	Initial friction angle	40°	40°	40°	40°	40°
	Maximum friction angle	48°	48°	48°	48°	48°
	Maximum dilation angle	15°	15°	15°	15°	15°
	Tensile strength [MPa]	10	10	10	10	10
	Maximum plastic strain	2e-3	2e-3	2e-3	2e-3	2e-3
	Deactivation criterion [mm/mm]	N/A	0.003	0.003	N/A	0.003
Carbon Leader Reef (CL)	Young's modulus [GPa]	70	70	70	70	70
	Poisson's ratio	0.25	0.25	0.25	0.25	0.25
	Density [kg/m³]	2700	2700	2700	2700	2700
	Initial cohesion [MPa]	23	23	23	23	23
	Minimum cohesion [MPa]	0.1	0.1	0.1	0.1	0.1
	Initial friction angle	40°	35°	35°	35°	35°
	Maximum friction angle	48°	40°	40°	40°	40°
	Maximum dilation angle	15°	15°	15°	15°	15°
	Tensile strength [MPa]	10	10	10	10	10
	Maximum plastic strain	2e-3	2e-3	2e-3	2e-3	2e-3
	Deactivation criterion [mm/mm]	N/A	0.023	0.008	N/A	0.0125
CL (upper) Contacts	Contact cohesion	0.5	0.5	0.5	0.5	0.5
	Contact friction angle	25°	25°	30°	15°	20°
CL (lower) Contacts	Contact cohesion	0.5	0.5	0.5	0.5	0.5
	Contact friction angle	25°	30°	40°	30°	30°
Qzite Contacts	Contact cohesion	0.5	-	-	0.5	0.5
	Contact friction angle	25°	-	-	30°	30°

http://dx.doi.org/10.17159/2411-9717/2017/v117n7a13

Further development of a chemistry proxy for geometallurgical modelling at the Mogalakwena mine

by R.P. Schouwstra*, D.V. de Vaux†, and Q. Snyman‡

Synopsis

The Mogalakwena platinum mine is Anglo American Platinum's flagship opencast operation and has been the focus of numerous optimization studies. The initial outcomes of a geometallurgical programme were reported on in 2013. This paper further describes the development of a geochemical proxy to identify different ore types at the operation and link these with various metallurgical parameters, with the aim of optimizing the value chain. At Mogalakwena, all blast-hole samples are submitted for chemical analysis by XRF prior to blasting, thus allowing the ore to be stockpiled and treated according to grade. This paper demonstrates that it would be possible to use the chemical data to stockpile and process ores according to ore type (rock type and grade), since preliminary results indicate that the metallurgical characteristics (*e.g.* hardness, flotation characteristics, rheology, *etc.*) are linked to rock composition, which defines rock types. This investigation formed part of the geometallurgical programme at Mogalakwena. The final objective of the programme focuses on risk mitigation with improved production forecasts and full implementation of the principles of geometallurgy, resulting in the optimization of metallurgical treatment and adding value to the bottom line.

Keywords

Platreef, geometallurgy, geochemistry, domains, discriminant analyses, ore type.

Introduction

Various studies of the Platreef, in the northern limb of the Bushveld Complex, have highlighted the complexity of the reef and its mineralization (Wagner, 1926; White, 1994; Kinnaird *et al.*, 2005; Holwell, 2006; Holwell and McDonald, 2006). Most studies have focused on the southern exposures – the major mining area during the earlier years of mining the Platreef, with a smaller number of studies undertaken on the areas to the north. In the southern area the Platreef rests on the sediments of the Transvaal Supergroup (banded iron formation and dolomites), whereas further north the footwall to the reef consists of granofels and Archaean granites (Figure 1).

As described by Schouwstra *et al.* (2013) the footwall to the reef has had a major impact on the Platreef composition, resulting in the presence of various ore types, each with certain metallurgical characteristics. The study by Schouwstra *et al.* (2013) described the dominance of four major ore types based on abundance and impact on metallurgical performance (resistance to grinding, flotation characteristics, rheology, *etc.*). These are:

- Pyroxenite, described by Holwell and McDonald (2006) as the best preserved 'primary' style of mineralization of the Platreef. The mine geologists use the term 'feldspathic pyroxenite' where the feldspar content is more than 10%. This definition is not internationally recognized, and Nex *et al.* (2006) propose to limit the use of the term to rocks in which the feldspar occurs interstitial to the pyroxene, rather than in a cumulus texture. They recommend the restriction of this term to material containing less than 20% feldspar. At higher feldspar contents, the rock should be classified as a melanorite or noriite. Pyroxenite is the dominant ore type at the Mogalakwena North operation and exhibits favourable metallurgical characteristics
- Parapyroxenite, compositionally a highly variable rock type, both in mineral content and appearance. This classification is also not an internationally accepted rock term. Originally the term was used to describe a hybrid pyroxenite resulting from the assimilation of copious amounts of footwall (dolomite) by the intruding Bushveld magma, but over the years the term parapyroxenite has been applied more frequently to describe rock types that are highly altered and difficult to identify. The wide variation in chemical and mineralogical composition results in

* *Independent Consultant, previously Anglo American Technical Solutions Research, South Africa*

† *Independent Mineral Processor, previously Anglo American Technical Solutions Research, South Africa.*

‡ *Anglo American Platinum, South Africa.*

 ISSN 2225-6253. Paper received May 2016; revised paper received May 2017.

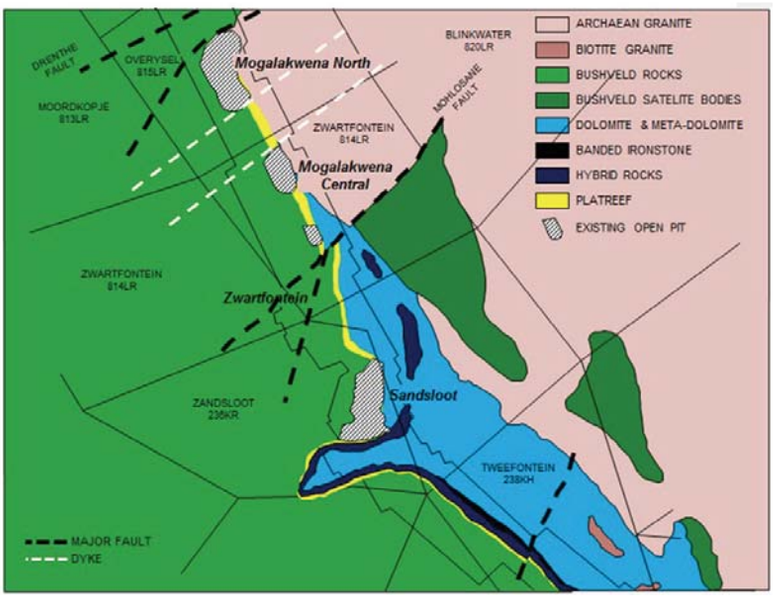

Figure 1—Geological map of the Mogalakwena area (Schouwstra *et al.*, 2013)

significant variation in metallurgical characteristics. Schouwstra *et al.* (2013) proposed subdividing the group into a high- and a low-calcium component (reflected mineralogically in the abundance of diopside). The metallurgical characteristics of the parapyroxenite grouping are also highly variable, and it was postulated that by dividing the group in a high- and a low-Ca subcategory the link to metallurgical characteristics could be improved

- Calc-silicate, basically a skarn rock resulting from dolomite-magma interaction. It displays typical metamorphic effects and is characterized by high contents of calcium-rich minerals (diopside, garnets, wollastonite, *etc.*). This rock type occurs at the footwall of the reef but is also present as rafts higher up in the reef stratigraphy. The contact with the pyroxenite is usually gradational via an intermediate zone of parapyroxenite. Both the calc-silicate and parapyroxenite are more common where the footwall consists of dolomite (the Sandsloot mining area). According to the information available, the calc-silicate has very poor metallurgical characteristics and is usually stockpiled
- Serpentinites are described as being fairly common in close proximity to major discontinuities such as the Drenthe and Mohlosane River faults. Mineralogical characterization indicated that many of the serpentinites contain less than 50% serpentine, whereas in other cases chlorite is the more abundant mineral phase (chloritization). However, there is no doubt that these rocks are highly altered and contain large amounts of hydrated magnesium silicate minerals. Available information indicates that the presence of large amounts of altered silicates adversely affects the rheology of the ore during processing.

As mentioned earlier, the footwall rocks are variable, with dolomite prominent in the southern areas of the Mogalakwena operations and granites and granofelses occurring in the north. The footwall rocks exhibit sporadic mineralization, normally associated with veining.

The hangingwall rocks consist of norites and gabbronorites and may also contain mineralization. Where mineralized, the norite is known as a hybrid norite.

Most of the mineralization can be described as disseminated sulphides with associated platinum group minerals (PGMs), although high sulphide grades do not necessarily indicate high platinum group element (PGE) values (Holwell and McDonald, 2006). There is also no clear link between rock type and PGE grade, with all rock types containing high and low grades, as well as barren areas.

More detailed descriptions of the mineralogy of the various rock types is given in Schouwstra *et al.* (2013).

The use of quantitative XRD to classify rock types

Given the difficulty of identifying the various rock types in hand specimen, especially the more altered or hybrid rock types, Schouwstra *et al.* (2013) used a combination of geochemistry and quantitative X-ray diffraction (XRD) to classify the various rock types. If it is possible to use chemistry as an indication or rock type and establish a link between rock type and metallurgical characteristics, then chemistry can be used as a direct indicator (or proxy) of metallurgical behaviour (ore type) – see Figure 2.

Quantitative XRD data was used to classify more than 200 samples into the different rock types, based on the following constraints.

- Pyroxenite group: mainly enstatite pyroxene, minor amounts of diopside, and less than 20% feldspar (higher feldspar contents would move the sample into the norite group)
- Parapyroxenite group: substantial amounts of diopside and other calcium-rich minerals (garnet, amphibole, *etc.*). A range of 15 to 25% diopside set the boundaries for the low-Ca parapyroxenites, whereas a diopside content of between 25 and 35% placed the sample in the high-Ca parapyroxenite class

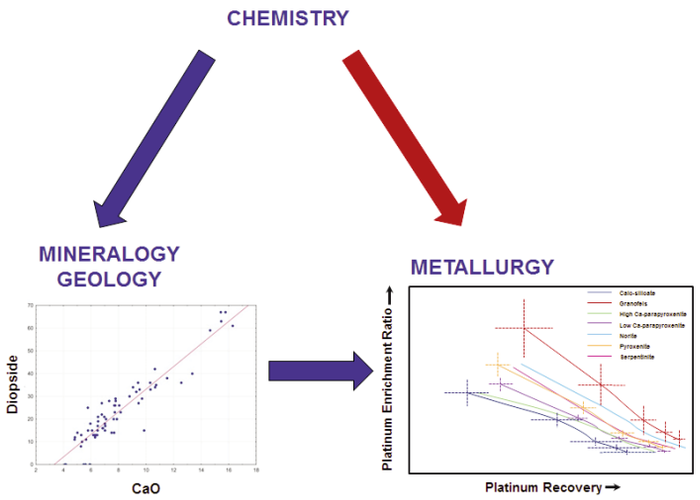

Figure 2—Ternary model: chemistry – mineralogy (rock type)—metallurgy (ore type)

- Calc-silicate group: samples containing in excess of 35% diopside were classified as calc-silicates
- Serpentinite: rocks containing more than 50% hydrated silicates such as serpentine and chlorite
- Granite and granofels (footwall): these rocks were easy to recognize from the high quartz and feldspar contents
- Norite (hangingwall): high plagioclase feldspar contents, with lesser amounts of pyroxene (mainly enstatite).

Although these constraints result in artificial boundaries and combine different rock groups (*i.e.* pyroxenite and feldspathic pyroxenite) into a single class, the classification is consistent and provides a framework for linking in various metallurgical characteristics. As such, the classification should not be seen as a geological tool, but rather as an initial geometallurgical domain classification.

After the rock classification by quantitative XRD, a discriminant analysis of the chemical data by X-ray fluorescence (XRF) was performed to establish whether the chemical data could explain the differences recognized by XRD.

Discriminant analysis

Discriminant analysis is a statistical technique that is used to determine which variables discriminate between two or more naturally occurring groups (Hill and Lewicki, 2006). In this case the groups were the rock types as discussed above, and the variables were the concentrations of the oxides of calcium, magnesium, and iron, and alumina and silica.

In the case of two groups and a single variable, identifying whether the variable does discriminate between the groups is relatively trivial. As the number of groups and variables increases, a single variable may not adequately discriminate between groups, but rather a combination of variables may be needed. The analysis therefore produces a new set of variables or roots, each of which is a linear function of the original variables in the analysis and has the following form:

$$Root = a + b1^{*}x1 + b2^{*}x2 + \ldots bm^{*}xm$$

where a is a constant, $b1$ to bm are regression coefficients, and $x1$ to xm are the original variable values.

If there are more than two groups, then more than one discriminant function can be estimated. The maximum number of functions is equal to the number of groups minus 1, or the number of variables, whichever is smaller.

In the examples presented below, Statistica software was used for the analyses and some of the graphical presentations.

In the case of the Platreef rocks, seven classes (*cf.* Figure 3) and five variables (CaO, MgO, Fe_2O_3, Al_2O_3, and SiO_2) were entered into the analysis and five roots were produced. Roots 1, 2, and 3 are plotted against each other in Figures 3a and 3b.

From an inspection of the two figures the following is evident:

- Very distinct groups or clusters are visible in the plots, indicating the significant potential of chemistry to discriminate between the groups
- Root 1 provides a good discrimination between calc-silicate, high- and low-calcium parapyroxenite, and pyroxenite

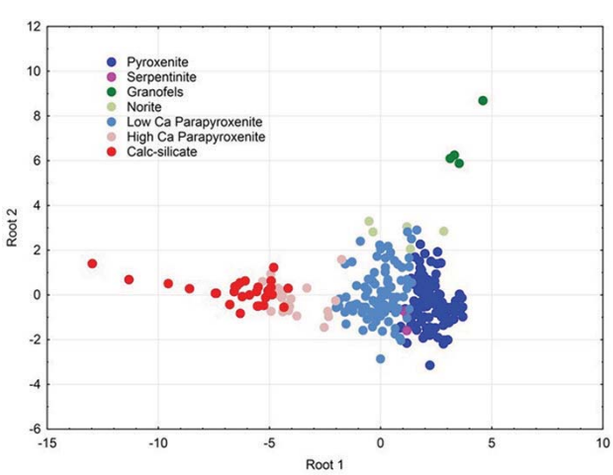

Figure 3a—Scatter plot of root 1 *vs.* root 2 as determined using discriminant analysis. Note that these two roots provide a good discrimination between the major rock groups, including the footwall and hangingwall

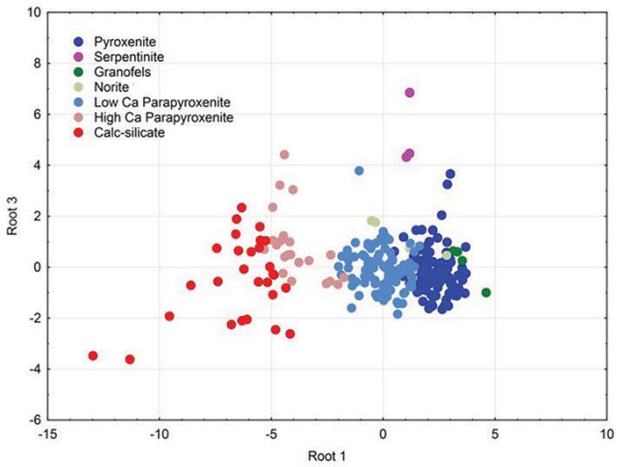

Figure 3b—Scatter plot of root 1 *vs.* root 3 as determined using discriminant analysis. The third root assists in the discrimination of serpentinite

- Root 2 discriminates between the above groups and granofels very well
- Root 2 discriminates between the first four groups and norite fairly well
- Root 2 does not discriminate between the pyroxenites, parapyroxenites, and calc-silicates.
- There is no discrimination of serpentinite from roots 1 or 2
- Root 3 provides discrimination for serpentinite.

As it turns out, root 1 is a strong function of CaO, as would be expected (Schouwstra *et al.*, 2013).

Root 1 accounts for 84.6 % of the discrimination between the rock types, root 2 a further 9.7%, and root 3 a further 4.5%. The remaining roots 4 and 5 contribute the remaining 1.2% and have not been plotted in Figure 3. These results indicate that routine XRF data can most likely be used to map the distribution of rock types in the mining area without the need for detailed mineralogical analysis. To test this approach, additional data-sets were made available by the Anglo American Platinum geology department for classification.

Classification of new data

Having performed the analysis on a set of classified data, the question then arises to what extent this technique can classify new samples based on their whole-rock chemistry. This would provide a quick computational method of classifying data robustly and consistently without any human error. Whether the classification is, strictly speaking, geologically or mineralogically correct is irrelevant if the subsequent classification can be linked to metallurgical performance in a consistent way. Initially, the scatter plots as described above were used to produce algorithms that would classify new samples based on where their calculated roots fell on these plots. This enabled a visualization of how the samples were distributed in the root 1, 2, 3 space and is useful in demonstrating the concept.

A more robust and computationally sound technique is to use the classification functions that are produced by the analysis to calculate the distances between each of the new data-sets and the arithmetic means of each of the categorized classes in the multi-dimensional space defined by the roots. It then follows that the class mean that lies closest to the new data-point defines the class of that new data-point. This is easily calculated on a spreadsheet.

The same approach can be applied to reclassify the original data-set so as to provide information on the goodness of fit of the original model. Using this approach, 89% of the samples were predicted correctly by the model. The worst classification was for norite, which had a success rate of 60%, but as there were only five data-points, one of which was identified as pyroxenite and another as low-calcium parapyroxenite, and as both of these ore types show similar metallurgical responses, this is not a cause for concern.

The other concern with the original algorithm is that when it is applied to bulk historical data obtained from operational sampling there are a significant number of data-points whose roots plot outside of the areas defined by the original XRD data-set. These are classified as unknown when the original algorithm is applied, but if the classification function approach is used it will force a fit into a classification which might or might not be correct. For this reason it is strongly recommended that although the model is robust, more classification work should be done on these 'unknown' samples to correctly identify them and then tune the classification functions accordingly. This process would improve the accuracy of the model with time, but this does not mean that versions of the model could not be implemented immediately and useful information obtained.

Testing the results of the discriminant analysis against geological information

For grade control and stockpiling purposes, all blast-hole samples from the Mogalakwena mine are sent to Anglo American Platinum's Eastern Bushveld Regional Laboratory for chemical analysis. Using a sampling interval of 2.5 m, each blast-hole representing bench thickness provides six samples for PGE analysis (by Sparc), as well as Cu, Ni, and S by XRF. A full XRF scan of the samples also provides quantitative information on the silicate-type compounds. At the start of the project, XRF analyses of approximately 180 000 sample points, representing blast-holes drilled in 2011, were provided for model testing. This data was used to classify the samples into their various rock types using the scatterplot-derived algorithms described earlier (Figure 4 - Schouwstra, 2013). Note that a number of samples are classified as unknown. Many of these are close to the norite-granite/granofels classification. The unknown category is most likely a reflection of the fact that only a few hangingwall and footwall samples were available during development of the discriminate analysis.

The calculated rock type classes were then compared to the geological model based on the descriptions and logs from the mine geologists (Figure 5). Note that rock discrimination by chemistry does not take textural characteristics such as grain size, foliation, brecciation, *etc.*) into account, and granofels (gneiss) and granite are therefore defined as one rock type. Also note that the chemical discrimination reduces the number of rocks to seven classes compared to the 14 common rock types used by the mine geologists.

Further development of a chemistry proxy for geometallurgical modelling

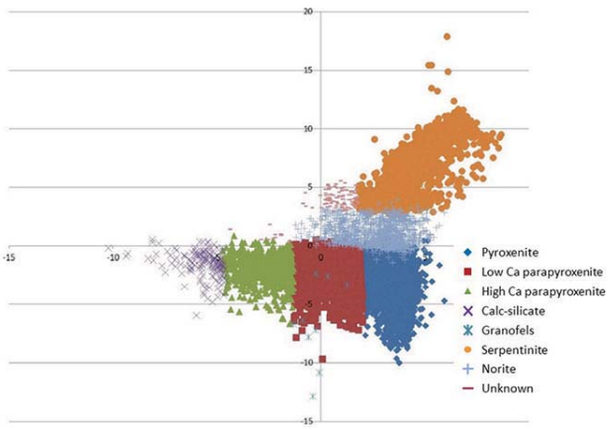

Figure 4— Discrimination plot of approximately 180 000 samples representing blast-holes drilled during 2011

Figure 5 visually demonstrates agreement between the reef package (pyroxenite, parapyroxenite, calc-silicate, and serpentinite), hangingwall, and footwall between the geological model and the rock type discrimination based on XRF data.

For further testing, a chemical data-set of over 50 000 samples comprising several benches was compared with geological data. Table I summarizes the data and compares the results of the chemical classification to the data from the geological model.

It is evident that there are some significant differences between the two methods. Notably, the distribution of samples classified as norite is considerably more than that identified by geologists. With the main differentiation based on the abundance of pyroxene *vs.* feldspar, it is quite possible that a number of high-feldspar pyroxenites (the so-

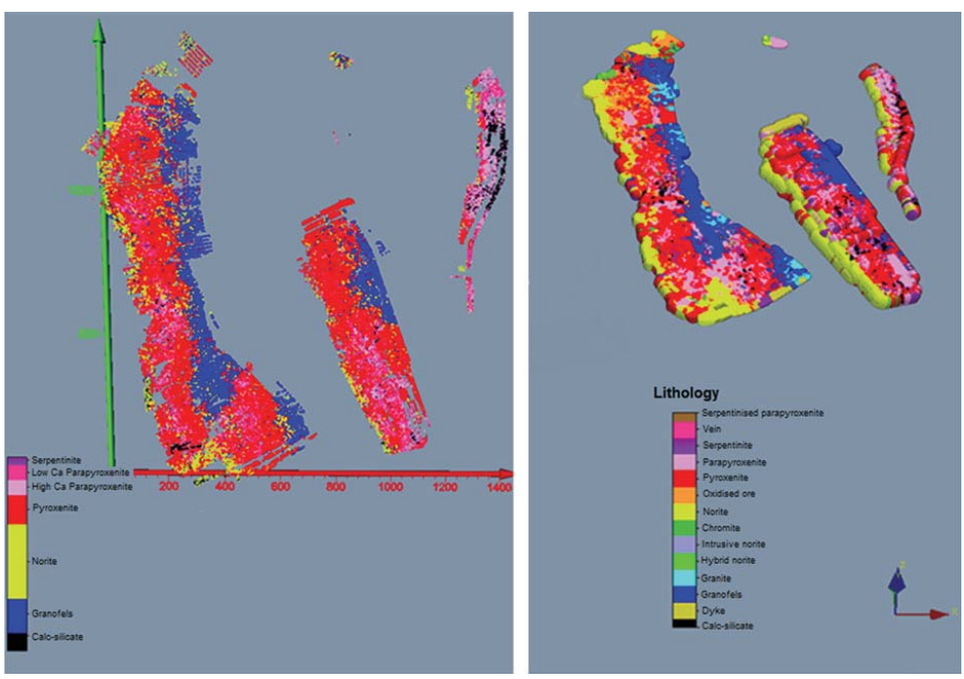

Figure 5—Plot of the geological model for Mogalakwena (right) compared with chemical classification of rock types (left)

Table I

A comparison between the chemical and geological classification of blast-hole samples from the Mogalakwena North operation

Rock type classification by chemistry			Geological classification		
n	Type	% Distribution	*n*	Type	% Distribution
10 048	Norite	19	5 233	Norite	11
16 441	Granofels-granite	31	14 386	Granofels-granite	31
18 640	Pyroxenite	35	22 917	Pyroxenite	50
4 493	Low-Ca parapyroxenite	9	437	Parapyroxenite	1
1 055	High-Ca parapyroxenite	2			
167	Calc-silicate	0	607	Calc-silicate	1
50	Serpentinite	0	2 541	Serpentinite	6
2 067	Unknown	4		Unknown	0
52 961		100	46 121		100

called feldspathic pyroxenites) might have been classed as norites. On the other hand, the geological classification of these samples as feldspathic pyroxenites might be incorrect.

The percentage of pyroxenite classification by chemistry is considerably lower than that identified by geological means. As mentioned earlier, some of the norites might belong with this group. However, if the group classified as low-Ca parapyroxenites is added to the pyroxene group the difference from the geological distribution is reduced significantly. The chemical differentiation between pyroxenite and low-Ca parapyroxenite is based on the amount of diopside present (which is reflected in the Ca content) and is thus an artificial boundary. The visual determination of the presence of a certain percentage of diopside is difficult, especially where the texture is fine-grained. The percentage high-Ca parapyroxenite corresponds with the geological classification of parapyroxenites and perhaps indicates that this highly metasomatosed rock is easier to identify.

Calc-silicate is scarce at the Mogakwena North operation, as reflected by both the chemical classification and the geological identification of this rock group. The Mogalakwena North operation contains very little serpentinite. Many samples described as serpentinite are very fine-grained and altered pyroxenite and parapyroxenite. In most cases, the alteration to the hydrated magnesium silicates (including serpentine and chlorite) is much less than 50%, putting the classification by visual means in question.

As the Mogalakwena North operation is characterized by a high percentage of pyroxenites the exercise was repeated on the Sandsloot operation (further to the south), which contain a higher percentage of parapyroxenites and calc-silicates (Table II).

As seen in the comparison with the Mogalakwena North blast-hole samples, the visual differentiation of the pyroxenite-parapyroxenite group is challenging and the results differ from the chemical classification. The combination of the pyroxenite and low-Ca parapyroxenite groups gives a similar distribution to that of the geologically identified pyroxenite group, whereas the high-Ca parapyroxenite distribution corresponds to that of the parapyroxenite as per the geological model. The amount of calc-silicate present (as calculated from the XRF data) is significantly higher than that in the geological model. No serpentinites were identified by either means.

Although the chemical classification on the blast-hole samples from Mogalakwena North and Sandsloot differs from that supplied by the geologists (visual identification), it is difficult to assess which one better reflects the real rock type distribution. Since the primary aim was to use chemistry as a proxy for ore type, a perfect fit with the geological model is not required—the chemical classification highlights differences in the distribution of the various rock components and delineates zones that are similar in composition. The chemical classification is well-defined and will be consistent as it is based on a quantitative chemical analysis. Figure 6 demonstrates the consistency in chemical classification *vs.* that achieved by visual identification. The figure is a combination of two different benches (2011 and 2013 data) and clearly highlights the disparity in visual identification over time (most likely by different geologists). The chemical classification shows a continuum between the two different sets of data.

Metallurgical characterization/behaviour of various samples representing the different rock types

Preliminary metallurgical characterization test work by Schouwstra *et al.* (2013) allowed the authors to highlight some distinct trends for certain rock groups. Since that time, additional laboratory-scale test work has firmed up on these trends but more work is still required, particularly on those rock types for which not many samples were readily available at that time. In addition, work is required on those rock types that the algorithm classified as unknown in order to decide if they can readily be combined with one of the other geometallurgical zones or need to be placed in a class on their own. Much of the work to date has been on the flotation response of these classifications. Hardness data is available, as well as some work on rheology, as a proxy for plant

Table II

A comparison between the chemical and geological classification of blast-hole samples from the Sandsloot operation

Rock type classification by chemistry			Geological classification		
n	Type	% Distribution	*n*	Type	% Distribution
875	Norite	6	1 064	Norite	11
48	Granofels-granite	0	0	Granofels-granite	0
1 530	Pyroxenite	11	3 542	Pyroxenite	37
3 322	Low-Ca parapyroxenite	23	3 509	Parapyroxenite	37
5 479	High-Ca parapyroxenite	38			
2 947	Calc-silicate	21	1 386	Calc-silicate	15
	Serpentinite	0		Serpentinite	0
146	Unknown	1		Unknown	0
14 347		100	9 501		100

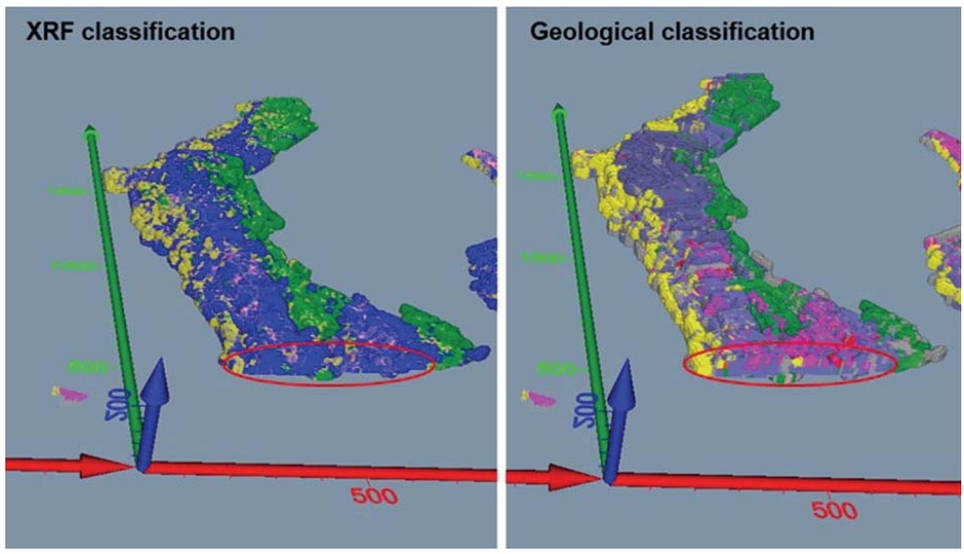

Figure 6—Plot of the geological *vs.* chemical classification over two benches (two sets of data, *i.e.* 2011 and 2013 blast-hole samples)

operability. This data needs to be included in any geometallurgical model that is ultimately put in place in the operation.

All the batch flotation test results on samples from the identified rock types were averaged, and their enrichment ratios (concentrate grade divided by feed grade) *versus* recovery responses are plotted in Figure 7. Seeing that the relationship between recovery and enrichment ratio is essentially a trade-off, it is important to look at the relationship between the two, and not one or the other in isolation. A particular sample might well produce a good recovery but at a sub-economic concentrate grade, for example. Figure 7 also displays the confidence limits. It is clear from these results that there are definite differences between the rock types. The granofels samples had the best flotation response, whereas calc-silicates and high-calcium parapyroxenites were the worst. This is in line with previous experience and was expected. The serpentinites constitute a small data-set, but were also consistently poor.

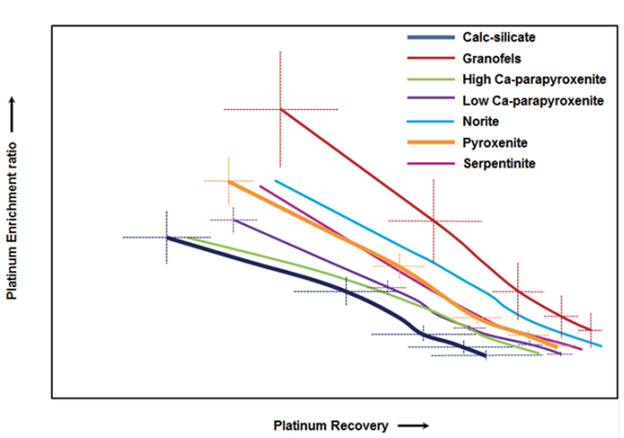

Figure 7—Enrichment ratio and recovery relationships for various rock types as determined in batch flotation laboratory tests

This data facilitates the fitting of a mathematical model to each rock type as described by Schouwstra *et al* (2013). The model defines the relationship between enrichment ratio and metal recovery, depending on the ore type. It thus becomes theoretically possible to predict, for a given ore classification and head grade, the recovery for a given concentrate grade, or the concentrate grade at a given recovery. This type of model can then be integrated into a geometallurgical simulator that provides expected plant performance, depending on the feedstock.

It must be emphasized that the data is from batch flotation tests carried out in ideal laboratory conditions and may be a poor predictor of plant performance. Pilot plant tests in a continuous operation are required to determine firstly, whether the trends identified manifest in a large-scale operation; and secondly, if so, what is the magnitude of the effects. Once this has been established a realistic geometallurgical model may be put in place. In addition, the synergistic or antagonistic effects of ore blending need to be established with confidence so that any decisions emanating from such a model are well-informed.

Combining metallurgical outcomes with chemical classification to define geometallurgical zones

The rock type characterization using XRF data differentiated between seven different rock types—these included the hangingwall and footwall rocks, which are infrequently mineralized.

Metallurgical test work highlighted that the low Ca-parapyroxenite is metallurgically compatible with the pyroxenite, and these two types can thus be combined into one geometallurgical zone. This geometallurgical zone comprises most of the current Mogalakwena North operation.

Where mineralized, the norite (limited data) and granite-granofels exhibit better metallurgical characteristics than the pyroxenites and can also be grouped together.

In terms of flotation characteristics, the high-Ca parapyroxenites behave similarly to samples from the serpentine group. However, with only a few samples belonging to the serpentine group available for testing, as well as some anecdotal evidence of this material having previously caused rheology issues in the operation, it is recommended that these two groups are regarded as two distinctive geometallurgical zones.

Test work has confirmed the poor recoveries previously obtained on calc-silicates, and rocks belonging to that group should be part of a separate geometallurgical domain.

Conclusion

Many reports on processing difficulties at Mogalakwena provided anecdotal evidence that there existed a link between rock type and metallurgical behaviour. This led to the working hypothesis that mine planning and ore processing based on rock type classification should improve production and assist with optimizing the milling and flotation regime.

Geological characterization and metal recovery potential are an integral part of a value-based spatial resource model that incorporates estimates of various aspects of the mining value chain into each of the smallest mining units, and ultimately leads to optimized mining decisions.

Using a geological rock type classification (using visual classification or X-ray diffractometry) would most likely lead to a rock model incorporating more than 15 rock types. Some of these rock types would have a very small volumetric distribution, complicating the mining process. Keeping the number of geometallurgical zones small—even though that might slightly increase the variation—makes the process more viable.

The initial study used CaO as an indicator of rock type, but using a more comprehensive set of chemistry data and a principal component analysis approach made it possible to subdivide the rocks in the Mogalakwena mine into seven different classes. Focusing on the mineralized rocks (*i.e.* ignoring the footwall and hangingwall) further reduces this to five for the whole mining operation or four for the Mogalakwena North pit, where the highly altered calc-silicate rock is poorly developed. Limiting the number of geometallurgical zones will obviously simplify the mining and process schedules.

The link between these different rock classes and metallurgical behaviour is tentative at the moment. Although our preliminary data corroborates some of the anecdotal evidence (*i.e.* calc-silicate has always been regarded as a problematic ore and is typically stockpiled for future processing), the data is limited, especially on the scarcer rock types. The data is also currently based on standard laboratory tests, using a standard grind, flotation times, and reagents.

It is therefore imperative to continue with the metallurgical characterization of the different ore types and link these to the proxy-based geometallurgical model. This should include test work on several blends of poor and good ores to determine the impact of blends on metallurgical throughput and recovery, as well as pilot plant confirmation and qualification of the trends observed. The impact of variable grade on recovery also needs to be better quantified.

It is further recommended that XRF characterization and modelling of proxies be continued. The models should be revised and improved as new information becomes available and as knowledge on the interaction between geological and metallurgical parameters improves.

The study thus far has shown that there is not much value in changing the mining method at Mogalakwena North (where only 10% of the rock types will have a deleterious effect on processing), but it is believed that selective mining by rock type will have a pronounced effect as mining moves towards areas where the rock type distribution is more variable and where the mining area contains a larger percentage of mineralization with detrimental metallurgical characteristics.

References

Hill, T. and Lewicki, P. 2006. Statitistics: Methods and Applications – A Comprehensive Reference for Science, Industry and Data Mining. 1st edn. Statsoft. pp.155–162.

Holwell, D.A. 2006. The roles of magmatism, contamination and hydrothermal processes in the development of Platreef mineralization, Bushveld Complex, South Africa, PhD thesis, Cardiff University.

Holwell, D.A. and McDonald, I. 2006. Petrology, geochemistry and the mechanisms determining the distribution of platinum-group element and base metal sulfide mineralization in the Platreef at Overysel, northern Bushveld Complex, South Africa. *Mineralium Deposita*, vol 41. pp. 575–598.

Kinnaird, J.D., Hurchinson, D., Schurmann, L., Nex, P., and De Lange, R. 2005. Petrology and mineralisation of the southern Platreef: northern limb of the Bushveld Complex, South Africa. *Mineralium Deposita*, vol 40. pp 576–597.

Nex, P., Kinnaird, J.D., Jones, B., and Colloty, A. 2006. Platreef rock type definitions and descriptions. Economic Geology Research Institute, University of the Witwatersrand, Johannesburg.

Schouwstra, R.P., De Vaux, D., Muzondo, T., and Prins, C. 2013. A geometallurgical approach at Anglo American Platinum's Mogalakwena operation. *Proceedings of the Second AusIMM International Geometallurgy Conference (Geomet 2013)*, Brisbane, Queensland, 30 September – 2 October 2013. Australasian Institute of Mining and Metallurgy, Melbourne. pp. 85–92. https://www.researchgate.net/publication/262973972_A_geometallurgical_approach_at_Anglo_American_Platinum%27s_Mogalakwena_operation

White J.A. 1994. The Potgietersrust prospect – Geology and exploration history. *Proceedings of the XVth CMMI Congress*, Johannesburg, South Africa. Glen, H.W. (ed.). vol. 3. *Symposium Series* no. 14. South African Institute for Mining and Metallurgy, Johannesburg. pp. 173–181

Wagner, A. 1929. The Platinum Deposits and Mines of South Africa, Oliver and Boyd, Edinburgh. ◆

The Southern African Institute of Mining and Metallurgy are hosting the

7th International Platinum Conference

'Platinum— A Changing Industry'

In Association with **AMI Precious Metals 2017**

18–19 October 2017 — Conference • 20 October — Technical Tours

Protea Hotel Ranch Resort, Polokwane, South Africa

BACKGROUND

The 7th International Platinum Conference is to be held in Polokwane, Limpopo, South Africa in October 2017.

The Platinum conference series has covered a range of themes since inception in 2004, and traditionally addresses the opportunities and challenges facing the platinum Industry. This prestigious event attracts key role players and industry leaders through:

- High quality technical papers and presentations
- Facilitating industry networking
- Having large, knowledgeable audiences
- Global participation, and
- Comprehensive support from industry role players.

The Platinum 2017 Conference will be held in association with the Precious Metals Development Network (PMDN) of the DST's Advanced Metals initiative (AMI Conference 2017)

Thie AMI conference presents a forum where scientists and technologists can come together to learn and discuss the latest advances in precious metals (platinum group metals and gold) science and technology.

The 2017 event will, under the guidance of the organising committee, structure a programme which covers critical aspects of this continually evolving and exciting industry.

However the success and relevance of this event to the industry really depends on your participation and support. You can participate in this event as an organising committee member, author/presenter, delegate or sponsor.

We look forward to your support and engagement in the 7th International Platinum Conference.

Thank you.

Dr Gordon Smith
Chair—Organising Committee

ABOUT THE VENUE

The Protea Hotel Ranch Resort Polokwane, on the Eastern Limb of the Southern African Bushveld is the exciting new venue for the 2017 Platinum Conference. Polokwane is the capital city and urban heartbeat of Limpopo, known as the gateway city as it is a stepping stone to a diversity of natural attractions from mountains to wilderness areas. The city is in close proximity to a number of Platinum operations allowing for multiple technical visits.

WHO SHOULD ATTEND

- Academics
- Business development managers
- Concentrator managers
- Consultants
- Engineers
- Exploration managers
- Explosives engineers
- Fund managers
- Geologists
- Hydrogeologists
- Innovation managers
- Investment managers
- Market researchers and surveyors
- Marketing managers
- Mechanical engineers
- Metallurgical managers
- Metallurgical consultants
- Metallurgists
- Mine managers
- Mining engineers
- New business development managers
- Planning managers
- Process engineers
- Product developers
- Production managers
- Project managers
- Pyrometallurgists
- Researchers
- Rock engineers
- Scientists
- Strategy analysts
- Ventilation managers

Sponsor bme · CiDRA Minerals Processing · ERIEZ · FLSmidth · Murray & Roberts · Murray & Roberts Cementation · RHI · SANDVIK

FOR FURTHER INFORMATION CONTACT:
Conference Co-ordinator: Gugulethu Charlie
E-mail: gugu@saimm.co.za •**Tel:** +27 11 834 1273/7 • **www.saimm.co.za**

SAIMM The Southern African Institute of Mining and Metallurgy

ami advanced metals initiative

INTERNATIONAL ACTIVITIES

2017

10–12 July 2017 — **Water 2017 Conference**
Lifeblood of the Mining Industry
Emperors Palace, Hotel Casino Convention Resort, Johannesburg
Contact: Camielah Jardine
Tel: +27 11 834-1273/7
Fax: +27 11 838-5923/833-8156
E-mail: camielah@saimm.co.za
Website: http://www.saimm.co.za

25–26 July 2017 — **Entrepreneurship in Mining Forum**
A Focus on New Business in Mining
De Beers, Johannesburg
Contact: Camielah Jardine
Tel: +27 11 834-1273/7
Fax: +27 11 838-5923/833-8156
E-mail: camielah@saimm.co.za
Website: http://www.saimm.co.za

3–4 August 2017 — **Building a Robust Mineral Industry** *Thriving under prolonged low commodity price environment*
Cresta Lodge, Msasa, Harare
Contact: Gugulethu Charlie
Tel: +27 11 834-1273/7
Fax: +27 11 838-5923/833-8156
E-mail: gugu@saimm.co.za
Website: http://www.saimm.co.za

4–9 August 2017 —**Rapid Underground Mine & Civil Access Conference 2017**
Emperors Palace, Hotel Casino Convention Resort, Johannesburg
Contact: Camielah Jardine
Tel: +27 11 834-1273/7
Fax: +27 11 838-5923/833-8156
E-mail: camielah@saimm.co.za
Website: http://www.saimm.co.za

15–16 August 2017 —**The SAMREC and SAMVAL Codes**
Advanced Workshop: Can you face your peers?
Emperors Palace, Hotel Casino Convention Resort, Johannesburg
Contact: Gugulethu Charlie
Tel: +27 11 834-1273/7
Fax: +27 11 838-5923/833-8156
E-mail: gugu@saimm.co.za
Website: http://www.saimm.co.za

22–24 August 2017 — **The biennial Southern African Coal Processing Society Conference and Exhibition**
'Coal Processing – the key to profitability'
Graceland Hotel, Casino and Country Club, Secunda
Contact: Gerda Craddock
Tel: +27 11 432-8918
E-mail: gerdac@mineralconcepts.co.za
Website: www.sacoalprep.co.za

30 August–1 September 2017 — **MINESafe Conference 2017** *Striving for Zero Harm—Driving Excellence through Compliance*
Emperors Palace, Hotel Casino Convention Resort, Johannesburg
Contact: Camielah Jardine
Tel: +27 11 834-1273/7
Fax: +27 11 838-5923/833-8156
E-mail: camielah@saimm.co.za
Website: http://www.saimm.co.za

11–15 September 2017 — **Uranium 2017 International Conference**
Extraction and Applications of Uranium — Present and Future
Swakopmund Hotel, Swakopmund, Namibia
Contact: Camielah Jardine
Tel: +27 11 834-1273/7
Fax: +27 11 838-5923/833-8156
E-mail: camielah@saimm.co.za
Website: http://www.saimm.co.za

20–21 September 2017 — **Global Mining Standards and Guidelines Group (GMSG)**
Creating community to drive operational excellence

INTERNATIONAL ACTIVITIES

2017

Emperors Palace, Hotel Casino Convention Resort, Johannesburg
Contact: Gugulethu Charlie
Tel: +27 11 834-1273/7
Fax: +27 11 838-5923/833-8156
E-mail: gugu@saimm.co.za
Website: http://www.saimm.co.za

30 September–6 October 2017 — **AfriRock 2017: ISRM International Symposium**—*Rock Mechanics for Africa*
Cape Town Convention Centre, Cape Town
Contact: Camielah Jardine
Tel: +27 11 834-1273/7
Fax: +27 11 838-5923/833-8156
E-mail: camielah@saimm.co.za
Website: http://www.saimm.co.za

6 October 2017 — **Empirical methods, rock mechanics, and structural geological methods useful for excavation in jointed/fractured media**
One-Day Short Course
Johannesburg
Contact: Camielah Jardine
Tel: +27 11 834-1273/7
Fax: +27 11 838-5923/833-8156
E-mail: camielah@saimm.co.za
Website: http://www.saimm.co.za

17–20 October 2017 — **AMI Precious Metals 2017**
The Precious Metals Development Network (PMDN)
Protea Hotel Ranch Resort, Polokwane
Contact: Camielah Jardine
Tel: +27 11 834-1273/7
Fax: +27 11 838-5923/833-8156
E-mail: camielah@saimm.co.za
Website: http://www.saimm.co.za

18–20 October 2017 — **7th International Platinum Conference**
Platinum—A Changing Industry
Protea Hotel Ranch Resort, Polokwane
Contact: Gugulethu Charlie
Tel: +27 11 834-1273/7
Fax: +27 11 838-5923/833-8156
E-mail: gugu@saimm.co.za
Website: http://www.saimm.co.za

25 October 2017 — **14th Annual Student Colloquium**
Johannesburg
Contact: Gugulethu Charlie
Tel: +27 11 834-1273/7
Fax: +27 11 838-5923/833-8156
E-mail: gugu@saimm.co.za
Website: http://www.saimm.co.za

6–7 November 2017 — **Coal Preparation Society of India**
5 International Conference & Exhibition
'Coal Washing: a sustainable approach towards a greener environment'
Silver Oak Hall, India Habitat Centre, Lodhi Road, New Delhi-110003, www.cpsi.org.in

Company Affiliates

The following organizations have been admitted to the Institute as Company Affiliates

3M South Africa (Pty) Limited

AECOM SA (Pty) Ltd

AEL Mining Services Limited

Air Liquide (PTY) Ltd

AMEC Foster Wheeler

AMIRA International Africa (Pty) Ltd

ANDRITZ Delkor(pty) Ltd

Anglo Operations Proprietary Limited

Anglogold Ashanti Ltd

Arcus Gibb (Pty) Ltd

Aurecon South Africa (Pty) Ltd

Aveng Engineering

Aveng Mining Shafts and Underground

Axis House Pty Ltd

Bafokeng Rasimone Platinum Mine

Barloworld Equipment -Mining

BASF Holdings SA (Pty) Ltd

BCL Limited (BCL001)

Becker Mining (Pty) Ltd

BedRock Mining Support Pty Ltd

Bell Equipment Limited

BHP Billiton Energy Coal SA Ltd

Blue Cube Systems (Pty) Ltd

Bluhm Burton Engineering Pty Ltd(BLU003)

Bouygues Travaux Publics

CDM Group

CGG Services SA

Chamber of Mines

Concor Opencast Mining

Concor Technicrete

Council for Geoscience Library

CRONIMET Mining Processing SA Pty Ltd

CSIR Natural Resources and the Environment (NRE)

Data Mine SA

Department of Water Affairs and Forestry

Digby Wells and Associates

DRA Mineral Projects (Pty) Ltd

Duraset

Elbroc Mining Products (Pty) Ltd

eThekwini Municipality

Expectra 2004 (Pty) Ltd

Exxaro Coal (Pty) Ltd

Exxaro Resources Limited

Filtaquip (Pty) Ltd

FLSmidth Minerals (Pty) Ltd (FFE001)

Fluor Daniel SA (Pty) Ltd

Franki Africa (Pty) Ltd-JHB

Fraser Alexander Group

Geobrugg Southern Africa (Pty) Ltd

Glencore

Goba (Pty) Ltd

Hall Core Drilling (Pty) Ltd

Hatch (Pty) Ltd

Herrenknecht AG

HPE Hydro Power Equipment (Pty) Ltd

IMS Engineering (Pty) Ltd

Ivanhoe Mines SA

Joy Global Inc.(Africa)

Kudumane Manganese Resources

Leco Africa (Pty) Limited

Longyear South Africa (Pty) Ltd

Lonmin Plc

Lull Storm Trading (Pty)Ltd T/A Wekaba Engineering

Magotteaux (Pty) Ltd

MBE Minerals SA Pty Ltd

MCC Contracts (Pty) Ltd

MD Mineral Technologies SA (Pty) Ltd

MDM Technical Africa (Pty) Ltd

Metalock Engineering RSA (Pty)Ltd

Metorex Limited

Metso Minerals (South Africa) Pty Ltd

MineRP Holding (Pty) Ltd

Mintek

MIP Process Technologies (Pty) Limited

MSA Group (Pty) Ltd

Multotec (Pty) Ltd

Murray and Roberts Cementation

Nalco Africa (Pty) Ltd

Namakwa Sands(Pty) Ltd

Ncamiso Trading (Pty) Ltd

New Concept Mining (Pty) Limited

Northam Platinum Ltd - Zondereinde

PANalytical (Pty) Ltd

Paterson & Cooke Consulting Engineers (Pty) Ltd

Perkinelmer

Polysius A Division Of Thyssenkrupp Industrial Sol

Precious Metals Refiners

Rand Refinery Limited

Redpath Mining (South Africa) (Pty) Ltd

Rocbolt Technologies

Rosond (Pty) Ltd

Royal Bafokeng Platinum

Roytec Global (Pty) Ltd

RungePincockMinarco Limited

Rustenburg Platinum Mines Limited

Salene Mining (Pty) Ltd

Sandvik Mining and Construction Delmas (Pty) Ltd

Sandvik Mining and Construction RSA(Pty) Ltd

SANIRE

SENET (Pty) Ltd

Senmin International (Pty) Ltd

Smec South Africa

SMS group Technical Services South Africa (Pty) Ltd

Sound Mining Solution (Pty) Ltd

SRK Consulting SA (Pty) Ltd

Technology Innovation Agency

Time Mining and Processing (Pty) Ltd

Timrite Pty Ltd

Tomra (Pty) Ltd

Ukwazi Mining Solutions (Pty) Ltd

Umgeni Water

VBKOM

Webber Wentzel

Weir Minerals Africa

Worley Parsons RSA (Pty) Ltd

SAFETY AND SUSTAINABILITY

Fraser Alexander is dedicated to the safety of people as one of our core strengths. Our Beyond-Zero-Harm Policy (always alert, always focused, never complacent) is firmly practised at Board and Exco levels, through to the operational front lines. This is evidenced by our Lost Time Injury Frequency Rate consistently outperforming the industry average.

Our aspiration is to leave a future behind for the communities around our operations by employing local talent, preserving the mining environment and unlocking the resource value to the benefit of all our stakeholders. We achieve operational excellence through development and empowerment of our local teams.

FRASER ALEXANDER TAILINGS SERVICES

Our broad focus is placed on safely sustaining the mining industry and managing risk. We continuously innovate on our services and currently manage and operate more than 120 tailings storage facilities (TSF's) and hydraulic mining sites worldwide.

Tailings deposition

With over 105 years of experience in cyclone, daywall, spigot and impoundment facilities, we are positioned to provide focused risk management on any tailings facility. We currently manage in excess of 100 tailings deposition operations globally, totalling more than 200 Mtpa.

Hydraulic mining

Our state-of-the-art hydraulic mining solutions enable our clients to unlock value from their dormant tailings facilities. We currently manage more than 25 hydraulic mining operations in Africa and South America, hydraulically mining, slurrying and pumping in excess of 50 Mtpa of tailings.

Due to our specialist technical capabilities and collaboration with our clients and design engineers, we have executed a number of turnkey hydraulic mining solutions across various commodities.

Risk management (Technical and Operations Risk Assessment System – TORAS)

Fraser Alexander is the largest outsourced tailings contractor on the African continent. Our most significant risk, and in turn that of our shareholders, is the inherent risk posed by our tailings deposition contracts. It is critical that this risk is understood, measured and managed appropriately. To this end, Fraser Alexander has implemented an internal Technical and Operational Risk Assessment System (TORAS) that is in line with international legislation, best practice and governance standards.

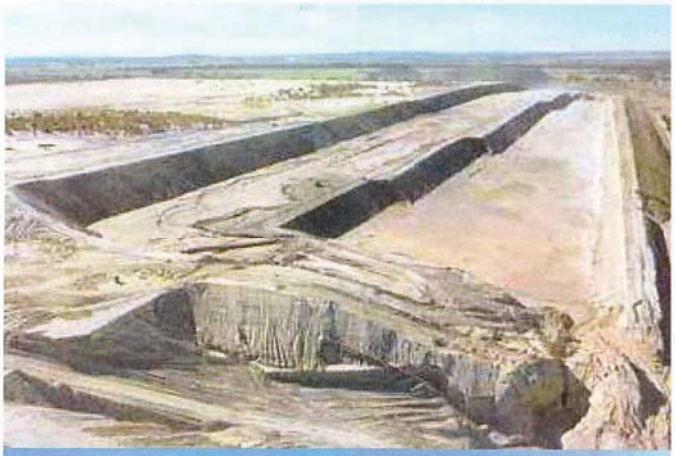

TORAS is used to measure and manage compliance of each and every deposition contract to set operating standards, technical criteria and required documentation. Suitable external parties are appointed to review TORAS in line with international best practice.

Tailings deposition represents significant business risk for mining companies, inherently associated with poor management of the tailings storage facility. An experienced expert tailings operator, in collaboration with the engineer of record and mine management, significantly reduces this risk.

FRASER ALEXANDER

fainfo@fraseralexander.co.za
South Africa: +27 11 929 3600
Zambia: +260 968 3229 68
www.fraseralexander.co.za

FRASER ALEXANDER

Fraser Alexander is your trusted mining services partner, delivering world-class outsourced services across the entire mining value chain. Operating in the mining industry since 1912, the company has been growing its innovative business across the globe.

OUR FOOTPRINT

Our presence spans across Botswana, Brazil, Côte d'Ivoire, Democratic Republic of Congo, Ghana, Mali, Namibia, South Africa, Tanzania, Zambia and Zimbabwe.

VISION

'To be the preferred outsourcing mining services partner in Africa'

MISSION

'We provide outsourced services and solutions to mining & heavy industry'

OUR TOTAL SERVICE OFFERING

We provide **outsourced services** and **related infrastructure** to **move, manage** and **add value** to **minerals, waste** and **water.**

Mining

- Hydraulic mining of tailings
- Mechanical remining of tailings and coal discards

Processing

Operation and maintenance of:

- Mineral processing plants
- Crushing and screening plants
- Water treatment plants

Moving

- Load and haul of waste and tailings
- Dry bulk materials handling
- Slurry pumps and pipelines

Deposition

Operation and maintenance of:

- Tailings disposal facilities
- Discard dumps

Construction

- Pre-deposition works for tailings and waste facilities
- Civil infrastructure
- Bulk, engineered earthworks

fainfo@fraseralexander.co.za | South Africa: +27 11 929 3600 | Zambia: +260 968 3229 68 | www.fraseralexander.co.za